UNIVERSITÀ DEGLI STUDI DI TRIESTE

XXXV CICLO DEL DOTTORATO DI RICERCA IN NANOTECNOLOGIE

PO FRIULI VENEZIA GIULIA - FONDO SOCIALE EUROPEO 2014/2020

Oxidation of Transition and Noble Metal Size-Selected Clusters Supported on Epitaxial Graphene

Settore scientifico-disciplinare: FIS/03 Fisica della Materia

DOTTORANDO
FEDERICO LOI

COORDINATORE
PROF. ALBERTO MORGANTE

SUPERVISORE DI TESI
PROF. ALESSANDRO BARALDI

CO-SUPERVISORE DI TESI
Dr. LUCA BIGNARDI

ANNO ACCADEMICO 2021/2022

UNIVERSITY OF TRIESTE

Department of Physics

Graduate School in Nanotechnology, Cycle XXXV

PhD Thesis

Oxidation of Transition and Noble Metal Size-Selected Clusters Supported on Epitaxial Graphene

Supervisor:
Prof. Alessandro Baraldi

Co-supervisor:
Dr. Luca Bignardi

Candidate:
Federico Loi

Academic Year 2021-2022

Abstract

Size-selected clusters have emerged in the past decades for their unique features, which often differ from those of their bulk analogues. In a cluster, the electronic and chemical features can be tuned be changing n, exact number of atoms composing them, offering an unmatched playground to look for new properties of matter. However, clusters are hard to handle due to their high reactivity and mobility when they are deposited on solid surfaces. In particular, understanding the interaction of supported metallic size-selected clusters with simple molecules such as oxygen and their oxidation process in conditions where the mass selection is not compromised is experimentally challenging.

During my PhD, I was able to focus on this aspect using ENAC (Exact Number of Atoms in each Cluster), the cluster source designed and built at the Nanoscale Materials Laboratory of the Elettra synchrotron facility in Trieste. The unique feature of ENAC is that it can be directly connected to the SuperESCA beamline of Elettra to deposit and study the cluster *in situ* by means of experimental techniques based on synchrotron radiation, such as X-ray photoelectron spectroscopy (XPS). This offers the opportunity to characterize the clusters in controlled conditions, avoiding critical issues such as the presence of contaminants and drastically limiting their diffusion.

In the first part of my research activity, I have been involved in the commissioning and optimization of the cluster source, and in its installation at the SuperESCA beamline. When this crucial goal was accomplished, I participated to the first experiment ever performed with the cluster source at the beamline. We studied the adsorption of size selected Ag_n clusters with $n = 1, 3$ and 7 on Ru(0001) by means of XPS and with the support of density functional theory (DFT) calculations. Our results indicate that using different clusters as building blocks, it is possible to form two-dimensional Ag islands on Ru(0001) with different degrees of order that depend on the size of the cluster. In particular, Ag_7, thanks to its hexagonal shape, was proven to be the best building block to minimized the density of defects on the islands. This experiment acted as benchmark to test the capabilities of ENAC, and was instrumental to address our investigation towards more complex systems.

The following experiments were dedicated to the main topic of my PhD project, i.e., the oxidation of graphene-supported size-selected clusters. We focused on three technologically relevant materials such as Ag, Pt and Fe. Especially in their oxide phase, these elements play major roles in several industrially relevant reactions such as the epoxidation of ethylene, the oxygen reduction reaction and the CO oxidation. Understanding their fundamental properties at the sub-nanoscale can offer the possibility to further optimize their catalytic activity and to reduce the cost of the catalysts. Epitaxial graphene, grown on Ru(0001) and Ir(111), is the template that was selected for the cluster deposition due to the combination between its low interaction with the clusters and to the high diffusion barriers on its corrugated moiré lattice. To further reduce the cluster mobility and preserve the mass selection, all the experiments were performed at the temperature of 20 K and the cluster oxidation was achieved by exploiting a method based on the photo-induced dissociation of physisorbed O_2, which led to an efficient production of atomic O in an extremely clean environment. The three different clusters, in a size range $n = 7 - 20$, were studied combining XPS with DFT calculation both in the metallic phase and after the exposure to oxygen. The analysis was performed by constantly comparing the properties of the clusters with their counterparts at larger scales, looking for analogies

and differences.

The oxidation of a Ag cluster composed of 11 atoms induced a final stoichiometry, as well as geometric and electronic features, similar to the AgO bulk oxide, proving that, unlike their metallic counterparts, bulk oxide features can appear also at the sub-nanoscale. Afterwards, we extended the study also to Ag_7 to investigate the core level shift anomaly of Ag, which is characterized by a negative shift upon oxidation. Our work highlighted a unique behavior of the Ag 3d core levels and Ag 4d-band with oxidation that is not observed in bulk and metallic surfaces, highlighting the different electronic properties of matter at this scale.

After Ag, we moved to Pt_n clusters, with $n = 7, 12$ and 13, supported on graphene epitaxially grown on Ir(111). Following the same approach adopted for Ag, we have shown that the stronger interaction with the substrate induces an asymmetric oxidation of the clusters, with the upper atoms that reach an higher oxidation state than those at the cluster/graphene interface. In particular, the atoms with the highest oxidation state resemble the Pt_3O_4 oxide phase, which is generally associated to an high chemical reactivity. Finally, we moved to the oxidation of Fe_n clusters for $n = 11, 12, 13, 15$ and 20 supported on graphene on Ru(0001). In this case, the oxidation led to homogeneous clusters with a stoichiometry close to $(FeO)_n$, where all the atoms reach an oxidation state 2+. This is in agreement with observation for clusters in the gas phase and in contrast with the properties of Fe at larger scales, where the FeO oxide phase is thermodinamically unstable.

The experiments that we performed withing my PhD project aim to extended our knowledge on the fundamental oxidation process at the sub-nanoscale in the case of graphene-supported size-selected clusters of various catalytically relevant materials to set the bases to further optimize their applications in nanostructerd catalysts.

List of Acronyms

2D two-dimensional

3D three-dimensional

AFM Atomic Force Microscopy

BE Binding Energy

CLS Core Level Shift

CN Coordination Number

DC Direct Current

DFT Density Functional Theory

DS Doniach-Šunjić

ENAC Exact Number of Atoms in each Cluster

ESCA Electron Spectroscopy for Chemical Analysis

FWHM Full Width at Half Maximum

GR Graphene

GR/Ir Graphene epitaxially grown on Ir(111)

GR/Ru Graphene epitaxially grown on Ru(0001)

HOPG Highly Oriented Pyrolytic Graphite

LDA Local Density Approximation

NEXAFS Near-Edge X-Ray Absorption Fine Structure

nmLab nanoscale materials Laboratory

ORR Oxygen Reduction Reaction

PBE Perdew–Burke-Ernzerhof

PDOS Projected Density of States

PE Pass Energy

PES Photoelectron Emission Spectroscopy

QMS Quadrupole Mass Spectrometer

RF Radio Frequency

RGA Residual Gas Analyzer

RT Room Temperature (300 K)

SCLS Surface Core Level Shift

STM Scanning Tunneling Microscopy

TEM Transmission Electron Microscopy

UHV Ultra High Vacuum

UV Ultraviolet

VASP Vienna Ab-initio Simulation Package

VUV Vacuum Ultra Violet

XAS X-ray Absorption Spectroscopy

XPS X-ray Photoelectron Spectroscopy

Contents

CHAPTER 1

Introduction

Driven by innate curiosity, mankind started manipulating the surrounding world starting from its very first appearance in our planet. It began with the development of tools for cutting, chopping or scraping and it has evolved over the centuries with an ever more refined level of precision, always paralleled by technological innovation. When this manipulation reaches the atomic scale, we enter the field of Nanotechnology. Here, some objects have properties that depend on the exact number of atoms composing them. They are known as *clusters*.

Clusters are generally defined as atomic agglomerates composed of less than 1000 atoms which can exhibit a large variety of fascinating physical and chemical properties that are not observed in their bulk counterparts [1, 2]. Their astonishing size-related behavior was first investigated for well-defined clusters in the gas-phase using pioneering techniques for cluster generation, based on laser ablation and mass spectrometers. These pivotal experiments showed that some clusters with a specific well-defined number of atoms were associated to a higher production yield and stability (Fig. 1.1)[3, 4]. The importance of this first result is perfectly described by the adjective that was attributed to those numbers: *magic*. The efforts to interpret this fascinating behavior led to the development of theoretical models to describe and predict the properties of the clusters. The jellium model [5, 6] describes how the individual atoms in the clusters delocalize the valence electrons over a uniformly charged spherical volume. This electron confinement leads to quantized orbitals labeled as, for example, 1S, 1P, 1D, 2S, 1F and 2P. When a cluster has just enough valence electrons to complete one of these shells, it becomes more stable. This happens when the clusters are composed of a number of atoms $n = 2$, 8, 18, 20, 34, 40 and 58, which correspond to the magic numbers measured for alkali and coinage metals (Cu, Ag and Au). In fact, the jellium model is based on the assumption that each atom in the cluster contributes with one single valence electron [7]. In other cases, such as for noble gas and transition metal clusters, the magic numbers can be related to the geometric structures. An enhanced stability is obtained based on the most dense icosahedral packing, with the most prominent peaks in mass spectra corresponding to completed icosahedral shells of 13, 55, 147 and 309 atoms (Fig. 1.2) [8].

Once the appearance of clusters with enhanced stability was proven, the attention shifted to a second question: what happens if you add or remove one or few atoms from a magic number cluster? The remarkable answer is that it becomes less stable and, therefore, more reactive [9, 10]. This simple concept set the basis for the application of clusters in catalysis, where the ability to tune selectivity and activity in chemical reactions through minor changes in cluster size and composition opens

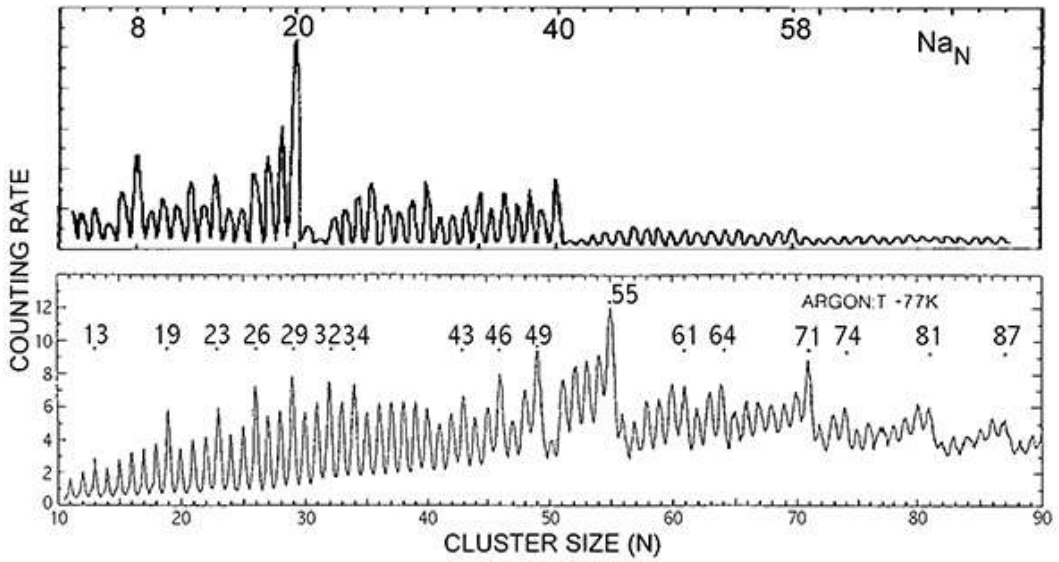

Figure 1.1: *Mass spectra measured for Ar and Na clusters. The intense peaks correspond to the magic numbers reported in the spectra and indicate enhanced stability. Adapted from Ref.s [8, 15].*

the doors to a new world of possibilities [11, 12]. Moreover, heterogeneous catalysis is a surface scenario, with bulk atoms that play an inert role in most reactions. Getting rid of those unnecessary atoms is particularly important as many catalysts are composed of precious metals. Clusters offer a great opportunity to overcome the limit imposed by the cost and low abundance of such metals, since they posses the highest ratio of surface-to-bulk atoms that nature can offer. This ratio drastically increases the number of under-coordinated atoms in the clusters compared to surfaces and nanoparticles. The coordination number of an atom, i.e., the number of atoms bonded to it, plays a key role in the reaction path of molecules on a surface [13] due to the modifications that it induces to the d-band center, a well known indicator of chemical reactivity [14]. Low coordinated sites, i.e., those composed of under-coordinated atoms, are considered to be the most active ones, and clusters, which are the structures with the highest density of under-coordinated atoms, have the potential to be the most reactive catalysts.

Due to their unique behavior, clusters represent an unprecedented playground to look for new properties of matter towards applications in several fields of science. Their properties are not related only on *which* atoms compose them, but also on *how many*. Therefore, it is possible to introduce n, the number of atoms in the clusters, as a third dimension of the periodic table [1, 16]. However, this fascinating discovery is inevitably accompanied by the need for a new characterization of this newly-defined periodic table, since the known properties of a material in the surface or bulk phase may drastically change at the sub-nanoscale. Such characterization has been extensively performed for a wide range of clusters, first in the gas-phase and later for clusters deposited on solid surfaces. The investigations in the gas-phase showcased once again the catalytic potential of the clusters in several reactions such as the activation of methane [17] and oxygen [18], or the breaking of C−C and C−H bonds in hydrocarbons [19, 20]. The transition from the gas-phase to supported clusters is a necessary step towards technological applications [21]. Two fundamental

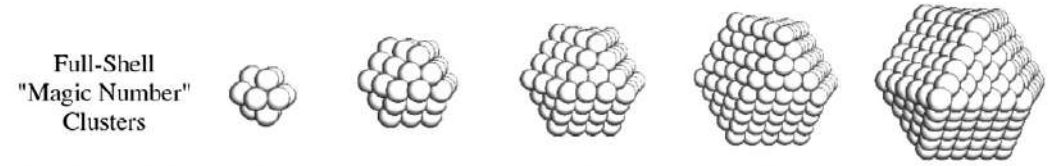

Full-Shell "Magic Number" Clusters					
Number of shells	1	2	3	4	5
Number of atoms in cluster	M_{13}	M_{55}	M_{147}	M_{309}	M_{561}
Percentage surface atoms	92%	76%	63%	52%	45%

Figure 1.2: *Stable geometries of the smallest closed shell magic number clusters according to the icosahedral packing and percentage of surface atoms for each of them. Adapted from [46].*

ingredients played a key role in moving towards this direction: (i) the continuous development of size-selected cluster sources that allow to produce, transport and deposit the clusters on suitable substrates in the so-called soft-landing conditions, i.e., with a kinetic energy per atom $E_K < 1$ eV/atom [22–24], and (ii) the possibility to fully exploit surface science techniques to characterize the supported clusters [11]. Besides microscopy techniques such as scanning tunneling microscopy (STM) [25], atomic force microscopy (AFM) [26] and transmission electron microscopy (TEM) [27], photoelectron emission spectroscopies (PES) played a crucial role in linking the geometric and electronic properties of the clusters to their catalytic reactivity [28, 29].

A major challenge that had to be faced when the clusters where first deposited on surfaces was their stability, since they are prone to sinter and agglomerate into larger structures. To overcome this problem, oxidized surfaces have been adopted as templates where to deposit the clusters, exploiting the high surface-cluster interaction to reduce the mobility of the atomic aggregates. Among the first XPS experiments in this context, it is important to mention the pioneering works by Cox and co-workers [29] and by the group of Eberhardt [30] who, in the '90s, studied the size-related features respectively of Pt_n and Au_n clusters deposited on the natural oxide coating of a Si wafer (Fig. 1.3a-c). Their results evidenced features in the XPS spectra of the clusters such as a size-dependent gaussian brodening and a positive core level shift with respect to the bulk references that were inversely linked to the cluster size. Similar features were later generalized and observed also in other systems such as size-selected Ag_n clusters deposited on sputter sputter-damaged highly oriented pyrolytic graphite (HOPG) [31], where the mobility and electronic properties of the clusters where compared to larger nanoparticles by means of XPS and STM measurements.

The studies on the fundamental properties of supported size-selected clusters where followed by experiments focused on their chemical activity in a wide range of reactions. Regarding the use of XPS, a prime example is the work by Anderson and co-workers on Pd_n clusters deposited on rutile $TiO_2(111)$, where XPS measurements were paralleled by an experimental analysis on the CO oxidation activity for clusters in a size range $n = 1 - 25$. By removing the contribution coming form final state effects to the size-dependent core level shifts of the supported clusters, the authors directly linked the Pd 3d binding energies to the CO oxidation activity (Fig. 1.3)

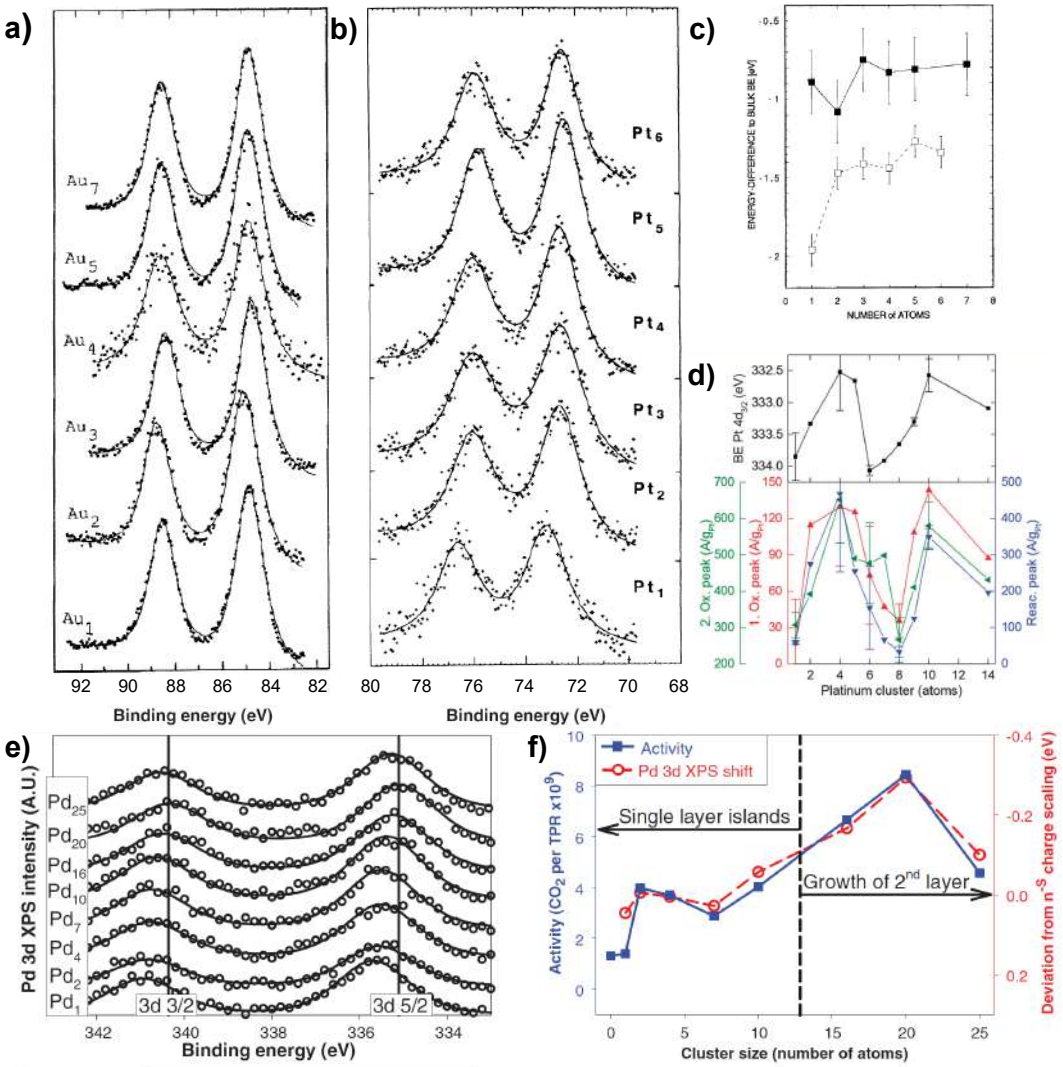

Figure 1.3: *a) Au 4f and b) Pt 4f core level XPS spectra of size-selected Au clusters deposited on the natural oxide coating of a Si wafer and c) $4f_{7/2}$ binding energy shift of the Au (filled squares) and Pt (open squares) clusters relative to the bulk values of 83.9 eV for Au and 71.2 eV for Pt as a function of size. a) Adapted from [29], b) from [30]. d) Comparison of the Pt $4d_{3/2}$ binding energy (top, note inverted scale) of Pt size selected clusters and the background-subtracted peak ethanol oxidation reaction currents per gram Pt for different cluster sizes. Red: 1st oxidation peak, green: 2nd oxidation peak, blue: reactivation peak. Adapted from [33]. e) Pd 3d core level XPS spectra for as-deposited Pd_n for n = 1, 2, 4, 7, 10, 16, 20, and 25 on TiO_2(110) and f) comparison of CO oxidation and deviation from expected Pd 3d core levels as a function of cluster size. Adapted from [32].*

[32]. The correlation between core level binding energies and chemical activity was further extended by the same group also to other clusters such as Pt_n deposited on indium tin oxide, where they investigated the electro-oxidation of ethanol [33].

The CO oxidation and other reactions were deeply investigated also in the case of size-selected Au_n clusters supported on magnesia [34], HOPG [35] and SiO_2 [36], where the combination of experiments and *ab-initio* theoretical calculations allowed

to reach a deep understanding of the behavior of gold at the nanoscale. As a matter of fact, size-selected clusters are well suited for computational calculations due to their well-defined and relatively small size. In the past 20 years, DFT calculations have been extensively adopted to support and interpret the experimental outcomes [37, 38], allowing to obtain information hardly accessible by experiments alone and to probe industrially significant reactions [39, 40].

Although supported metallic size-selected clusters have been intensively studied in the last 25 years, much less has been done on oxidized size-selected clusters. Transition metal oxides are widely used as the primary catalysts in industrially relevant reactions such as the epoxidation of ethylene [41], the oxidation of CO [42] and the ammoxidation of alkenes [43, 44]. Therefore, oxidized size-selected clusters present a wide range of interesting applications, also in the field of inverse catalysis, where an oxide nanostructure is supported on a metallic substrate. The limited amount of reports on oxidized clusters is related to the fact that an unambiguous mass selection can be affected by the presence of oxygen due to the mass vicinity and overlap of metallic and partially oxidized clusters in the same mass spectrum [12]. A different approach that has been adopted involves the production of $(WO_3)_n$ and $(MoO_3)_n$ clusters obtained from high temperature sublimation of the corresponding bulk oxide. This process, although it does not grant an accurate mass selection, leads to preferential sublimation of trimers, whose properties have been intensively investigated on several different substrates [45].

It is clear that the general task of characterizing clusters in the three-dimensional periodic table gets drastically more complicated in the case of oxides, as they reveal a structural complexity that is higher than for metals. At the same time, the ability to understand at atomic level the behavior of matter is of paramount importance to achieve an atomically precise control in the design of low-nuclearity supported catalysts [47, 48]. The work performed on size-selected oxidized clusters with precise stoichiometry provides precious information on their behavior and potential applications, but a fundamental questions remain unanswered. How does the transition from the metallic to the oxide phase take place at the sub-nanoscale? Does it follow the same rules that apply for bulk materials, or the oxidation process is dominated by the unique electronic and geometric structure of the clusters? Some effort has been dedicated to this topic, but the study of the oxidation of supported size-selected clusters in conditions where the clusters are not partially oxidized already by the interaction with the surface (as when they are deposited on oxide layers) and where the mass selection is preserved is experimentally challenging. For example, the oxidation and chemical reactivity of Ag_n clusters deposited on sputter-damaged HOPG were greatly limited by the strong interaction with the surface defects that were used to anchor the clusters [31]. On the other hand, the deposition of size-selected clusters of the same element on free standing graphene at room temperature led to the agglomeration of the clusters into nm-sized Ag-nanodots of 2-3 nm size [49]. Moreover, the experiment was partially affected by contaminants arising from the fact that the clusters where not characterized *in situ*.

Herein, I will present the work I performed in this framework, exploiting the possibility to produce and characterize size-selected clusters *in situ* in UHV conditions offered by the newly built cluster source ENAC (Exact Number of Atoms in each Cluster). ENAC can be connected directly to the SuperESCA beamline of the Elettra synchrotron facility (Fig. 1.4), where it is possible to investigate the adsorption and oxidation of size-selected clusters of transition and noble metals deposited on different

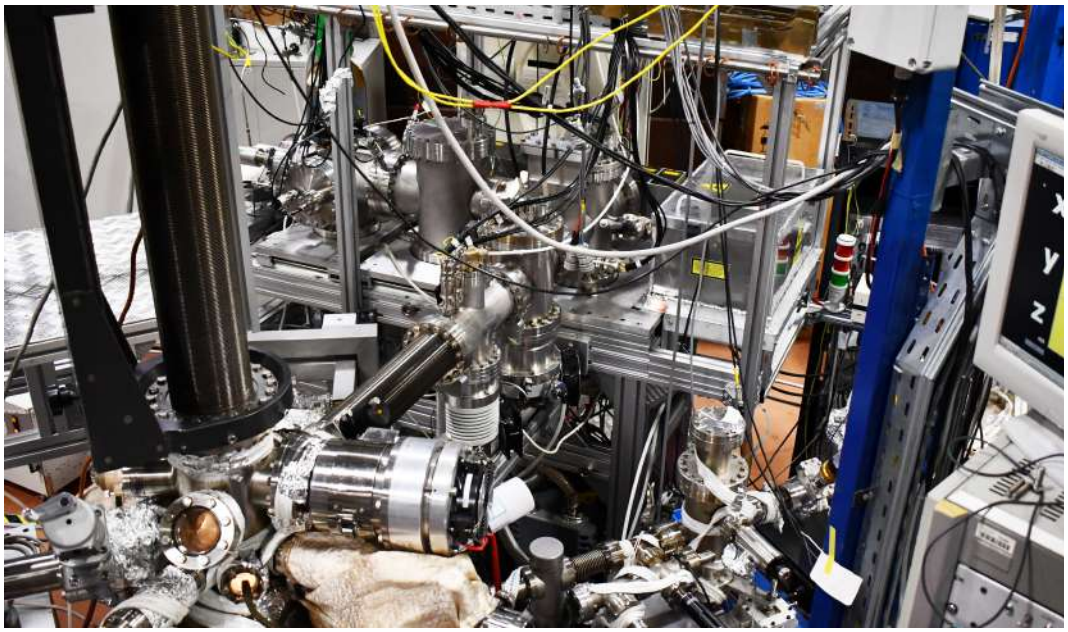

Figure 1.4: *Photograph of ENAC (top center) connected to the prechamber of the SuperESCA beamline (bottom left) taken in June 2020 during the first beamtime performed using the clusters source.*

substrates by means of synchrotron-based XPS, the prime technique to investigate the oxidation state of matter [50].

ENAC played a central role in my research activity. The possibility to connect it directly to the SuperESCA beamline offers a unique opportunity to investigate the properties of supported size-selected clusters *in situ* at different temperatures and with an extremely low degree of contaminants. The connection of the two experimental setups was the first accomplishment of my PhD activity, which allowed me to further proceed with my research project. For this reason, the first part of chapter 1 is dedicated to the description of the working principles of the cluster source, to the role played by UHV in the measurements and in the sample preparation and to the SuperESCA beamline. The second part focuses on the XPS technique and on the data analysis performed to interpret the experimental data. Finally, the last section of the chapter introduces the DFT calculations that were performed in collaboration with the group of prof. Dario Alfé from University College London to support the experimental results for different clusters and substrates.

The following five chapters are dedicated to the studies on size-selected clusters of Ag, Pt and Fe in a size range $n = 1, 20$. Each chapter begins with a introduction that describes the main objectives of the experiments and contextualizes them into a general picture on the state of the art in the field. The three materials have been selected for the relevance in the field of catalysis, especially in their oxide phase. Moreover, we selected three transition metals with different atomic masses, ranging from 56 amu for Fe up to 195 amu for Pt, to test the efficiency of ENAC in mass-selecting clusters in a wide mass range.

The first experiment described in chapter 2.6 focuses on the deposition Ag_n clusters composed of 1, 3 and 7 atoms at RT on a Ru(0001) surface to to investigate their adsorption and the formation of two-dimensional Ag islands using size-selected clusters as building blocks. This experiment involved a relatively well-known template

and acted as a benchmark to prove the capabilities of this experimental station to investigate this regime of matter with atomic precision. To results that we obtained were essential in the moving to more complex system: the oxidation of noble and transition metal clusters supported on epitaxial graphene.

The template we used for the cluster oxidation is epitaxial graphene. This is a inert substrate with a relatively weak interaction with the cluster, therefore it can be used to study their properties while, in first instance, neglecting the graphene-substrate interaction. Graphene was epitaxially grown on Ru(0001) for the deposition of Ag_n and Fe_n for the highly corrugated morphology of the resulting moiré lattice that can drastically reduce the cluster diffusion. In the case of Pt_n clusters, the overlap between the Ru 4s and Pt 4f core levels does not allow to use the same substrate to perform XPS studies. Therefore, graphene was grown on Ir(111). This template has a reduced corrugation compared to graphene/Ru(0001), but the mobility of the clusters is limited by the interaction of Pt with C, which is stronger than for Ag and Fe [51, 52]. The graphene layers are grown *in situ* following well established procedures that have been studied and optimized in the past decade at the SuperESCA beamline and that are reported in chapter 1. To further reduce the cluster mobility on the surface the temperature of the sample was kept to the extremely low temperature T = 20 K for all the stages of the experiments.

The first study presented in chapter 4 is dedicated to the oxidation of graphene-supported Ag clusters composed of 11 atoms. In this chapter it is also described the oxidation method that we adopted to oxidize the clusters at a temperature (T = 20 K) where the O_2 dissociation barriers on the different clusters cannot be overcome. It is based on the production of atomic oxygen in extremely clean conditions by inducing the dissociation of physisorbed O_2 with the secondary photoelectrons obtained by irradiating the sample with a high flux of photons in the soft X-ray range. With this method, we where able to highly oxidized the Ag_{11} clusters and, by combining the experimental outcomes with DFT calculations, we concluded that the oxidized Ag clusters present a stoichiometry and hybrid structure that strongly resembles the AgO bulk oxide phase, with the presence of atoms with two distinct oxidation states, 1+ and 3+. Thanks to the low interaction of Ag with graphene, in chapter 5 we were able to further investigate the electronic modifications induced by O adsorption on each single atom composing the clusters. We extended the study also to a smaller cluster composed of 7 atoms and discovered that, despite the similarity with the bulk oxide, the Ag−O bonds in the clusters behave differently if compared to bulk and surfaces and they are the cause of an anomalous trend in the Ag 3d core level binding energies for increasing oxidation state.

In chapter 6 we extended the use of the same oxidation method for the clusters composed of the other precious metal, Pt. In particular, we investigated the oxidation of graphene-supported Pt_n clusters with $n = 7, 12, 13$ combining XPS with DFT calculations. Our results indicate that, despite the direct interaction between graphene and Pt is relatively low, a rehybridization of the C atoms induced a charge redistribution in the clusters that causes an asymmetric oxidation, with the Pt atoms further away from the surface that reach an higher oxidation state (close to 2+) than those at the cluster/graphene interface, which remain close to the metallic phase. Similarly to the case of Ag, the oxidized part of the clusters presents local geometric and electronic features that resemble a bulk oxdide phase, Pt_3O_4.

Reducing the size of expensive metals such as Pt in catalysts constitutes a possible approach to overcome their high cost and low abundance. Another viable strategy

relies on replacing them with cheaper elements with a higher efficiency-to-cost ratio. Fe clusters are among the best candidates in this respect [53], and thus the subject of the experiments described in chapter 7. We oxidized graphene-supported Fe_n clusters for $n = 11, 12, 13, 15$ and 20, and we found that the oxidation process leads the clusters to an homogeneous final structure composed of only atoms with oxidation state 2+, which can be linked to the formation of the $(FeO)_n$ stoichiometry. We attributed a lower reactivity to the magic cluster Fe_{13}, comparing the trend of the Fe 2p binding energies to the lineshape of the spectral components obtained through the fitting analysis.

Finally, in chapter 8, the results obtained for the different clusters are compared and contextualized into a larger picture. Moreover, a few words are dedicated to the description of the future perspectives related to the presented results and to the cluster source ENAC. During my research activity, the potentialities of ENAC kept growing everyday, as it was tested for the production of size-selected clusters composed by a wide range of transition and noble metals. An important upgrade of the system concerns the possibility to extend the amount of experimental techniques for the characterization of the clusters. In particular, some preliminary testing on the use of X-ray absorption spectroscopy (XAS) at the SuperESCA beamline have given excellent results. Moreover, a low-temperature STM dedicated to ENAC is currently under development. This instrument will offer the possibility to study the mobility of the clusters on different substrates and to find those that suitable to study the clusters also at higher temperature and pressure and to transport the samples to various other laboratories and beamlines for a more complete characterization.

References

[1] U. Heiz and U. Landman, *Nanocatalysis*, NanoScience and Technology (Springer Berlin Heidelberg, 2007).

[2] J. Alonso, *Structure and Properties of Atomic Nanoclusters* (Imperial College Press, 2005).

[3] W. D. Knight, K. Clemenger, W. A. de Heer, W. A. Saunders, M. Y. Chou, and M. L. Cohen, Electronic shell structure and abundances of sodium clusters, Phys. Rev. Lett. **52**, 2141 (1984).

[4] M. M. Kappes, P. Radi, M. Schär, and E. Schumacher, Probes for electronic and geometrical shell structure effects in alkali-metal clusters. photoionization measurements on K_xLi, K_xMg and K_xZn ($x < 25$), Chem. Phys. Lett. **119**, 11 (1985).

[5] W. Ekardt, Dynamical polarizability of small metal particles: Self-consistent spherical jellium background model, Phys. Rev. Lett. **52**, 1925 (1984).

[6] S. N. Khanna and P. Jena, Assembling crystals from clusters, Phys. Rev. Lett. **69**, 1664 (1992).

[7] T. Omoda, S. Takano, and T. Tsukuda, Toward controlling the electronic structures of chemically modified superatoms of gold and silver, Small **17**, 2001439 (2021).

[8] H. Haberland, *Clusters of Atoms and Molecules: Theory, Experiment, and Clusters of Atoms*, Applications of Mathematics No. v. 1 (Springer-Verlag, 1994).

[9] T. Imaoka, H. Kitazawa, W.-J. Chun, S. Omura, K. Albrecht, and K. Yamamoto, Magic number Pt_{13} and misshapen Pt_{12} clusters: Which one is the better catalyst?, J. Am. Chem. Soc. **135**, 13089 (2013).

[10] Y. Lei, F. Mehmood, S. Lee, J. Greeley, B. Lee, S. Seifert, R. E. Winans, J. W. Elam, R. J. Meyer, P. C. Redfern, D. Teschner, R. Schlögl, M. J. Pellin, L. A. Curtiss, and S. Vajda, Increased silver activity for direct propylene epoxidation via subnanometer size effects, Science **328**, 224 (2010).

[11] E. C. Tyo and S. Vajda, Catalysis by clusters with precise numbers of atoms, Nat. Nanotechnol. **10**, 577 (2015).

[12] S. Vajda and M. G. White, Catalysis applications of size-selected cluster deposition, Acs Catal. **5**, 7152 (2015).

[13] A. Baraldi, S. Lizzit, G. Comelli, M. Kiskinova, R. Rosei, K. Honkala, and J. K. Nørskov, Spectroscopic link between adsorption site occupation and local surface chemical reactivity, Phys. Rev. Lett. **93**, 046101 (2004).

[14] B. Hammer and J. K. Nørskov, Theoretical surface science and catalysis–calculations and concepts, in *Advances in Catalysis*, Vol. 45 (Academic Press, 2000) pp. 71–129.

[15] W. A. de Heer, The physics of simple metal clusters: experimental aspects and simple models, Rev. Mod. Phys. **65**, 611 (1993).

[16] U. Heiz, A. Sanchez, S. Abbet, and W.-D. Schneider, Catalytic oxidation of carbon monoxide on monodispersed platinum clusters: Each atom counts, J. Am. Chem. Soc. **121**, 3214 (1999).

[17] U. Achatz, C. Berg, S. Joos, B. S. Fox, M. K. Beyer, G. Niedner-Schatteburg, and V. E. Bondybey, Methane activation by platinum cluster ions in the gas phase: effects of cluster charge on the Pt_4 tetramer, Chem. Phys. Lett. **320**, 53 (2000).

[18] S. M. Lang, T. M. Bernhardt, R. N. Barnett, B. Yoon, and U. Landman, Hydrogen-promoted oxygen activation by free gold cluster cations, J. Am. Chem. Soc. **131**, 8939 (2009).

[19] F. Dong, S. Heinbuch, Y. Xie, J. J. Rocca, E. R. Bernstein, Z.-C. Wang, K. Deng, and S.-G. He, Experimental and theoretical study of the reactions between neutral vanadium oxide clusters and ethane, ethylene, and acetylene, J. Am. Chem. Soc. **130**, 1932 (2008).

[20] D. Schröder and H. Schwarz, C−H and C−C bond activation by bare transition-metal oxide cations in the gas phase, Angew. Chem. Int. Ed. Engl. **34**, 1973 (1995).

[21] C. Dong, Y. Li, D. Cheng, M. Zhang, J. Liu, Y.-G. Wang, D. Xiao, and D. Ma, Supported metal clusters: Fabrication and application in heterogeneous catalysis, Acs Catal. **10**, 11011 (2020).

[22] R. E. Smalley, Laser studies of metal cluster beams, Laser Chem. **2**, 957420 (1983).

[23] K. Bromann, C. Félix, H. Brune, W. Harbich, R. Monot, J. Buttet, and K. Kern, Controlled deposition of size-selected silver nanoclusters, Science **274**, 956 (1996).

[24] T. Masubuchi, J. F. Eckhard, K. Lange, B. Visser, M. Tschurl, and U. Heiz, An efficient laser vaporization source for chemically modified metal clusters characterized by thermodynamics and kinetics, Rev. Sci. Instrum. **89**, 023104 (2018).

[25] R. E. Palmer, S. Pratontep, and H. G. Boyen, Nanostructured surfaces from size-selected clusters, Nat. Mater. **2**, 443 (2003).

[26] V. N. Popok, I. Barke, E. E. B. Campbell, and K.-H. Meiwes-Broer, Cluster-surface interaction: From soft landing to implantation, Surf. Sci. Rep. **66**, 347 (2011).

[27] D. Pearmain, S. J. Park, Z. W. Wang, A. Abdela, R. E. Palmer, and Z. Y. Li, Size and shape of industrial Pd catalyst particles using size-selected clusters as mass standards, Appl. Phys. Lett. **102**, 163103 (2013).

[28] D.-C. Lim, C.-C. Hwang, G. Ganteför, and Y. D. Kim, Model catalysts of supported au nanoparticles and mass-selected clusters, Phys. Chem. Chem. Phys. **12**, 15172 (2010).

[29] D. M. Cox, W. Eberhardt, P. Fayet, Z. Fu, B. Kessler, R. D. Sherwood, D. Sondericker, and A. Kaldor, Electronic structure of deposited monosized metal-clusters, Z. Phys. D Atom. Mol. Cl. **20**, 385 (1991).

[30] W. Eberhardt, P. Fayet, D. M. Cox, Z. Fu, A. Kaldor, R. Sherwood, and D. Sondericker, Photoemission from mass-selected monodispersed Pt clusters, Phys. Rev. Lett. **64**, 780 (1990).

[31] R. Dietsche, D. C. Lim, M. Bubek, I. Lopez-Salido, G. Ganteför, and Y. D. Kim, Comparison of electronic structures of mass-selected ag clusters and thermally grown ag islands on sputter-damaged graphite surfaces, Applied Physics A **90**, 395 (2008).

[32] W. E. Kaden, T. Wu, W. A. Kunkel, and S. L. Anderson, Electronic structure controls reactivity of size-selected Pd clusters adsorbed on TiO_2 surfaces, Science **326**, 826 (2009).

[33] A. von Weber, E. T. Baxter, S. Proch, M. D. Kane, M. Rosenfelder, H. S. White, and S. L. Anderson, Size-dependent electronic structure controls activity for ethanol electro-oxidation at Pt_n/indium tin oxide (n = 1 to 14), Phys. Chem. Chem. Phys. **17**, 17601 (2015).

[34] A. Sanchez, S. Abbet, U. Heiz, W.-D. Schneider, H. Häkkinen, R. N. Barnett, and U. Landman, When gold is not noble: nanoscale gold catalysts, J. Phys. Chem. A **103**, 9573 (1999).

[35] D. C. Lim, R. Dietsche, M. Bubek, T. Ketterer, G. Ganteför, and Y. D. Kim, Chemistry of mass-selected au clusters deposited on sputter-damaged hopg surfaces: The unique properties of au8 clusters, Chemical Physics Letters **439**, 364 (2007).

[36] D. C. Lim, R. Dietsche, M. Bubek, G. Ganteför, and Y. D. Kim, Oxidation and reduction of mass-selected au clusters on sio2/si, ChemPhysChem **7**, 1909 (2006).

[37] B. Yoon, H. Häkkinen, U. Landman, A. S. Wörz, J.-M. Antonietti, S. Abbet, K. Judai, and U. Heiz, Charging effects on bonding and catalyzed oxidation of co on au8 clusters on mgo, Science **307**, 403 (2005).

[38] F. R. Negreiros, E. Aprà, G. Barcaro, L. Sementa, S. Vajda, and A. Fortunelli, A first-principles theoretical approach to heterogeneous nanocatalysis, Nanoscale **4**, 1208 (2012).

[39] A. M. Joshi, W. N. Delgass, and K. T. Thomson, Mechanistic implications of aun/ti-lattice proximity for propylene epoxidation, J. Phys. Chem. C **111**, 7841 (2007).

[40] S. Lee, L. M. Molina, M. J. López, J. A. Alonso, B. Hammer, B. Lee, S. Seifert, R. E. Winans, J. W. Elam, M. J. Pellin, and S. Vajda, Selective propene epoxidation on immobilized au6-10 clusters: The effect of hydrogen and water on activity and selectivity, Angewandte Chemie **121**, 1495 (2009).

[41] T. Pu, H. Tian, M. E. Ford, S. Rangarajan, and I. E. Wachs, Overview of selective oxidation of ethylene to ethylene oxide by Ag catalysts, Acs Catal. **9**, 10727 (2019).

[42] S. Dey, G. C. Dhal, D. Mohan, and R. Prasad, Advances in transition metal oxide catalysts for carbon monoxide oxidation: a review, Adv. Compos. Hybrid Mater. **2**, 626 (2019).

[43] H. Kung, *Transition Metal Oxides: Surface Chemistry and Catalysis*, Ecosystems of the World No. v. 45 (Elsevier, 1989).

[44] J. Fierro, *Metal Oxides: Chemistry and Applications*, Chemical Industries (CRC Press, 2005).

[45] R. Rousseau, D. A. Dixon, B. D. Kay, and Z. Dohnálek, Dehydration, dehydrogenation, and condensation of alcohols on supported oxide catalysts based on cyclic $(WO_3)_3$ and $(MoO_3)_3$ clusters, Chem. Soc. Rev. **43**, 7664 (2014).

[46] R. H. Crabtree, Clusters, nanoparticles, materials, and surfaces (2014) pp. 353–382.

[47] S. Mitchell, R. Qin, N. Zheng, and J. Pérez-Ramírez, Nanoscale engineering of catalytic materials for sustainable technologies, Nat. Nanotechnol. **16**, 129 (2021).

[48] S. Mitchell and J. Pérez-Ramírez, Atomically precise control in the design of low-nuclearity supported metal catalysts, Nat. Rev. Mater. **6**, 969 (2021).

[49] M. Al-Hada, S. Peters, L. Gregoratti, M. Amati, H. Sezen, P. Parisse, S. Selve, T. Niermann, D. Berger, M. Neeb, and W. Eberhardt, Nanoparticle formation of deposited agn-clusters on free-standing graphene, Surface Science **665**, 108 (2017).

[50] K. Siegbahn, D. Hammond, H. Fellner-Feldegg, and E. F. Barnett, Electron spectroscopy with monochromatized x-rays, Science **176**, 245 (1972).

[51] D. Martoccia, P. R. Willmott, T. Brugger, M. Björck, S. Günther, C. M. Schlepütz, A. Cervellino, S. A. Pauli, B. D. Patterson, S. Marchini, J. Wintterlin, W. Moritz, and T. Greber, Graphene on Ru(0001): A 25×25 supercell, Phys. Rev. Lett. **101**, 126102 (2008).

[52] X. Liu, C. Z. Wang, M. Hupalo, W. C. Lu, M. C. Tringides, Y. X. Yao, and K. M. Ho, Metals on graphene: correlation between adatom adsorption behavior and growth morphology, Phys. Chem. Chem. Phys. **14**, 9157 (2012).

[53] A. Zitolo, V. Goellner, V. Armel, M.-T. Sougrati, T. Mineva, L. Stievano, E. Fonda, and F. Jaouen, Identification of catalytic sites for oxygen reduction in iron- and nitrogen-doped graphene materials, Nat. Mater. **14**, 937 (2015).

CHAPTER 2

Experimental setup and techniques

This chapter is dedicated to the description of the experimental setup and of the experimental and theoretical techniques that were involved to perform the experiments described in this thesis. First off, the cluster source ENAC is presented starting from a brief general introduction on cluster sources, followed by a description of its working principle and components and finishing with a description of the mechanisms involved in the cluster deposition on a sample. In the second part of the chapter, the importance of UHV will be discussed in relation to presence of contaminants on the chamber that could potentially compromise an experiment involving size-selected clusters due to their particularly high expected reactivity. In this regard, the method adopted to prepare the sample in UHV conditions will be described, starting from the sample cleaning and then moving the GR growth. Afterwards, I will move to the description of the SuperESCA beamline of the Elettra synchrotron facility where the experiments of this thesis have been performed and to XPS, the experimental technique that was adopted to characterize the graphene-supported size-selected clusters. Finally, the last section of the clusters is dedicated to an introduction to DFT and to provide the technical details of the calculations that were performed to support the experimental data.

2.1 The cluster source ENAC

ENAC is the cluster source that has being designed and built at the nmLab in collaboration with the group of Prof. Heiz from the Technische Universität München. The design and working principles of this cluster source are an evolution of the project developed by Prof. Heiz and co-workers [1], where laser ablation is adopted to produced plasma from a metal target. The plasma is then thermalized by a carrier gas and undergoes a supersonic jet expansion, leading to clusterization.

Pioneering machines based on laser ablation were developed by Smalley [2] and Maruyama [3] in the '80s, and have been further developed by Heiz's group [1, 4, 5]. Another family of cluster sources uses magnetron sputtering to produce tha plasma that will generate the clusters [6, 7], but this approach has the drawback of presenting difficulties when dealing with ferromagnetic materials. On the contrary, laser ablation is a very versatile and reliable approach that allows for the creation of plasmas of most elements. The unique feature that characterizes ENAC is that it was designed with the possibility to be connected directly to the SuperESCA beamline of the Elettra synchrotron facility to perform *in situ* studies on supported size-selected clusters by means of experimental techniques bases on synchrotron radiation.

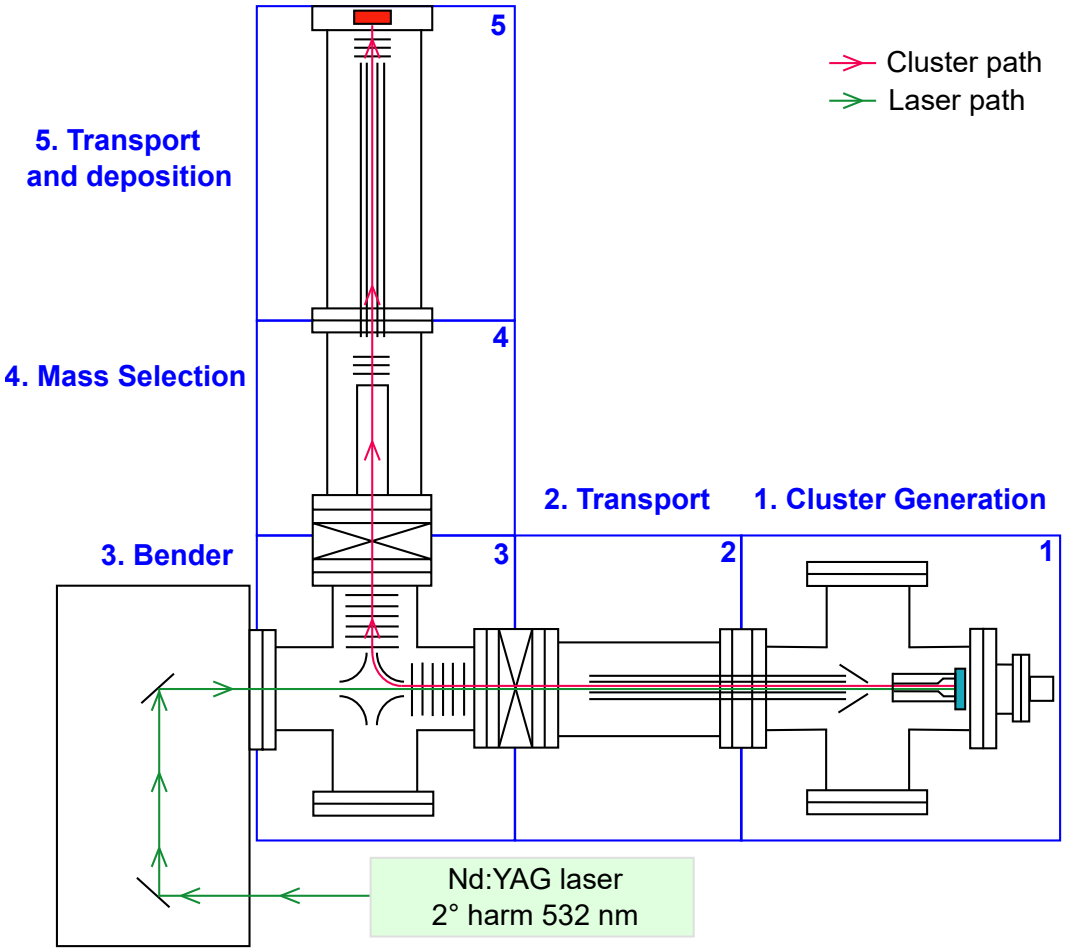

Figure 2.1: *Schematic representation of ENAC. The five different sections are indicated. The red (green) line represent the cluster (laser) path.*

ENAC can be schamatically divided into five sections (Fig. 1.1). In the first section, the clusters are generated from the plasma that is thermalized in a gas carrier that undergoes a supersonic jet expansion. After the supersonic expansion, which takes place in a carrier gas inside a specially shaped nozzle, the clusters are already formed with a mass dispersion that depends on many parameters such as the laser power and the pressure of the carrier gas. The second section is dedicated to transport the cluster towards regions of increasingly better vacuum by exploiting an octupole ion guide and different sets of electrostatic lenses. In the third section, an electrostatic bender is used to select the charge of the clusters and remove the neutral ones from the cluster beam. For mass selection purposes, charged clusters are required, with the additional limit that neutral clusters cannot be manipulated by the electrostatic fields. After the bender, the size of the cluster is selected with atomic precision exploiting an Extrel quadrupole mass spectrometer (QMS), capable of selecting aggregates with a mass up to 16000 amu. At this point, the mass selection is completed and the clusters are ready to be deposited. However, a fifth stage is required to further transport the size-selected clusters onto the sample located at the center of the SuperESCA preparation chamber. Finally, the clusters can be deposited on the sample in soft-landing conditions.

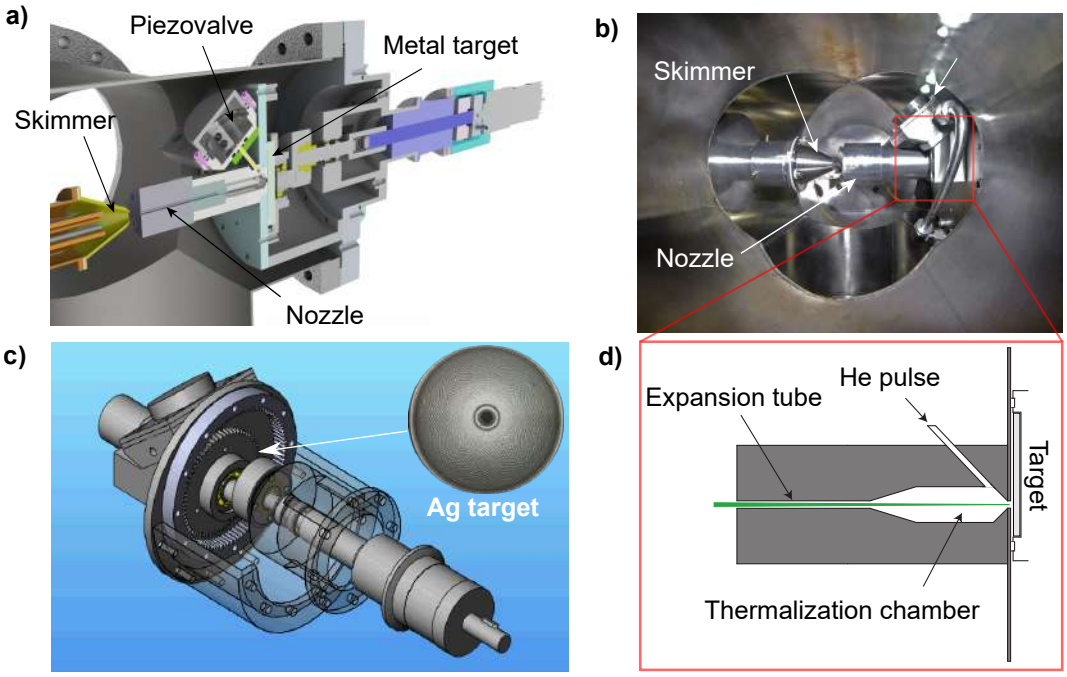

Figure 2.2: *a)Schematic representation and b) photograph of the first section of ENAC. c) Sketch of the mechanism that allows the target to rotate and an insert shows an ablated Ag target. d) Section of the nozzle, where the supersonic expansion begins.*

2.1.1 Cluster generation

In the first stage of ENAC, the clusters are generated from a metal target. A sketch and a photograph of this section are shown in Fig. 1.2a and b. The ablation of a metallic target is performed using the output of a pulsed Nd:YAG laser, equipped with a second harmonic-generation crystal (light wavelength $\lambda = 532$ nm). The repetition rate is 120 Hz, with a pulse that lasts 7 ns and with a tunable energy per pulse between 3 and 140 mJ. The choice of the wavelength is due to practical considerations, since the laser enters the vacuum chamber of the cluster source through a fused silica window. The wavelength of 532 nm grants the maximum possible transmission of the laser beam through the window and therefore minimizes the thermal stress. To further increase the power density on the metal target and optimize the ablation process, the laser beam is focused by a convex lens with a 1200 mm focal length which reduces the diameter of the laser spot profile on the target to less than 1 mm. The target is a cylinder of 45 mm diameter and 3 mm thick and, if it were fixed on a static position, it would quickly be ablated only in the 1 mm spot hit by the laser pulse. To prevent this from happening, the target is constantly in motion, so that all the surface is subsequently exposed to the laser in a uniform way. This movement is achieved by letting the sample rotate simultaneously around two eccentric circles: the laser, therefore, draws a cycloidal path on the target. The mechanism allowing this movement is sketched in Fig. 1.2c, where an insert shows the ablated Ag target that has been used for the experiments reported in this thesis. In this target, it is possible to notice the cycloidal path followed by the laser beam.

Once the plasma is created, it has to be cooled down to favor the formation of the clusters. The cooling process is achieved by a carrier gas pulse that is injected through

an opening placed close to where the plasma is generated [8]. The carrier gas (He, in our case) accelerates the ionized particles within tha plasma into a thermalization chamber inside a specially designed nozzle (Fig. 1.2d). In this chamber, the plasma is cooled down by energy transfer to the nozzle inner walls through the carrier gas. At this stage, small, hot clusters are formed. The temperature of the clusters is further decreased and they are allowed to aggregate during the adiabatic expansion from the tube of the nozzle into the vacuum chamber [9]. The fundamental mechanism that describes the cooling and condensation of the plasma in the supersonic expansion is extremely complex from a theoretical perspective, since the system is in a strongly non-equilibrium thermodynamic state [10, 11]. It leads to formation of both neutral and charged clusters; the charge can be positive or negative, and it is usually unitary. The cross section of the electron capture process in a collision is generally lower than that of the loss, unbalancing the population of positively and negatively charged clusters in favor of the former family. For this reason, the ENAC cluster source focuses on the production of ionized clusters with a unitary positive charge, although it could as well be used also for negatively charged one.

The clusterization process and the mass-dispersion of the clusters that leave nozzle depend on several parameters. Some of them are linked to the geometry of the thermalization chamber and therefore are kept constant during an experiment, although the nozzle can be easily removed and replaced with a different one. Other parameters that can be tuned during an experiment to modify the cluster generation are the laser power, the characteristics of the gas pulse and the carrier gas itself. The gas injection is obtained and controlled through a home-built piezoelectric valve. It is composed of a piezoelectric disk glued to a stainless steel diaphragm with conductive epoxy, whose center has a needle that seals an aperture by means of an elastic O-ring (Fig. 1.3a). A potential in the order of -300 V can be applied to the piezoelectric disk to deform it and to bend the metallic diaphram, opening the channel that connects the piezo valve to the thermalization chamber. By applying the voltage to the piezo valve using different signal shapes, it is possible to change the pulse duration and the He pressure in the thermalization chamber. The latter is going to be a fraction of the pressure inside the piezo valve, which typically is within 3 and 15 bar. Pulse duration, He pressure and the time delay between the laser and gas pulses are all parameters that affect the supersonic expansion and, therefore, determine the mass distribution. The carrier gases that are employed in similar cluster sources are typically noble gases, which do not chemical interact with the clusters. For the experiments described in this thesis, we decided to work with He due to its high thermal conductivity compared to the other noble gases [12].

The supersonic expansion takes place outside the nozzle, where the clusters propagate within the He carrier gas. The expansion of a gas in this conditions leads to a zone of silence, where the particles contained within are moving with narrow kinetic energy distribution in linear trajectories without colliding with each other. The zone of silence is bound to the sides by a barrel shock, and to the front by a Mach disk (Fig. 1.3b) [14]. By placing a conical skimmer within the zone of silence, it is possible to obtain a collimated beam behind it and drastically reduce the pressure that propagates from the first section of the cluster source to the others. This process depends on the relative pressure inside the nozzle and in the vacuum chamber. In particular, given the pressures that are necessary for the clusterization of the plasma (few bar), the pressure outside the nozzle must remain below 10^{-1} mbar. This requirement is achieved thanks to a Pfeiffer Okta 1000 roots pump with

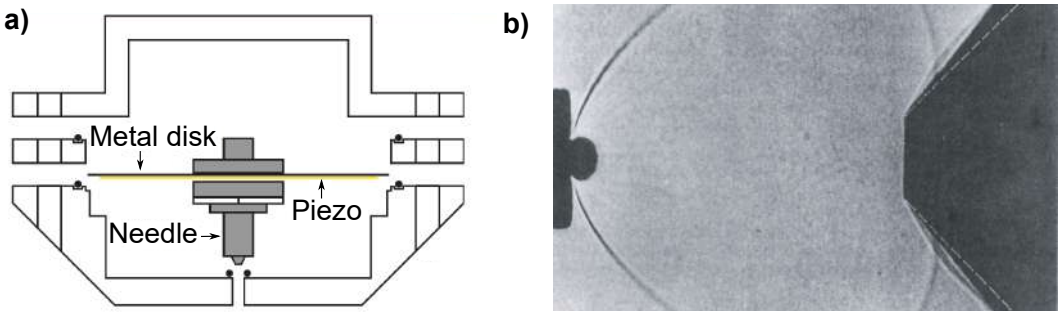

Figure 2.3: *a) Section of the piezoelectric valve used in ENAC. b) Shadowgram of the silence zone in the supersonic expansion of N_2 from a reservor. Barrel shock and Mach disk are visible. A conical skimmer is placed inside the silence zone to obtain a N_2 beam. Adapted from. [13].*

a pumping speed of 1200 m^3/h which is connected directly to the chamber, and is pre-pumped by a double stage 80 m^3/h Edwards rotary vane pump.

2.1.2 Cluster transport

After the skimmer, a cluster beam is formed and potentially ready for the mass selection. However, the maximum background pressure allowed for a safe operation of the QMS is 10^{-5} mbar, which does not allow to place it already in the second section of ENAC, where the pressure in working conditions can reach 10^{-3} mbar. Moreover, an even lower pressure will be needed in the last stages of the cluster source in order to ensure that no significant amounts of contaminants are deposited together with the clusters. Therefore, intermediate chambers are needed to build a differential pumping system to progressively decrease the background pressure in the cluster source, where each chamber (but the first one) is pumped by turbomolecular pump (pumping speed ~ 600 m^3/h at 1×10^{-3} mbar).

The use of several stages requires to efficiently transport the cluster beam through them. For this purpose, ENAC is equipped with several sets of electrostatic lenses and with two octupole wave guides. The first octupole is located in the second section of the cluster source, behind the skimmer. The octupoles (Fig. 1.4) are composed of 8 cylindrical rods, and a radio frequency (RF) voltage is applied to alternating bars, so that half of them are always oscillating in counter phase with the other half. In addition, a direct current (DC) offset is applied to all of them [4]. The second octupole, which is located after the QMS to transport the clusters onto the sample, follows the same working principles, although it is 200 mm longer than the first one (600 mm against 400 mm) and requires slightly different voltages to operate. The combination of the RF with the DC offset determines an electromagnetic field with a relatively wide interval of charge-to-mass ratios that can be efficiently transported [15].

The electrostatic lenses used in ENAC are based on the typical Einzel lens configuration, which are a set of three consecutive coaxial elements with cylindrical symmetry (Fig. 1.5a) [16]. In their original design, Einzel lenses are used to focus a beam of charged particle by setting the first and last lenses to the same voltage, while the potential applied to the intermediate lens determines the focal length. In more complex setups, such as those used in ENAC, it is possible to tune the two focal points into asymmetric position by changing the voltage of the first lens with

Figure 2.4: *Technical drawing (left) and photographs of the first (center) and second (right) octupoles.*

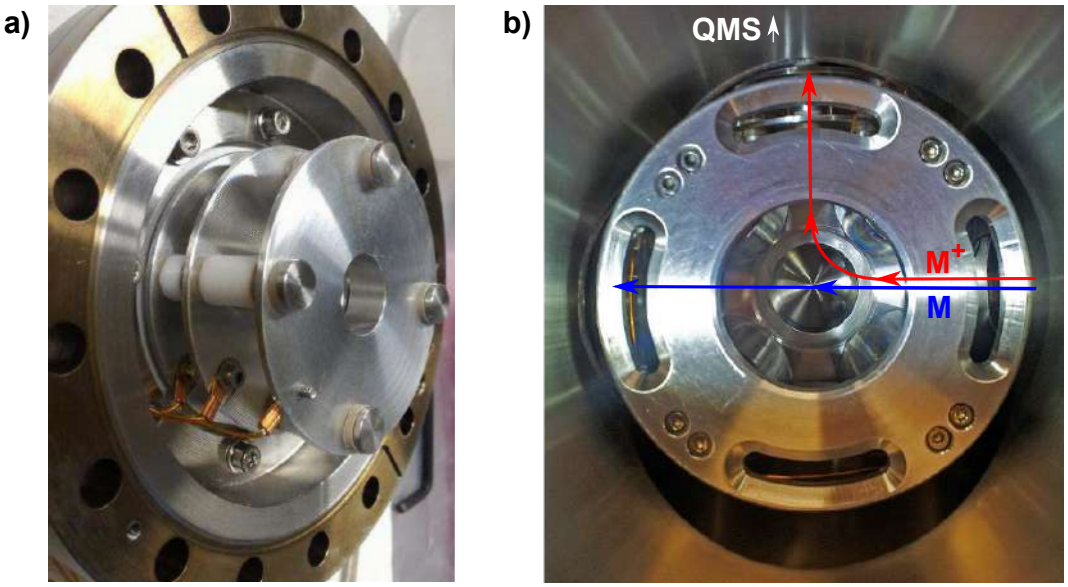

Figure 2.5: *a) Set of three electrostatic lenses mounted on a CF100 flange. b) Top view of the bender inside ENAC. Charged (M^+, red) and neutral (M, blu) metallic clusters arrive from the right. The trajectory of the positively charged is deflected by* 90° *towards the QMS, while neutral clusters proceed straight*

respect to the third one, or by adding two (or four) more lenses to the system. In total, ENAC counts three sets of asymmetric Einzel lenses and two sets of seven lenses. They are used to focus the cluster beam through the pinholes that separate each chamber of the differential pumping system, as well as to focus the clusters inside the QMS and on the sample.

Another electrostatic element that plays a central role in the cluster source is the bender, which is located in the third stage of ENAC. This element is a quadrupole positioned with its axis vertical with respect to the cluster source plane. Its working principles are based on the application of two different electrostatic potentials to each couple of bars opposite to each other. This generates constant-potential surfaces, which are symmetrical with respect to the plane connecting opposite rods. Ions entering the bender laterally, passing between two rods with different potentials, are deflected to one direction or the other based on the sign of their charge. The bender has the role to select the charge of the cluster and, in particular, remove neutral clusters from the beam. If the cluster source was built in a straight line configuration, without the bender, unselected neutral clusters would inevitably be passively transported by the carrier gas through all the machine and deposited on

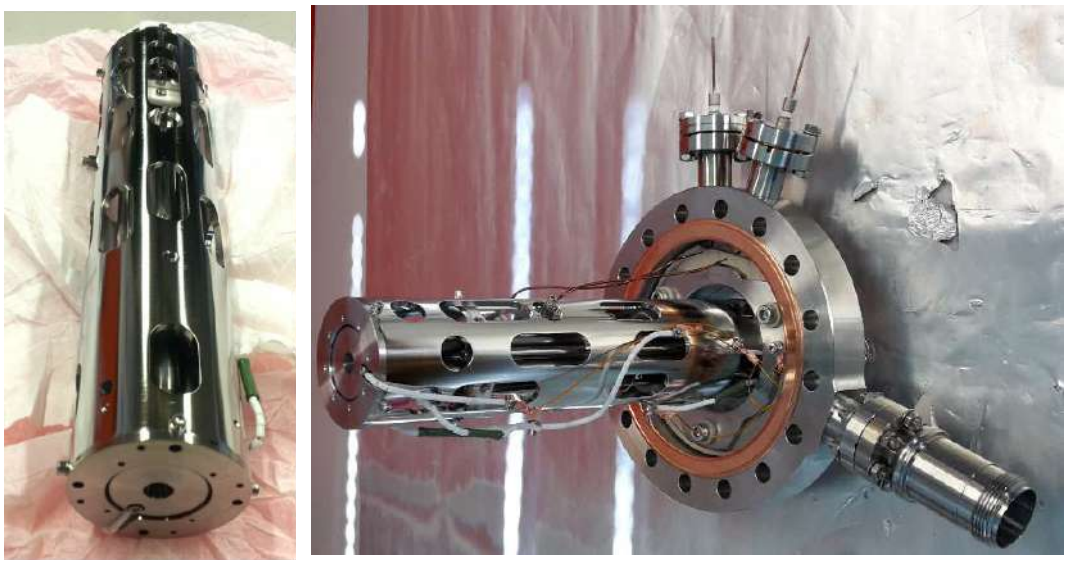

Figure 2.6: *Photographs of the QMS. On the right, the device on its own, while on the left it is shown connected to a CF100 flange in its final configuration.*

the sample. On the contrary, the bender ensures that only clusters with the selected charge can proceed their path through the cluster source and enter the QMS, which is located in the fourth chamber of ENAC, connected with an angle of 90° with respect to the first part of the machine (see Fig. 1.1).

2.1.3 Mass selection

After the bender, the cluster beam is composed of positively charged clusters with a tight mass-dispersion. As a matter of fact, all the electrostatic elements of the system, and in particular the bender, act to narrow the mass distribution of the clusters. This is due to the fact that different parameters used to transport the charged particles will work more efficiently for a specific range of mass-to-charge ratio m/q than for another. However, a mass selection with atomic precision is achieved only in the fourth section of ENAC, thanks to an Extrel 150QC RF-DC QMS, which is capable of selecting cluster with masses in the range from 10 to 16 000 amu (Fig. 1.6). This mass range allows to mass select, for example, Ag_n^+ clusters from $n = 1$ up to $n = 150$, Pt_n^+ clusters for $n = 1-82$ and Fe_n^+ clusters for $n = 1-286$. However, the highest n achievable for a specific elements is limited by its isotopic abundance. For example, Mo has a mass of about 96 amu, therefore it would be possible to mass-select Mo_n^+ clusters up to $n = 166$. However, this element shows several stable isotopes with masses ranging from 92 amu (14.84 %) up to 98 amu (24.16 %) [17]. The large isotopic distribution limits the highest number n obtainable for Mo clusters in the sense that the mass of Mo_{100}^+ will be centerd at 9600 amu, but with a distribution within 9200 and 9800 amu, which will inevitably overlap with the peaks of Mo_{99}^+ and Mo_{101}^+, centered respectively at 9504 and 9696 amu.

The working principles of the QMS are based on the application of the sum of a DC bias U and a RF potential $V\,cos(\omega t)$, with two opposite bars in counter phase with the other two. The equation of motion of a charged particle in the generated field is described by Mathieu's equations [15]. In summary, it is possible to define two orthogonal planes that share a common z-axis defined as the one parallel to the

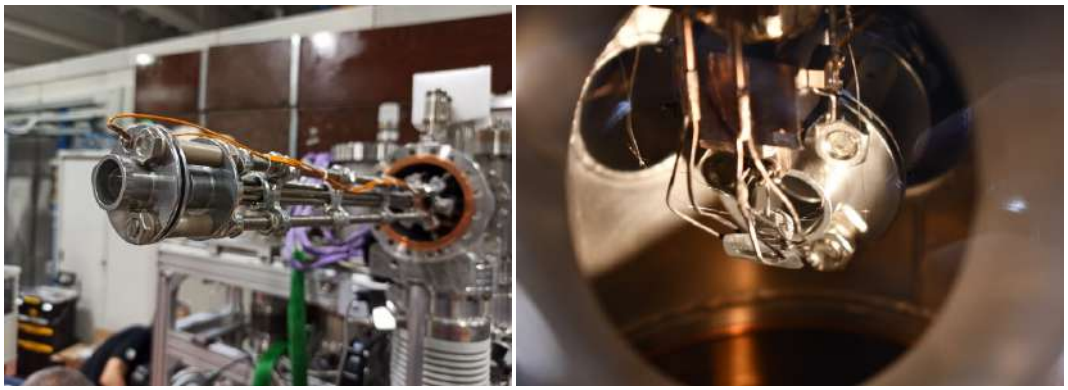

Figure 2.7: *Pictures of the last set of electrostatic lenses of ENAC before and after connecting the cluster source to the SuperESCA beamline.*

QMS axis. According to Mathieu's equations, one of the two planes will act as a high pass mass filter, while the second as a low pass mass filter. Therefore, by tuning U and V it is possible to operate the QMS as a narrow band pass filter, and only the particles having a certain m/q ratio will follow a non-diverging trajectory inside the QMS and exit the device [18].

2.1.4 Cluster deposition

The fifth and final section of ENAC acts to transport the mass-selected clusters from the QMS onto the sample. It is composed of a first set of 7 electrostatic lenses that collect the clusters after the QMS and guide them inside a 600 mm octupole. Finally, the charged particles exiting the octuople are focused onto the sample by a last set of three lenses (Fig. 1.7). The cluster current on the sample is monitored by using a Keithley model 6487/E picoammeter, allowing to test the capabilities of ENAC by performing mass scans on the sample. Few examples for the elements that are studied in this thesis are shown in Fig. 1.8 for different mass ranges. Each peak corresponds to a different cluster landing on the sample. It is important to underline that these spectra do not represent the mass distribution of the clusters landing on the sample simultaneously, but they are acquired by changing the QMS parameter to progressively transport clusters with different m/q ratio and measuring the correspondent current on the sample. During a deposition, all the parameters of the cluster source (in particular of the QMS) are fixed so that only the clusters with the selected m/q ratio are deposited on the sample.

The coverage of deposited clusters can be calculated from the current measured on the sample. For example, a current of 100 pA corresponds to $\sim 6\times10^{10}$ elementary charges reaching the sample per second. Since all the clusters carry a unitary charge, this value also corresponds to the amount of clusters that are being deposited. Finally, to convert this value into a surface density, it is necessary to know the area of the cluster spot on the sample. The diameter of the spot profile can be measured by depositing the clusters on the sample and acquiring XPS spectra on the core levels of the clusters in different positions and calculating the spectral intensity in each point. For example, for the experiments on Ag clusters, the spot had a Gaussian profile with a FWHM of ~ 6 mm (Fig. 1.9). Therefore, a current of 100 pA correspond to a deposition of $\sim 2 \times 10^{11}$ clusters $s^{-1}cm^{-2}$.

Another important issue that has to be addressed in a cluster deposition experi-

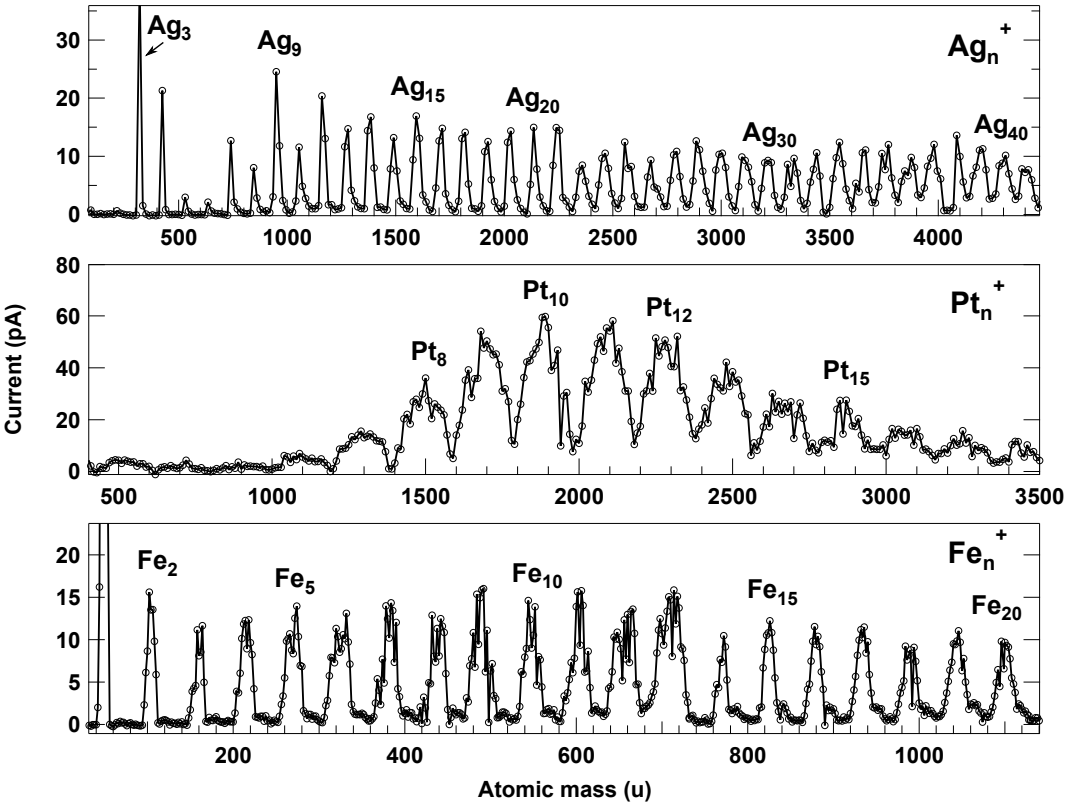

Figure 2.8: *Mass spectra acquired on the sample at the SupeESCA beamline for Ag_n^+,Pt_n^+ and Fe_n^+ clusters. The spectra are optimized in different conditions and for different ranges based on the material and on the experiment.*

ment is that the clusters must be deposited in the so-called soft-landing condition in order to preserve their integrity on the surface. Previous studies have shown that this corresponds to a kinetic energy of the clusters $E_{kin} < 1$ eV/atom [2, 5, 19]. The average kinetic energy of a cluster can be measured performing a voltage scan on the sample (Fig. 1.10). While the cluster beam in on, the cluster current is measured as a function of a positive potential, called retarding potential V_R, that is applied on the sample. Since the clusters are positively charged, V_R will progressively deflect them from the sample. As long as the kinetic energy of the clusters is higher than the applied V_R, a current will still be measured on the sample. Finally, for V_R larger than a value $V_R^\star = E_{kin}$, the cluster current will decrease to zero and the kinetic energy of the clusters is obtained. If E_{kin} is larger than 1 eV/atom, it is possible to apply the necessary voltage V_R' to reduce the kinetic energy to $E_{kin}' = E_{kin} - V_R'$ and satisfy the soft-landing conditions. In practice, the kinetic energy of the clusters has Gaussian distribution centered at E_{kin} and with a width ΔE_{kin}, requiring a slightly larger V_R to ensure that also the clusters with the highest kinetic energy in the tail of the distribution satisfy the soft-landing condition. For example, the voltage scan acquired for the deposition of a Pt_{10}^+ cluster is shown in Fig. 1.10, where the average is 13.5 eV, which has to be decreased to less than 10 eV to satisfy the soft-landing condition. However, the cluster energy have a Gaussian distribution with $\Delta E_{kin} = 3$ V. ΔE_{kin} corresponds to 2σ of the Gaussian distribution, meaning that $\sim 98\,\%$ of the clusters have a kinetic energy lower than $E_{kin} + \Delta E_{kin} = 16.5$ eV. Therefore a retarding voltage $V_R > 6.5$ ensures that more than 98 % of them are soft-landed on

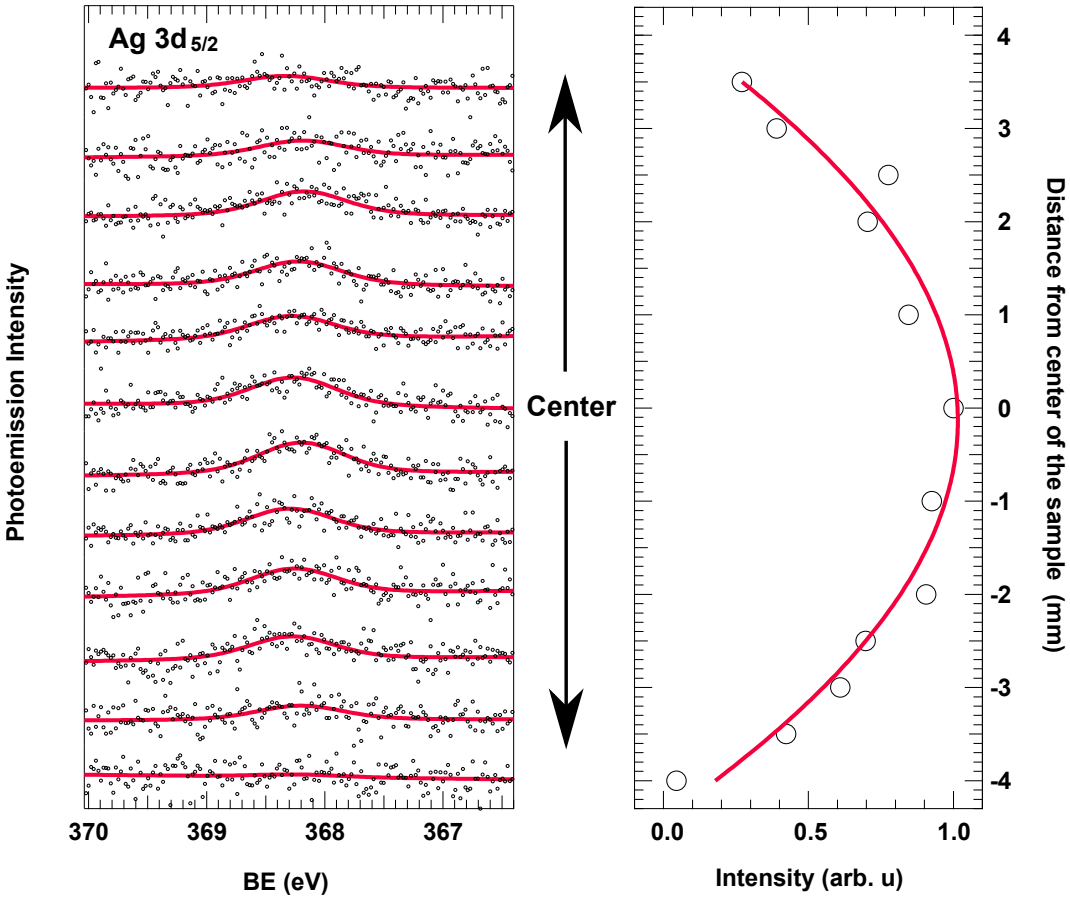

Figure 2.9: *On the left, Ag $3d_{5/2}$ core level acquired after a cluster deposition on Ru(0001) in different positions of the sample. Black circles are the experimental data, red lines correspond to the fit. On the right, the spectral intensity profile.*

the sample.

Currently, the cluster source is fully functional both as a standalone machine as well as in combination with the SuperESCA beamline. It has been tested with a large variety of metals, such as Fe, Ag, Pt, Mo, W and Ta and can potentially be used also form bimetallic clusters by using a metallic target of the related alloy. The experiment described in this thesis are the first ones that have been carried out with ENAC at the SuperESCA beamline, but the cluster source gets constantly upgraded and its potential application can further grow, as discussed in the last chapter Conclusions and Future perspectives.

2.2 Ultra high vacuum

Ultra high vacuum (UHV) is the vacuum regime characterized by pressures lower than 10^{-9} mbar. Similar background pressure are often mandatory in surface science to maintain a sample pristine for enough time to perform an experiment. In fact, the contamination of a surface can be qualitatively estimated for a given pressure by using the Hertz-Knudsen formula [20]:

$$\Phi = \frac{P}{\sqrt{2mk_BT}},$$

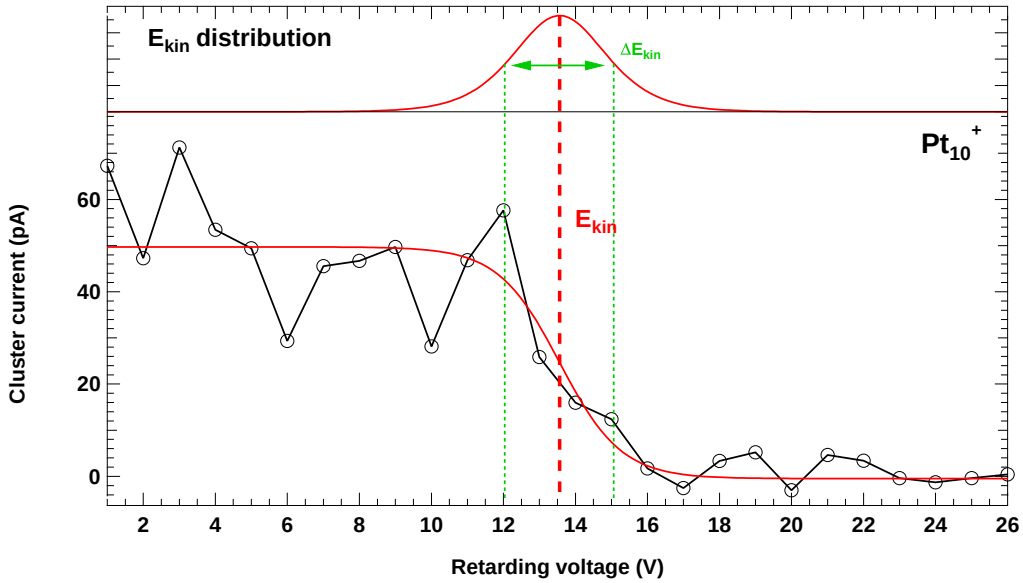

Figure 2.10: *Voltage scan acquired for a Pt_{10}^{+} cluster deposited on Ir(111) and distribution of the kinetic energy E_{kin}.*

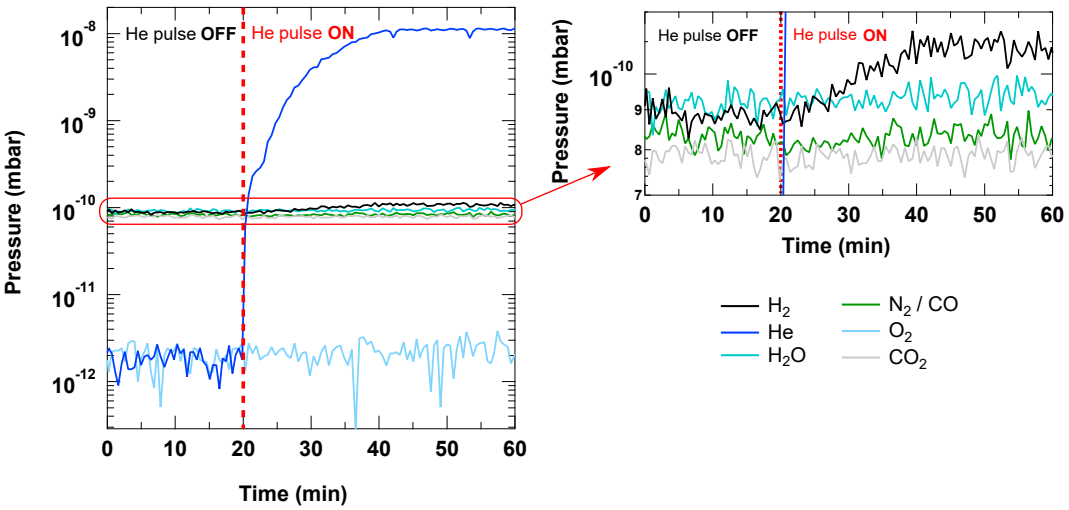

Figure 2.11: *Partial pressure of different gases in the experimental chamber over time. The red vertical line at $t = 20$ min indicates the moment when a deposition started and the He gas carrier arrived in the chamber.*

where P is the background pressure of a molecular gas of mass m, T is the temperature and k_B is the Boltzmann constant. Assuming a sticking coefficient of 1, which describes the case in which all the molecules that arrive on the surface are adsorbed, a temperature of 300 K, and a pressure of 10^{-6} mbar, the surface would result completely covered by contaminants in about 1 s. The assumption on the sticking coefficient is not far from the reality in case of reactive transition metal surfaces, and it can be even more realistic in case of sub-nanometer clusters. Therefore, it is necessary to work in UHV conditions to maintain a sample clean for a time scale long enough to perform an experiment without a relevant contribution arising from contaminants in the background.

During a cluster deposition with ENAC, the pressure in the chamber increases due to the He carrier gas. Despite the differential pumping system, the pressure in the chamber where the sample is located is in order of 10^{-8} mbar. Since a typical deposition time can last between 20 min and 1h 30min, depending on the desired coverage, such pressure could potentially contaminate the sample. However, measurements with a Residual Gas Analyzer (RGA) showed that in these condition the atmosphere is entirely composed of inert He (Fig. 1.11). All the gases that could typically contaminate the sample (H_2O, N_2, CO, O_2 and CO_2) result not to be affected by the high He pressure, and after 40 minutes in working conditions their partial pressure was unaltered and below 10^{-10} mbar. The only gas that was affected by the He pressure was H_2, but it only slightly increased by $\sim 2 \times 10^{-11}$ mbar. This was a fundamental preliminary result for the success of the experiments performed with ENAC at the SuperESCA beamline, since it indicates that the contribution from contaminants can be neglected.

2.3 Sample preparation

Most of the experiments reported in this thesis are performed depositing the size-selected clusters on epitaxial graphene (GR). Growing a high quality GR layer with a low density of defects was of paramount importance for the experiment, since they could act as anchoring sites for the clusters and greatly affect their properties [21]. This can be done by following well-established procedures that have been developed and refined over the past decade [22].

2.3.1 Sample cleaning

A fundamental preliminary step is to clean the metallic surface, which can be done by several Ar^+ sputtering cycles followed by annealing ramps. With the sputtering, the first few layer of the surface are removed, together with any adsorbate or thin layer that may have been formed before placing the sample in the UHV chamber. The annealing ramps allow the atoms on the surface, which shows a certain degree of roughening after the sputtering, to migrate and form large terraces with a high degree of order. To further remove contaminants that may be dissolved into the bulk, a standard procedure that is adopted for transition metals such as Ir and Ru is to perform further annealing ramps in partial pressures of O_2 and, subsequently, H_2. The former is necessary to remove C that may be dissolved into the bulk and that segregate back to the surface during the annealing. In this way, C reacts with O, forming gaseous species such as CO and CO_2 which can desorb by thermal annealing. The annealing in H_2 pressure is then used to remove residual O from the surface by forming H_2O, which desorbs at lower temperatures thatn atomic O.

Specifically, the Ru(0001) surface was cleaned with repeated cycles of Ar^+ sputtering, annealing ramps up to 1570 K in UHV and up to 1100 K in a 1×10^{-7} mbar background pressure of O_2. For this surface, the H_2 cycle is not needed since O desorbs at 1570 K [23]. The Ir(111) surface was prepared following a similar procedure. The annealing was performed up to 1450 K and the sample was exposed to both O_2 (three temperature ramps up to 1080 K with a pressure of 2×10^{-7} mbar) and H_2 (two temperature ramps up to 870 K with a pressure of 5×10^{-8} mbar) [24].

2.3.2 Graphene growth

The GR growth was achieved with the chemical vapor deposition of C_2H_4 on the Ir(111) and Ru(0001) surfaces. This method allows to cover almost completely the metal surfaces with a single layer of GR characterized by a high crystalline quality [25]. This procedure is based on a chemical reaction of C_2H_4 with the surfaces. In the reaction, the precursor molecule is decomposed, producing C species adsorbed on the surface, while H atoms combine thanks to their high mobility and desorb as H_2. By increasing the temperature, the C species gain enough mobility to migrate on the surface and either form nucleation centers for GR islands or attach to already nucleated ones [26]. The growth on Ru(0001) is performed at T = 1100 K, with partial C_2H_4 pressure initially set to 5×10^{-9} mbar for 15 minutes and successively increased to 5×10^{-8} for 5 minutes [27]. Similarly, the growth on Ir(111) consist of five temperature ramps to 1420 K in a C_2H_4 partial pressure of 5×10^{-8} mbar, followed by two ramps at the same temperature with a pressure of 3×10^{-7} mbar [28]. In both cases, the quality of the graphene layer was verified by the low energy electron diffraction apparatus available at the SuperESCA beamline, and by XPS measurements of the C 1s core level. In particular, the XPS spectrum of graphene on Ir(111) (GR/Ir, Fig. 1.12a), acquired at a photon energy of 400 eV and at T = 20 K, can be described by a single, sharp component centered at a BE of 284.06 eV [24, 28]. The spectrum of the layer on Ru(0001) (GR/Ru, Fig. 1.12b) shows two characteristic components [29] which partially overlap with the Ru $3d_{3/2}$ core level. The two components arise from the highly corrugated morphology of the interface due to the strong C-Ru interaction. The component C_1 (dark gray, BE = 285.14 eV) correspond to C atoms close to the surface, while C_2 (light gray, BE = 284.41 eV) accounts for those atoms further away from the surface. On the contrary, the C-Ir interaction is weaker, and all the C atoms show a similar BE [28].

2.4 The SuperESCA beamline

Elettra is a third generation synchrotron radiation facility located in Basovizza, Trieste (Italy). Synchrotron radiation is generated by radially accelerating relativistic electrons to induce the emission of a highly collimated photon beam in the tangential direction. The storage ring, which operates in top-up mode, is composed of different insertion devices that transport, focus and bend the electrons. Elettra is optimized to work in the VUV and X-ray range, where it can reach a spectral brightness of up to 10^{19} photons s/mm^2/mrad^2/0.1%bw.

SuperESCA is the first operating beamline of Elettra. The insertion device to produce the photons that are used for the experiments consists of two consecutive 46-period undulators. The generated radiation is distributed into several harmonics of a fundamental frequency, with a FWHM of a few eV. The photon energy can be tuned in the range 90 - 1500 eV by changing the gap between the two magnet arrays of the undulators, and it is further monochromatized by a plane grating Zeiss SX700 [30]. When the photon beam arrives on the sample at the beamline end-station, it can reach a resolving power of $E/\Delta E = 10^4$ for $h\nu < 500$ eV [31]. The high photon flux, combined with the high energy resolution and with the possibility to precisely tune the photon energy offers the opportunity to perform high resolution XPS measurements also for low-density systems, such as the case of supported size-selected clusters.

The SuperESCA workstation is composed of two UHV chambers disposed verti-

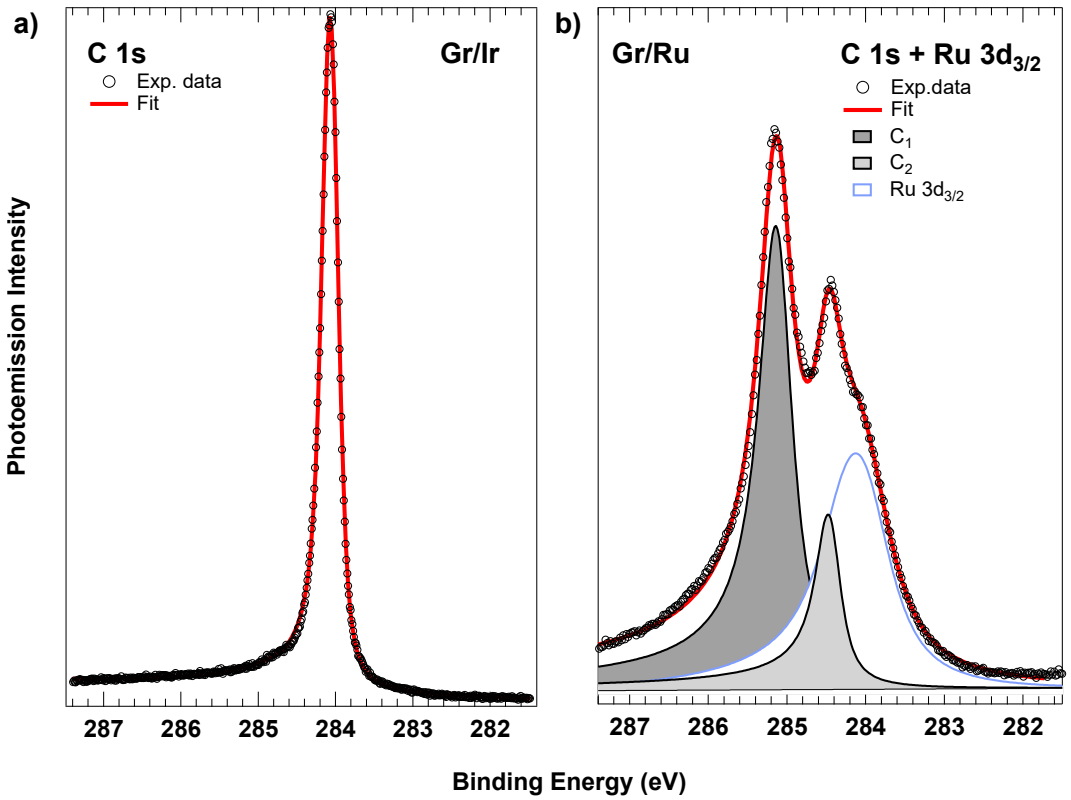

Figure 2.12: *C 1s XPS spectra acquired for graphene on Ir(111) (on the left) and Ru(0001) (on the right). Black circles are the experimental data points, red lines are the fit and the filled areas are different spectral components.*

cally and separated by a valve (Fig. 1.13). The top chamber is dedicated to sample preparation and it is equipped with instrumentation devoted to sample preparation such as a sputter gun, a RGA and a doser. Moreover, it is possible to connect different evaporators and use them without compromising the pressure of the bottom chamber, which is devoted to experimental measurements. It is to the preparation chamber that ENAC can be connected for the *in situ* cluster deposition. Once the sample is prepared, it can be moved to the experimental chamber using a manipulator with four degrees of freedom (x, y and z axis and polar angle), which allows to cool down the sample to 20 K and to heat it up to above 1570 K, either by filament irradiation or electron bombardment. The experimental chamber is equipped with a low-energy electron diffraction apparatus and with a 150 mm radius hemispherical electron energy analyzer. The analyzer is the instrument in charge of the detection of photo-electrons and of measuring their kinetic energy. Its working principles are strictly related to its shape. It is composed of two concentric hemispheres of radius $R_1 > R_2$ separated by a vacuum region (Fig. 1.14). Two slits (entrance and exit) are located at the center of the two edges of the vacuum region at $R_0 = (R_1 + R_2)/2$. By applying different potentials V_1 and and V_2 to the hemispheres, it is possible to generate an electric field in the vacuum region such that only those electrons (charge e) entering from the entrance slit with a given E_{kin} defined as

$$E_{kin} = e\,(V_1 - V_2)\left(\frac{R_2}{R_1} - \frac{R_1}{R_2}\right)^2$$

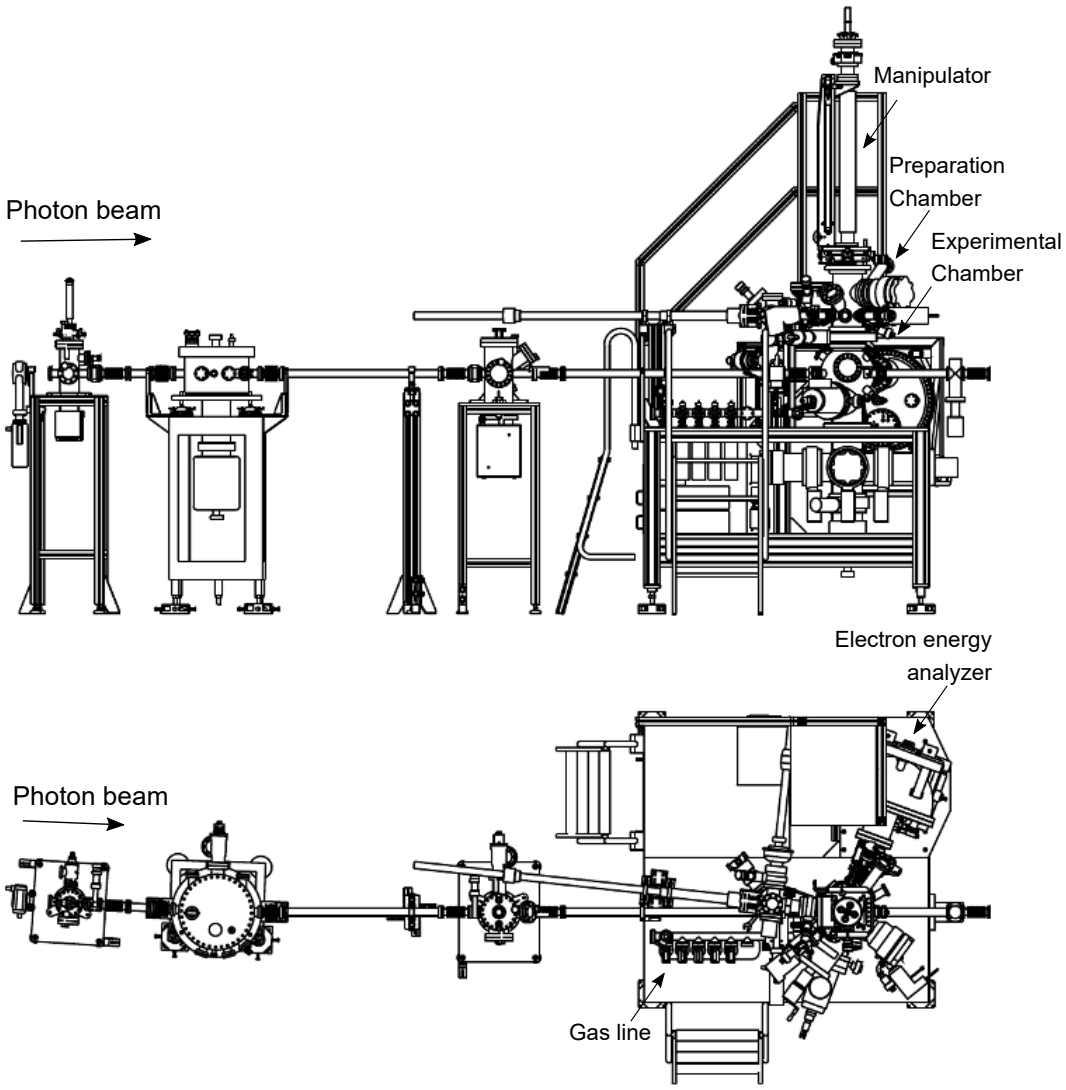

Figure 2.13: *Technical drawing of the SuperESCA end-station at the Elettra synchrotron. The photon beam arrives from the left and enters the experimental chamber on the right side, where the hemispherical electron energy analyzer is visible. Recognizable elements include the two-chamber structure, with the preparation chamber (where ENAC can be connected) above the experimental chamber, the manipulator, and the gas line.*

are refocused after traveling for 180° and are able to exit through the exit slit, finally reaching the homemade microchannel plate-based delay-line detector.

The instrumental energy resolution of the device is proportional to the kinetic energy required to travel through it, which is called pass energy (PE) and, given R_1 and R_2, depends on the voltage applied to the hemispheres. To keep the resolution constant and remove the dependency on the energy of the electrons that have to be measured, the electron analyzer operates in constant PE mode. During a data acquisition, V_1 and V_2 are kept constant, while a set of retarding lenses located between the sample and the entrance slit reduce the kinetic energy of the incoming electrons. Given the initial kinetic energy of the electron E_{kin}, the retarding potential

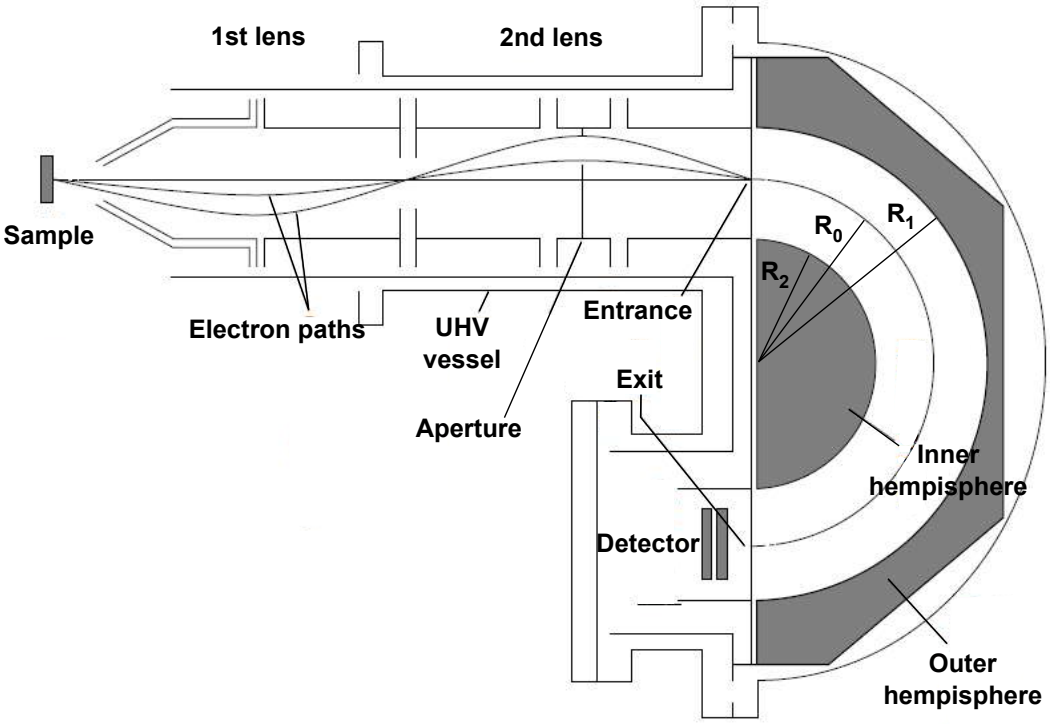

Figure 2.14: *Sketch of a concentric hemispherical analyzer connected to the retarding lenses and to the detector. The trajectory of the electrons entering the system with the selected kinetic energy is also shown, going from the left to the bottom right.*

V_R and PE, the condition that has to be satisfied for the electrons to reach the detector is

$$E_{kin} - V_R = PE.$$

Since V_R and PE are known, by changing the former it is possible to perform an energy scan.

Working in constant PE modes brings several advantages. First of all, as mentioned before, it keeps the instrumental energy resolution constant during an acquisition. Secondly, the retarding lenses can also be used to collect electrons from a wider solid angle, increasing the overall signal. Finally, PE is typically between one and two order of magnitude smaller than the original kinetic energy E_{kin} of the electrons, therefore the instrumental resolution is increased by the same factor.

2.5 High-resolution X-ray core-level photoelectron spectroscopy

X-ray photoelectron spectroscopy (XPS), also known as Electron spectroscopy for chemical analysis (ESCA), is a surface-sensitive quantitative experimental techniques based on the photoelectric effect that can be used to identify the chemical elements present in a material or on a surface, as well as their chemical environment. It was developed by Kai Siegbahn, who recorded the first XPS spectrum of cleaved sodium chloride in 1954 [32]. Few years later in 1964, Siegbahn published a comprehensive study of XPS as a useful analytic tool in material science [33], and for which he was

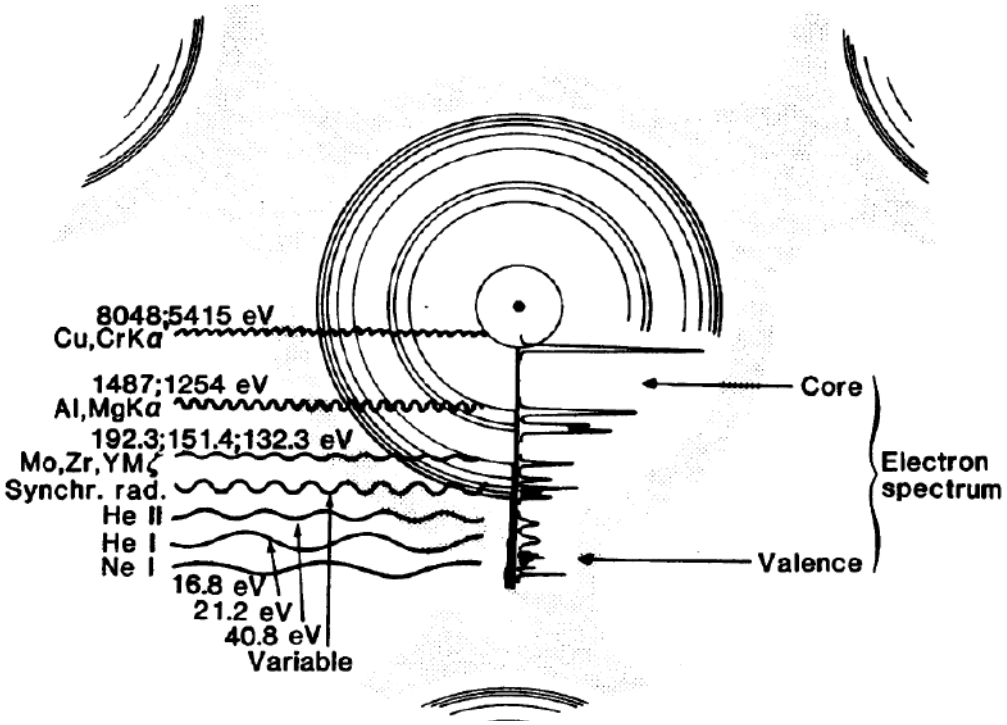

Figure 2.15: *Schematic representation of the regions of binding energies that are accessible with different photon sources. Adapted from Siegbahn's Nobel lecture [34].*

awarded the Nobel Prize for Physics in 1981 [34].

The photoemission process at the basis of XPS can be described as a three-step phenomenon: (i) the electrons are optically excited from a bound state to the continuum; (ii) the excited electrons propagate through the material, towards the surface; (iii) the electrons exit the material. As schematically described in Fig. 1.15, different radiation energies allow to excite electrons from different shells. In particular, with soft X-rays it is possible to photoemit electrons from the core levels of an atom, which generally show negligible dispersion due to their highly localized atomic-like character. When an electron with a binding energy E_B (with respect to the Fermi energy) is photoemitted from a sample using a photon energy $h\nu$, its kinetic energy E_{kin} in the vacuum is given by the following energy conservation law:

$$E_{kin} = h\nu - E_B - \Phi_S,$$

where Φ_S is the sample work function. When the photoelectron is detected by an analyzer, its kinetic energy is affected by the work function of the device Φ_A, which is known. If the Fermi levels of sample and analyzer are aligned (which is the case if they are connected to the same ground), the kinetic energy of the electron inside the anlyzer can be written as

$$E_{kin,A} = E_{kin} + (\Phi_S - \Phi_A),$$

as schematically described in Fig. 1.16. By replacing the initial expression of E_{kin} into this formula, it is possible to relate the measured $E_{kin,A}$ entirely to the photon energy $h\nu$, to the work function of the analyzer Φ_a and to the binding energy E_B:

$$E_{kin,A} = h\nu - E_B - \Phi_A$$

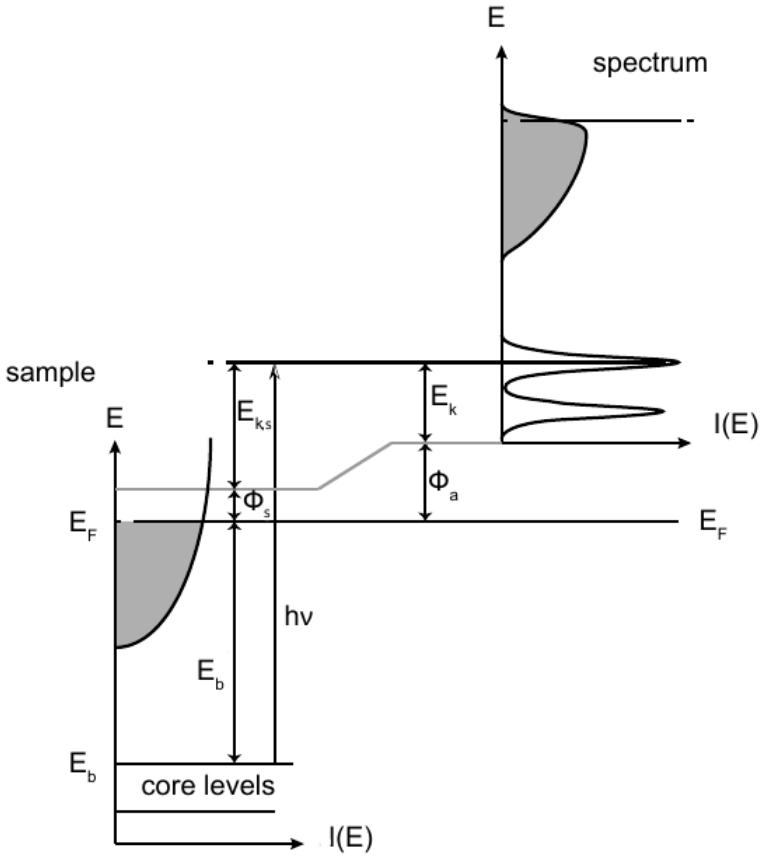

Figure 2.16: *Schematic representation of the XPS process. On the left, the initial state of the photoemission process. On the right, the corresponding photoemission signal obtained with a photon energy* $h\nu$*.*

and, since the former two are known, E_B is obtained.

The utility of XPS comes from the huge amount of information contained in the binding energy of a core electron [35]. First of all, it is a clear fingerprint of elements present on the sample, giving to XPS chemical sensitivity. Moreover, the binding energy is affected by the chemical environment of the emitting atom. A chemical bond affects the valence band of the involved atoms by lowering the density of state of the oxidized element and increasing that of the reduced one. Therefore, the core levels are affected by the charge modification around the nucleus, and their binding energy increases (decrease) if electrons have been removed from (added to) the valence band [36–38]. Similarly, the core level of an electron in a transition metal is affected by the number of nearest neighbors (coordination number) of the emitting atom. Different coordination number modifies the position and shape of the electron d-band, and the core level binding energies are modified accordingly [39]. However, the experimentally measured binding energy does not contain information only from the initial-state system, i.e., the system prior the photoexcitation, but it is also influenced by the final state, which is an atom with a hole in its core level, plus a photoexcited electron. This can be described by analyzing the photoemission process with a semiclassical approach, where the electromagnetic field is treated classically, while a quantum-mechanical description is used for matter. The one-

particle Hamiltonian of an electron subject to an electromagnetic field is:

$$i\hbar\frac{\partial\psi}{\partial t} = \left[\frac{1}{2m}\left(\hat{\mathbf{p}} - \frac{e}{c}\hat{\mathbf{A}}\right)^2 + \hat{V}\right]\psi = \hat{H}\psi,$$

where ψ is the electron wave function, $\mathbf{A}$ is the vector potential of the electromagnetic field and V is the unperturbed potential of the material. In the Coulomb gauge ($\nabla \cdot \hat{\mathbf{A}} = 0$), the Hamiltonian can be simplified exploiting the fact that the vector potential commutes with the momentum operator ($\left[\hat{\mathbf{p}}, \hat{\mathbf{A}}\right] = 0$). Therefore, the expression inside the brackets can be written as

$$\left(\hat{\mathbf{p}} - \frac{e}{c}\hat{\mathbf{A}}\right)^2 = \hat{p}^2 - 2\frac{e}{c}\hat{\mathbf{A}}\cdot\hat{\mathbf{p}} + \left(\frac{e}{c}\right)^2\hat{A}^2.$$

For typical experimental conditions, the quadratic term in $\mathbf{A}$ can be neglected, since it is one order of magnitude smaller than the first term. In a first-order perturbation, the Hamiltonian can then be split into two terms: an unperturbed Hamiltonian $\hat{H}_0$, plus an interaction Hamiltonian $\hat{H}'$, which takes into consideration the effects of the electromagnetic field:

$$\hat{H}' = -\frac{e}{mc}\hat{\mathbf{A}}\cdot\hat{\mathbf{p}}.$$

In this scenario, the transition rate between the initial state ψ_i and the final state ψ is expressed by Fermi's Golden Rule in the time-dependent perturbation theory:

$$\frac{d\omega}{dt} \propto |\langle\psi_f|\hat{H}'|\psi_i\rangle|^2\delta(E_f - E_i - h\nu),$$

where E_f and E_i are the eigenvalues of the unperturbed Hamiltonian in the final and initial state, respectively, and $h\nu$ is the photon energy. The binding energy that can be measured experimentally corresponds to $BE = E_f - E_i$ (or $-BE$, depending on the formalism) and therefore takes into account both the so-called initial and final state effects. While the former correspond to properties of the emitting atom prior the photoexcitation (to be noted that $E_i = E_B$) and are linked to its chemical state, the latter are of difficult interpretation without the support of theoretical calculations [23, 40]. In some cases, final-state effects give a dominant contribution to the measured binding energies, leading to unexpected results. A remarkable example is the case Ag, whose 3d core level shifts to lower binding energies when the metal is oxidized. In chapter 5, this effect is studied for Ag clusters, were we show that the unique electronic properties of these objects can have implications on the behavior of the core level binding energies.

2.5.1 Data analysis

The typical XPS spectrum consists of a curve describing the number of photoelectron emitted per unit time as a function of the binding energy BE, which is an approximation of the initial state binding energy E_B and is obtained by measuring the kinetic energy E_{kin} while precisely knowing $h\nu$ and Φ_A, as discussed above. Since the BE is referred, by definition, with respect to the Fermi level of the sample, it is calibrated by measuring the kinetic energy of those electron at $E_B = 0$, i.e., at the Fermi level. A schematic representation of a XPS spectrum is shown in Fig. 1.16 (right).

The lineshape of photoemission peaks depends on severl factors such as: (i) an intrinsic broadening due to the finite core-hole lifetime; (ii) the experimental resolution;

(iii) an inhomogeneous broadening; (iv) inelastic scattering of the photoelectrons. The first contribution originates from the quantum nature of the system, with a shorter lifetime τ of the core-hole that leads to a larger uncertainty on E_B. This effect induces a Lorentzian broadening whose FWHM is inversely proportional to τ. The experimental resolution depends on the energy resolution of the radiation and of the electron energy analyzer. The inhomogeneous broadening accounts for the presence of emitting atoms of the same chemical species, but in slightly different environments that modify their E_B by less than the experimental resolution. An example are surface defects or different atoms composing a small size-selected cluster. Finally, the inelastic scattering of the photoelectrons with phonons in the solid can induce small losses or gains of energy from the solid to the photoelectron, and *vice versa*. These three latter effects can be described by a Gaussian distribution whose FWHM will be the sum in quadrature of the broadening induced by each of them. Therefore, a good approximation of the lineshape of the photoemission peaks can be obtained from the convolution between a Lorentzian and a Gaussian distribution. The resulting function is called Voigt function, which is one of the most commonly used functions for the analysis of XPS data [41].

Another important contribution to the lineshape which is not taken into account by th Voigt function is given by the excitation by photoelectrons to electron core-hole pairs close to the Fermi level. This process depends directly on the density of states close to the Fermi energy and it is therefore particularly evident in the case of metals, while it can be neglected in the case of insulators with a large energy gap. It induces an asymmetric loss of energy of the photoelectrons, which manifests in the spectrum as a tail in the high energy side of each peak. It is possible to include this contribution by modifying the Lorentzian lineshape associated to the intrinsic broadening into a Donjach-Šunjić function (DS) [42]:

$$DS_{\gamma\alpha}(E) = \frac{\Gamma(1-\alpha)}{(E^2+\gamma^2)^{(1-\alpha)/2}} \cdot \cos\left(\frac{\pi\alpha}{2} + (1-\alpha)\mathrm{atan}(E/\gamma)\right),$$

where $\Gamma(x)$ is the Euler gamma function, α is the asymmetry parameter and γ is related to the FWHM of the initial Lorentzian distribution ($L = 2\gamma$).

In this thesis, the experimental XPS data were fitted with a DS function convoluted with a Gaussian broadening to obtain information also from the asymmetry parameter α. It is important to notice that for $\alpha = 0$ the DS function reverts back to a Lorentz distribution and the fitting function becomes a Voigt function [43]. The data analysis was carried out with the Igor Pro data analysis software, and all the parameters of the fitting functions where obtained from a least-squares fit of the experimental data. The errors associate to each fitting parameter are obtained by summing in quadrature systematic errors with those obtained from the fitting operations. In particular, the intrinsic error associated to the measured BE, i.e., the accuracy, can be as low as 20 meV when the signal-to-noise ratio is sufficiently high thanks to the high photon flux available at the SuperESCA beamline. The same intrinsic error was applied to the lineshape parameters, and the lower limit of the Gaussian width was set to the energy resolution Δ of the beamline, which is approximately 40 meV for photon energies below 500 meV and increases up to 180 meV for a photon energy of 900 eV.

2.6 Density functional theory calculations

Given the unique properties of size-selected clusters, it is not always possible to interpret the data simply by comparison with experiments performed on larger scales. Therefore, we complemented the experimental data with DFT calculations performed in collaboration with the group of prof. Dario Alfè from University College London.

DFT is a successful theory that has emerged in the past decades to calculate the electronic structure of atoms, molecules, solids [44] and, more recently, clusters [45–48]. The strength of DFT compared to traditional electronic structure methods that attempt to find approximate solutions to the Schrödinger equation of N interacting electrons moving in an external potential, is that it uses the one-body density as fundamental variable. This approach drastically decreases the number of spatial variables from the $3N$ of the wave function to just three, making calculations feasible even for large systems.

DFT was first put on a firm theoretical footing by Walter Kohn and Pierre Hohenberg in 1964 [49] and further developed by the same Walter Kohn together with Lu Jeu Sham in a work that won them the Nobel prize in chemistry in 1998 [50]. Since then, Khon-Shan theory has been applied in several different ways to calculate the structural and electronic properties of matter, applying different approximations that better fit the topic that has to be studied. Some examples are the local-density approximation (LDA), which is based upon exact exchange energy for a uniform electron gas, or Hybrid functional, a class of approximations which partially incorporate the Hartree-Fock theory [51].

When paired with experimental XPS, DFT calculations can be extremely useful as they allow to calculate the modifications on the geometry and on the relative core level BEs of atoms within a same sample and upon, for example, the interaction with adsorbants [52, 53]. In particular, it is possible to estimate the core-electron BEs in the final-state approximation by exploiting the use of a pseudo potential to include also contributions for final-state effects. The pseudo potential is built in such a way to correspond to the energy of an atom with an hole in the core level. Therefore, the calculation is performed with the pseudo potential replacing the nucleus of the emitting atom and by adding an extra electron to the valence band, which accounts for the excited state. In order to avoid an interaction between core holes of near emitting atoms, in this approximation it is necessary to build large unit cells composed of several tens of atoms, such as those used in this thesis. The CLSs calculated with this method typically agrees with experiments within 20 meV [53–55].

Besides the calculations on the CLSs, in this thesis DFT calculations where exploited to perform Bader charge analysis in the clusters and to calculate the projected density of states (PDOS). In a Bader charge analysis, the system is considered as divided into atoms by zero flux surfaces defined as a 2D surface on which the charge density passes through a minimum upon crossing the surface[56]. The Bader charge of an atom is the total charge within the volume defined around each atom (Bader volume). This quantity is a good approximation to the total charge of an atom and can be used to estimate, for example, the oxidation state [57]. The density of states (DOS) is the number of different states at a particular energy level that electrons in a material are allowed to occupy [58]. The PDOS gives the projection of a particular orbital of a particular atom of the system on the total density of states. It follows that the sum of all the PDOS is equal to the DOS. Similar calculations are extremely

useful in several branch of material science, and in chemical-physics and catalyisis, as they give access to quantities such as the d-band center, a well know indicator of chemical reactivity [59].

While I was not directly involved to perform the DFT calculations, I contributed to the preparation of the input files and I have extensively performed the data analysis on the output data. The input of the calculations were carefully prepared to better replicate the experimental conditions, and the output data has been accurately analyzed together with the experimental data to improve the knowledge on the geometric and electronic properties of the graphene-supported size-selected clusters, both in the metallic and oxide phase.

The DFT calculations were performed as implemented in the Vienna Ab-initio Simulation Package (VASP) code, which allows to use post-DFT corrections such as hybrid functionals [60]. To include the contribution coming from the corrugated moiré GR lattice on the stability and properties of the supported clusters, the minimum energy configurations were calculated by describing the system as a complete moiré cell supported by 4 metal layers (Ru or Ir, based on the experiment), for an overall number of 914 atoms (excluding the clusters) for the experiments on Ru(0001). A vacuum interspace of at least 15 Å between metal layers was used to minimize the interaction between periodic images of the slab along the direction perpendicular to the surface. The bottom two layers of the metal where kept frozen at their bulk geometry. The rest of the system was fully relaxed until the largest residual force was less than 0.015 eV/Å. The projector augmented method (PAW) [61] was employed, using PBE potentials [62]. The plane wave cutoff was set to 400 eV, and we performed the relaxations by sampling the Brillouin zone using the Γ point. To obtain the partial density of states, we have performed single point DFT calculations, using the geometries obtained with the rev-vdw-DF2 functional [63].

References

[1] U. Heiz, F. Vanolli, L. Trento, and W.-D. Schneider, Chemical reactivity of size-selected supported clusters: An experimental setup, Rev. Sci. Instrum. **68**, 1986 (1997).

[2] R. E. Smalley, Laser studies of metal cluster beams, Laser Chem. **2**, 957420 (1983).

[3] S. Maruyama, L. R. Anderson, and R. E. Smalley, Direct injection supersonic cluster beam source for FTFT studies of clusters, Rev. Sci. Instrum. **61**, 3686 (1990).

[4] M. A. Röttgen, K. Judai, J.-M. Antonietti, U. Heiz, S. Rauschenbach, and K. Kern, Conical octopole ion guide: Design, focusing, and its application to the deposition of low energetic clusters, Rev. Sci. Instrum. **77**, 013302 (2006).

[5] T. Masubuchi, J. F. Eckhard, K. Lange, B. Visser, M. Tschurl, and U. Heiz, An efficient laser vaporization source for chemically modified metal clusters characterized by thermodynamics and kinetics, Rev. Sci. Instrum. **89**, 023104 (2018).

[6] S. Pratontep, S. J. Carroll, C. Xirouchaki, M. Streun, and R. E. Palmer, Size-selected cluster beam source based on radio frequency magnetron plasma sputtering and gas condensation, Rev. Sci. Instrum. **76**, 045103 (2005).

[7] J. Jašík, S. Valtera, M. Vaidulych, M. Bunian, Y. Lei, A. Halder, H. Tarábková, M. Jindra, L. Kavan, O. Frank, S. Bartling, and S. Vajda, Oxidative dehydrogenation of cyclohexene on atomically precise subnanometer $Cu_{4-n}Pd_n$ ($0 \leq n \leq 4$) tetramer clusters: the effect of cluster composition and support on performance, Faraday Discuss. , (2023).

[8] P. Milani and W. A. deHeer, Improved pulsed laser vaporization source for production of intense beams of neutral and ionized clusters, Rev. Sci. Instrum. **61**, 1835 (1990).

[9] G. D. Stein, Cluster beam sources: Predictions and limitations of the nucleation theory, Surf. Sci. **156**, 44 (1985).

[10] J. M. Soler, N. García, O. Echt, K. Sattler, and E. Recknagel, Microcluster growth: Transition from successive monomer addition to coagulation, Phys. Rev. Lett. **49**, 1857 (1982).

[11] G. Scoles, *Atomic and Molecular Beam Methods*, Atomic and Molecular Beam Methods No. v. 1 (Oxford University Press, 1988).

[12] M. A. Duncan, Invited review article: Laser vaporization cluster sources, Rev. Sci. Instrum. **83**, 041101 (2012).

[13] M. D. Morse, Supersonic beam sources, Exp. Methods Phys. Sci. **29**, 21 (1996).

[14] M. Abbet, Mach disk in underexpanded exhaust plumes, AIAA J. **9**, 512 (1971).

[15] M. Abramowitz, I. Stegun, and D. A. McQuarrie, Handbook of mathematical functions, Am. J. Phys. **34**, 177 (1966).

[16] A. Adams and F. H. Read, Electrostatic cylinder lenses II: Three element einzel lenses, J. Phys. E: Sci. Instrum. **5**, 150 (1972).

[17] T. Prohaska, J. Irrgeher, J. Benefield, J. K. Böhlke, L. A. Chesson, T. B. Coplen, T. Ding, P. J. H. Dunn, M. Gröning, N. E. Holden, H. A. J. Meijer, H. Moossen, A. Possolo, Y. Takahashi, J. Vogl, T. Walczyk, J. Wang, M. E. Wieser, S. Yoneda, X.-K. Zhu, and J. Meija, Standard atomic weights of the elements 2021 (IUPAC technical report), Pure Appl. Chem., **94**, 573 (2022).

[18] P. E. Miller and M. B. Denton, The quadrupole mass filter: Basic operating concepts, J. Chem. Educ. **63**, 617 (1986).

[19] K. Bromann, C. Félix, H. Brune, W. Harbich, R. Monot, J. Buttet, and K. Kern, Controlled deposition of size-selected silver nanoclusters, Science **274**, 956 (1996).

[20] Thermodynamics and kinetics of adsorption and desorption (2012) pp. 185–228.

[21] I. Fampiou and A. Ramasubramaniam, Binding of Pt nanoclusters to point defects in graphene: Adsorption, morphology, and electronic structure, J. Phys. Chem. C **116**, 6543 (2012).

[22] L. Bignardi, P. Lacovig, R. Larciprete, D. Alfè, S. Lizzit, and A. Baraldi, Exploring 2 D materials at surfaces through synchrotron-based core-level photoelectron spectroscopy, Surf. Sci. Rep. , 100586 (2023).

[23] S. Lizzit, A. Baraldi, A. Groso, K. Reuter, M. V. Ganduglia-Pirovano, C. Stampfl, M. Scheffler, M. Stichler, C. Keller, W. Wurth, and D. Menzel, Surface core-level shifts of clean and oxygen-covered Ru(0001), Phys. Rev. B **63**, 205419 (2001).

[24] F. Loi, L. Sbuelz, P. Lacovig, D. Lizzit, L. Bignardi, S. Lizzit, and A. Baraldi, Growth mechanism and thermal stability of a MoS_2-graphene interface: A high-resolution core-level photoelectron spectroscopy study, J. Phys. Chem. C **124**, 20889 (2020).

[25] M. Batzill, The surface science of graphene: Metal interfaces, CVD synthesis, nanoribbons, chemical modifications, and defects, Surf. Sci. Rep. **67**, 83 (2012).

[26] P. Lacovig, M. Pozzo, D. Alfè, P. Vilmercati, A. Baraldi, and S. Lizzit, Growth of dome-shaped carbon nanoislands on Ir(111): The intermediate between carbidic clusters and quasi-free-standing graphene, Phys. Rev. Lett. **103**, 166101 (2009).

[27] D. Alfè, M. Pozzo, E. Miniussi, S. Günther, P. Lacovig, S. Lizzit, R. Larciprete, B. S. Burgos, T. O. Menteş, A. Locatelli, and A. Baraldi, Fine tuning of graphene-metal adhesion by surface alloying, Sci. Rep. **3**, 2430 (2013).

[28] F. Presel, H. Tetlow, L. Bignardi, P. Lacovig, C. A. Tache, S. Lizzit, L. Kantorovich, and A. Baraldi, Graphene growth by molecular beam epitaxy: an interplay between desorption, diffusion and intercalation of elemental C species on islands, Nanoscale **10**, 7396 (2018).

[29] S. Ulstrup, P. Lacovig, F. Orlando, D. Lizzit, L. Bignardi, M. Dalmiglio, M. Bianchi, F. Mazzola, A. Baraldi, R. Larciprete, P. Hofmann, and S. Lizzit, Photoemission investigation of oxygen intercalated epitaxial graphene on Ru(0001), Surf. Sci. **678**, 57 (2018).

[30] W. Jark, Soft x-ray monochromator configurations for the elettra undulators: A stigmatic SX_{700}, Rev. Sci. Instrum. **63**, 1241 (1992).

[31] A. Abrami, M. Barnaba, L. Battistello, A. Bianco, B. Brena, G. Cautero, Q. H. Chen, D. Cocco, G. Comelli, S. Contrino, F. DeBona, S. Di Fonzo, C. Fava, P. Finetti, P. Furlan, A. Galimberti, A. Gambitta, D. Giuressi, R. Godnig, W. Jark, S. Lizzit, F. Mazzolini, P. Melpignano, L. Olivi, G. Paolucci, R. Pugliese, S. N. Qian, R. Rosei, G. Sandrin, A. Savoia, R. Sergo, G. Sostero, R. Tommasini, M. Tudor, D. Vivoda, F. Wei, and F. Zanini, Super ESCA: First beamline operating at elettra, Rev. Sci. Instrum. **66**, 1618 (1995).

[32] K. Siegbahn and K. Edvarson, β-ray spectroscopy in the precision range of 1 : 105, Nucl. Phys. **1**, 137 (1956).

[33] K. Siegbahn and V.-S. I. Upsala, *Esca; Atomic, Molecular and Solid State Structure Studies by Means of Electron Spectroscopy by Kai Siegbahn (And Others).*, Nova Acta Regiae Societatis Scientiarum Upsaliensis, Ser. 4, V.20 (1967).

[34] K. Siegbahn, Electron spectroscopy for atoms, molecules, and condensed matter, Science **217**, 111 (1982).

[35] S. Hüfner, *Photoelectron Spectroscopy: Principles and Applications*, Advanced Texts in Physics (Springer, 2003).

[36] C. S. Fadley, S. B. M. Hagstrom, M. P. Klein, and D. A. Shirley, Chemical effects on core-electron binding energies in iodine and europium, J. Chem. Phys. **48**, 3779 (1968).

[37] K. Siegbahn, Electron spectroscopy - an outlook, J. Electron Spectrosc. **5**, 3 (1974).

[38] S. Hüfner, *Photoelectron Spectroscopy: Principles and Applications*, Springer Series in Solid-State Sciences (Springer Berlin Heidelberg, 2013).

[39] A. Zangwill, *Physics at Surfaces* (Cambridge University Press, 1988).

[40] M. V. Ganduglia-Pirovano, M. Scheffler, A. Baraldi, S. Lizzit, G. Comelli, G. Paolucci, and R. Rosei, Oxygen-induced Rh $3d_{5/2}$ surface core-level shifts on Rh(111), Phys. Rev. B **63**, 205415 (2001).

[41] G. H. Major, T. G. Avval, D. I. Patel, D. Shah, T. Roychowdhury, A. J. Barlow, P. J. Pigram, M. Greiner, V. Fernandez, A. Herrera-Gomez, and M. R. Linford, A discussion of approaches for fitting asymmetric signals in X-ray photoelectron spectroscopy (XPS), noting the importance of Voigt-like peak shapes, Surf. Interface Anal. **53**, 689 (2021).

[42] S. Doniach and M. Sunjic, Many-electron singularity in X-ray photoemission and X-ray line spectra from metals, J. Phys. C: Solid State Phys. **3**, 285 (1970).

[43] B. Moeini, M. R. Linford, N. Fairley, A. Barlow, P. Cumpson, D. Morgan, V. Fernandez, and J. Baltrusaitis, Definition of a new (doniach-sunjic-shirley) peak shape for fitting asymmetric signals applied to reduced graphene oxide/graphene oxide xps spectra, Surf. Interface Anal. **54**, 67 (2022).

[44] G. Bassani, G. Liedl, and P. Wyder, *Encyclopedia of Condensed Matter Physics*, Encyclopedia of Condensed Matter Physics No. v. 1 (Academic, 2005).

[45] L. D. Socaciu, J. Hagen, T. M. Bernhardt, L. Wöste, U. Heiz, H. Häkkinen, and U. Landman, Catalytic CO oxidation by free Au_2^-: Experiment and theory, J. Am. Chem. Soc. **125**, 10437 (2003).

[46] J. Alonso, *Structure and Properties of Atomic Nanoclusters* (Imperial College Press, 2005).

[47] Y. Lei, F. Mehmood, S. Lee, J. Greeley, B. Lee, S. Seifert, R. E. Winans, J. W. Elam, R. J. Meyer, P. C. Redfern, D. Teschner, R. Schlögl, M. J. Pellin, L. A. Curtiss, and S. Vajda, Increased silver activity for direct propylene epoxidation via subnanometer size effects, Science **328**, 224 (2010).

[48] H. Zhai and A. N. Alexandrova, Fluxionality of catalytic clusters: When it matters and how to address it, ACS Catal. **7**, 1905 (2017).

[49] P. Hohenberg and W. Kohn, Inhomogeneous electron gas, Phys. Rev. **136**, B864 (1964).

[50] W. Kohn, Nobel lecture: Electronic structure of matter—wave functions and density functionals, Rev. Mod. Phys. **71**, 1253 (1999).

[51] A. D. Becke, A new mixing of Hartree-Fock and local density-functional theories, J. Chem. Phys. **98**, 1372 (1993).

[52] L. Bianchettin, A. Baraldi, S. de Gironcoli, S. Lizzit, L. Petaccia, E. Vesselli, G. Comelli, and R. Rosei, Geometric and electronic structure of the NRh(100) system by core-level photoelectron spectroscopy: Experiment and theory, Phys. Rev. B **74**, 045430 (2006).

[53] L. Bianchettin, A. Baraldi, S. de Gironcoli, E. Vesselli, S. Lizzit, L. Petaccia, G. Comelli, and R. Rosei, Core level shifts of undercoordinated Pt atoms, J. Chem. Phys. **128**, 114706 (2008).

[54] A. Baraldi, Structure and chemical reactivity of transition metal surfaces as probed by synchrotron radiation core level photoelectron spectroscopy, J. Phys.: Condens. Matter **20**, 093001 (2008).

[55] A. Baraldi, L. Bianchettin, E. Vesselli, S. de Gironcoli, S. Lizzit, L. Petaccia, G. Zampieri, G. Comelli, and R. Rosei, Highly under-coordinated atoms at Rh surfaces: interplay of strain and coordination effects on core level shift, New J. Phys. **9**, 143 (2007).

[56] G. Henkelman, A. Arnaldsson, and H. Jónsson, A fast and robust algorithm for bader decomposition of charge density, Comp. Mater. Sci. **36**, 354 (2006).

[57] N. Seriani, Z. Jin, W. Pompe, and L. C. Ciacchi, Density functional theory study of platinum oxides: From infinite crystals to nanoscopic particles, Phys. Rev. B **76**, 155421 (2007).

[58] W. Harrison, *Electronic Structure and the Properties of Solids: The Physics of the Chemical Bond*, Dover Books on Physics (Dover Publications, 1989).

[59] B. Hammer and J. K. Nørskov, Theoretical surface science and catalysis–calculations and concepts, in *Advances in Catalysis*, Vol. 45 (Academic Press, 2000) pp. 71–129.

[60] G. Kresse and J. Furthmüller, Efficient iterative schemes for ab initio total-energy calculations using a plane-wave basis set, Phys. Rev. B **54**, 11169 (1996).

[61] P. E. Blöchl, Projector augmented-wave method, Phys. Rev. B **50**, 17953 (1994).

[62] J. P. Perdew, K. Burke, and M. Ernzerhof, Generalized gradient approximation made simple, Phys. Rev. Lett. **77**, 3865 (1996).

[63] I. Hamada, van der Waals density functional made accurate, Phys. Rev. B **89**, 121103 (2014).

CHAPTER 3

Adsorption of size-selected Ag clusters on Ru(0001)

This chapter is dedicated to the first experiment performed with the ENAC cluster source connected to the SuperESCA beamline. It involves a relatively well-know surface, a Ru(0001) single crystal, where we deposited size-selected Ag clusters at room temperature in soft-landing conditions. The aim of this work was to test the capabilities of the ENAC - SuperESCA apparatus in the measurements of size-related features of supported size-selected clusters. Specifically, we exploited the sensitivity of XPS to atoms with different coordination number (CN) to study the formation of Ag two-dimensional islands on Ru(0001). This experiment was designed as a benchmark to test the experimental apparatus because, despite the apparent simplicity of the system, silver has a peculiar valence band electronic structure which makes the distinction of the effects due to reduced coordination arduous to reveal using XPS, even with synchrotron radiation [1].

Besides its important role for the characterization of the experimental apparatus, this work is contextualized in the research field that aims to use atomically precise nanomaterials as building blocks to form extended structures [2]. The ability to tailor the properties of crystalline solids by controlling their composition and structure at the atomic level presents unique opportunities for the design of new functional materials and the discovery of novel phenomena. By tuning the CN of the atoms in a material using different clusters, one can directly tune its physical and chemical properties. The importance of this quantity is well recognized in the field of heterogeneous catalysis [3]: the chemical properties of a wide range of catalytic active nanoparticles materials are determined by the presence of a large density of under-coordinated atoms sitting at defect sites, edges, corners, and nanofacets [4, 5]. The importance of these local configurations was revealed both in noble [6, 7] and transition metal [8] nanoparticles, for which it has been demonstrated that a high concentration of low-coordination atomic sites results in an increased chemical reactivity [9] towards several reactions, such as the promotion of the O_2 adsorption and activation [6] or the chemical conversion of N-heterocyclic carbene molecules [10].

When XPS reaches the high resolution achievable employing synchrotron radiation, it becomes an excellent tool to investigate the CN of a 2D island supported on a metallic surface [11]. In the experiment described in this chapter, we fully exploited this possibility using a combined experimental and theoretical approach to compare different Ag $3d_{5/2}$ binding energies (BE) to the density of fully- and under-coordinate atoms in the islands. With this method, we were able to conclude that the hexagonal

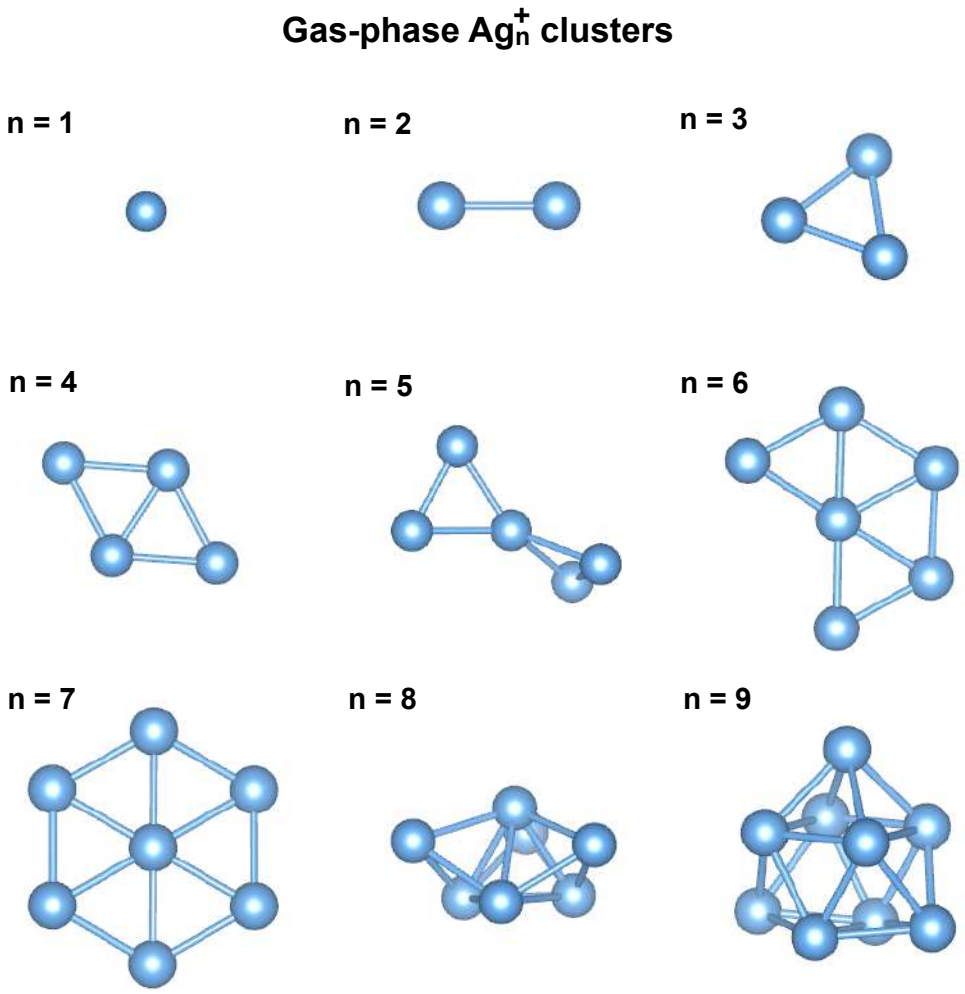

Figure 3.1: *Minimum energy configuration of size-selected Ag_n^+ clusters in the gas-phase with $n = 1 - 9$ according to our DFT calculations.*

Ag cluster composed of 7 atoms serves as building block to form islands with a close-packed atomic arrangement.

The results reported in this chapter have been published in *The Journal of Phyisical Chemistry C*, with the title "Atomic Undercoordination in Ag Islands on Ru(0001) Grown via Size-Selected Cluster Deposition: An Experimental and Theoretical High-Resolution Core-Level Photoemission Study" [12].

3.1 Description of the experiment

The aim of this experiment is to use Ag size-selected clusters to form 2D islands on the Ru(0001) surface and to combine experimental and theoretical XPS to link different spectral features to size-related effects associated to the original clusters used as building blocks. To carry out this study, we performed preliminary DFT calculations on the structures of Ag_n^+ clusters in the gas-phase (Fig. 3.1) to identify the best candidates to perform our experiment. Since our goal is to form 2D islands, we focused on clusters with a planar geometry. In particular, our choice fell on Ag_7, the largest 2D cluster, and Ag_3. According to our calculations, which are in agreement

with previous reports [13], both clusters posses symmetric planar shapes which could potentially nicely fit an ordered close-packed atomic arrangement. Moreover, we included in the study the monomer Ag_1 to provide a comparison with a more similar system to the one obtainable using a conventional Ag evaporator to form the islands.

The islands are formed from the diffusion of the clusters on the Ru(0001) surface at T = 300 K (RT), which depends on the low interaction and immiscibility of Ag in Ru [14]. As a matter of fact, this temperature is more than sufficient to promote an efficient cluster diffusion. The diffusion rate Γ of an Ag adatom adsorbed on the Ru(0001) surface is given by the formula

$$\Gamma = \nu \exp^{-\Delta E/k_B T},$$

where ν is the pre-exponential factor, associated to the phonon frequency and typically is in the order of $10^{13}\, s^{-1}$, T is the temperature of the substrate, ΔE is the diffusion barrier and k_B is the Boltzmann constant [15, 16]. The diffusion barrier that we calculated using the Nudged Elastic Band method [17, 18] is $\Delta E = 59$ meV, in agreement with the value reported by Ref. [19]. Given this value and the temperature T = 300 K, one obtains $\Gamma \sim 1 \times 10^{12}\, s^{-1}$. To better visualize the mobility associated to this diffusion rate, it is possible to calculate the mean squared displacement $\sqrt{\langle r^2 \rangle}$ that an adsorbed Ag atom diffusing on Ru(0001) will travel per second [16]:

$$\sqrt{\langle r^2 \rangle} = a\sqrt{\Gamma t},$$

where $a = 2.71$ Å is the surface lattice parameter of Ru(0001). The mean squared displacement represents the deviation of the position of the atom with respect to a reference position over time. In our case, it is in the order of the hundreds of micrometers, thous ensuring an efficient diffusion for the formation of the islands. These calculations refer specifically to the mobility of single atoms. In general, the diffusion barrier of larger islands scales as the inverse of their radius, meaning that larger clusters are expected to have a higher diffusion barrier [20]. However, this dependency is too weak ($\propto N^{1/2}$) to significantly affect the mobility of Ag_3 and Ag_7 clusters with respect to the monomers: the mean squared displacement for Ag_7 according to this law of proportionality is still in the order of few micrometers. To avoid the formation of 3D structures, we dosed a very low amount of clusters, with a Ag atomic coverage of about 0.6 % ML, calculated with respect to the Ru(0001) surface density $\rho_s = 1.57 \times 10^{15}$ atoms cm^{-2}. Given the elevated diffusion rate of the clusters, this low coverage does not prevent the formation of the 2D island, since the average distance of the isolated clusters on the surface upon deposition assuming a random distribution is about 50 nm, widely within the average displacement over time.

Once the islands are formed, it is possible to exploit the sensitivity of XPS to different in-plane CN to evaluate whether they possess an ordered structure or not. As sketched in Fig. 3.2, an ordered island with a close-packed atomic arrangement is characterized by a high percentage of atoms with CN = 6 an a minor abundance of atoms with CN = 4 and 3 at the island edges. When we lower the degree of order and include defects in our model, the abundance of atoms with CN = 6 will decrease in favor of under-coordinated local morphologies. In particular, the presence of defects can be spotted by the presence of atoms with CN = 5, which appear if we remove one single atom from the center of a ordered island. As mentioned before, this kind of analysis is extremely challenging for Ag islands, where the CLS induced by different

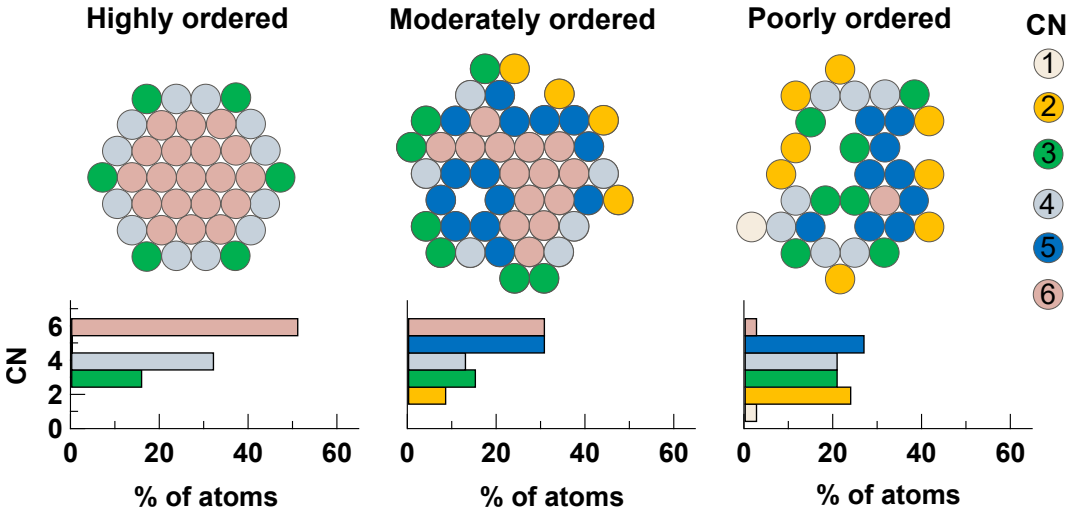

Figure 3.2: *Schematic model of the correlation between order and in-plane CN in 2D islands of similar sizes. Starting from the left, a highly ordered island in the hexagonal close-packed arrangement is characterized by a high density of atoms with in-plane CN = 6 and a minor density of atoms with in-plane CN = 4 and 5 at the island edges. As the degree of order decreases (formation of defects inside the island and irregular edges) the density of atoms with CN = 6 decreases and atoms with CN = 5 become the most dominant ones.*

CN can be difficult also using cutting edge synchrotron-based high resolution XPS. But when coupled with DFT calculations, and with the atomic precision of ENAC, the model I just described can be used to characterize the island formation.

3.2 XPS measurements: surface and clusters

The first step of the experiment was the measurement of the $3d_{5/2}$ core level spectrum of a Ag(111) single crystal to establish the most accurate way to measure the core electron BE of Ag atoms. This served as a reference for comparing the experimental and theoretical results and to convert theoretically calculated BE shifts into absolute BE values. As anticipated, the measurement of core level shifts (CLS) arising from lower CN in the case of Ag is a very challenging task. This applies also to the measurement of the surface core level shift (SCLS), the shift between the core level of atoms sitting on the surface with respect to those in the bulk. One of the effects that contribute to the SCLS is the lower CN of surfaces atoms: for an fcc crystals such as Ag, surface atoms show a CN = 9, while fully coordinated bulk atoms possess a CN = 12. Andersen *et al.* [1] have found that the surface component of the $3d_{5/2}$ spectrum of clean Ag(111) is indeed difficult to discern from the bulk component, presenting a SCLS that was estimated to be smaller than -100 meV, if not completely absent (Fig 3.3a). Figure 3.3b shows the Ag $3d_{5/2}$ spectrum of the clean Ag(111) surface that we measured with a photon energy of 470 eV at RT, together with the spectral decomposition. The unusual asymmetric spectral lineshape toward lower BEs, which cannot be justified by electron-hole pair excitation or energy losses, as it would result in the build-up of a tail at higher BEs, does indeed reveal the presence of a multi-component structure. The spectrum can be properly fitted with two components at 368.20 and 368.05 eV, which, based on the comparison with the spectra in Fig 3.3a,

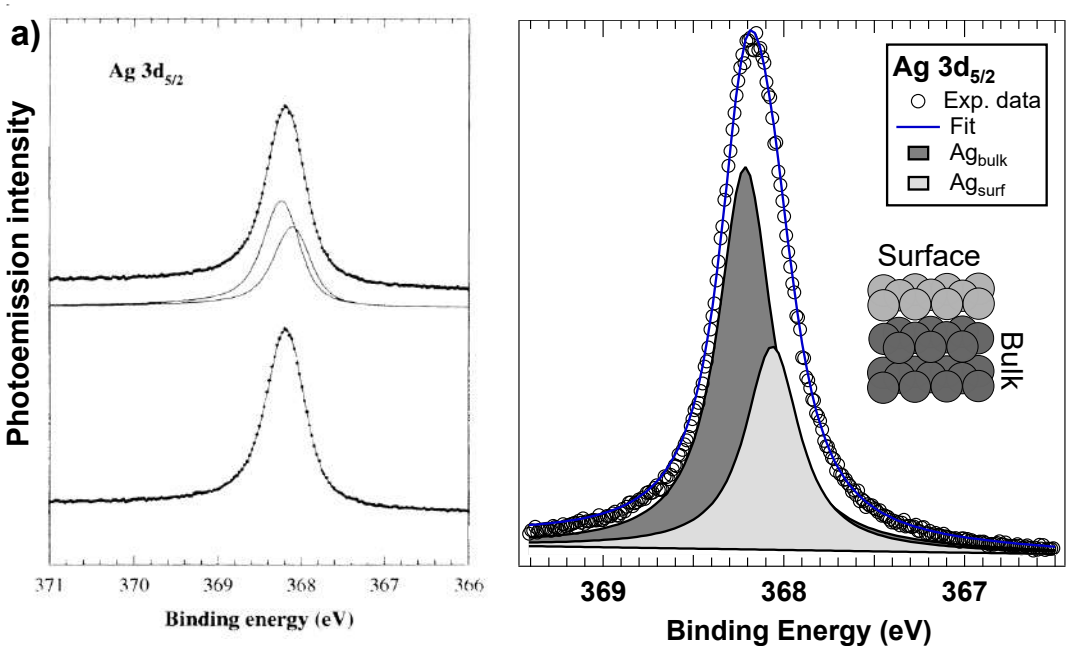

Figure 3.3: *a) Ag $3d_{5/2}$ spectrum from an Ag(111) surface measured at a photon energy of 450 eV fitted by either one or two Doniach-Šunjić lines according to Ref. [1]. b) Same core level spectrum we measured from the Ag(111) surface with a photon energy of 470 eV and at T = 300 K. The spectral components obtained by the fit originate from bulk (Ag_{bulk}) and first layer (Ag_{surf}).*

can be associated to bulk (Ag_{surf}) and first-layer (Ag_{bulk}) components. The values for the lineshape parameters Γ (Lorentzian) and G (Gaussian) resulting from the fit are reported in Tab 3.1. The asymmetry parameter α was found to be 0 for both bulk and surface components, confirming a low density of states at the Fermi level, as expected for a noble metal. Our analysis shows a SCLS = -150 ± 20 meV, which is slightly larger than the one previously reported *et al.* [1]. We tested our result performing DFT calculations on a Ag(111) slab composed of 11 layers of a 5×5 surface unit cell. According to this calculation, the SCSL is -146 ± 20 meV with respect to the bulk component, confirming the peak assignment and supporting the outcomes of our spectral analysis.

After this preliminary analysis on the Ag(111) single crystal, we can focus to the Ag $3d_{5/2}$ spectra measured upon deposition of Ag_1, Ag_3 and Ag_7 clusters on the Ru(0001) (Fig. 3.4). The first clear outcome of the experiment is the large CLS of Ag clusters deposited on Ru(0001) with respect to the Ag(111) surface of about 300 meV. Interestingly, this shift slightly increases reducing the size of the clusters. The Ag $3d_{5/2}$ BEs of the clusters and the lineshape parameters obtained fitting each spectrum with one single component are reported in Tab. 3.1. The size-related trend of the Ag $3d_{5/2}$ BEs is a result which gets us closer to the main goal of this experiment, i.e., appreciate and understand size-related features in our spectra. However, the CLS are, as expected, very small: the BEs of the three spectra are within a window of 30 meV. Anyhow, it is still possible to appreciate the shift of the spectral maximum, given the good signal-to-noise ratio (considering the extremely small Ag coverage). The difference spectra, plotted in the right panel of Fig. 3.4, show the shift of the spectral intensity toward higher BEs as the cluster sizes increase.

	BE (eV)	Γ (eV)	G (eV)
Ag_{bulk}	368.20 ± 0.02	0.34± 0.03	0.07± 0.02
Ag_{surf}	368.05 ± 0.02	0.34± 0.03	0.07± 0.02
Ag_1	367.87 ± 0.03	0.35± 0.03	0.22± 0.03
Ag_3	367.89 ± 0.03	0.34± 0.03	0.21± 0.03
Ag_7	367.90 ± 0.03	0.35± 0.03	0.23± 0.03

Table 3.1: *Fitting parameters obtained from the spectral analysis performed with Doniach-Šunjić lines. The asymmetry parameter α was found to be 0 for all the Ag $3d_{5/2}$ spectra.*

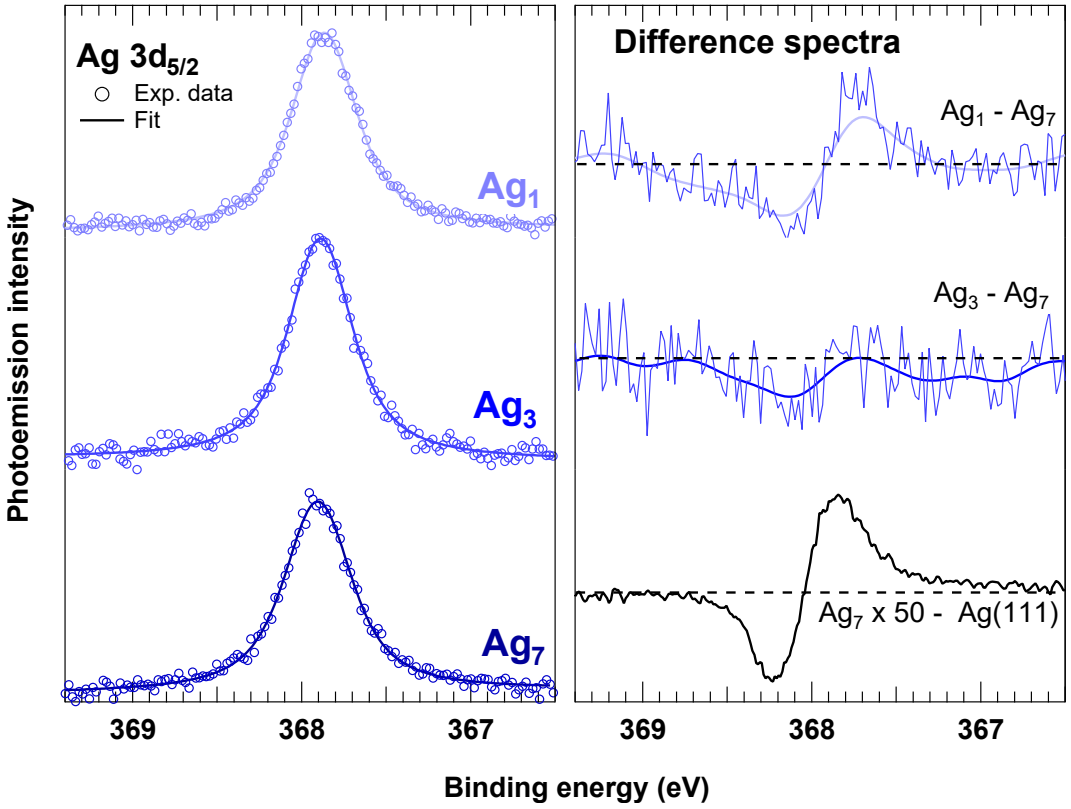

Figure 3.4: *On the left panel, Ag $3d_{5/2}$ core level spectra measured after the deposition of Ag_n size-selected clusters on the Ru(0001) surface with a photon energy of 470 eV. On the right panel, the difference spectra Ag_7 (×50) - Ag(111), $Ag_3 - Ag_7$ and $Ag_1 - Ag_7$.*

Given the small differences spotted in the spectra, it is not possible for us to get to a deeper, atomic-level understanding of our system with experimental data alone. Nevertheless, the trend of the BEs and the G parameter obtained from the analysis of the clusters, which are remarkably higher than for the extremely ordered Ag(111) single crystal surface, suggests that the spectra we are measuring may be composed of different components, associated to nonequivalent atoms in the islands formed by the clusters. However, the BEs of different components appear to be too close to each others to be clearly distinguished experimentally. This is when DFT calculations can come to help.

3.3 DFT calculations

To obtain a thorough understanding of the experimentally prepared system, we resorted to DFT calculations. Our theoretical analysis is divided into two parts. First, we investigated the structure and preferred adsorption sites for the three different types of clusters. Secondly, we studied the evolution of the BEs of the atoms composing islands of increasing size, in particular calculating the Ag 3d CLS associated to different in-plane CN.

3.3.1 Cluster adsorption

We calculated the adsorption energy of the clusters in the four main sites available in the Ru(0001) surface: three-fold fcc, three-fold hcp, bridge, and on-top (Tab. 3.2). The on-top adsorption site was investigated only of the monomer Ag_1 since it appeared to be markedly the least favorite configuration. For all the Ag_n clusters, the three-fold adsorption sites resulted to be the most stable configurations. Both fcc and hcp sites gave similar results due the very large covalent radius of Ag atoms (~ 1.60 Å), indicating therefore a negligible influence of the second layer Ru atoms [21, 22]. The two-fold bridge adsorption configurations is less preferred by about 50 meV. The results in the case of single adatoms are in agreement with previously reported DFT calculations [19]. The trend of the adsorption energies, which increase with cluster size, indicates an attractive Ag−Ag interaction which favors the formation of small compact Ag islands on the Ru(0001) surface.

The increasing adsorption energy with cluster size is accompanied by an increase of the average Ag−Ru distance between the clusters and the Ru atoms sitting in the surface underneath (Fig. 3.6). This distance is calculated as the average distance of each Ag atom with respect to the N Ru atoms of the N-fold adsorption sites. In the case of the most favorite configurations, it goes from 2.78 Å for Ag_1 (a value that is once again in agreement with previous findings [19]) to 2.85 Å (Ag_7), as shown in Fig. 3.6a.

A closer look to Ag−Ru distance of each single cluster in the atoms reveals that the Ag_7 islands are not perfectly flat, but the atom sitting the center of the hexagon is slightly lifted up with respect to the remaining 6 atoms (Fig. 3.6b), following a similar trend observed for dome-shaped C nanoisland on Ir(111)[11], even if the effect in our case is much less pronounced. The Ag−Ru distance for the Ag atom at the center of the hexagone is almost 2.92 Å, 3 % larger than for the Ag atoms surrounding it. This trend suggests a relationship between the Ag−Ru distance and the in-plane CN, since the atom of at the center of the clusters is the only one with CN = 6. If we consider the values for all the clusters, we find that the Ag−Ru distance increases

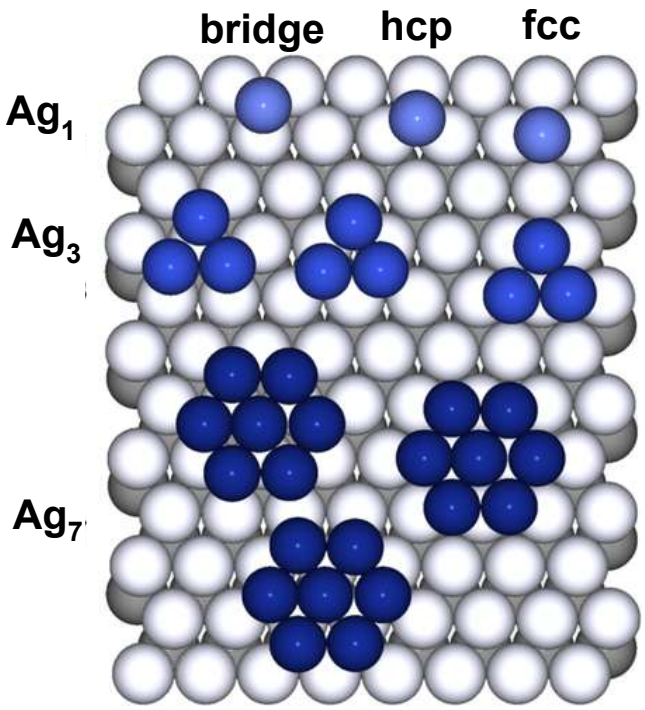

Figure 3.5: *Schematic ball model of the different adsorption configurations of Ag_1, Ag_3 and Ag_7 clusters tested in the DFT calculations. Blue balls correspond to Ag, white and gray balls correspond to surface and bulk Ru, respectively.*

Cluster	fcc	hcp	bridge	top
Ag_1	2.48	2.48	2.42	2.076
Ag_3	2.57	2.57	2.52	
Ag_7	2.65	2.65	2.60	

Table 3.2: *Adsorption Energies (in eV) for the different combinations of clusters and adsorption sites investigated in the DFT calcualtions.*

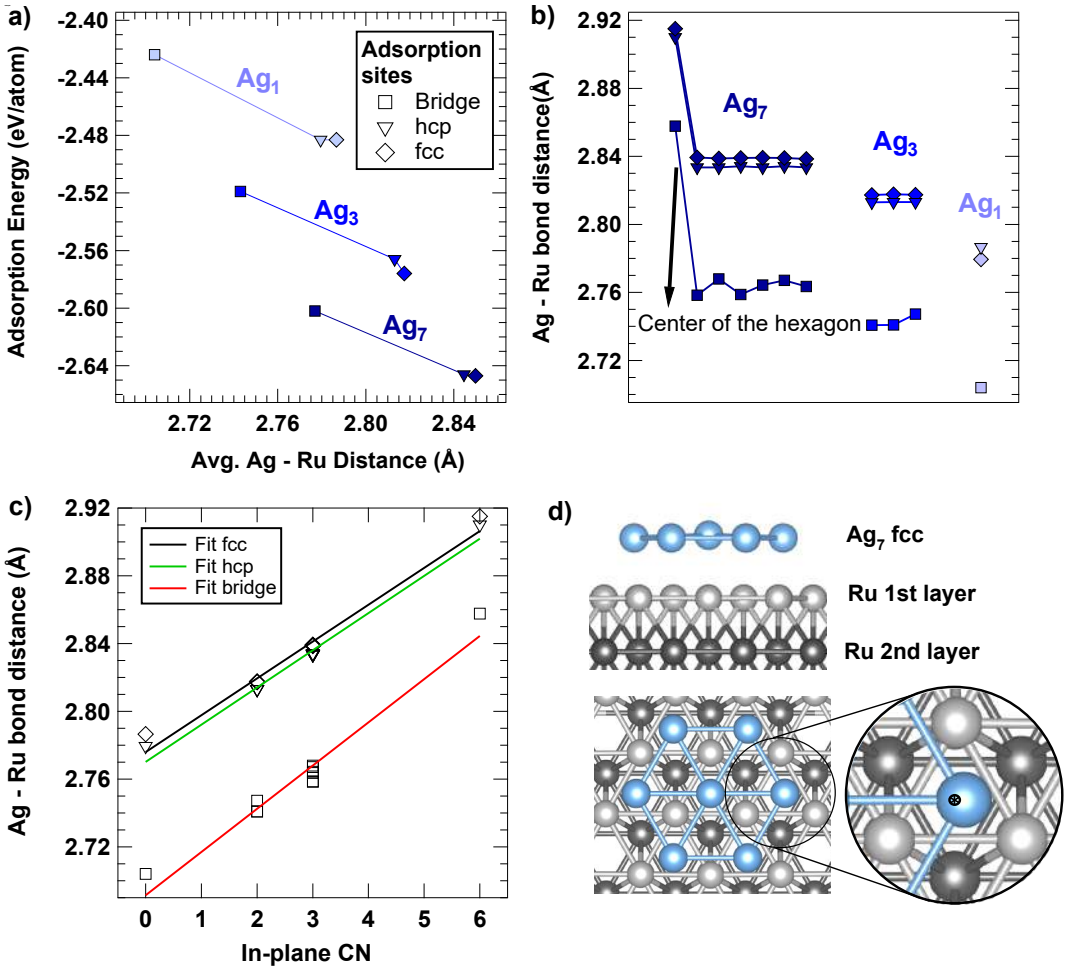

Figure 3.6: *a) Adsorption energy per Ag atom as function of the average Ag−Ru distance for the different cluster and adsorption site combinations probed by DFT calculations. b)Ag−Ru bond distance for each single Ag atom in the adsorbed clusters. c) Ag−Ru bond distance of the atoms in the clusters as a function of the in-plane CN and linear fit for each adsorption site. d) Side and top view of the DFT calculated minimum energy configuration of an Ag_7 cluster adsorbed in the fcc site. A zoomed view of an outer Ag atom of the cluster shows that it is not located at the center of the adsorption site. Blue balls correspond to Ag, white and gray balls correspond to surface and bulk Ru, respectively.*

linearly with a slop that is very similar in all the adsorption configurations: 0.022 and 0.025 Å CN^{-1} for the three-fold and bridge sites, respectively (Fig. 3.6c).

The slightly corrugated morphology of Ag_7 cluster is also related to the lattice mismatch between the cluster and the Ru(0001) surface. The corrugation makes the hexagon composed by the outer atoms in the cluster shrinks, and those atoms can get closer to the center of the three-fold adsorption site, as shown in Fig. 3.6d. In fact, the lattice mismatch of the two structures is more pronounced due to an expansion of the Ag−Ag bond length when the clusters are adsorbed on the surface, which we are now going to analyze.

The dependence of the Ag−Ag bond length on the size and adsorption site of the clusters, which addresses the issue of induced strain in the Ag bonds [23], is reported

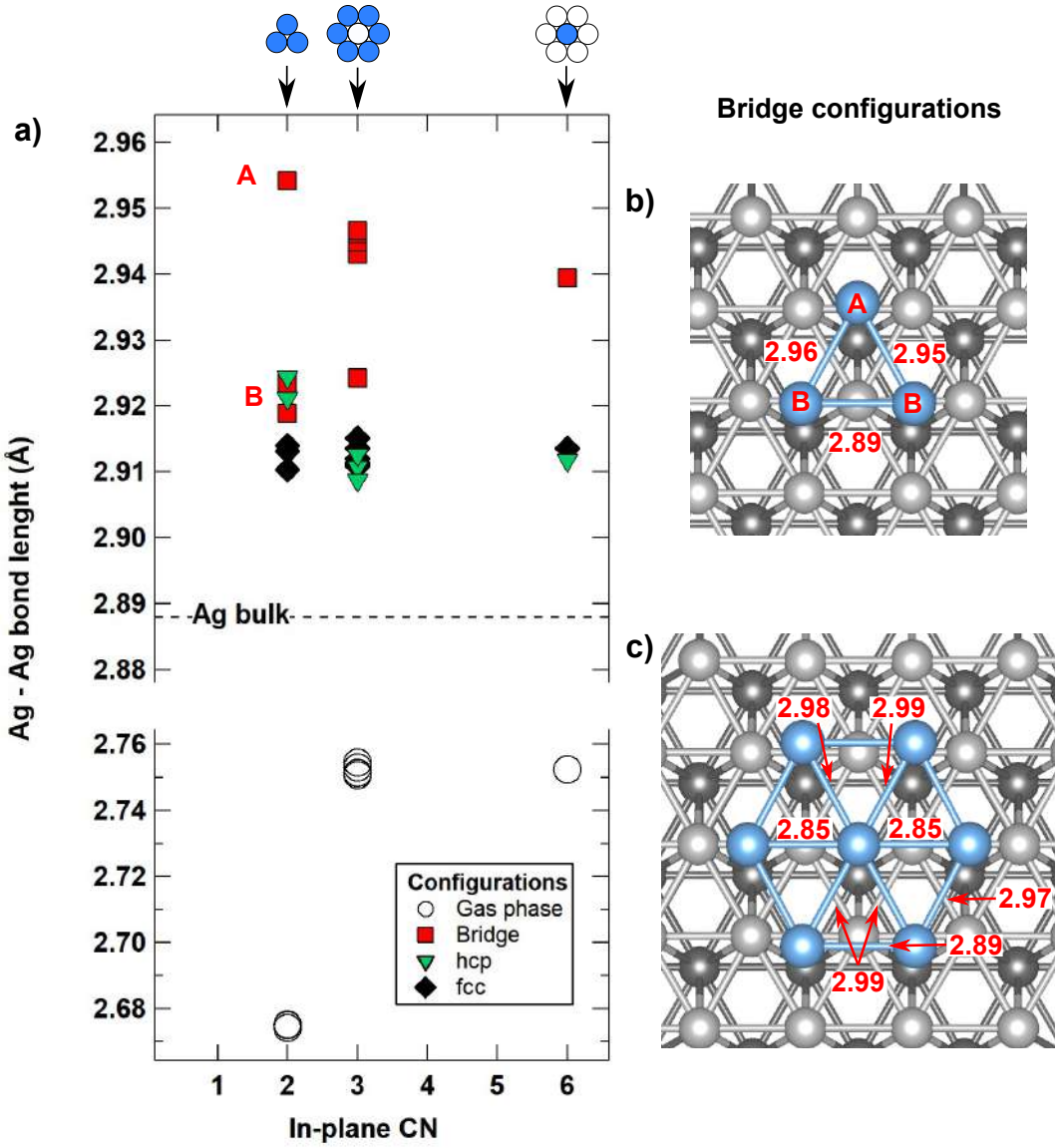

Figure 3.7: *a) Calculated Ag−Ag bond length for Ag_3 and Ag_7 clusters both in the gas-phase and for different adsorption configurations on the Ru(0001) surface. The value for Ag in the bulk is reported for reference. CN = 2 corresponds to atoms forming the Ag_3 cluster, CN = 3 to Ag atoms in the outer hexagonal ring of Ag_7 and CN = 6 to the atom at its center. b) Top view of the DFT calculated minimum energy configuration of Ag_3 and c) Ag_7 clusters adsorbed in the bridge site and representative bond lengths.*

in Fig. 3.7a. The distances reported in the figure were obtained by calculating the average distance from the nearest neighbors for each atom in the clusters. We report as well the values calculated for Ag_3 and Ag_7 in the gas-phase as a reference. If we take as a reference the bulk value $d = 2.887$ [24], which is also reported in Fig. 3.7a, we observe a shrinking of the Ag−Ag bonds for the clusters in the gas-phase of ca. -7% for Ag_3 and ca. -4% for Ag_7. The opposite happens when the clusters are adsorbed on the surface, with a strain ranging from ca. 3% for Ag_7 on bridge adsorption sites to about 1% for Ag_7 on 3-fold adsorption sites. Despite the lack of

dependence on the in-plane CN, the bond lengths are modified in a different way based on the adsorption site. In particular, in the case of adsorption in *fcc* sites the Ag−Ag bonds are closer to the bulk value and they are almost the same for all the nonequivalent atoms in the clusters (ca. 2.91 Å). On the contrary, the bond lengths for clusters in bridge sites are longer and we can appreciate a large dispersion for atoms in the same cluster. For example, based on the bond lengths, we can identify two different types of atoms in the Ag_3 cluster: one has a bond length slightly above 2.95 Å (atom A in Fig. 3.7a and b), while the remaining 2 atoms have shorter bond lengths of ca. 2.92 Å (atoms B). To understand this behavior, we can analyze the relaxed structure of the Ag_3 cluster adsorbed in the bridge site shown in Fig. 3.7b, where I reported the bond lengths and labeled the A and B Ag atoms accordingly to their average bond lengths. We can see that the bond length between the two B atoms (B−B) is shorter with respect to the distance between atoms B and A (A−B). This is related to the fact that a longer B−B bond length would push the B atoms towards the less favorable on-top adsorption site. On the contrary, a longer A−B bond length pushes all the atoms towards the most favorite three-fold adsorption sites. The same applies also for Ag_7 when adsorbed on bridge sites (Fig. 3.7c). This model also explains why the Ag−Ag bond lengths in clusters adsorbed in three-fold sites are shorter than those in bridge sites. In fact, as we already saw in Fig. 3.6d, longer bond lengths for cluster in *fcc* and *hcp* sites would further push them away from the center of the adsorption sites, closer to less favorite on-top and bridge positions.

The results I just reported indicate that the interaction of the clusters with the substrate is rather weak, although it is far from negligible. It decreases for larger clusters, but it is strong enough to play a role in their morphology as a consequence of the fact that the Ag atoms prefer to sit in three-fold sites. This information is of pivotal importance for our analysis: if all the atoms in the clusters possess the same configuration with respect to the Ru(0001) surface, the differences in the XPS Ag $3d_{5/2}$ are entirely related to the in-plane morphology of the 2D islands. It follows that we can now study the core level shifts as a function of the in-plane CN with the nearest Ag atoms.

3.3.2 Core level shift *vs* in-plane coordination

The calculated $3d_{5/2}$ core level shifts in the various Ag structures with different in-plane CN is reported in Fig. 3.8. Here, we considered the three clusters adsorbed in the most favorite *fcc* sites. We also included calculations on larger islands composed of 13 and 19 atoms (see Fig. 3.8) to test the effects caused by increasing island size and to increase the data statistic. The larger islands where obtained adding additional Ag atoms starting from Ag_7 and preserving the hexagonal close-packed arrangements. The new structures are composed of Ag atoms with CN ranging from 2 to 6. To correctly evaluate the CN Ag_{19} island, one has to consider the periodic conditions of the unit cell. The atoms at the corner of the islands, which appear to be in a configuration with CN = 3, are actually bonding to the corner of island in the adjacent unit cells and therefore their CN raises to 4. Atoms with CN = 1 are not consistent with the hexagonal close-packed structures and do not appear in any of the configurations that we considered.

Figure 3.8 shows a remarkable linear dependence of the core level shift with a proportionality coefficient between the shift and the number of Ag nearest neighbors of 25 ± 5 meV per bond. The very small shift predicted by the theoretical calculations

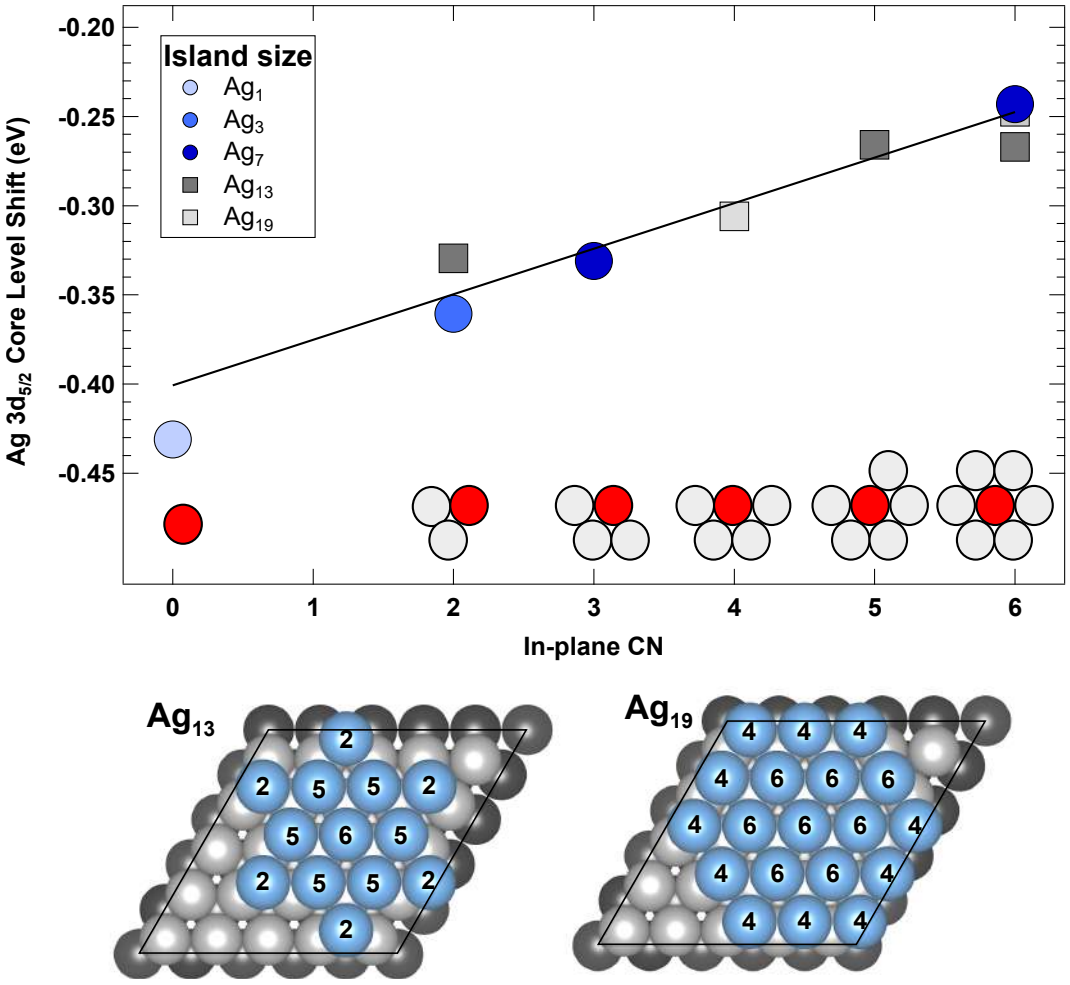

Figure 3.8: *Calculated Ag $3d_{5/2}$ core electron binding energy shifts dependence on the in-plane coordination number (CN) for island of different size, starting to the single clusters to larger islands composed of 13 and 19 atoms which are displayed. The CN of each atom in the larger islands is reported.*

further proves that measuring the structure-related properties of under-coordinated Ag clusters/islands on a transition metal surface is extremely challenging. When we compare the changes in core levels of under-coordinated configurations (but in this case, for 3D systems) obtained upon formation of Rh adatoms and dimers on (111) and (100) rhodium surfaces [25], a value of 130 meV per bond ($3d_{5/2}$ core level) is 5 times larger than the one obtained for our system. A large difference has also been obtained in the case of under-coordinated Pt atoms when measuring the Pt $4f_{7/2}$ core level shift for which a value of 120 meV per bond was found [26].

If we compare this result to the experimental data previously reported, we can see that the trend where larger clusters lead to an overall BE 30 meV larger than with Ag_1 monomers indicates an higher degree of order, since the theoretical calculations indicate that higher BEs are associated to higher CN. For this reason, we are now going to analyze the experimental data under the light of the theoretical results we just discussed.

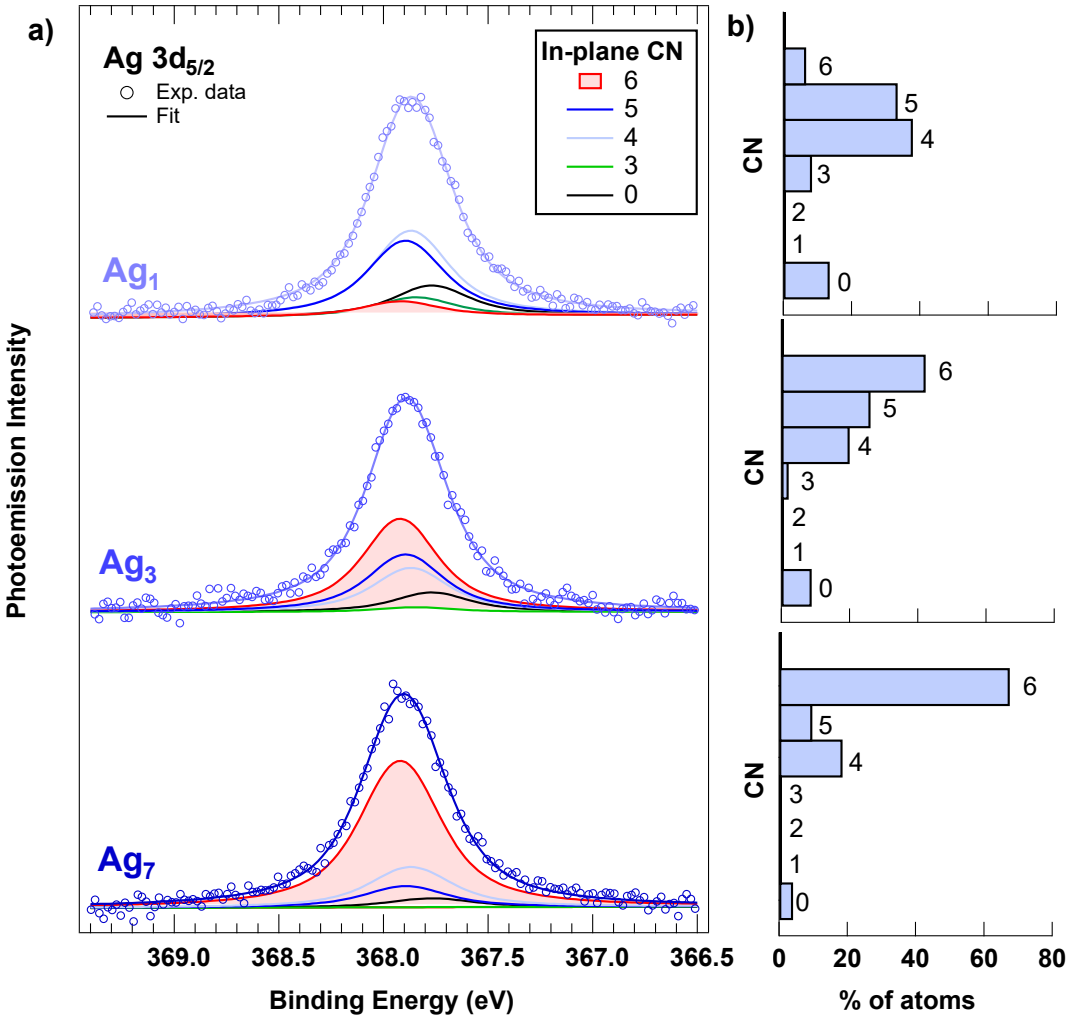

Figure 3.9: *Ag $3_{5/2}$ core level spectra measured after the deposition of Ag_n size-selected clusters on the Ru(0001) surface fitted using seven components separated by 25 meV, according to the DFT results. On the right side of each spectrum, an histogram shows the percentage of atoms with each CN according to the fit.*

3.4 Gliding building blocks induce high order

In Fig. 3.9 the calculated CN-dependent core electron binding energy shift was used to fit the Ag $3d_{5/2}$ spectra measured after deposition of Ag_1, Ag_3, and Ag_7 on Ru(0001) using a method already applied in the case of the analysis of the C 1s spectrum of a graphene layer on Re(0001) [27] and Ru(0001) [28]. Each spectrum has been fitted using seven components spaced by 25 meV, each corresponding to a different CN ranging from CN = 0 to CN = 6. In general, DFT calculations provide only the relative CLS of the atoms in the slab rather than the absolute BE of the core level. To obtain an absolute reference to fit the data, we combined the experimental and theoretical work performed on the Ag(111) single crystal. The relative CLS of the islands were calculated using as a reference the theoretical BE of atoms in the bulk of the Ag(111) single crystal previously calculated; subsequently, this value has been aligned to the experimentally measured one (368.20 eV), as extrapolated from the Ag $3d_{5/2}$ core level spectrum reported in Fig. 3.3. Therefore, the calculated CLSs of

the Ag islands with respect to the theoretical bulk value can be directly compared to the experimental ones with respect to the corresponding bulk BE.

The modification in the spectral weight previously discussed is consistent with this data analysis, showing that the islands composed of Ag_7 clusters possess the highest density of atoms in CN = 6. This clearly suggests that Ag_7 is very mobile even at T = 300 K and quite large islands are present on the surface after deposition. Since the populations of CN = 5 and 4 atoms are very low, the islands formed are expected to present a high degree of order, thus suggesting that Ag_7 is a good building block to form a hexagonal close-packed atomic arrangement. While the population of CN = 5 and 4 species is very small, the component related to CN = 1 - 3 cannot be detected within our error bar. The presence of a small component related to atoms with CN = 0, i.e., monomers, may indicate that a very small percentage of the Ag_7 clusters dissociates upon impacting the surface despite the soft-landing conditions. However, even if the cluster energy increases with size, we cannot exclude the activation of an Ostwald ripening process where the Ag atoms at the edges of the formed 2D islands detach from the larger structure and migrate on the surface. The same process was found in the case of monodisperse Pd_{19} clusters deposited on Rh(111) [29], where although the Pd−Pd binding energy was considerably lower than the binding energy of the clusters to the substrate.

The density of atoms with CN = 6 decreases when the islands are formed using smaller building blocks. For Ag_7, the percentage of atoms with the highest CN = 6 is above 60 %, for Ag_3 it decreases to about 40 % and in the islands formed using monomers it is below 10 %. The decreased density of atoms with the highest CN is accompanied by an increase of under-coordinated atoms with CN = 4 and 5. In particular the latter, which according to the model proposed in Fig. 3.2 are associated to the formation of defects in the 2D islands, corresponds to one third of the total atoms in the structures formed using Ag_1. To explain this result, we can take into account that the deposition took place at a substrate temperature (300 K) much lower than the value used to achieve a well ordered Ag adlayer structure on Ru(0001), which is between 690 [33] and 790 K [34]. Despite the fact that the deposition temperature we used was high enough to make the Ag atoms highly mobile on this surface, it could not be sufficient to promote the formation of a full close-packed atomic arrangement, producing instead a lot of local defects (CN = 5 and 4). For a similar system, i.e., Au on Ru(0001) [30], the deposition at RT resulted in the formation of a dendritic structure caused by kinetic limitations (Fig. 3.10a), which was found to be thermodynamically unstable [35].

The good mobility of Ag_7 and its ability to form islands with the lowest density of defects can be a direct consequence of the morphology of this cluster. If we ideally think of Ag_7 as flat and unbreakable, it is possible to form a 2D Ag layer by simply aligning the clusters along the <120> direction, forming a 2D island having atoms in the inner part with CN = 6 and atoms at the edges with CN = 4 and 3. A further factor that promote the formation of ordered island using Ag_7 is the weak interaction of this cluster with the substrate, since we have shown in Fig. 3.6 that this configuration is characterized by the longest Ag−Ru distance.

The result that larger cluster diffuse better than single atoms can be counter-intuitive, since typically the diffusion coefficient scales as the inverse radius of the island [20]. According to previous studies on the diffusion of deposited clusters to grow nanostructures, the higher mobility of Ag_7 can be related to a gliding mechanism, in which all the atoms of the island move simultaneously (Fig. 3.10b,c) [31, 32]. This

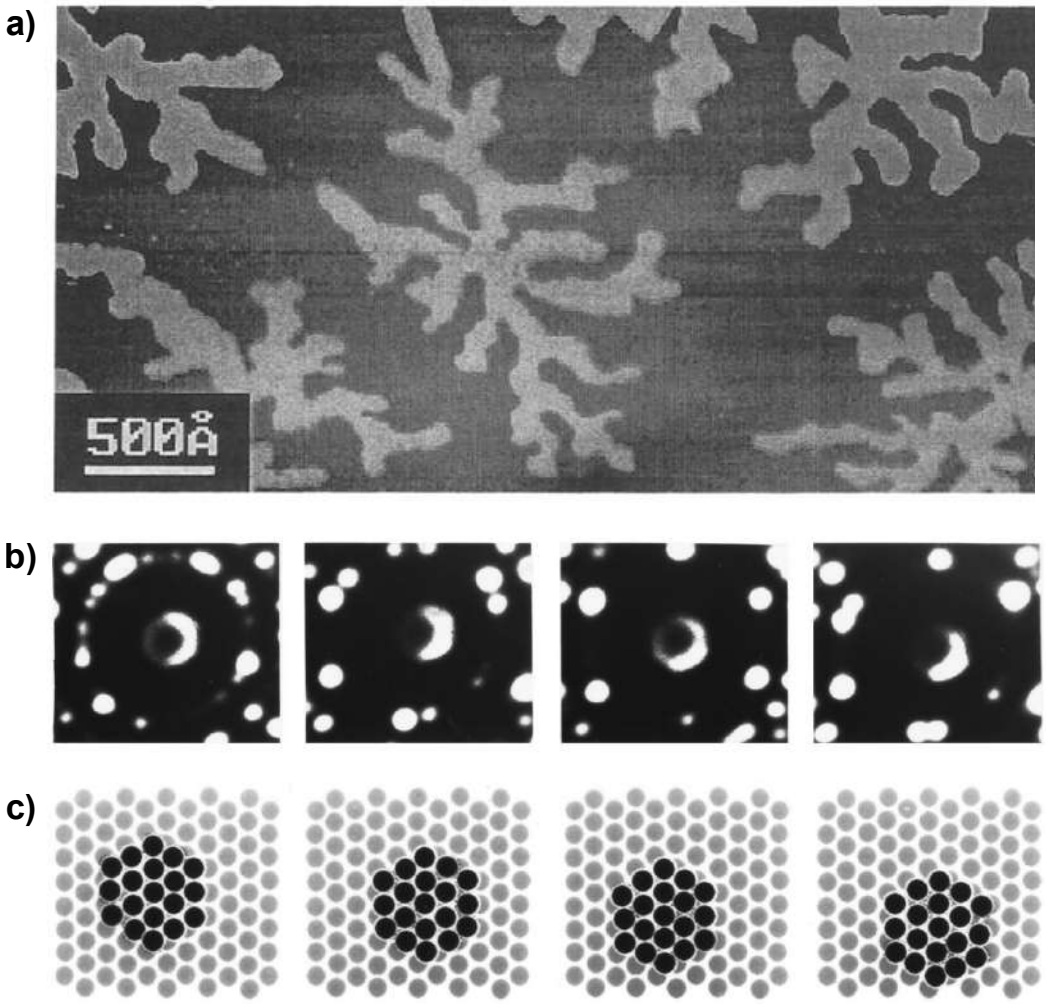

Figure 3.10: *a) STM image of a 0.3 ML non-annealed Au film on Ru(0001) showing two-dimensional islands of highly dendritic structure on large terraces. Adapted from [30]. b) Successive positions of a gliding Ir_{19} 2D cluster on an Ir(111) surface observed by field ion microscopy at low temperature and c) corresponding models. The motion takes place at T = 690 K and the figures correspond to 6, 10, and 14 heating intervals of 10 seconds each. Adapted from [31], original data from [32].*

mechanism was studied specifically for Ag islands on a Ru(0001) surface and it was predicted to be favorable for the smallest islands composed by less than 20 atoms, while a dislocation motion, where a row of atoms move simultaneously from fcc to hcp sites, becomes favorite for larger structures [36, 37].

Besides the growth method, we cannot ignore the role played by surface steps, which have been found to be the preferential attachment site in the case of the growth of Ag on Ru(0001) at room temperature [38]. For a very similar system, although at much larger coverage with respect to the ones used in our work, i.e., deposition of 0.1 ML of Ag on Re(0001) at room temperature [39], atoms bind exclusively at step edges where they form irregularly shaped small atomic aggregates. In particular, it was found that adatoms do not wet step edges and are responsible for an irregular and fairly porous shape of individual Ag aggregates, with large "cavities" caused by a

totally unidirectional growth. Since the electronic structure of Re is quite comparable to Ru, we can imagine a similar behavior in our systems, which would contribute in populating CNs lower than 6, especially in the case of monomers.

3.5 Conclusions

In this chapter, I discussed the outcomes of the first experiment performed coupling ENAC with the SuperESCA beamline of Elettra. We deposited Ag_n size-selected clusters, with $n = 1, 3, 7$, on a Ru(0001) single crystal surface to study the formation of 2D Ag islands using different clusters as building blocks. With a combined experimental and theoretical XPS analysis we were able to appreciate size-related features in the Ag $3d_{5/2}$ core level spectra and we understood that the Ag_7 cluster, thanks to its hexagonal morphology and the low interaction with the substrate, allows to minimize the defects in the islands compared to the smallest clusters. The possibility to tune the order and the density of under-coordinated atoms in the islands using different building blocks can have relevant implications due to the chemical importance of this quantity in determining the catalytic activity of a system [40].

This experiment proved the capabilities the the ENAC -SuperESCA setup to investigate matter the nano- and sub-nanoscale with atomic precision. Therefore, thanks to the insight gained from this work, we were able to move to the study of the oxidation of supported size-selected clusters, which has been the main topic of my research activities.

References

[1] J. Andersen, D. Hennig, E. Lundgren, M. Methfessel, R. Nyholm, and M. Scheffler, Surface core-level shifts of some 4d-metal single-crystal surfaces: Experiments and ab initio calculations, Phys. Rev. B **50**, 17525 (1994).

[2] E. A. Doud, A. Voevodin, T. J. Hochuli, A. M. Champsaur, C. Nuckolls, and X. Roy, Superatoms in materials science, Nat. Rev. Mater. **5**, 371 (2020).

[3] L. Liu and A. Corma, Metal catalysts for heterogeneous catalysis: From single atoms to nanoclusters and nanoparticles, Chem. Rev. **118**, 4981 (2018).

[4] C. Q. Sun, Dominance of broken bonds and nonbonding electrons at the nanoscale, Nanoscale **2**, 1930 (2010).

[5] C. Sun, *Electron and Phonon Spectrometrics* (Springer Singapore, 2021).

[6] M. D. Hughes, Y.-J. Xu, P. Jenkins, P. McMorn, P. Landon, D. I. Enache, A. F. Carley, G. A. Attard, G. J. Hutchings, F. King, E. H. Stitt, P. Johnston, K. Griffin, and C. J. Kiely, Tunable gold catalysts for selective hydrocarbon oxidation under mild conditions, Nature **437**, 1132 (2005).

[7] T. Fujita, P. Guan, K. McKenna, X. Lang, A. Hirata, L. Zhang, T. Tokunaga, S. Arai, Y. Yamamoto, N. Tanaka, Y. Ishikawa, N. Asao, Y. Yamamoto, J. Erlebacher, and M. Chen, Atomic origins of the high catalytic activity of nanoporous gold, Nat. Mater. **11**, 775 (2012).

[8] N. Tian, Z.-Y. Zhou, S.-G. Sun, Y. Ding, and Z. L. Wang, Synthesis of tetrahexahedral platinum nanocrystals with high-index facets and high electro-oxidation activity, Science **316**, 732 (2007).

[9] C. Vogt and B. M. Weckhuysen, The concept of active site in heterogeneous catalysis, Nat. Rev. Chem. **6**, 89 (2022).

[10] C.-Y. Wu, W. J. Wolf, Y. Levartovsky, H. A. Bechtel, M. C. Martin, F. D. Toste, and E. Gross, High-spatial-resolution mapping of catalytic reactions on single particles, Nature **541**, 511 (2017).

[11] P. Lacovig, M. Pozzo, D. Alfè, P. Vilmercati, A. Baraldi, and S. Lizzit, Growth of dome-shaped carbon nanoislands on Ir(111): The intermediate between carbidic clusters and quasi-free-standing graphene, Phys. Rev. Lett. **103**, 166101 (2009).

[12] L. Sbuelz, F. Loi, M. Pozzo, L. Bignardi, E. Nicolini, P. Lacovig, E. Tosi, S. Lizzit, A. Kartouzian, U. Heiz, D. Alfé, and A. Baraldi, Atomic undercoordination in Ag islands on Ru(0001) grown via size-selected cluster deposition: An experimental and theoretical high-resolution core-level photoemission study, J. Phys. Chem. C **125**, 9556 (2021).

[13] G. U. Gamboa, A. C. Reber, and S. N. Khanna, Electronic subshell splitting controls the atomic structure of charged and neutral silver clusters, New J. Chem. **37**, 3928 (2013).

[14] A. V. Ruban, H. L. Skriver, and J. K. Nørskov, Surface segregation energies in transition-metal alloys, Phys. Rev. B **59**, 15990 (1999).

[15] K. Oura, V. Lifshits, A. Saranin, A. Zotov, and M. Katayama, *Surface Science: An Introduction*, Advanced Texts in Physics (Springer Berlin Heidelberg, 2013).

[16] S. J. Lombardo and A. T. Bell, A review of theoretical models of adsorption, diffusion, desorption, and reaction of gases on metal surfaces, Surf. Sci. Rep. **13**, 3 (1991).

[17] G. Henkelman, B. P. Uberuaga, and H. Jónsson, A climbing image nudged elastic band method for finding saddle points and minimum energy paths, J. Chem. Phys. **113**, 9901 (2000).

[18] G. Henkelman and H. Jónsson, Improved tangent estimate in the nudged elastic band method for finding minimum energy paths and saddle points, J. Chem. Phys. **113**, 9978 (2000).

[19] Y. Lu, Q. Sun, Y. Jia, and P. He, Adsorption and diffusion of adatoms on Ru(0001): A first-principles study, Surf. Sci. **602**, 2502 (2008).

[20] J. M. Wen, S. L. Chang, J. W. Burnett, J. W. Evans, and P. A. Thiel, Diffusion of large two-dimensional Ag clusters on Ag(100), Phys. Rev. Lett. **73**, 2591 (1994).

[21] J. C. Slater, Atomic radii in crystals, J. Chem. Phys. **41**, 3199 (1964).

[22] E. Clementi, D. L. Raimondi, and W. P. Reinhardt, Atomic screening constants from scf functions. II. atoms with 37 to 86 electrons, J. Chem. Phys. **47**, 1300 (1967).

[23] C. Q. Sun, Y. Wang, Y. Nie, Y. Sun, J. Pan, L. Pan, and Z. Sun, Adatoms-induced local bond contraction, quantum trap depression, and charge polarization at Pt and Rh surfaces, J. Phys. Chem. C **113**, 21889 (2009).

[24] I. Lončarić and V. Despoja, Benchmarking van der waals functionals with non-contact RPA calculations on graphene-Ag(111), Phys. Rev. B **90**, 075414 (2014).

[25] A. Baraldi, L. Bianchettin, E. Vesselli, S. de Gironcoli, S. Lizzit, L. Petaccia, G. Zampieri, G. Comelli, and R. Rosei, Highly under-coordinated atoms at Rh surfaces: interplay of strain and coordination effects on core level shift, New J. Phys. **9**, 143 (2007).

[26] L. Bianchettin, A. Baraldi, S. de Gironcoli, E. Vesselli, S. Lizzit, L. Petaccia, G. Comelli, and R. Rosei, Core level shifts of undercoordinated Pt atoms, J. Chem. Phys. **128**, 114706 (2008).

[27] E. Miniussi, M. Pozzo, A. Baraldi, E. Vesselli, R. R. Zhan, G. Comelli, T. O. Menteş, M. A. Niño, A. Locatelli, S. Lizzit, and D. Alfè, Thermal stability of corrugated epitaxial graphene grown on Re(0001), Phys. Rev. Lett. **106**, 216101 (2011).

[28] D. Alfè, M. Pozzo, E. Miniussi, S. Günther, P. Lacovig, S. Lizzit, R. Larciprete, B. S. Burgos, T. O. Menteş, A. Locatelli, and A. Baraldi, Fine tuning of graphene-metal adhesion by surface alloying, Sci. Rep. **3**, 2430 (2013).

[29] Y. Fukamori, M. König, B. Yoon, B. Wang, F. Esch, U. Heiz, and U. Landman, Fundamental insight into the substrate-dependent ripening of monodisperse clusters, Chemcatchem **5**, 3330 (2013).

[30] G. Pötschke, J. Schröder, C. Günther, R. Q. Hwang, and R. J. Behm, A STM investigation of the nucleation and growth of thin Cu and Au films on Ru(0001), Surf. Sci. **251-252**, 592 (1991).

[31] P. Jensen, Growth of nanostructures by cluster deposition: Experiments and simple models, Rev. Mod. Phys. **71**, 1695 (1999).

[32] S. C. Wang and G. Ehrlich, Diffusion of large surface clusters: Direct observations on Ir(111), Phys. Rev. Lett. **79**, 4234 (1997).

[33] H. Zajonz, D. Gibbs, A. P. Baddorf, and D. M. Zehner, Nanoscale strain distribution at the Ag/Ru(0001) interface, Phys. Rev. B **67**, 155417 (2003).

[34] W. L. Ling, J. C. Hamilton, K. Thürmer, G. E. Thayer, J. de la Figuera, R. Q. Hwang, C. B. Carter, N. C. Bartelt, and K. F. McCarty, Herringbone and triangular patterns of dislocations in Ag, Au, and AgAu alloy films on Ru(0001), Surf. Sci. **600**, 1735 (2006).

[35] K. Meiwes-Broer, *Metal Clusters at Surfaces: Structure, Quantum Properties, Physical Chemistry*, Cluster physics (Springer Berlin Heidelberg, 2000).

[36] J. C. Hamilton, M. S. Daw, and S. M. Foiles, Dislocation mechanism for island diffusion on fcc (111) surfaces, Phys. Rev. Lett. **74**, 2760 (1995).

[37] J. C. Hamilton, Magic size effects for heteroepitaxial island diffusion, Phys. Rev. Lett. **77**, 885 (1996).

[38] A. Mascaraque, T. Onur Menteş, K. F. McCarty, J. F. Marco, A. K. Schmid, A. Locatelli, and J. de la Figuera, Valence band circular dichroism in nonmagnetic Ag/Ru(0001) at normal emission, J. Phys.: Condens. Matter **23**, 305006 (2011).

[39] M. Parschau, D. Schlatterbeck, and K. Christmann, Nucleation and growth of silver films on a rhenium (0001) surface: a combined STM and LEED study, Surf. Sci. **376**, 133 (1997).

[40] B. Hammer and J. K. Nørskov, Theoretical surface science and catalysis–calculations and concepts, in *Advances in Catalysis*, Vol. 45 (Academic Press, 2000) pp. 71–129.

CHAPTER 4

Bulk motifs in oxidized Ag_{11} clusters on graphene.

Periodic ordering of atoms in crystalline structures is a key feature that links geometric and electronic properties of a material. When the size of a crystal decreases to the order of tens of nanometers, the structural properties are still dominated by the outer crystal plane characteristics [1, 2]. Starting from the early 2000s, when it finally became feasible to produce noble-metal nanocrystals through colloidal synthesis [3, 4], heterogeneous catalysis took tremendous advantage from the availability of nanomaterials with well-defined facets or surface structures [5]. Compared to a bulk metal, the surface of a nanocrystal is inherently heterogeneous. As shown in Fig. 4.1, in the surface of a nanocrystals can coexist various types of facets with atoms differing in coordination number. It has long been established that both the activity and selectivity of a heterogeneous catalyst are dependent on the arrangement of atoms on the surface [6], therefore the possibility to tune the presence of one type of facet rather than the others offers great potential to enhance the catalytic activity and/or selectivity towards a specific reaction. For example, Pd concave nanocubes enclosed by 24 {730} facets exhibit much higher catalytic activity toward the Suzuki coupling of iodobezene and phenylboronic acid to form biphenyl when compared with the conventional Pd nanocubes with flat faces [7].

More recently, this approach has been extended for the synthesis of oxide nanomaterials, whose structure complexity is higher than for metals [8, 9]. In the case of oxides, crystal planes determine not only the surface geometry, but also the surface composition, strongly affecting the catalytic properties of the system [10, 11]. For example, Cu_2O cubes enclosed with the {100} crystal planes, Cu_2O octahedra enclosed with the {111} crystal planes, and Cu_2O rhombic dodecahedra enclosed with the {110} crystal planes (Fig. 4.1b) have shown distinct morphology-dependent catalytic properties that can be well correlated with the surface compositions and structures of exposed crystal planes [10]. Similarly, cubic and octahedral Ag_2O nanocrystals (Fig. 4.1c) were used as precursor to obtain Ag nanoparticles with a catalytic activity in methanol partial oxidation that was related to the initial geometry of the system [12].

When we move to the sub-nanoscale, this correlation with the outer crystal planes breaks down, and atomic metal clusters composed of less than few tens of atoms begin to show peculiar structural arrangements which are now dominated by their size [13] and chemical composition [14, 15]. Of particular interest are clusters composed of coinage metals, whose properties can be described according to the

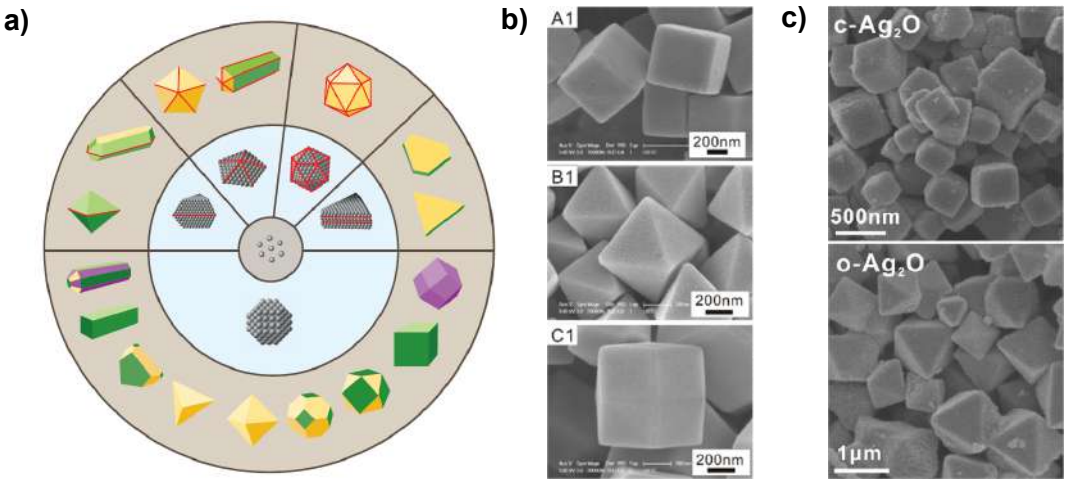

Figure 4.1: *a) Examples of metal nanocrystals with different shapes (outer tan ring) and the corresponding seeds that lead to their growth (inner blue ring). The green, yellow, and purple colors correspond to* {100}*,* {111}*, and* {110} *facets, respectively. The intersection of multiple crystal facets are delineated by red lines. Adapted from Ref. [5]. b) Scanning electron microscopy images of capping-ligand-free* Cu_2O *cubes (A1), octahedra (B1) and rhombic dodecahedra (C1). Adapted from Ref. [10]. c) Scanning electron microscopy images of cubic (c-) and octahedral (o-)* Ag_2O *nanocrystals. Adapted from Ref. [12].*

jellium model [16] and have been intensively studied for the rational development of cluster-based materials [17]. The geometry of this class of clusters is determined by their electronic structure, which is composed of filled d-states and of one s-electron [14]. For example, a relativistically enhanced sd hybridization and d-d interaction leads to two-dimensional structures for the smallest clusters [18]. Despite the exact turning point from 2D to 3D structures is still debated, it is generally located in the range $n = 11 - 13$ for Au_n clusters, and for $n = 6 - 7$ in the case of Ag_n and Cu_n (Fig. 4.2) [14].

The electronic and geometric properties of matter, and specifically of clusters, are intimately linked to each other. In the past decade, wide efforts have been devoted to the development of innovative strategies to simultaneously manipulate these two factors at the sub-nanoscale. A widely diffuse approach is to use different ligands to isolate, characterize and tune the properties of the clusters [17, 19]. For example, using electronegative ligands to reduce the electron count in the core of noble metal clusters to the magic number 8, which corresponds to the closure of a superatomic electronic shell, it is possible to induce the formation of nanoparticles with a metal core composed of 13 atoms in a closed packed icosahedral arrangement [20, 21]. However, the behavior of metallic clusters and their geometric and electronic evolution in elementary processes such as oxidation is still unclear and debated. In particular, it is not understood yet how the local geometric configuration and the oxidation state in size-selected cluster are affected by their unique electronic and geometric structures.

To gain insight into this fundamental aspect, we studied the oxidation of Ag_{11} clusters supported on graphene epitaxially grown on Ru(0001) and compared it with its bulk counterpart. Such experiment is of particular relevance since Ag oxides play

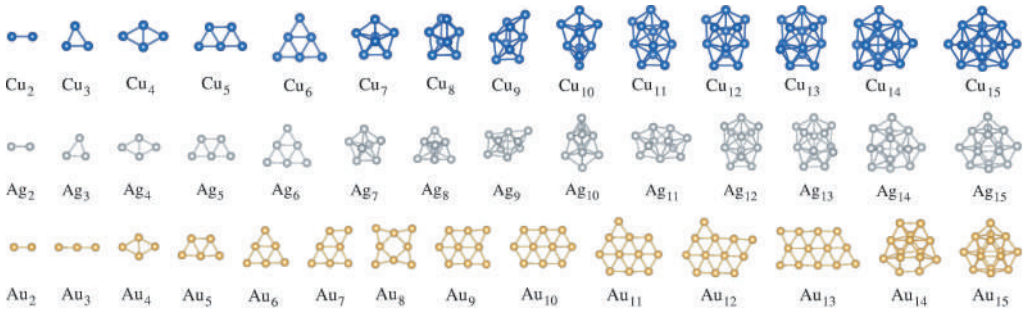

Figure 4.2: *DFT calculated global minimum configurations obtained for neutral TM_n clusters in gas-phase, where TM = Cu, Ag, Au and $n = 2 - 15$. Adapted from Ref. [14].*

a crucial role in the industrially relevant ethylene epoxidation reaction [22], and it was performed exploiting the full potential of the ENAC - SuperESCA apparatus combined with *ab initio* DFT calculations. The clusters were deposited *in situ* on the substrate kept at T = 20 K to avoid their diffusion and preserve the mass selection. The oxidation was achieved with a method based on the photo-induced dissociation of physisorbed O_2 molecules to obtain atomic O and overcome the high dissociation barrier of O_2 on Ag clusters. A direct comparison between experiment and theory allowed to quantify the O coverage on the clusters, indicating that an Ag:O atomic ratio close to 1 can be reached. Finally, further DFT calculations focused on the most abundant oxidized clusters obtained experimentally showed the appearance of hybrid structures with local coordination, electronic properties, and charge state of Ag and O atoms very similar to those of the AgO bulk oxide phase, implying potential applications for the clusters in the ethylene epoxidation reaction.

The results reported in this chapter have been published in the *Journal of Material Chemistry A*, with the title "Oxidation at the sub-nanoscale: oxygen adsorption on graphene-supported size-selected Ag clusters" [23].

4.1 Cluster deposition and XPS measurements

For our study, we chose to investigate the oxidation of Ag_{11}, a symmetric 3D cluster with an open electronic shell $|1S^2|1P^6|1D^3|$. Based on our DFT calculations, in the gas phase this cluster has the geometry of a 6-atoms triangular prims with 5 extra Ag atoms capping all of its facets (Fig. 4.3a). This symmetric 3D structure is optimal for a comparison with bulk materials. Moreover, the open shell configuration and the odd number of atoms composing the cluster induce a higher reactivity compared, for example, to the magic cluster Ag_8 [24]. The $Ag_{11}{}^+$ mass-selected positive clusters were produced using ENAC and deposited under soft-landing conditions on GR/Ru, on which they are electronically neutralized.

The GR/Ru template, which was grown by the chemical vapor deposition of ethylene (C_2H_4) on Ru(0001) following the procedure described in the Experimental section, was chosen for several reasons. Ag-carbon nanostructures have been studied in a wide range of fields for their optical [25], antibacterial [26] and catalytic [27] properties. In particular, the experimental study of supported Ag clusters and nanoparticles has been carried out on highly oriented pyrolytic graphite (HOPG) due to its inert surface properties, making it a useful substrate for model systems.

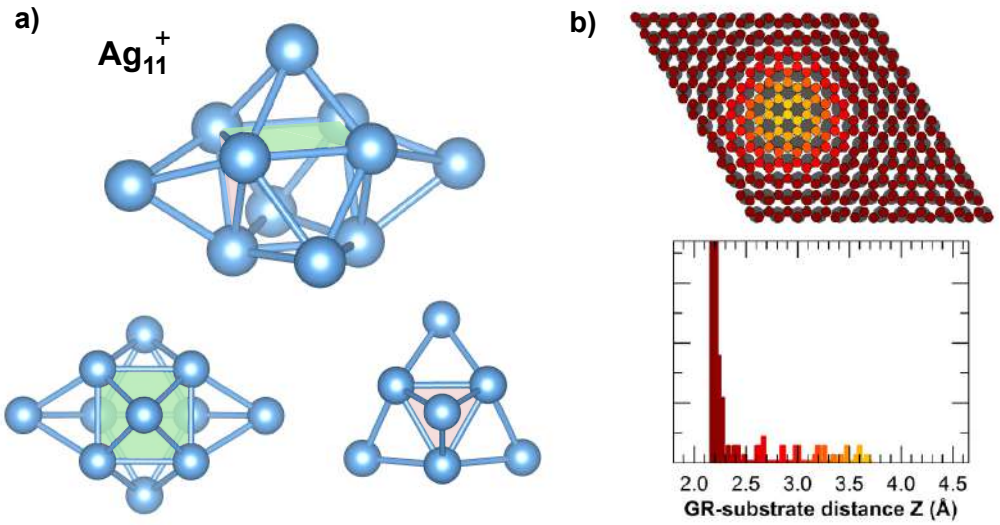

Figure 4.3: *a) DFT calculated minimum energy configuration of the Ag_{11}^{+} cluster in the gas-phase under different different perspectives. The square and triangular sides of the triangular prism at his core are highlighted in green and pink. b) Theoretical results of the GR/Ru moiré unit cell with C atoms colored base on their distance from the substrate reported in the bottom panel. Dark gray circles are surface Ru atoms. Adapted from Ref. [34].*

The main drawback of using HOPG relays on the high mobility of clusters at room temperature [28], which can be partially overcome by sputter-damaging the surface to create defects sites to stabilize the Ag clusters [29]. However, by doing so, the strong interaction between the clusters and the surface defect can alter their properties. In particular, the interaction of Ag nanoparticles on this surface was shown to lead to the formation of silver carbonate, which was responsible for the catalytic deactivation of the nanoparticles [30]. On the contrary, the adsorption energy of Ag atoms on GR/Ru is in the range of 20-30 meV [31–33] and indicates a very weak interaction with graphene. Therefore, the contribution from the interaction with the substrate to the geometric and electronic properties of the clusters should be negligible.

Despite the low interaction, which generally implies a high mobility of the clusters, GR/Ru is an optimal template due to the corrugated morphology of its moiré pattern (Fig. 4.3b). The deposition and growth of metallic [35, 36] and oxide [37, 38] clusters at room temperature was studied both experimentally and by means of DFT calculations, showing the formation of mono-dispersed clusters or cluster-assembled materials on the fcc region of the GR/Ru interface, where they are closer to the Ru(0001) surface. Similarly, the corrugation accounts for a reduced mobility of Ag atoms with respect to free-standing Gr, since they tend to remain confined in the depressed region of the carbon network [39]. However, given the extremely low interaction of Ag with Gr with respect to other transition metals, it was necessary to further reduce the cluster diffusion on the surface the sample by keeping it at a temperature of T = 20 K throughout the experiment. In addition, the density of clusters on the surface was kept always below 9×10^{-3} cluster/nm^2, which ensured a statistical occupation of one Ag_{11} for about 3000 carbon atoms., i.e., ca. 9 moiré unit cells of GR/Ru.

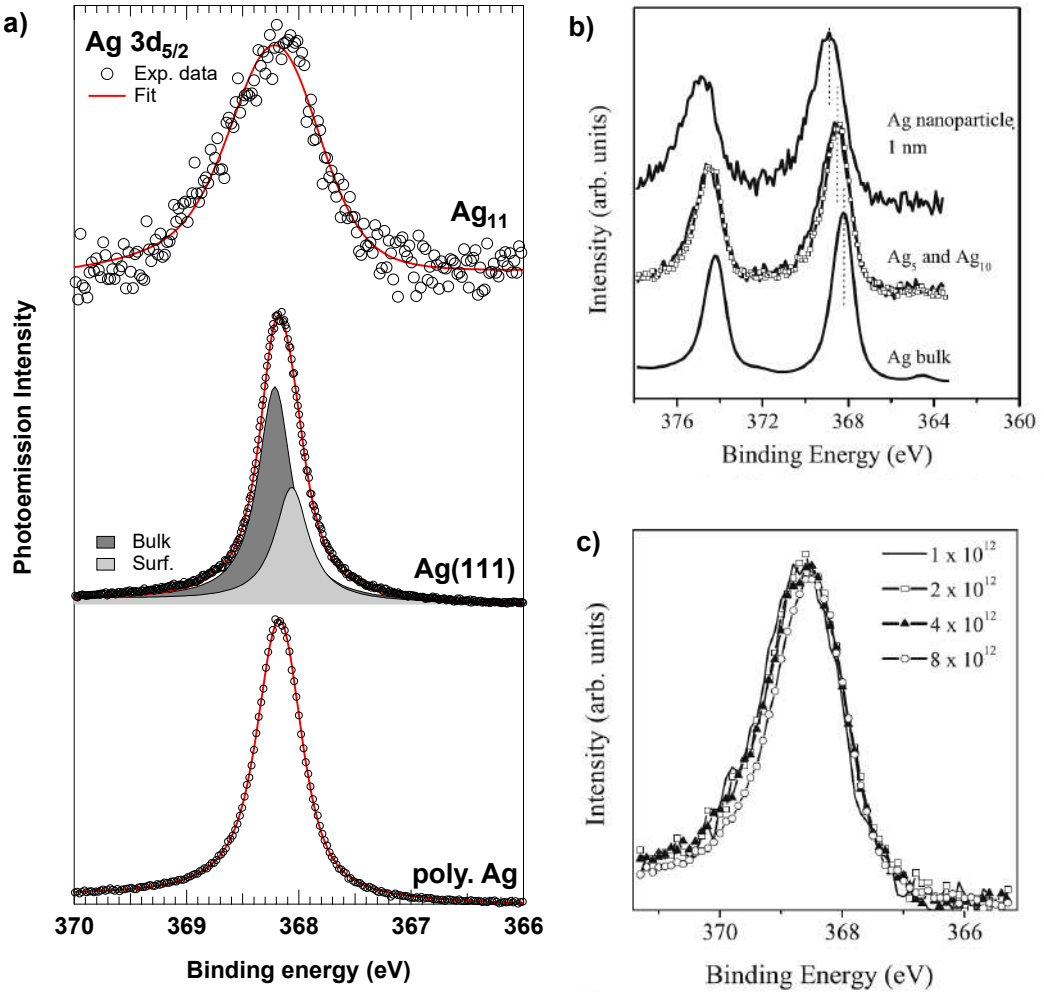

Figure 4.4: *a) Ag $3d_{5/2}$ core level spectra of Ag_{11} cluster on GR/Ru acquired at T = 20 K with a photon energy of 470 eV and same core level of an Ag(111) surface and Ag polycristalline slab. b) Ag 3d level spectra of Ag bulk, Ag_5 and Ag_{10} (spectrum with squared dots) clusters deposited on sputter-damaged HOPG, and 1 nm-sized Ag islands prepared using thermal evaporation of Ag atoms on the same substrate. c) Same spectrum of the Ag_{13} cluters Ag 3d for different cluster coverage, normalized for the total coverage. The number of clusters estimated by measuring the sample current for each sample is given in the figure. b) and c) are adapted from Ref. [29].*

The deposited clusters were characterized by means of high resolution XPS measurements performed *in situ* at the SuperESCA beamline, where the Ag $3d_{5/2}$ spectra were acquired in normal emission and with a photon energy of 470 eV, with a total energy resolution better than 50 meV. Figure 4.4a shows a comparison between the Ag $3d_{5/2}$ core level of the as-deposited Ag_{11} cluster, an Ag(111) single crystal surface and an Ag polycrystalline slab, with the latter two acquired at T = 300 K. As discussed in the previous chapter, the Ag(111) surface was fitted with two components separated by 150 meV, one associated to bulk atoms (368.20 $\pm$0.02 eV) and the second to surface atoms (368.05 $\pm$0.02 eV). The XPS spectra of the polycristalline sample and of the supported Ag_{11} clusters were fitted with a single component that

in both cases was centered at 368.17 ±0.02 eV. The Ag $3d_{5/2}$ binding energies of the clusters are rather similar to bulk and polycrystalline sample, in great contrast with the experiment described in the previous chapter where smaller Ag clusters were deposited on bare Ru(0001). This results agrees with previous XPS measurement performed by Dietsche *et al.* [29] for size-selected Ag_n clusters supported on sputter-damaged HOPG (Fig. 4.4b,c). Here, no significant difference in the Ag 3d BEs where found for clusters in the range $n = 3 - 16$. However, XPS was sensitive to different particle sizes based on the FWHM, which increased for decreasing cluster size. The high FWHM was used as a criteria to valuate the cluster nucleation, which was estimated to take place at a coverage between 4 and 8 $\times 10^{12}$ clusters (Fig. 4.4c). The total cluster coverage in our experiment ($\sim 1 \times 10^{12}$) and the FWHM of ~ 0.95 eV, greater than the values obtained from the fitting analysis of the Ag(111) surface and polycrystalline sample (FWHM in the range of 0.35 - 0.55 eV) allows to exclude the possibility of sintering. The larger width of the core level spectra of supported size-selected clusters is not a peculiarity of Ag, but it is a rather general trend that was observed also, for example, for Au [40], Pt [41] and Cu [42] clusters supported on different substrates. It is generally attributed to the combination of different effects such as a different lifetime broadening of the hole state for different particle sizes [29], phonon broadening [41], to the large number of nonequivalent atoms in the clusters with respect to the fcc arrangement of the bulk and to the various possible deposition sites and orientations of the supported clusters.

4.2 Cluster oxidation at T = 20 K

An important issue to address for the cluster oxidation is that the energetic barrier for O_2 dissociation cannot be overcome at T = 20 K . Theoretical calculations predicted that for Ag_n clusters in the gas-phase with $n > 5$, the adsorption of dissociated O_2 is more favorable than the adsorption of the intact O_2 molecule. However, despite the presence of severely under-coordinated atoms in the clusters, the calculated O_2 dissociation barrier seems to be even higher than that for Ag single crystal surfaces [43].

A potential solution to overcome this problem is the use of plasma-based atomic oxygen beams. However, this methods counts several drawbacks for our purpose, such as a high level of contamination arising from the high background pressure that cannot be avoided and the presence of energetic ions which could induce structural modifications on cluster and substrate. Therefore, in order to achieve a complete O_2 dissociation on the clusters, we had to rely on a different strategy which turns the low temperature of the system from a limitation into an advantage.

It is well known that at this temperature the dissociation of physisorbed O_2 can be induced by inelastic electron tunneling [44, 45] or by irradiation of UV light [46]. This mechanism is induced by the excitation of a non-bonding ground state to the repulsive σ^*(O-O) state which leads to dissociation [46]. More recently, a similar approach was adopted for a synchrotron radiation XPS study on the O adsorption on Pt(111) at T = 33 K. In this work, it was shown that the excess amount of photoelectrons produced by the high photon flux can induce the dissociation of O_2 molecules physisorbed on the Pt surface, leading to the formation of surface oxides and atomic oxygen. [47]. To test the possibility to extend this method to our system, we first studied the physisorption of O_2 on bare GR/Ru at T = 20 K. The C 1s XPS spectrum of clean GR/Ru is shown in Fig. 4.5a, with its two characteristic

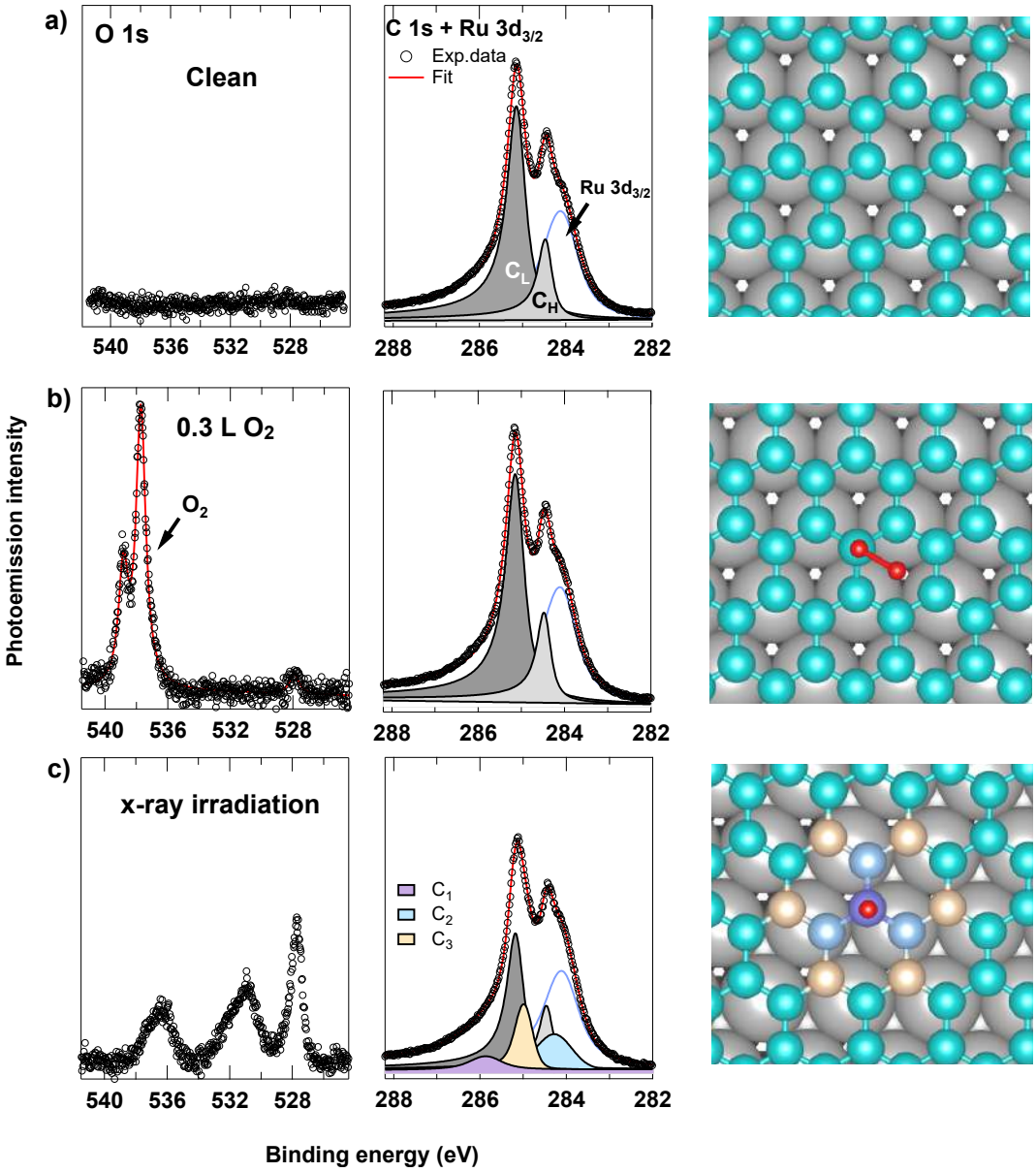

Figure 4.5: *a) O 1s and C 1s spectra of the clean GR/Ru at T = 20 K, b) after a dose of 0.3 L of O_2 and c) after irradiating the system with physisorbed O_2 for 15 minutes. Next to each set of spectra, the DFT calculated configurations of Gr/Ir clean, with a physisorbed O_2 molecule and with the formation of enolate. Gray balls stand for surface Ru atoms, red stands for O and turquoise, yellow, light blue and purple stand for C atoms with different C 1s BEs.*

components centered at 285.14 and 284.41 eV and a ratio of $\sim$ 3.5 [48]. The two components arise from the highly corrugated morphology of this interface and are associated to C atoms in the low (C_L) and high (C_H) regions of the moiré lattice with respect to the Ru(0001) plane [49]. In the same region of the C 1s core level, the Ru $3d_{3/2}$ can be fitted with a single component centered at $\sim$ 284.1 eV.

Upon dosing 0.3 L of O_2 at T = 30 K, the O 1s spectrum shows two peaks separated by 1.12 eV (the largest one centered at 537.72 eV) which are the fingerprint of

physisorbed O_2 (Fig. 4.5b). These peaks arise from the interaction between remaining 1s electron and unpaired final states of $1\pi_g^*$ level with different spin configurations ($^4\Sigma$ and $^2\Sigma$) [50]. The presence of physisorbed O_2 does not modify the C 1s spectrum. This result is supported by DFT calculations that we performed for a O_2 adsorbed on the fcc site of a Gr/Ir moiré unit cell, which did not induce any modification on the C 1s core level BEs. Afterwards, the sample was kept under a constant flux of photons at 400 eV for about 15 minutes, leading to a successful dissociation of O_2 as shown in Fig. 4.5c. After the exposure, both the O 1s and C 1s spectra are modified. In particular, the the O 1s double peak associated to physisorbed O_2 is not longer observed, while three new components appear. From the fitting analysis of the C 1s spectrum we could also individuate three new components: C_1 (shifted by +700 ± 100 meV with respect to C_H), C_2 (shifted by -930 ± 50 meV) and C_3 (shifted by -190 ± 50 meV). To relate this result with the presence of atomic oxygen on the surface, we performed DFT calculations on the C 1s CLS induced by the formation of enolate on the Gr, i.e., with one O binding ontop of a C atom of the graphene layer. According to the most recent studies on the oxidation of GR/Ru, the enolate species is expected to dominate over the formation of epoxide for low O coverages [51]. Our calculations indicate that O adsorbed in this configurations affects the C 1s BEs of graphene atoms differently depending on the distance from O: the atom which binds directly to O undergoes a positive CLS of +550 ± 20 meV, while its first and second nearest neighbors suffer a negative CLS respectively of -830 ± 50 meV and -190 ± 20 meV. The BEs of the C remaining atoms are not affected by the O adsorption. These results are in good agreement with the spectral analysis of the C 1s spectrum, proving the effective O_2 dissociation: C_1, C_2 and C_3 components correspond respectively to atoms binding with O to form enolate species and to their first and second nearest neighbors. The small difference between experimental and theoretical results in the C 1s BEs and the presence of a wide range on nonequivalent O 1s components can be related to O adsorption on different sites of the moiré cell, to the formation of epoxy species and to O binding to Gr defects [51, 52].

A complete characterization of this system will require further DFT calculations and XPS measurements which fall outside of the scope of this thesis. In fact, due to the very low coverage of Ag_{11} cluster on the surface, we cannot appreciate the effect induced by cluster adsorption and oxidation to the C 1s and O 1s spectra. On the contrary the oxidation of the Ag_{11} can be followed by measuring the Ag $3d_{5/2}$ core level, despite the extremely low cluster density. The O_2 dissociation is not caused directly by the photons, but by the low-energy secondary photoelectrons that are produced and is affected by the photon energy only to a minor extent. Therefore, we used the same photon energy and beamline parameters that were adopted for measuring the Ag $3d_{5/2}$ core levels, with a photon flux of $< 10^{16}$ photons $s^{-1}\,cm^{-2}$. The spectra acquired after exposing the sample to 0.1 L (light blue) and 0.5 L of O_2 (blue) and to X-rays are compared to the as-deposited spectrum in Fig. 4.6a. The oxidation resulted in a Ag $3d_{5/2}$ CLS towards lower binding energies, confirming the same trend observed for single crystal Ag(111) [53–55] and Ag(100) [56] surfaces or Ag polycrystalline silver foils [57] under high flux of atomic oxygen. We tested the oxidation of the clusters also at higher temperature with an O_2 dose of 10 L at 77 K (Fig. 4.6b), which resulted in the Ag 3d spectrum remaining almost unaltered, confirming that the oxidation only occurs due to the X-ray induced dissociation of physisorbed molecular O_2.

We analyzed the experimental data for increasing oxygen coverage with the

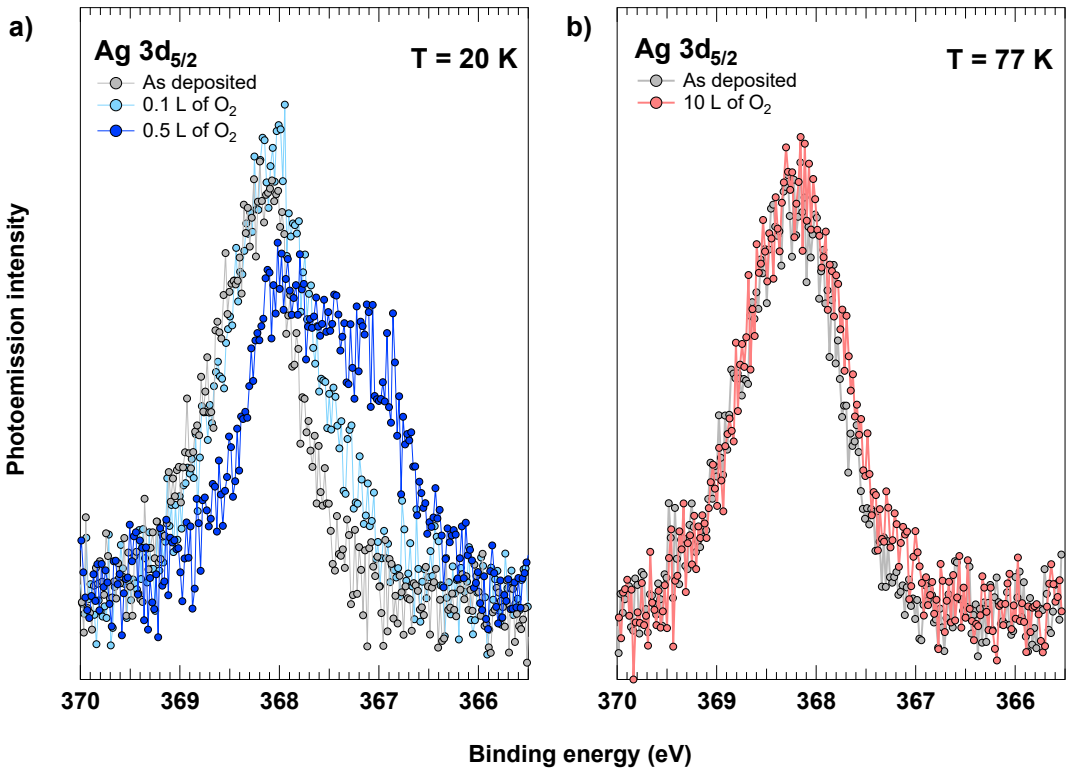

Figure 4.6: *a) Ag $3d_{5/2}$ core level spectra of Ag_{11} cluster on GR/Ru acquired at T = 20 K as-deposited and after two oxygen exposures of 0.1 L and 0.5 L, each followed by 40 minutes of soft X-ray irradiation to induce the O_2 dissociation. b) Same core level acquired for Ag_{11} deposited at T = 77 K and after an exposure to 10 L of O_2 followed by 40 minutes of soft X-ray exposure.*

support of DFT calculations. In particular, we calculated the structures and Ag $3d_{5/2}$ BEs for oxidized $Ag_{11}O_{2m}$ clusters in the range $m = 0 - 6$. We focused on clusters with an even number of O atoms because the latter is obtained from the dissociation of O_2 molecules physisorbed on the clusters and previous reports on this dissociation process induced by inelastic electron tunneling proved that O atoms obtained with this approach remain localized between one and three lattice parameters from the adsorption site of the molecule [44, 45]. The DFT calculated minimum energy structures of the graphene-supported $Ag_{11}O_{2m}$ clusters are shown in Fig. 4.7. The calculations are performed starting from the Ag_{11} cluster deposited on the graphene moiré cell supported by four Ru layers, and successively adding an increasing amount of oxygen. The clusters are placed on the fcc valley of the corrugated Gr layer, where the interaction with the Ru(0001) surface underneath increases its stability [35, 36].

To compare the theoretical calculations to the experimental results, we used the DFT calculated Ag 3d BEs of each atom composing the oxidized cluster to build the relative Doniach-Šunjić line (Fig. 4.8a). To do so, it was necessary to align the theoretically calculated BEs to the experimental values and to define the best lineshape parameters for the Doniach-Šunjić functions, i.e., the Lorentzian (L) and Gaussian (G) widths and the asymmetry parameter α. Therefore, first we fitted the as-deposited spectrum using 11 Doniach-Šunjić functions, each associated to

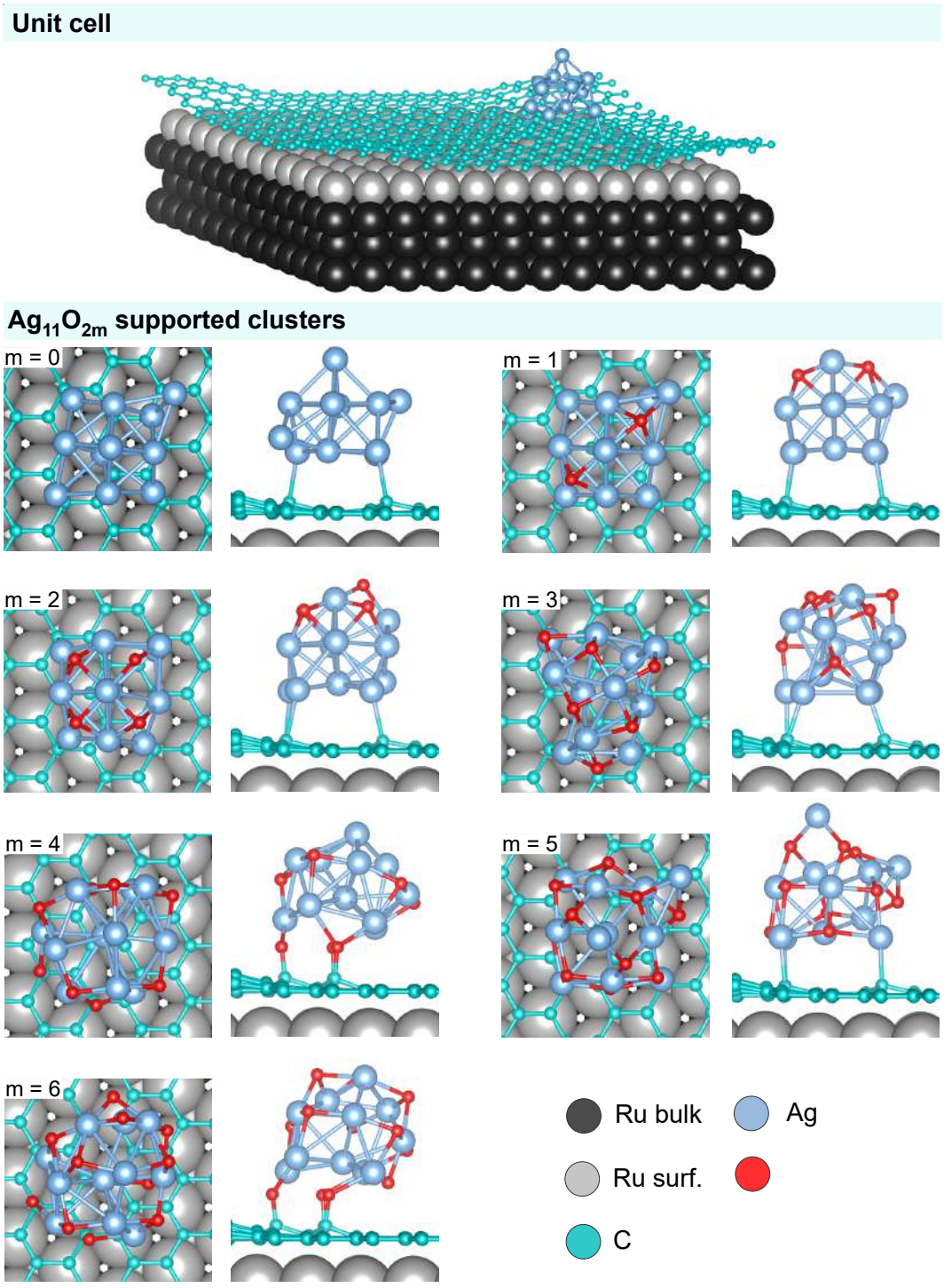

Figure 4.7: *Complete unit cell used for the DFT calculations and top and side zoomed views of the minimum energy configurations calculated for* $Ag_{11}O_{2m}$ *with* $m = 0 - 6$.

one atom of the cluster. In the fitting process, the 11 components were required to have the same area and lineshape, and the relative BE distances were fixed to the ones obtained from the DFT calculations. The best fit, which is shown in Fig. 4.8b

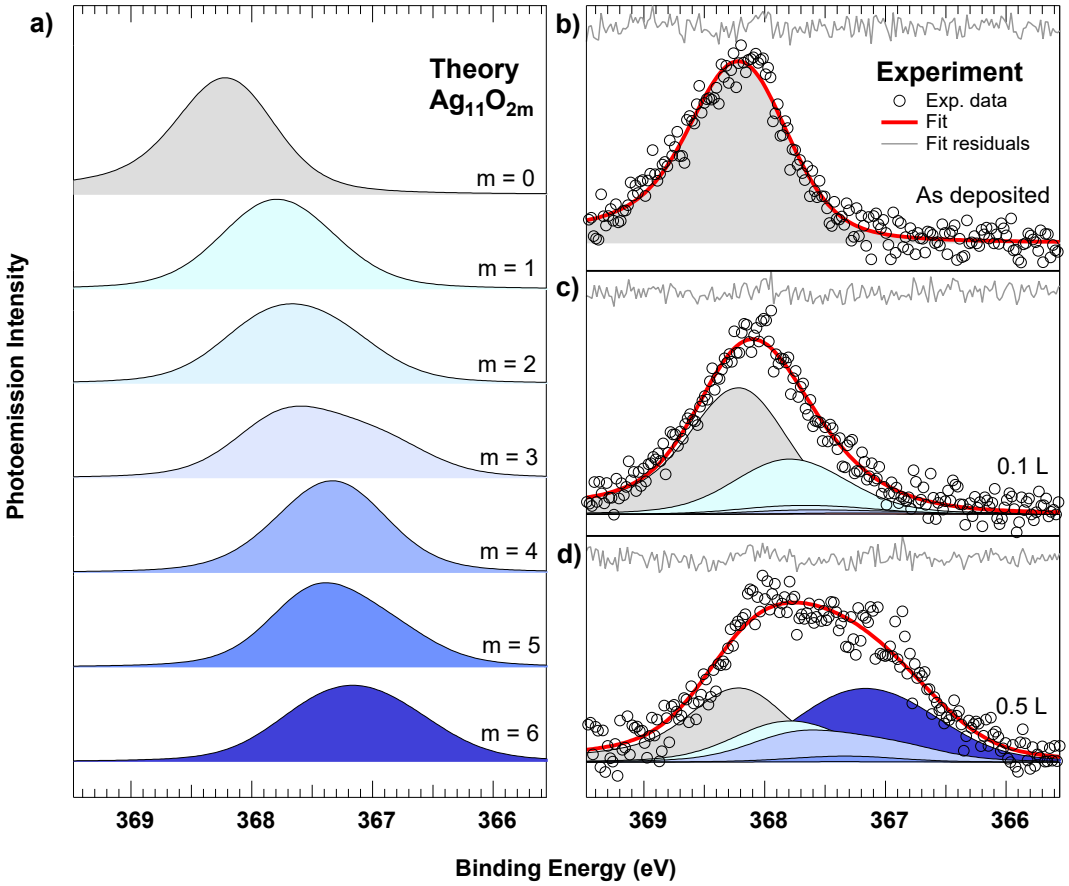

Figure 4.8: *a) Doniach-Šunjić functions built from the DFT calculated Ag $3d_{5/2}$ core levels for $Ag_{11}O_{2m}$ clusters with $m = 0 - 6$. b) Fitting analysis of the experimental Ag $3d_{5/2}$ core levels of as-deposited, c) mildly and d) highly oxidized Ag_{11} clusters performed with the DFT calculated spectra.*

together with the fitting residuals, was obtained for L = 0.3 eV, G = 0.7 eV and $\alpha = 0.09$. The L parameter is in good agreement with our findings presented in the previous chapter for the clusters supported on bare Ru(0001) and for the Ag(111) surface. The good agreement between experimental and theoretical spectra, which is shown by the fitting residuals in Fig. 4.8b, offer further proofs that the mass selection is preserved on the surface. With this result, it was possible to align theoretical and experimental BEs and build the Doniach-Šunjić lines of all the oxidized clusters using the same lineshape obtained for Ag_{11}. The only difference is that α was set to 0 given the reduced density of states at the Fermi level expected for oxides [58]. The resulting spectra are centered to progressively lower BEs, in agreement with the experimental evidence, and possess peculiar lineshapes dominated by the presence of several nonequivalent atoms in each oxidized clusters. These lines were then used to fit the experimental data.

After the first exposure of 0.1 L of O_2, the analysis indicates the formation of different $Ag_{11}O_{2m}$ clusters (Fig. 4.8c). The most abundant clusters on the sample are unreacted Ag_{11} ($57 \pm 5\%$) and $Ag_{11}O_2$ ($32 \pm 5\%$), while the percentage rapidly decreases for $Ag_{11}O_4$ and $Ag_{11}O_6$, which are at the edge of the detection limit. $Ag_{11}O_{2m}$ clusters with $m > 3$ are obtained after exposing the clusters to an additional

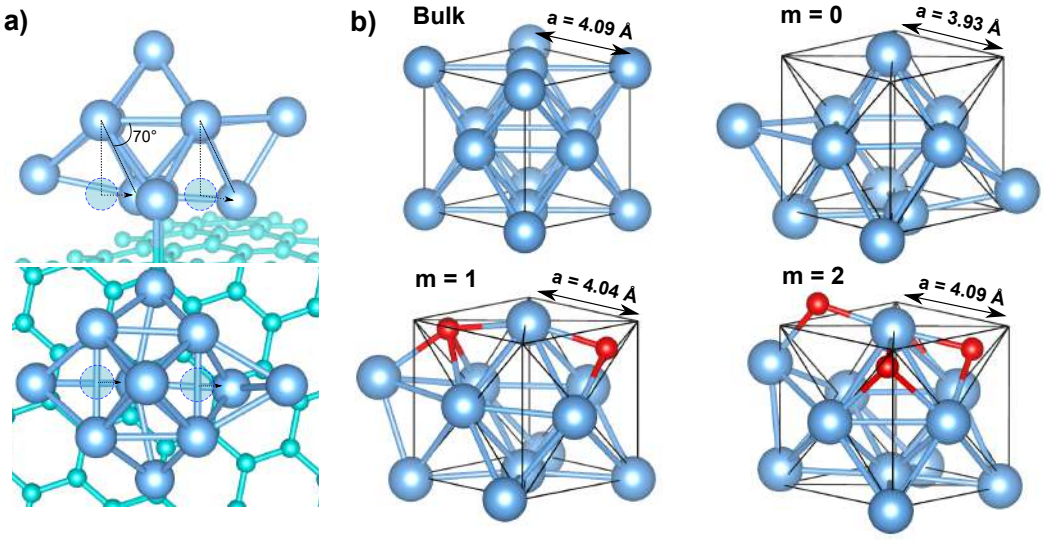

Figure 4.9: *a) View of the pristine cluster supported on GR/Ru with the geometrical modifications induced by the interaction with the substrate schematically described. b) Ag bulk in its fcc crystal structure and comparison with the minimum energy configurations of $Ag_{11}O_{2m}$ clusters ($m = 0 - 2$) fitting fcc unit cells.*

0.5 L of O_2 (Fig. 4.8d). In this case, the spectral analysis suggests that an Ag:O atomic ratio close to 1 can be reached, with the $Ag_{11}O_{12}$ representing 40 $\pm$5% of the total spectral weight. The different intensities of clusters with different oxygen converges can be linked to their adsorption energy per oxygen atom (E_b), which drastically changes in a non-monotonic fashion. For example, the higher abundance of $Ag_{11}O_{12}$ can be attributed to a E_b 0.4 eV higher with respect to its nearest neighbor $Ag_{11}O_{10}$. A similar trend applies to $Ag_{11}O_2$ and $Ag_{11}O_4$: the latter has a 0.5 eV lower E_b compared to the former and does not give a detectable contribution to the overall spectral weight.

$Ag_{11}O_{12}$ is the most abundant cluster in our system according to the comparison of DFT calculations and experimental XPS. Despite the presence in the fitting analysis of several components which could increase the error bar in the attribution of the spectral areas associated to each cluster, it is important to underline that without the presence of $Ag_{11}O_{12}$, the fitting analysis does not converge to acceptable χ^2 values. The stoichiometry of this cluster is close to the structure of the AgO bulk phase, which presents an hybrid composition of Ag(I) and Ag(III) ions [59]. Therefore, it is worth proceeding in a more accurate analysis of the electronic and geometric structure of this and the other oxidized clusters by means of DFT calculations to have an accurate comparison with the different bulk oxide phases.

4.3 Structural and electronic analysis of $Ag_{11}O_m$ clusters

The geometry of the Ag_{11} cluster is slightly distorted upon deposition. It assumes a three-layer structure, with its core that is modified from a right triangular prism into an oblique triangular prism with an angle of $\sim 70°$ (Fig. 4.9a), and the two

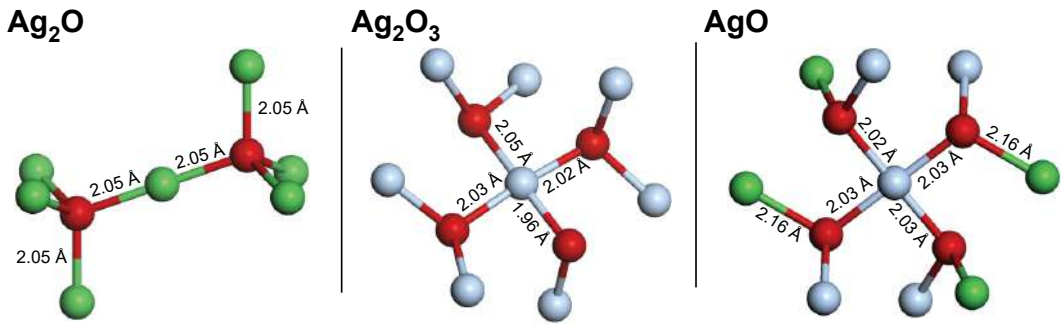

Figure 4.10: *Coordination environment of Ag(I) and Ag(III) ions of Ag_2O, Ag_2O_3 and AgO bulk oxides, with experimental bond lengths. Adapted from Ref. [59].*

atoms capping the triangular facets of the prism that follow the modification. With this geometry, the cluster moves towards an ordered crystalline fcc structures with the appearance of an octahedral motif. The octahedron, which is the core of the fcc crystal structure, is formed by one of the vertex of the triangular prism, which upon adsorption is at the cluster/graphene interface, almost centered with respect to the topmost square facet, by the square facet itself and by the Ag atom sitting in the four-fold site on top of the cluster. As shown in Fig. 4.9b, in the fcc unit cell of bulk Ag (lattice parameter $a = 4.09$Å [60]) the 6 atoms centered in the cubic facets form an octahedron, with the remaining 8 atoms at the corners of the cube that cape each of its facets. Similarly, the Ag_{11} cluster fits well a cubic fcc structure with a lattice parameter $a = 3.93$Å, with the atoms composing the newly formed octhaderon placed at the center of the 6 facets of the cubic cell and 4 more atoms close to the bottom corners of the cube. The structure gets progressively more ordered and more similar to the bulk crystal by increasing the oxygen coverage on the cluster. For $m = 1$, ten out of the eleven atoms of the clusters sit approximately on the sites of a fcc unit cell with a lattice parameter $a = 4.04$ Å, with only the topmost corners that are left empty. Finally, for $m = 2$ also the 11th atom of the cluster approaches an fcc site in one of the top corners of the cube, and the $Ag_{11}O_4$ cluster now fits a unit cell with the same lattice parameter $a = 4.09$ Å of Ag bulk crystals.

Such resemblance to a bulk crystalline ordered structure is absolutely uncommon in clusters of this size. It was previously observed only in the kernel of larger protected Ag and Au clusters such as Ag_{70} [61], Au_{28} [62] and Au_{36} [63]. The progressive evolution from a triangular-prism structure to a fcc-like cluster with a complete octahedral core could pave the road towards the understanding of the transition from cluster to bulk-like crystalline structures.

Besides the effects on the global morphology of the clusters, O adsorption induces the formation of local structural motifs which are the building blocks of the Ag bulk oxides. The adsorption of 2 O atoms ($m = 1$) leads to the formation of a linear O−Ag−O configuration on the topmost part of the cluster, which is the typical local geometry of d^{10} Ag(I) ions in Ag_2O and AgO bulk oxides (Fig. 4.10) [59]. The O−Ag bond length of 2.10 Å is slightly larger (2.5%) when compared to the experimental findings for Ag_2O bulk systems (2.10 Å) [64], but it is consistent with calculations performed with similar DFT formalism [59]. With the adsorption of two extra O atoms ($m = 2$), the linear geometry is replaced by a square-planar AgO_4 unit typical of the d^8 Ag(III) ions in the AgO and Ag_2O_3 bulk phases. The average

Ag−O in the AgO_4 unit decreases to 2.05 Å, which is still slightly larger than the experimental bulk values of AgO and Ag_2O_3, that range between 1.96 and 2.05 Å [65, 66], but is consistent with the values obtained with similar DFT calculations [59]. This outcome can also be compared with the oxidation process of single crystal silver surfaces. The square-planar AgO_4 is very dissimilar to the local morphology of the several reconstructed Ag(111) surfaces that have been deeply investigated by means of several experimental and theoretical techniques [54, 67, 68]. The only proposed structure with similar AgO_4 sub-units is the $c(4 \times 8)$ phase, which is obtained for an O coverage of 0.5 ML and was only recently confirmed by state-of-the-art simulations based on first-principles total energy calculations combined with atomistic structure learning algorithm developed for structural determination [69].

Finally, a large structural reconstruction of the cluster is obtained for $Ag_{11}O_{12}$ ($m = 6$), i.e., the cluster with the highest oxygen density probed in our calculations and the most abundant cluster after the 0.5 L O_2 dose accordingly to our previous analysis. This cluster does not show an fcc structure, but it is composed of both Ag atoms forming AgO_4 units (typical of d^8 Ag(III) ions) and in a linear O−Ag−O structure characteristic of Ag(I) ions with d^{10} orbitals. This hybrid composition is very similar to the AgO bulk phase, which is also composed of Ag(I) and Ag(III) ions [59]. Moreover, the average Ag-O bond lengths in the cluster are consistent with the experimental findings and theoretical calculations on this bulk oxide: the Ag(I)-O and Ag(III)-O bond lengths in the bulk are 2.16 Å and 2.03 Å, while the correspondent values we calculated in the $Ag_{11}O_{12}$ clusters are 2.17 Å and 2.06 Å.

To further compare the oxidized clusters to their bulk counterparts, we performed a Bader charge analysis and calculated the projected density of states (PDOS) of atoms in the clusters with different local environment and with different oxidation state. To have a more consistent comparison, we performed the same calculations for the two bulk oxides Ag_2O and AgO.

Starting from $Ag_{11}O_2$, the Bader charge in the Ag atoms forming the linear O−Ag−O motif is very similar to the value calculated for the Ag(I) ions in Ag_2O: $0.49e$ and $0.47e$, respectively. Similarly, the Bader charge analysis on the atom forming the square-planar AgO_4 unit in $Ag_{11}O_4$ resulted to be $0.96e$, very similar to the value calculated for Ag(III) ions in the AgO bulk oxide ($0.99e$). The appearance of a single Ag(III) (and Ag(I)) ion in the clusters is intriguing, since it is co-occurring with a clear breakdown of the superatomic behavior, with a single atom of the atomic agglomerate that reaches a different oxidation state than the others. Finally, $Ag_{11}O_{12}$ can be compared with the hybrid AgO bulk oxide. We obtained values of $0.58e$, $0.96e$ and $-0.77e$ respectively for Ag(I), Ag(III) and O ions in the cluster, differing by less than 13% from the values of $0.65e$, $0.99e$ and -0.85e that we calculated for their counterparts in the bulk phase.

The PDOS of different ions in the oxidized $Ag_{11}O_{2m}$ clusters are compared to bulk Ag_2O and AgO bulk oxides in Fig. 4.11. Starting from the metallic state ($m = 0$), the PDOS is in agreement with that of similar systems involving Ag atoms and small clusters on graphene [70, 71], with the Ag 4d band almost entirely confined in the range $\epsilon_F - \epsilon = 6 - 2.5$ eV and with its maximum at 3.5 eV. For $m = 1$ ($Ag_{11}O_2$), Ag(I) ions in the cluster are again very similar to their counterparts in the Ag_2O bulk oxide. The Ag 4d and O 2p states dominate the energy range from 7 to 4 eV, with a small contribution coming from the s-states. The maximum of the Ag 4d band in the cluster shifts towards the Fermi energy and is now between 3.1 and 2.7 eV, similar to the position of the maximum for Ag_2O ($3.4 - 2.8$ eV). The two

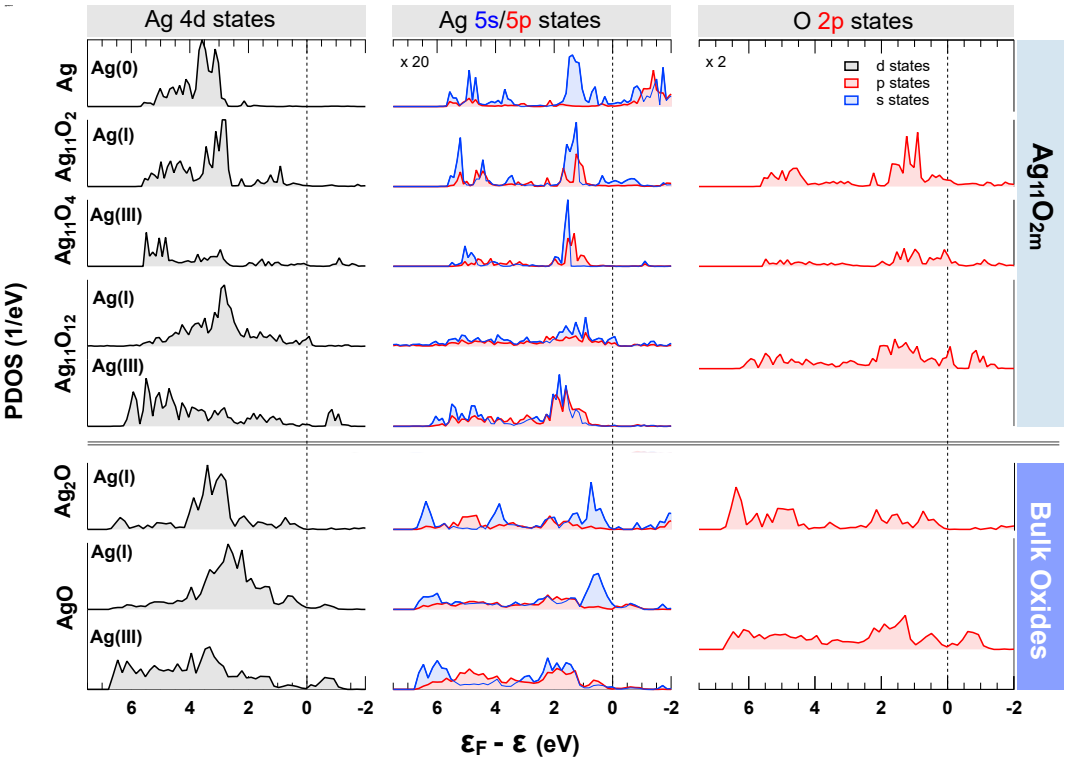

Figure 4.11: *Calculated PDOS for different ions forming the $Ag_{11}O_{2m}$ supported clusters ($m = 0, 1, 2$ and 6) compared to Ag_2O and AgO bulk oxides. The contributions to the total PDOS from Ag 4d, 5p, 5s and O 2p-states are reported.*

systems look alike also in the region closer to the Fermi energy ($2.0 - 0.0$ eV), where the valence band is a mixture of Ag 4d and O 2p states, with a small contribution coming from Ag 5s, while the conduction band is a mixture of Ag 4d, 5s and 4p states. Moving to $m = 2$, the Ag 4d band of the atom in the square-planar AgO_4 unit drastically decreases in the energy range 4.0 - 2.0 eV, while an anti-bonding state appears above the Fermi energy. This structure is very similar to the one we calculated for Ag(III) ions forming AgO, which show a similar anti-bonding state and a almost homogeneous distribution of Ag 4d states in the range 7 - 1 eV. For the highly oxidized $Ag_{11}O_{12}$, the hybrid geometric structure is reflected also on the PDOS, with clear difference between the two non-equivalent Ag species. Also in this case, the Ag ions in the square-planar AgO_4 and linear $O-Ag-O$ units are very similar to the Ag(III) and Ag(I) ions in the AgO bulk oxide. For the former family of ions, the d-band is spread in the energy range from 6.3 to 0.8 eV (from 6.8 to 1.0 eV for Ag(III) in AgO), and an anti-bonding state is located above the Fermi energy. For the ions in the linear units, the d-band is mainly localized in the range 3.5 - 2.3 eV and is peaked at 2.8 eV. Similarly, Ag(I) in AgO is mainly confined in the energy region 3.6 - 1.6 eV and reaches its maximum at 2.7 eV.

The clear appearance of bulk motifs at this scale seems to be a peculiar behavior of oxides, since it is not observed for metallic clusters or other elements such as Si [72], B [73] and C [74]. On the contrary, it was observed that $(WO_3)_n$ and $(MoO_3)_n$ clusters for $n = 1 - 4$ obtained from high temperature sublimation of the corresponding bulk oxides preserve their original structure [75]. Our work extends this concept also

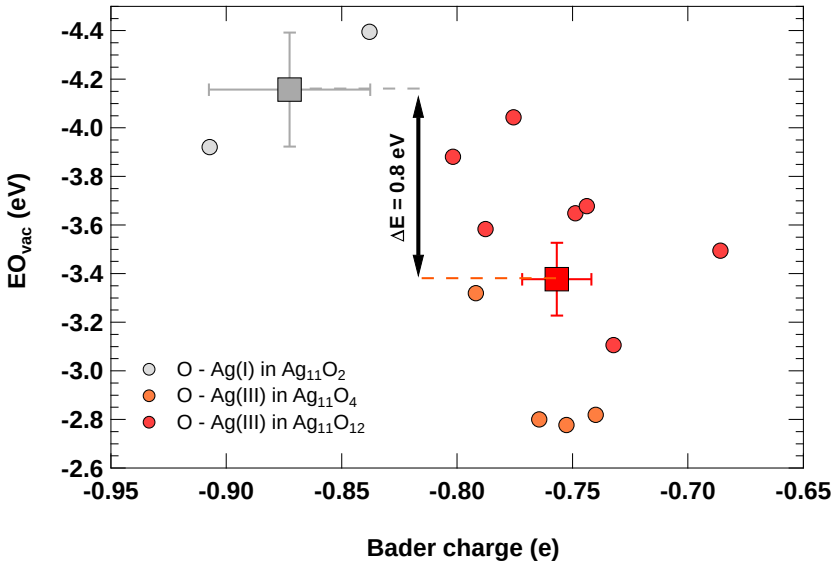

Figure 4.12: *Calculated oxygen vacancy formation energy (EO_{vac}) of different O atoms bonding to Ag(I) (gray) and Ag(III) (red) ions in the $Ag_{11}O_{2m}$cluster ($m = 1, 2, 6$) expressed as a function of their Bader charge. Large squares of each color correspond to the average of the corresponding set of values.*

for oxidized clusters obtained from the chemical oxidation of their supported metal counterparts, rather than from the direct fragmentation of bulk oxides. This new understanding can have important implications on the atomically precise design of sub-nano catalysts [76]. The appearance of bulk oxide motifs in the Ag clusters can also have important implications on their technological exploitation, in particular in the ethylene epoxidation reaction, for which Ag is the main catalyst [22]. To investigate the catalytic reactivity of the different atoms in our clusters, we performed calculations on the oxygen vacancy formation energy (EO_{vac}). This value corresponds to the energy required to remove one O atom from the cluster and can be used to predict the trend of catalytic performance [77]. Figure 4.12 shows the relationship between EO_{vac} and the Bader charge of O atoms binding to different Ag ions in the clusters. The result is that the average EO_{vac} (large squares) is lower for O atoms binding with Ag(III) ions and forming the square-planar AgO_4 units, suggesting that the formation of this specific local geometry, where O atoms show the lowest Bader charge, can play a key role in the chemical reactivity of the clusters.

4.4 Conclusions

The geometric evolution from single atoms to three dimensional structures represents a crucial topic in nanoscience. This issue is particularly relevant in the case of the formation of nano-oxides, whose structural complexity is matched only by their potentialities in heterogeneous catalysis. In this respect, we investigated the oxidation of an Ag_{11} cluster supported on epitaxial graphene on Ru(0001), combining XPS with synchrotron radiation and *ab initio* DFT calculations. The clusters where produced with the cluster source ENAC and deposited in soft-landing conditions on the sample at T = 20 K to prevent sintering. To achieve a high degree of oxidation on the

cluster at this low temperature, we exploited a method based on the dissociation of phyisisorbed O_2 induced by secondary electrons generated by soft X-ray irradiation. In this way, we were able to oxidize the clusters with very small O_2 exposure and preserving the mass selection.

Our analysis on the oxidized spectra indicated that a single Ag_{11} cluster can bond with up to 12 O atoms, reaching a final stoichiometry similar to the AgO bulk oxide. A deeper analysis based on the outputs of DFT calculations on the local geometries, Bader charge distribution and PDOS further highlighted the similarities of the clusters with their bulk conterparts. In particular the oxidized $Ag_{11}O_{12}$ cluster reaches a final hybrid structure formed of d^{10} Ag(I) and d^8 Ag(III) ions, the same composition of the AgO bulk phase. The presence of bulk-like motifs in the clusters shows that matter at this scale behaves in a different way with respect to the widely-investigated world of solid surfaces. Moreover, this result supports the application of oxidized size-selected Ag clusters for chemical reactions such as the epoxidation of ethylene. In this regard, calculations on the oxygen vacancy formation energy in the clusters highlighted the important role played by the appearance of Ag(III) ions in square-planar AgO_4 units, which lead to O atoms with a lower Bader charge and higher EO_{vac}.

References

[1] Y. Xia, Y. Xiong, B. Lim, and S. E. Skrabalak, Shape-controlled synthesis of metal nanocrystals: Simple chemistry meets complex physics?, Angew. Chem. Int. Ed. **48**, 60 (2009).

[2] Y. Shi, Z. Lyu, M. Zhao, R. Chen, Q. N. Nguyen, and Y. Xia, Noble-metal nanocrystals with controlled shapes for catalytic and electrocatalytic applications, Chem. Rev. **121**, 649 (2021).

[3] Y. Sun and Y. Xia, Shape-controlled synthesis of gold and silver nanoparticles, Science **298**, 2176 (2002).

[4] Y. C. Cao, R. Jin, and C. A. Mirkin, Nanoparticles with raman spectroscopic fingerprints for DNA and RNA detection, Science **297**, 1536 (2002).

[5] A. Ruditskiy, H.-C. Peng, and Y. Xia, Shape-controlled metal nanocrystals for heterogeneous catalysis, Annu. Rev. Chem. Biomol. Eng. **7**, 327 (2016).

[6] L. Liu and A. Corma, Metal catalysts for heterogeneous catalysis: From single atoms to nanoclusters and nanoparticles, Chem. Rev. **118**, 4981 (2018).

[7] M. Jin, H. Zhang, Z. Xie, and Y. Xia, Palladium concave nanocubes with high-index facets and their enhanced catalytic properties, Angew. Chem. Int. Ed. **50**, 7850 (2011).

[8] G. R. Patzke, Y. Zhou, R. Kontic, and F. Conrad, Oxide nanomaterials: Synthetic developments, mechanistic studies, and technological innovations, Angew. Chem. Int. Ed. **50**, 826 (2011).

[9] Y. Liang, Y. Li, H. Wang, J. Zhou, J. Wang, T. Regier, and H. Dai, Co_3O_4 nanocrystals on graphene as a synergistic catalyst for oxygen reduction reaction, Nat. Mater. **10**, 780 (2011).

[10] W. Huang, Oxide nanocrystal model catalysts, Acc. Chem. Res. **49**, 520 (2016).

[11] G. A. Mutch, S. Shulda, A. J. McCue, M. J. Menart, C. V. Ciobanu, C. Ngo, J. A. Anderson, R. M. Richards, and D. Vega-Maza, Carbon capture by metal oxides: Unleashing the potential of the (111) facet, J. Am. Chem. Soc. **140**, 4736 (2018).

[12] M. Yang, R. You, D. Li, Z. Zhang, and W. Huang, Methanol partial oxidation over shaped silver nanoparticles derived from cubic and octahedral Ag_2O nanocrystals, Catal. Lett. **149**, 2482 (2019).

[13] J. Wang, G. Wang, and J. Zhao, Density-functional study of $au_n(n = 2 - -20)$ clusters: Lowest-energy structures and electronic properties, Phys. Rev. B **66**, 035418 (2002).

[14] A. S. Chaves, M. J. Piotrowski, and J. L. F. Da Silva, Evolution of the structural, energetic, and electronic properties of the 3d, 4d, and 5d transition-metal clusters (30 TM_n systems for n = 2–15): a density functional theory investigation, Phys. Chem. Chem. Phys. **19**, 15484 (2017).

[15] F. Baletto and R. Ferrando, Structural properties of nanoclusters: Energetic, thermodynamic, and kinetic effects, Rev. Mod. Phys. **77**, 371 (2005).

[16] W. A. de Heer, The physics of simple metal clusters: experimental aspects and simple models, Rev. Mod. Phys. **65**, 611 (1993).

[17] T. Omoda, S. Takano, and T. Tsukuda, Toward controlling the electronic structures of chemically modified superatoms of gold and silver, Small **17**, 2001439 (2021).

[18] H. Häkkinen, M. Moseler, and U. Landman, Bonding in Cu, Ag, and Au clusters: Relativistic effects, trends, and surprises, Phys. Rev. Lett. **89**, 033401 (2002).

[19] S. Li, X.-S. Du, B. Li, J.-Y. Wang, G.-P. Li, G.-G. Gao, and S.-Q. Zang, Atom-precise modification of silver(I) thiolate cluster by shell ligand substitution: A new approach to generation of cluster functionality and chirality, J. Am. Chem. Soc. **140**, 594 (2018).

[20] C. P. Joshi, M. S. Bootharaju, M. J. Alhilaly, and O. M. Bakr, $[Ag_{25}(sr)_{18}]^{-}$, J. Am. Chem. Soc. .

[21] M. R. Narouz, S. Takano, P. A. Lummis, T. I. Levchenko, A. Nazemi, S. Kaappa, S. Malola, G. Yousefalizadeh, L. A. Calhoun, K. G. Stamplecoskie, H. Häkkinen, T. Tsukuda, and C. M. Crudden, Robust, highly luminescent Au_{13} superatoms protected by n-heterocyclic carbenes, J. Am. Chem. Soc. **141**, 14997 (2019).

[22] T. Pu, H. Tian, M. E. Ford, S. Rangarajan, and I. E. Wachs, Overview of selective oxidation of ethylene to ethylene oxide by Ag catalysts, Acs Catal. **9**, 10727 (2019).

[23] F. Loi, M. Pozzo, L. Sbuelz, L. Bignardi, P. Lacovig, E. Tosi, S. Lizzit, A. Kartouzian, U. Heiz, D. Alfè, and A. Baraldi, Oxidation at the sub-nanoscale: oxygen adsorption on graphene-supported size-selected Ag clusters, J. Mater. Chem. A **10**, 14594 (2022).

[24] C. M. Aikens, R. Jin, X. Roy, and T. Tsukuda, From atom-precise nanoclusters to superatom materials, J. Chem. Phys. **156**, 170401 (2022).

[25] J. Li and C.-y. Liu, Ag/graphene heterostructures: Synthesis, characterization and optical properties, Eur. J. Inorg. Chem. **2010**, 1244 (2010).

[26] I. Lado-Touriño and A. Páez-Pavón, Interaction between graphene-based materials and small Ag, Cu, and CuO clusters: A molecular dynamics study, Nanomaterials **11** (2021).

[27] M. Manadé, F. Viñes, and F. Illas, Transition metal adatoms on graphene: A systematic density functional study, Carbon **95**, 525 (2015).

[28] M. Al-Hada, S. Peters, L. Gregoratti, M. Amati, H. Sezen, P. Parisse, S. Selve, T. Niermann, D. Berger, M. Neeb, and W. Eberhardt, Nanoparticle formation of deposited Ag_n-clusters on free-standing graphene, Surf. Sci. **665**, 108 (2017).

[29] R. Dietsche, D. C. Lim, M. Bubek, I. Lopez-Salido, G. Ganteför, and Y. D. Kim, Comparison of electronic structures of mass-selected Ag clusters and thermally grown Ag islands on sputter-damaged graphite surfaces, Appl. Phys. A **90**, 395 (2008).

[30] S. H. Jeong, D. C. Lim, J.-H. Boo, S. B. Lee, H. N. Hwang, C. C. Hwang, and Y. D. Kim, Interaction of silver with oxygen on sputtered pyrolytic graphite, Appl. Catal., A **320**, 152 (2007).

[31] Z. Zhou, F. Gao, and D. W. Goodman, Deposition of metal clusters on single-layer graphene/Ru(0001): Factors that govern cluster growth, Surf. Sci. **604**, L31 (2010).

[32] X. Liu, C. Z. Wang, M. Hupalo, W. C. Lu, M. C. Tringides, Y. X. Yao, and K. M. Ho, Metals on graphene: correlation between adatom adsorption behavior and growth morphology, Phys. Chem. Chem. Phys. **14**, 9157 (2012).

[33] X. Liu, Y. Han, J. W. Evans, A. K. Engstfeld, R. J. Behm, M. C. Tringides, M. Hupalo, H.-Q. Lin, L. Huang, K.-M. Ho, D. Appy, P. A. Thiel, and C.-Z. Wang, Growth morphology and properties of metals on graphene, Prog. Surf. Sci. **90**, 397 (2015).

[34] F. Presel, N. Jabeen, M. Pozzo, D. Curcio, L. Omiciuolo, P. Lacovig, S. Lizzit, D. Alfè, and A. Baraldi, Unravelling the roles of surface chemical composition and geometry for the graphene-metal interaction through C1s core-level spectroscopy, Carbon **93**, 187 (2015).

[35] B. Wang, B. Yoon, M. König, Y. Fukamori, F. Esch, U. Heiz, and U. Landman, Size-selected monodisperse nanoclusters on supported graphene: Bonding, isomerism, and mobility, Nano Lett. **12**, 5907 (2012).

[36] D. Yi, W. Zhao, and F. Ding, Stable AA-stacked Pt nanoclusters supported on graphene/Ru(0001) and the selective catalysis: A theoretical study, ACS Appl. Nano Mater. **2**, 2921 (2019).

[37] R. T. Frederick, Z. Novotny, F. P. Netzer, G. S. Herman, and Z. Dohnálek, Growth and stability of titanium dioxide nanoclusters on graphene/Ru(0001), J. Phys. Chem. B **122**, 640 (2018).

[38] Z. Novotny, F. P. Netzer, and Z. Dohnálek, Cerium oxide nanoclusters on graphene/Ru(0001): Intercalation of oxygen via spillover, Acs Nano **9**, 8617 (2015).

[39] B. F. Habenicht, D. Teng, L. Semidey-Flecha, D. S. Sholl, and Y. Xu, Adsorption and diffusion of 4d and 5d transition metal adatoms on graphene/Ru(0001) and the implications for cluster nucleation, Top. Catal. **57**, 69 (2014).

[40] D. M. Cox, W. Eberhardt, P. Fayet, Z. Fu, B. Kessler, R. D. Sherwood, D. Sondericker, and A. Kaldor, Electronic structure of deposited monosized metal-clusters, Zeitschrift für Physik D Atoms, Molecules and Clusters **20**, 385 (1991).

[41] W. Eberhardt, P. Fayet, D. M. Cox, Z. Fu, A. Kaldor, R. Sherwood, and D. Sondericker, Photoemission from mass-selected monodispersed Pt clusters, Phys. Rev. Lett. **64**, 780 (1990).

[42] S. Peters, S. Peredkov, B. Balkaya, N. Ferretti, A. Savci, A. Vollmer, M. Neeb, and W. Eberhardt, Inner-shell photoionization spectroscopy on deposited metal clusters using soft x-ray synchrotron radiation: An experimental setup, Rev. Sci. Instrum. **80**, 125106 (2009).

[43] S. Klacar, A. Hellman, I. Panas, and H. Grönbeck, Oxidation of small silver clusters: A density functional theory study, J. Phys. Chem. C **114**, 12610 (2010).

[44] B. C. Stipe, M. A. Rezaei, W. Ho, S. Gao, M. Persson, and B. I. Lundqvist, Single-molecule dissociation by tunneling electrons, Phys. Rev. Lett. **78**, 4410 (1997).

[45] C. Sprodowski, M. Mehlhorn, and K. Morgenstern, Dissociation of oxygen on Ag(100) induced by inelastic electron tunneling, J. Phys.: Condens. Matter **22**, 264005 (2010).

[46] X. Zhu, S. R. Hatch, A. Campion, and J. M. White, Surface photochemistry. II. wavelength dependences of photoinduced dissociation, desorption, and rearrangement of O_2 on Pt(111), J. Chem. Phys. **91**, 5011 (1989).

[47] Y. S. Kim, A. Bostwick, E. Rotenberg, P. N. Ross, S. C. Hong, and B. S. Mun, The study of oxygen molecules on pt (111) surface with high resolution x-ray photoemission spectroscopy, J. Chem. Phys. **133**, 034501 (2010).

[48] S. Ulstrup, P. Lacovig, F. Orlando, D. Lizzit, L. Bignardi, M. Dalmiglio, M. Bianchi, F. Mazzola, A. Baraldi, R. Larciprete, P. Hofmann, and S. Lizzit, Photoemission investigation of oxygen intercalated epitaxial graphene on Ru(0001), Surf. Sci. **678**, 57 (2018).

[49] D. Martoccia, P. R. Willmott, T. Brugger, M. Björck, S. Günther, C. M. Schlepütz, A. Cervellino, S. A. Pauli, B. D. Patterson, S. Marchini, J. Wintterlin, W. Moritz, and T. Greber, Graphene on Ru(0001): A 25×25 supercell, Phys. Rev. Lett. **101**, 126102 (2008).

[50] A. Nilsson, R. E. Palmer, H. Tillborg, B. Hernnäs, R. J. Guest, and N. Mårtensson, Orientation-dependent final-state effects in photoelectron spectra of physisorbed molecules, Phys. Rev. Lett. **68**, 982 (1992).

[51] Z. Novotny, M.-T. Nguyen, F. P. Netzer, V.-A. Glezakou, R. Rousseau, and Z. Dohnálek, Formation of supported graphene oxide: Evidence for enolate species, J. Am. Chem. Soc. **140**, 5102 (2018).

[52] R. Larciprete, S. Fabris, T. Sun, P. Lacovig, A. Baraldi, and S. Lizzit, Dual path mechanism in the thermal reduction of graphene oxide, J. Am. Chem. Soc. **133**, 17315 (2011).

[53] C. Heine, B. Eren, B. A. J. Lechner, and M. Salmeron, A study of the O/Ag(111) system with scanning tunneling microscopy and x-ray photoelectron spectroscopy at ambient pressures, Surf. Sci. **652**, 51 (2016).

[54] M. E. Turano, R. G. Farber, E. C. N. Oskorep, R. A. Rosenberg, and D. R. Killelea, Characterization of oxygenaceous species formed by exposure of Ag(111) to atomic oxygen, J. Phys. Chem. C **124**, 1382 (2020).

[55] J. Schnadt, A. Michaelides, J. Knudsen, R. T. Vang, K. Reuter, E. Lægsgaard, M. Scheffler, and F. Besenbacher, Revisiting the structure of the $p(4 \times 4)$ surface oxide on Ag(111), Phys. Rev. Lett. **96**, 146101 (2006).

[56] M. Gajdoš, A. Eichler, and J. Hafner, Ab initio density functional study of O on the Ag(001) surface, Surf. Sci. **531**, 272 (2003).

[57] T. C. Kaspar, T. Droubay, S. A. Chambers, and P. S. Bagus, Spectroscopic evidence for Ag(iii) in highly oxidized silver films by x-ray photoelectron spectroscopy, J. Phys. Chem. C **114**, 21562 (2010).

[58] G. H. Major, N. Fairley, P. M. A. Sherwood, M. R. Linford, J. Terry, V. Fernandez, and K. Artyushkova, Practical guide for curve fitting in x-ray photoelectron spectroscopy, Journal of Vacuum Science & Technology A **38**, 061203 (2020).

[59] J. P. Allen, D. O. Scanlon, and G. W. Watson, Electronic structures of silver oxides, Phys. Rev. B **84**, 115141 (2011).

[60] M. Diantoro, R. Fitrianingsih, N. Mufti, and A. Fuad, Synthesis of silver nanoparticles by chemical reduction at various fraction of MSA and their structure characterization, Aip Conf. Proc. **1589**, 257 (2014).

[61] Y.-M. Su, Z. Wang, G.-L. Zhuang, Q.-Q. Zhao, X.-P. Wang, C.-H. Tung, and D. Sun, Unusual fcc-structured Ag_{10} kernels trapped in Ag_{70} nanoclusters, Chem. Sci. **10**, 564 (2019).

[62] C. Zeng, T. Li, A. Das, N. L. Rosi, and R. Jin, Chiral structure of thiolate-protected 28-gold-atom nanocluster determined by x-ray crystallography, J. Am. Chem. Soc. **135**, 10011 (2013).

[63] C. Zeng, H. Qian, T. Li, G. Li, N. L. Rosi, B. Yoon, R. N. Barnett, R. L. Whetten, U. Landman, and R. Jin, Total structure and electronic properties of the gold nanocrystal $Au_{36}(sr)_{24}$, Angew. Chem. Int. Ed. **51**, 13114 (2012).

[64] P. Norby, R. Dinnebier, and A. N. Fitch, Decomposition of silver carbonate; the crystal structure of two high-temperature modifications of Ag_2CO_3, Inorg. Chem. **41**, 3628 (2002).

[65] B. Standke and M. Jansen, Ag_2O_3, a novel binary silver oxide, Angew. Chem. Int. Ed. Engl. **24**, 118 (1985).

[66] M. Jansen and P. Fischer, Eine neue darstellungsmethode für monoklines silber(I,III)oxid (AgO), einkristallzüchtung und röntgenstrukturanalyse, J. Less Common. Met. **137**, 123 (1988).

[67] N. M. Martin, S. Klacar, H. Grönbeck, J. Knudsen, J. Schnadt, S. Blomberg, J. Gustafson, and E. Lundgren, High-coverage oxygen-induced surface structures on Ag(111), J. Phys. Chem. C **118**, 15324 (2014).

[68] M. E. Turano, L. B. F. Juurlink, M. Z. Gillum, E. A. Jamka, G. Hildebrandt, F. Lewis, and D. R. Killelea, Oxygen-induced surface reconstructions on curved Ag(111), Journal of Vacuum Science & Technology A **39**, 053201 (2021).

[69] H. L. Mortensen, S. A. Meldgaard, M. K. Bisbo, M.-P. V. Christiansen, and B. Hammer, Atomistic structure learning algorithm with surrogate energy model relaxation, Phys. Rev. B **102**, 075427 (2020).

[70] M. R. Mananghaya, G. N. Santos, and D. Yu, Small transition metal cluster adsorbed on graphene and graphene nanoribbons: A density functional based tight binding molecular dynamics study, Org. Electron. **63**, 355 (2018).

[71] R. M. Del Castillo and L. E. Sansores, Study of the electronic structure of Ag, Au, Pt and Pd clusters adsorption on graphene and their effect on conductivity, Eur. Phys. J. B **88**, 248 (2015).

[72] P. Mélinon, B. Masenelli, F. Tournus, and A. Perez, Playing with carbon and silicon at the nanoscale, Nat. Mater. **6**, 479 (2007).

[73] H.-J. Zhai, Y.-F. Zhao, W.-L. Li, Q. Chen, H. Bai, H.-S. Hu, Z. A. Piazza, W.-J. Tian, H.-G. Lu, Y.-B. Wu, Y.-W. Mu, G.-F. Wei, Z.-P. Liu, J. Li, S.-D. Li, and L.-S. Wang, Observation of an all-boron fullerene, Nat. Chem. **6**, 727 (2014).

[74] W. I. F. David, R. M. Ibberson, J. C. Matthewman, K. Prassides, T. J. S. Dennis, J. P. Hare, H. W. Kroto, R. Taylor, and D. R. M. Walton, Crystal structure and bonding of ordered C_{60}, Nature **353**, 147 (1991).

[75] R. Rousseau, D. A. Dixon, B. D. Kay, and Z. Dohnálek, Dehydration, dehydrogenation, and condensation of alcohols on supported oxide catalysts based on cyclic $(WO_3)_3$ and $(MoO_3)_3$ clusters, Chem. Soc. Rev. **43**, 7664 (2014).

[76] S. Mitchell, R. Qin, N. Zheng, and J. Pérez-Ramírez, Nanoscale engineering of catalytic materials for sustainable technologies, Nat. Nanotechnol. **16**, 129 (2021).

[77] D. Widmann and R. J. Behm, Activation of molecular oxygen and the nature of the active oxygen species for CO oxidation on oxide supported Au catalysts, Acc. Chem. Res. **47**, 740 (2014).

CHAPTER 5

Anomalous core level shifts in oxidized Ag_n clusters

The concept of oxidation state was introduced over two centuries ago to describe the stepwise increase in the amount of oxygen bound by elements that form more than one oxide [1]. Its formal definition relies on a well agreed set of electron counting rules [2], although the concept itself of oxidation state and its relationship with ionicity and charge state have been debated for decades [3–5]. To date, the dispute still continues [2, 6–8], but what is certain is that this trait of matter plays a key role in modern materials science [9–12].

Starting from the pioneering work by Siegbahn and co-workers [13], X-ray photoelectron spectroscopy stood up as one of the central experimental techniques to study the oxidation state of matter in different shapes and environment. Adsorption of oxygen leads to a CLS due to its high electronegativity that affects the charge localization and the electric field generated in a crystal. In particular, according to an electrostatic model that is typically used to rationalize chemical shifts [14], the shift of a core state at site i is given by

$$\Delta E_i = kq_i + \sum_{j \neq i} \frac{q_j}{R_{ij}},$$

where q_i is the net charge on the i-th atom, k is the Coulomb repulsion integral between valence and core states, and R_{ij} is the distance between between the i-th and j-th nuclei [15]. According to this model, higher oxidation states, which are associated to a higher positive charge in the oxidized ion, lead to higher BEs [16, 17]. The possibility to distinguish different components associated to different oxidation states with XPS is of paramount importance to characterize and understand the behavior of matter in different chemical environments [9, 10].

Among transition metals, there are few exceptions to this general trend. The first one to be reported was the case of silver, whose Ag 3d core levels move towards lower BEs for increasing oxygen densities [19, 21]. The first evidence of this anomaly dates back to 1973, when Gunnar Schön reported that the Ag $3d_{5/2}$ BE in Ag_2O powders is lower (367.7 ± 0.1 eV) than for a clean Ag foil (368.1 ± 0.1 eV) [22]. Similar experimental studies have been performed in the following decades for different Ag oxide systems in combination with *ab initio* DFT calculations, confirming this anomalous trend. More recent assignments of the binding energies of Ag(0), Ag(I) and Ag(III) oxidations state in highly oxidized Ag films (Fig. 5.1a) correspond to 368.24, 367.30 and 366.80 eV, respectively [18]. Similarly, the O adsorption on Ag(111)

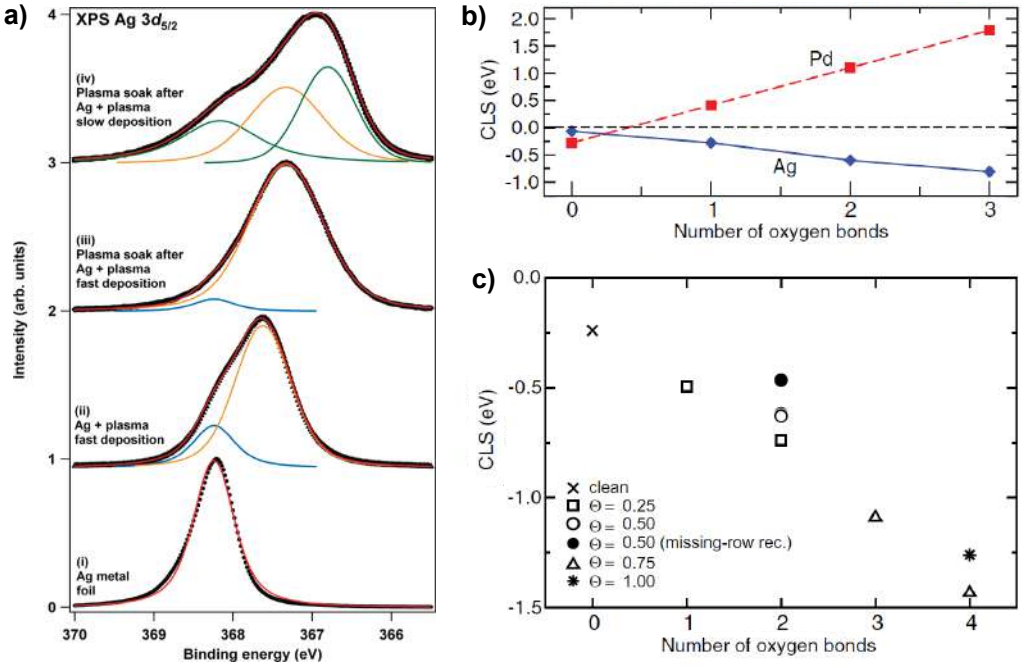

Figure 5.1: *a) High resolution XPS Ag $3d_{5/2}$ core levels for polycrystalline silver foil, as well as oxidized silver films deposited with atomic oxygen under different conditions and fitting analysis with Voigt functions. Adapted from [18]. b) DFT calculated 3d CLSs for Pd(111), Ag(111) and c) Ag(100) as a function of oxygen-metal bonds. The CLSs are expressed with respect to the bulk counterpart. b) Adapted from [19]. c) Adapted from [20].*

[19] and Ag(100) [20] single crystal surfaces leads to an increasing negative CLS that scales with the number of bonds (N_B) that an emitting Ag atom is forming with O (Fig. 5.1b,c). In their study on the oxidation of Ag(111), Grönbeck and co-workers where able to link the reversed photoemission CLS of Ag oxides to their peculiar valence band [19]. In particular, they adopted a complementary experimental and theoretical approach to compare the oxygen adsorption on Ag(111) and Pd(111) involving the study on the CLSs, a Bader charge analysis and calculations on the d-band modifications induced by O adsorption. With this method, they evidenced how bonding of oxygen to the two metals is substantially different character: for Pd, the bonding includes contributions of the d-states, whereas for Ag, the bonding is attributed mainly to s-states. In particular, while for Pd the shifts of the d-band center ($\Delta\epsilon_d$) are proportional both to N_B and to the Pd 3d CLSs, in the case of Ag the d-band is nearly unaffected by O adsorption, despite a clear metal-to-oxygen charge transfer (Fig. 5.2). Therefore, they concluded that the negative CLS of Ag can be attributed to final-state due to the fact that the screening of the core-hole occurs in metal s-states of bonding character, rather than on d-states.

Understanding the oxidation of Ag is extremely relevant due to its catalytic applications [23, 24]. However, the dominant contribution of final-state effects to the Ag 3d CLSs makes this task much more arduous. When the modifications of the core level BEs are dominated by initial-state effects, they are typically proportional to the d-band center shifts $\Delta\epsilon_d$ [19, 25, 26], which is a well know indicator of chemical reactivity according to the Hammer-Nørskov model [27]. For this reason, they are

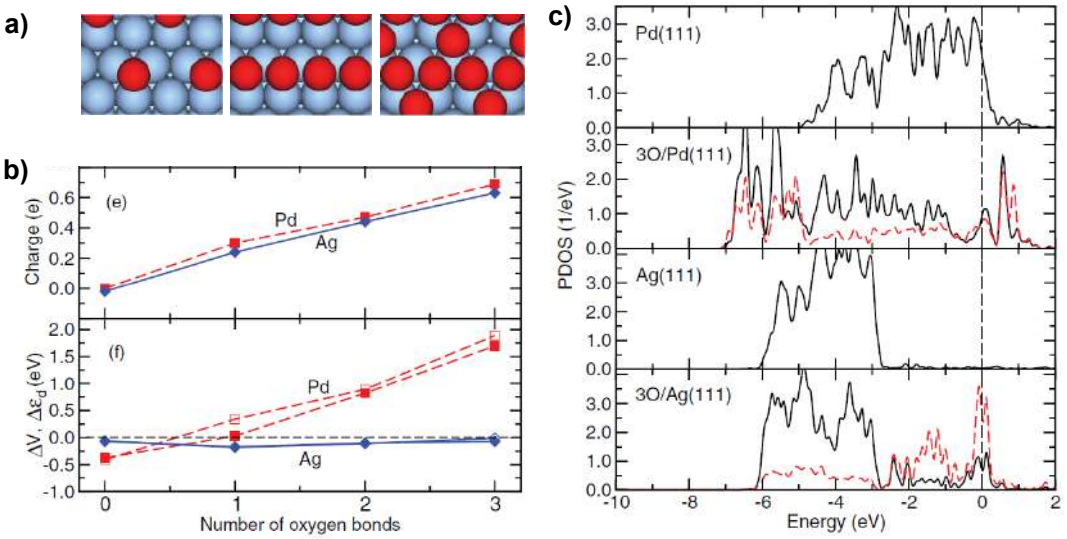

Figure 5.2: *a) Structural models for O adsorption at 0.25 (left), 0.5 (center), and 0.75 (right) ML coverage used. b) Bader charge, $\Delta\epsilon_d$ and initial-state contributions ΔV for Pd(111) and Ag(111) as a function of oxygen-metal bonds. c) PDOS of Pd(111), 3O/Pd(111), Ag(111), and 3O/Ag(111) (from top to bottom). The energies are reported with respect to the corresponding Fermi energy. Solid (dashed) lines correspond to projection on metal 4d-states (O 2p-states). a-c) Adapted from [19].*

rich in information about the chemical properties of a material. On the contrary, final-state effects, which are related the presence of a core-hole in the final-state of the photoemission process, are difficult to explain without the support of specific DFT calculations. This applies also to size-selected clusters, where the possibility to disentangle final- and initial-state effects led in the past to link the experimentally measured XPS CLS to their chemical reactivity [28]. In the case of small clusters, the contribution arising from initial- and final-state effects is different compared to their bulk counterparts, as they are greatly affected by the reduced size and unique electronic properties [29–33]. Therefore, one may wonder: what happens to the Ag CLS anomaly at the sub-nanoscale? In the previous chapter we have seen that O adsorption progressively shifts the overall Ag 3d BE of clusters towards lower values, confirming the trend observed for bulk and surface oxidation. However, we have also seen that the Ag 4d-band is greatly affected by O adsorption, contrary to the case of Ag(111) oxidation [19]. This suggests that the O adsorption on the clusters is indeed different with respect to surfaces. Motivated by this aspect and by the technological relevance of Ag oxides, we further investigated the effects of O adsorption in the cluster to understand the Ag 3d CLS of each atom composing them as a function of the number of oxygen bonds N_B per Ag atom. In particular, we followed the approach used by Grönbeck and co-workers to study the oxidation of Ag(111), focusing our experiment and theoretical calculations on the Ag_{11} and Ag_7 clusters deposited on graphene epitaxially grown on Ru(0001). The hybrid structure that Ag_{11} reaches upon oxidation allows the study of the CLS of Ag ions with different oxidation state within the same cluster, resulting very suited for this study. Moreover, we implemented the work including an experimental and theoretical analysis on the oxidation of Ag_7, the largest two-dimensional cluster according to our

DFT calculations (see chapter 2.6) to test the role played by the cluster morphology on its electronic properties. Our results indicate that the Ag $3d_{5/2}$ CLS of the atoms in the clusters follows the negative trend typical of Ag for low N_B, but the trend breaks down for larger O densities. In particular, Ag(III) ions ($N_B = 4$) show a smaller CLS compared to Ag(I), closer to Ag(0). This effect is directly linked to the role played by the d-band center which drastically changes for an increasing number of Ag-O bonds, enhancing the initial-state contribution to the overall CLS. This is a striking difference compared to the oxidation of Ag on larger scales and it indicates that the well-established trends found in bulk matter and on solid surfaces might differ greatly for atomic clusters because of their reduced size and unique electronic properties.

The results reported in this chapter have been published in the journal *Applied surface science* with the title "Breakdown of the correlation between oxidation states and core electron binding energies at the sub-nanoscale" [34].

5.1 Cluster deposition and oxidation

The generation and deposition of Ag_7^+ clusters on GR/Ru is performed mimicking the experiment described in the previous chapter to allow for a direct comparison with the results obtained for Ag_{11}^+ . The temperature of the system is T = 20 K and the total cluster coverage corresponds to a statistical occupation of one cluster every 9 moiré cells to prevent cluster sintering and preserve the mass selection.

Figure 5.3a shows a comparison of the Ag $3d_{5/2}$ spectra of acquired for Ag_7 and Ag_{11} clusters (top) after the deposition on GR/Ru and with Ag_7 deposited on bare Ru(0001) (bottom). On GR/Ru, the Ag $3d_{5/2}$ core level of Ag_7 is centered at 368.24 ± 0.02 eV, 70 ± 40 meV higher than Ag_{11} (368.17 ± 0.02 eV). This small difference is consistent with the work by Dietsche and co-workers fo Ag_n clusters supported on sputter-damaged highly oriented pyrolitic graphite [35]. They reported small Ag 3d CLSs towards lower binding energies (less than 100 meV) for increasing cluster size that co-occurs with a decrease of the full-width-half-maximum of the spectra. Similarly, the spectral analysis that we performed for Ag_7 and Ag_{11} on GR/Ru indicates a larger Gaussian width (G) for the smaller cluster (G = 0.97 ± 0.02 eV *vs* 0.73 ± 0.02 eV). It is interesting to compare these values with the ones obtained for the same Ag_7 cluster deposited on bare Ru(0001). In this latter case, the G parameter was 0.23 ± 0.02 eV, much smaller than on GR/Ru. This difference can be accounted to (i) the higher inhomogeneity of the moiré lattice of GR/Ru with respect to the highly ordered Ru(0001) surface and (ii) to the lower interaction of the clusters with graphene rather than with Ru. The combination of these two factors increases the possible adsorption configurations of the clusters on the surface, which contribute to the Gaussian broadening [36].

The oxidation of Ag_7 was performed in two different steps, with exposures of 0.1 and 0.5 L of O_2 in the same conditions applied for Ag_{11} to induce the photo-dissociation of physisorbed O_2 with soft X-ray irradiation at T = 20 K. The XPS spectra are shown in Fig. 5.3b. To analyze the data, we performed DFT calculations of on the minimum energy configurations of oxidized Ag_7 clusters in the fcc cell of a complete moiré cell supported by 4 Ru layers (Fig. 5.4). Specifically, we built the Doniach-Šunjić line associated to the calculated Ag $3d_{5/2}$ BEs of Ag_7O_m clusters with an even number of O atoms and used them to fit the experimental data. The fitting residuals obtained for the clean clusters indicate a good agreement between

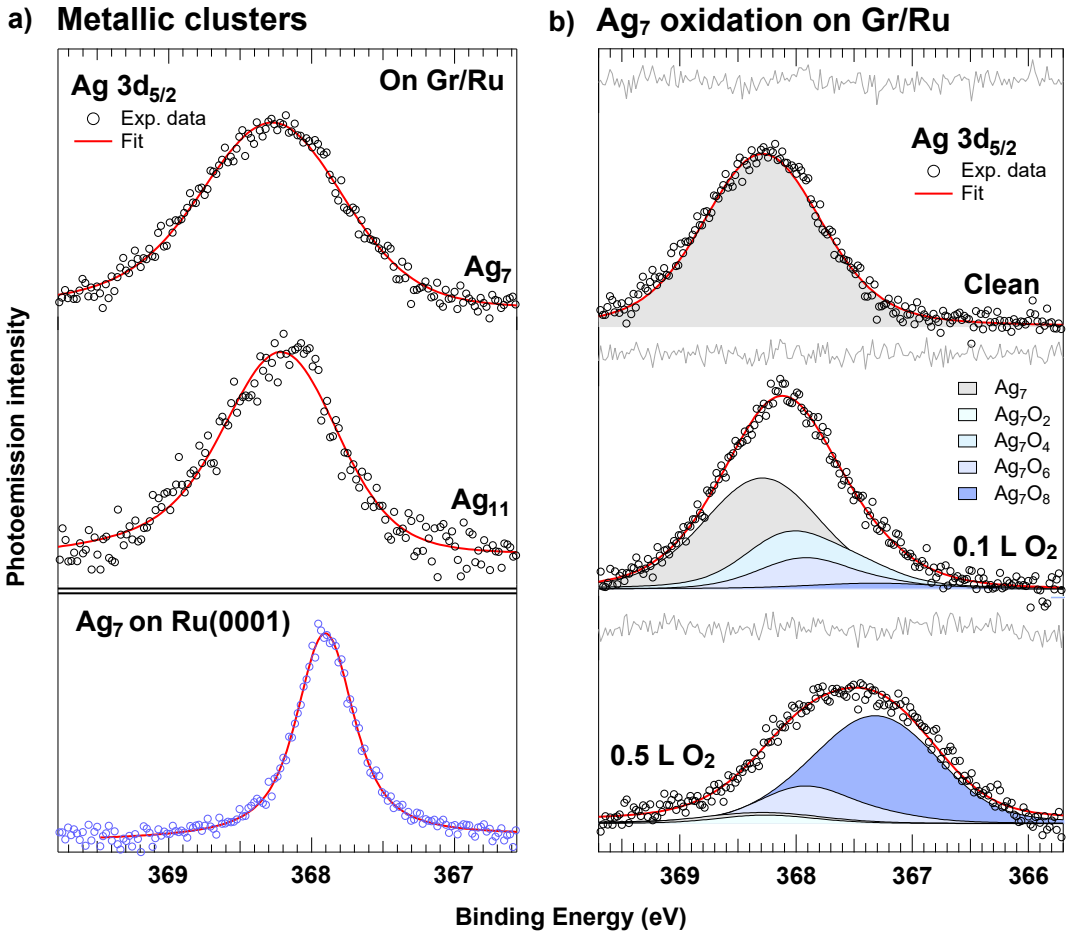

Figure 5.3: *a) Ag $3d_{5/2}$ core level spectra of pristine Ag_7 and Ag_{11} cluster on GR/Ru and Ag_7 on Ru(0001) with a photon energy of 470 eV. The spectra on GR/Ru are acquired at T = 20 K, while the spectrum on Ru(0001) at T = 300 K. b) Same core level of the Ag_7 cluster for different oxidation steps (from the top clean, 0.1 L and 0.5 L of O_2) acquired at T = 20 K and after soft X-ray irradiation. The spectra are fitted using the DFT calculated spectra of oxidized Ag_7O_m clusters ($m = 0, 2, 4, 6, 8$.*

experiment and theory. For the lowest O_2 dose, Ag_7 reaches an higher density of O with respect to Ag_{11}. While for the larger cluster we only detected Ag_{11} and $Ag_{11}O_2$, for Ag_7 almost 30 ± 5 % of the total spectral weight can be associated to Ag_7O_4. Moreover, our analysis indicates also a small amount of Ag_7O_6 (15 ± 5 %). Finally, after the largest O_2 dose of 0.5 L, almost 70 ± 5% of the total spectral area can be associated to Ag_7O_8.

The fact that a higher percentage of Ag_7 cluster can reach a Ag-to-O ratio above 1 compared to Ag_{11} can be related to its smaller size and two-dimensional structure. Although neither Ag_7 or Ag_{11} posses atoms in their bulk, the latter has several atoms at the cluster/graphene interface, where physisorbed O_2 may not bind as easily as in the other sites of the cluster. On the contrary, all the atoms forming Ag_7 are directly exposed, which may facilitate the O_2 physisorption. It is also important to notice that Pt clusters of similar sizes where reported to have an O affinity which increases with decreasing size, resulting in smaller clusters being easier to oxidized than larger ones [37]. Therefore, a similar effect may apply also for Ag, thus facilitating the oxidation

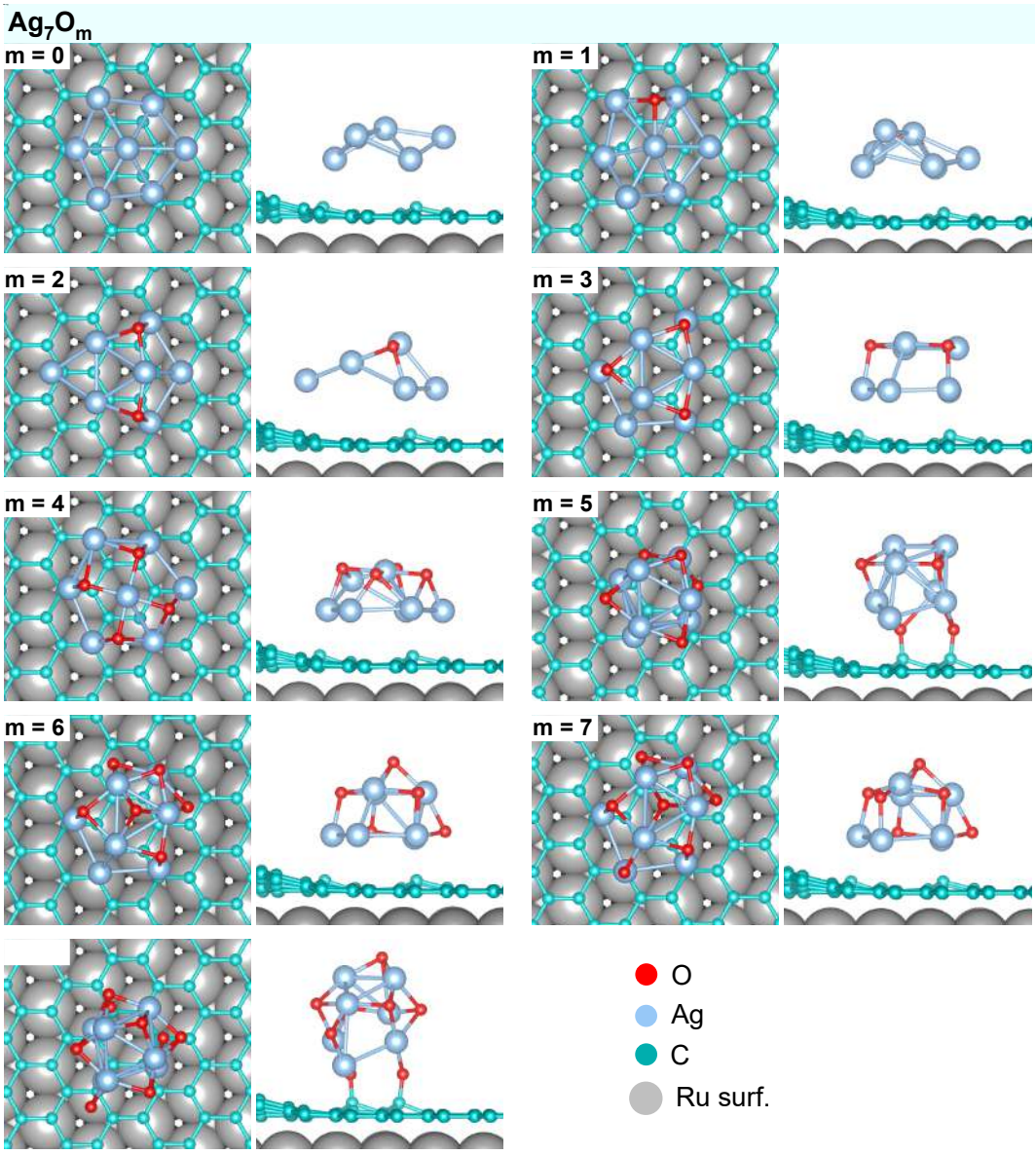

Figure 5.4: *Top and side views of the relaxed minimum energy configurations calculated for graphene-supported Ag_7O_m clusters for $m = 1 - 8$.*

of Ag_7 with respect to Ag_{11}. Despite this difference, in both cases highest O-to-Ag ratio achievable by the clusters with our oxidaton method at T = 20 K appears to be slightly larger than 1, with a final stoichiometry similar to the bulk phase AgO.

The experimental data indicates that, also for Ag_7, higher oxygen exposures lead to a negative Ag $3d_{5/2}$ CLS, suggesting once again that the Ag anomaly is somehow preserved also at this scale. However, due to the large intrinsic Gaussian width and to the co-existence of different oxidized clusters on the surface, it is not possible to obtain information on the behavior of the different atoms composing the cluster as a function of the number of O bonds. To reach an atomistic understanding on this fundamental aspect, we relied on *ab initio* DFT calculations.

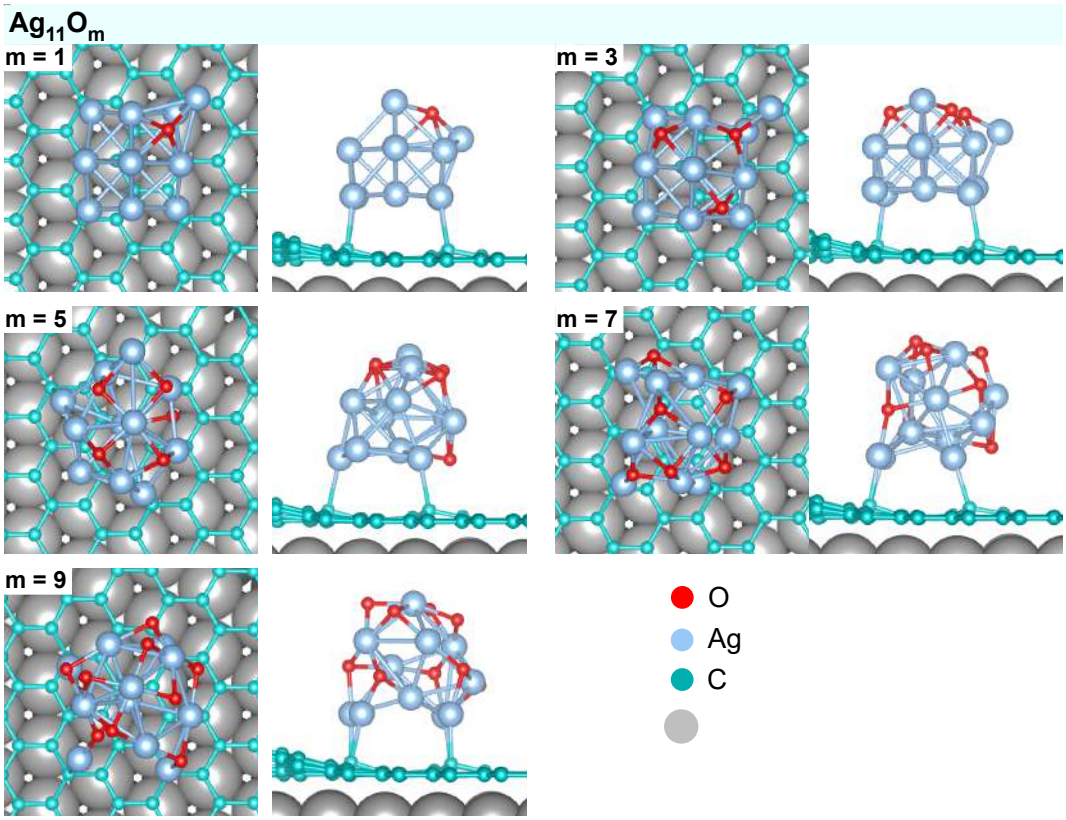

Figure 5.5: *Top and side views of the relaxed minimum energy configurations calculated for graphene-supported $Ag_{11}O_m$ clusters with an odd number of O atoms in the range $m = 1 - 9$.*

5.2 Core level shift anomaly in clusters

The CLS anomaly of oxidized Ag clusters was studied for Ag_7O_m ($m = 0 - 8$) and $Ag_{11}O_m$ ($m = 0 - 10$ and 12). We extended the calculations also to clusters with an odd number of O atoms to increase the data statistics, although such clusters were not used to fit the experimental data. The minimum energy configurations of Ag_7O_m and of the newly calculated $Ag_{11}O_m$ clusters with odd m obtained from the DFT calculations are shown in Fig. 5.4 and Fig. 5.5, respectively. For our study, we define N_B as the number of oxygen atoms that are bound to a given Ag atom with a O−Ag bond length below the threshold value of 2.30 Å. This value arises from the typical O−Ag distance in bulk oxides such as Ag_2O, AgO and Ag_2O_3 [38], oxidized silver surfaces [20, 39] and small Ag clusters in the gas-phase [40], which ranges from 1.90 to 2.30 Å. The CLSs are expressed using as reference the the bulk Ag $3d_{5/2}$ BE that we fitted from the Ag(111) spectrum in the previous chapters (BE = 368.20 eV).

Figure 5.6a a shows the calculated Ag $3d_{5/2}$ CLS of the atoms in the oxidized clusters as a function of the number of oxygen bonds N_B. For N_B = 0 - 2, the CLS progressively increases, but the linear trend surprisingly breaks down for larger values. Specifically, for Ag_7 the trend is linear in the range N_B = 0 - 2 with a slope of -0.34 eV/N_B, while for Ag_{11} the linear trend continues up to N_B = 3 with a steeper slope of -0.41 eV/N_B. Such values are similar to those found for a Ag(100) surface up to

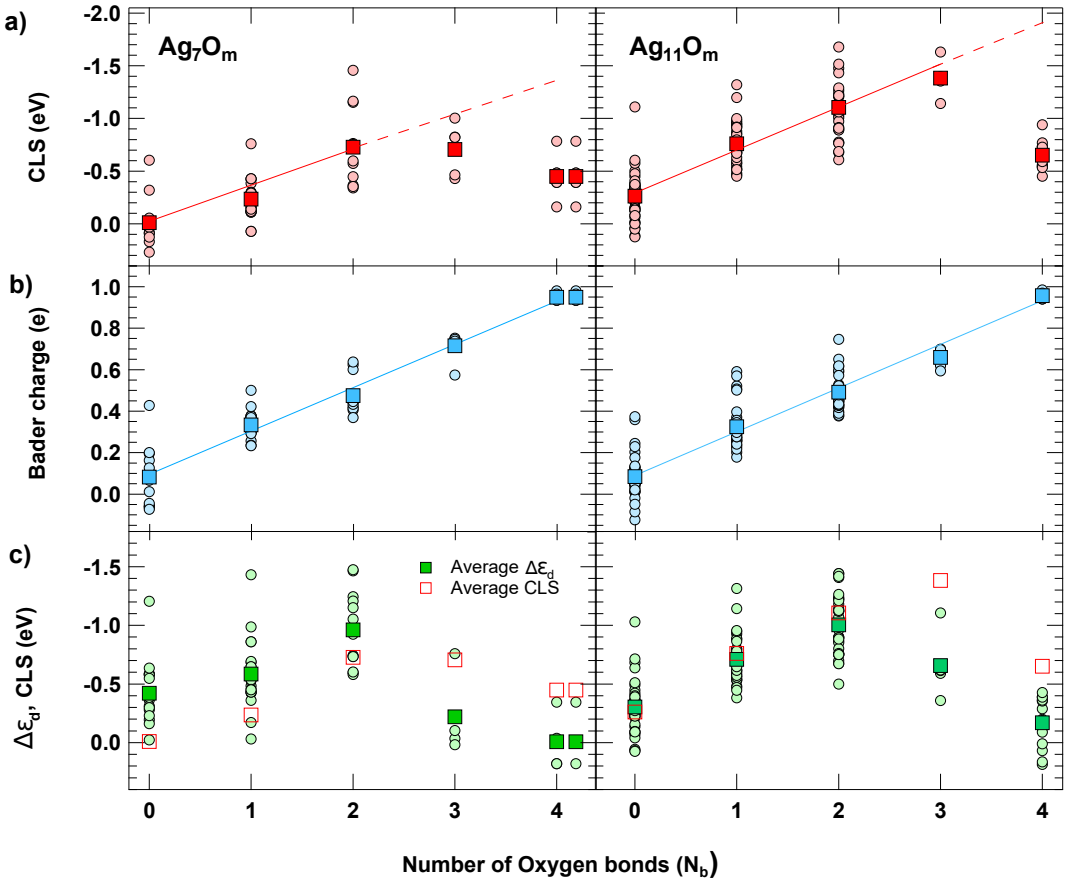

Figure 5.6: *a) DFT calculated Ag $3d_{5/2}$ CLS, b) Bader charge and c) $\Delta\epsilon_d$ of Ag atoms forming oxidized Ag_7O_m ($m = 1-8$) and $Ag_{11}O_m$ ($m = 1-10, 12$) clusters as a function of N_B. Circles are calculated values of the different atoms composing the clusters, squares represent the average value for each N_B.*

$N_B = 4$ (Fig. 5.1c), where the CLS increases by -0.29 eV/N_B. On the contrary, for $N_B = 4$, i.e., for those atoms possessing a square-planar AgO_4 geometry and with oxidation state 3+, the CLS in the clusters decreases. It is particularly meaningful to compare the CLSs of atoms with $N_B = 2$ and 4, since they can be formally attributed to Ag(I) and Ag(III) ions. The CLS associated to Ag(I) is -0.7 $\pm$ 0.3 eV (BE = 367.5 $\pm$ 0.3 eV) in Ag_7 and -1.1 $\pm$ 0.3 eV (BE = 367.1 $\pm$ 0.3 eV). These results are in close agreement with the values obtained for the oxidation of Ag films with atomic O, where the component associated to Ag(I) was found at 367.3 eV [18]. The large error bars of the calculated CLSs arise from the standard deviation associated to the BE dispersion for each N_B, with the core level energies that are affected by other contributions coming, for example, from different metallic coordination numbers [41] and interatomic distances [30]. For Ag(III), the CLS in both clusters deacreases, with the BEs that move back towards the metallic value. In the case of Ag_7, the $3d_{5/2}$ calculated CLS is -0.4 $\pm$ 0.2 (BE = 367.80 $\pm$ 0.2 eV). For Ag_{11}, the CLS is -0.7 $\pm$ 0.1 eV (BE = 367.50 $\pm$ 0.1 eV). Therefore, the Ag $3d_{5/2}$ BEs associated to different oxidation states in the clusters are ordered as Ag(0) > Ag(III) > Ag(I), breaking the general trend that associates higher oxidation states to higher CLSs.

Similar trend inversions in the core electron BEs upon oxidation are not generally

new in nature. They occur in other systems such as cobalt, where Co(III) exhibits a lower BE than Co(II) [42], and in alkali metals such as barium, where Ba(II) in BaO shows a lower BE than metallic Ba(0) [43]. These effects arise from competition of several initial-state effects such as the charge on the cation, which accounts for positive CLSs, and the Madelung potential of the surrounding crystal lattice, which lowers the observed BEs [42, 43]. However, in the case of Ag this anomaly in the already anomalous 3d CLSs appears to be related to the reduced size of the clusters, since it does not occur at larger scales [18–20]. To investigate its origin, we performed a Bader charge analysis and studied the effects induced by O adsorption on the Ag 4d-band with a similar procedure adopted by Grönbeck and co-workers to study the reversed CLS on Ag(111) [19].

The results of the Bader charge analysis are shown in Fig. 5.6b, where the charge of each single atom in the clusters is expressed as a function of N_B. Both for Ag_7 and Ag_{11}, the positive charge in Ag cations increases linearly in the whole range $N_B = 0 - 4$ with a slope of 0.21 e/N_B (linear correlation coefficient 0.95 $\pm$ 0.02) . This behavior mimics the oxidation of Ag(111), where a similar slope of 0.22 e/N_B can be extrapolated in the interval $N_B = 0 - 3$. The average charge in the clusters for Ag cations with $N_B = 2$ is 0.48 $\pm$ 0.09e in both clusters, in agreement with the value of 0.47 $\pm$ 0.02e that we calculated for Ag(I) cations in bulk Ag_2O in the previous chapter. Similarly. the average charge in Ag cations with $N_B = 4$ is 0.95 $\pm$ 0.03e, in close agreement with our calculations for Ag(III) ions in AgO (0.99 $\pm$ 0.02). This analysis clearly indicates that the oxidation state of the Ag atoms in the clusters increases linearly with N_B as it happens for Ag(111). Therefore, the non-monotonic trend of the CLS is not caused by an anomalous charge transfer effects between oxygen and Ag atoms.

A very different result is obtained from the second part of the analysis shown in Fig. 5.6c, where we focused on the changes in the Ag d-band center $\Delta\epsilon_d$ induced by O adsorption. In the oxidation of Ag(111) this value is nearly unperturbed by the presence of O, while for the clusters it drastically changes for different N_B. It reaches the highest value of -1 $\pm$ 0.3 eV (with respect to the bulk reference of metallic Ag that we calculated to be $\epsilon_d^B = 3.92$ eV) for $N_B = 2$, where the negative sign indicates an upshift towards the Fermi energy. For $N_B = 4$, $\Delta\epsilon_d$ decreases back to 0.0 $\pm$ 0.2 eV for Ag_7 and to -0.2 $\pm$ 0.2 eV for Ag_{11}, following a very similar trend than the Ag $3d_{5/2}$ CLS. The response of the d-band to the O adsorption indicates that the Ag−O bonds in the clusters clearly involves Ag 4d-states, while for metallic surfaces the bonding is attributed mainly to s-states.

The role played by the Ag 4d states in the Ag−O bonds is better highlighted in Fig. 5.7, where we report the Ag 4d and O 2p partial density of states (PDOS) projected onto a representative set of atoms for each N_B. For $N_B = 0$, the clusters look rather similar to Ag(111) (Fig. 5.2c), with a width of the d-band of $\sim$ 3 eV, from 6 to 3 eV below the Fermi energy. However, the oxidation affects the width of these states in Ag(111) scarcely, with small features that appear in the range 2 - 0 eV. They can be assigned to bonding and antibonding combinations of Ag 3d and O 2p states, but they never cross the Fermi energy [19]. On the contrary, the d-band of the clusters broadens upon oxidation, reaching a width of $\sim$ 7 eV and, for $N_B = 3 - 4$, it forms antibonding states above the Fermi energy. The final valence band of the clusters is more similar to those of oxidized transition metals such as Pd (Fig. 5.2c) [19], Ru [26] and Rh [25]. In such metals, the d-band broadening and the fact that it crosses the Fermi energy requires an adjustment of the center of the

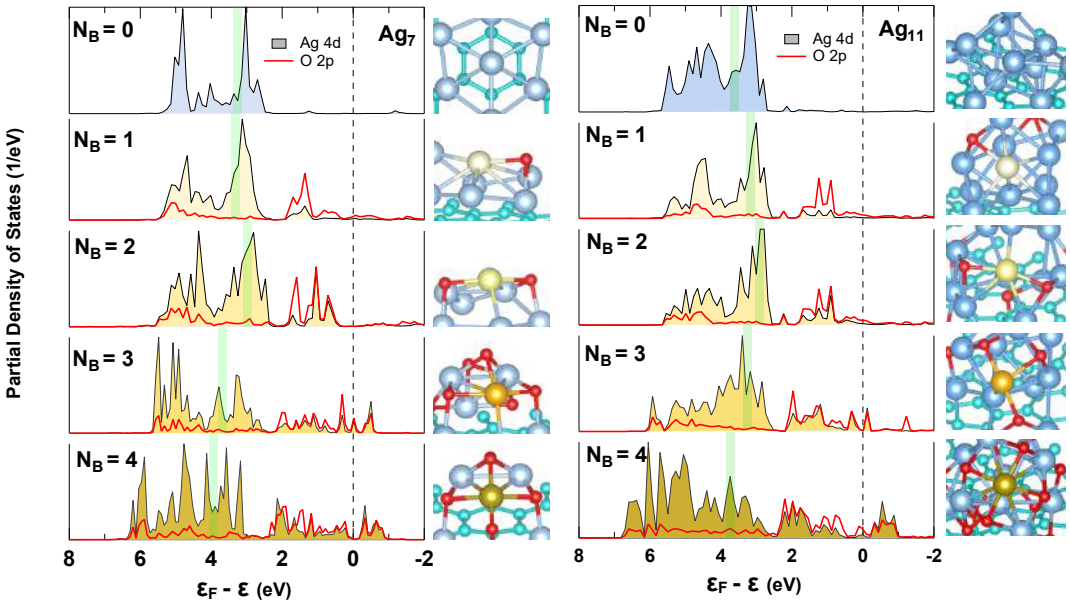

Figure 5.7: *Calculated PDOS for a representative set of Ag atoms forming the oxidized Ag_7O_m $(m = 1 - 8)$ and $Ag_{11}O_m$ $(m = 1 - 10, 12)$ clusters for each N_B. On the side of the PDOS, the ball model of the associated relaxed structure where the atom of each N_B is highlighted. The red vertical lines indicate the position of the d-band ceter ϵ_D.*

d-band ϵ_d, which shifts to higher energies to preserve charge neutrality. According to a simple model that assumes rectangular bands, even the core levels follow this shift and inherit their typical positive CLSs [44]. Therefore, the CLS anomaly in the clusters can be attributed to this behavior of the d-band and is directly liked to $\Delta\epsilon_d$.

It is crucial to underline that the CLS inversion for the highest oxidation state does not clash with the experimental data, where a higher O_2 exposure leads to progressively BEs. This trend is consistent with the average Ag $3d_{5/2}$ BEs obtained from our calculations for an increasing O density in the clusters, which is shown in Fig. 5.8. What happens here is that the smaller CLS of Ag(III) is counterbalanced by the higher value of Ag(I) ions and, due to the hybrid structure of the clusters and to the large Gaussian width of the spectra, it is not possible to disentangle the two contributions and experimentally appreciate the CLS anomaly.

5.3 Discussion: Implications of the CLS anomaly

The presence of an anomalous trend in the Ag 3d CLS of the clusters has several interesting implications. First of all, it clearly underlines once again the uniqueness of the clusters with respect to their counterparts at larger scales. For Ag, it is not possible to extend the well-known trend studied for metallic surfaces and bulk materials to the sub-nanoscale due to the high reactivity of the clusters and to the role played by the d-band in the Ag−O bonds. This result may apply also to other materials such as alkali metals. As we briefly discussed before, alkali metals such as Ba can present anomalous CLS upon oxidation, with Ba(II) in BaO that shows a lower BE than in the metallic phase [43]. This effect was associated to a large Madelung potential

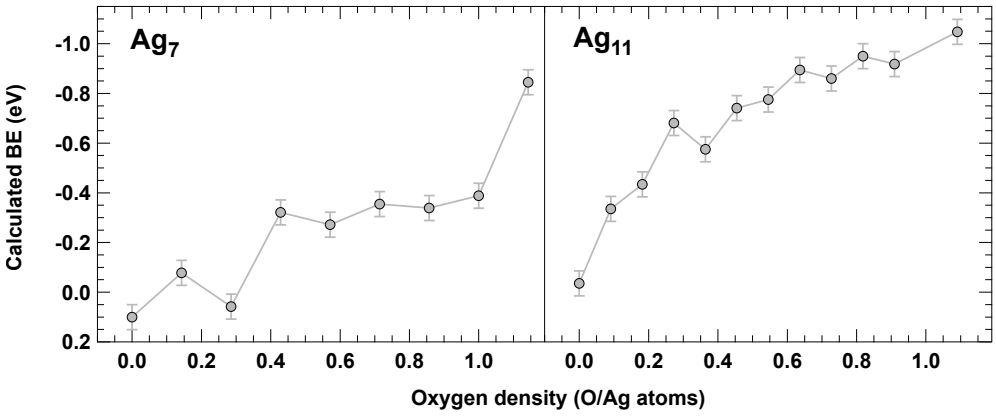

Figure 5.8: *Average DFT calculated Ag $3d_{5/2}$ CLS of oxidized Ag_7 and Ag_{11} clusters as a function of the oxygen density.*

at the cation sites, which acts to decrease the core level BEs from the values of a free cation. The Madelung potential is related to crystalline structure of a bulk material and to the interatomic distances [45], therefore it is reasonable to expect its contribution to the CLS to change for small clusters, which do not typically show a crystalline structure [46]. More in general, this result could be extended also to other elements of the periodic table due to different contributions of initial- and final-state effects in the clusters. It would be particularly interesting to study the effect of oxidation on an element such as Si, whose oxide is one of the most important and studied in material science and electronics, and it is often considered as a model system to explain the correlation between CLSs and oxidation state [47, 48].

A second interesting outcome of our results concerns the negative $\Delta\epsilon_d$ induced by O adsorption on the clusters. According to the Hammer-Nørskov model, the position of the d-band center ϵ_d is an indicator of the chemical reactivity of a system [27]. The closer ϵ_d is to the Fermi energy, the higher is the reactivity of a system. This model is extensively used in nanotechnology for electronic band-engineering, where a nanomaterial is doped with other elements to induce a shift of ϵ_d and enhance their catalytic properties [49–52]. For example, the d-band center of Ag-based nanoparticles was successfully shifted by almost 0.2 eV towards the Fermi energy by doping them with Pd atoms and forming an alloy [53]. Remarkably, the ϵ_d of atoms in the clusters with $N_B = 2$ is shifts by 1 ± 0.3 eV, and its shift is accompanied by a proportional CLS in the Ag 3d core level. This suggests that the reactivity of the atoms in the clusters increases with oxidation and that the evolution of their chemical properties can be followed by means of a powerful technique such as high resolution XPS. In particular, Ag(I) ions ($N_B = 2$) appear to be the most reactive one according to their largest $\Delta\epsilon_d$. This could facilitate the formation of the higher oxidation state 3+ through a mechanism known in surface science as indirect interaction, where one adsorbate modifies the electronic structure of a surface in such a way that the adsorption energy of a second adsorbate is changed [27]. It is common that the adsorption of O or other adsorbants leads to a downshift (away from the Fermi energy) of the d-states of the neighboring surface atoms, making it harder for a second adsorbate to bond on the same surface [25, 26, 54, 55]. In our clusters, the O adsorption induces an upshift of the d-states, which facilitates the adsorption of

new adsorbates [56, 57] and the formation of the higher Ag(III) oxidation state. This effect is extremely interesting if we consider the potential applications of the oxidized Ag clusters in the ethylene epoxidation reactions. As we discussed in the previous chapter, the oxygen vacancy formation energy in the clusters indicates that O atoms binding to Ag(III) are easier to remove and therefore are the main candidates to promote the epoxidation of ethylene. This reaction would imply the reduction of Ag(III) cations, since they will lose an O atom [23, 58]. However, this would be accompanied by a downshift of ϵ_d, which facilitates the formation of new Ag−O bonds to reach again the Ag(III) oxidation state to continue the reaction.

5.4 Conclusions

The oxidation state of matter can be probed by XPS thanks to the correlation of the exact peak position of the core level lines to the oxidation level of the emitting atom. Generally, oxidation increases the BE of a core electron, but there are few exceptions to this trend. Ag is one of the most striking case, with a linear but negative CLS for increasing oxidation states [18]. This behavior is attributed to its peculiar electronic band structure and to a major contribution coming from final-state effects to the overall CLS.

The electronic properties and the valence band structure of matter are known to change at the sub-nanoscale for size-selected clusters [31], potentially affecting the anomalous 3d CLS trend of Ag. To investigate this aspect, we studied the oxidation of graphene-supported Ag_7 and Ag_{11} clusters with a combined experimental and theoretical approach. High resolution XPS on the pristine clusters was sensitive to their size, with small differences in the Ag $3d_{5/2}$ BEs and with a larger Gaussian width for the smaller cluster [35]. Upon oxidation, the spectra shift towards lower BEs, confirming the negative correlation between oxidation state and CLS. However, DFT calculation revealed an anomaly in the typical negative CLS trend of the Ag 3d core levels: Ag(III) cations show an higher BE compared to Ag(I), closer to Ag(0). This effect cannot be appreciated experimentally due to the large intrinsic Gaussian width of the spectra and to the hybrid structure of the clusters which are composed of both Ag(III) and Ag(I) cations for higher O densities. We were able to attribute this anomaly to the different behavior of the Ag 4d-band in the clusters with respect to metallic surfaces, with the d-band barycenter ϵ_d that shifts for different O coverages. This quantity is an indicator of chemical reactivity and is linked to the Ag $3d_{5/2}$ core levels [44], which are induced to follow a similar trend. This allows to study the chemical properties of the clusters by means of XPS, since the negative CLS can be associated to a higher reactivity of the oxidized clusters with respect to their metallic phase. Our results suggest that oxidized size-selected Ag clusters can be taken in consideration as low-nuclearity supported catalysts and clearly indicate that the well established trends that have been studied for metallic surfaces and bulk materials cannot be generally extended to the sub-nanoscale.

References

[1] F. Wöhler and R. Fittig, *Wöhler's Grundriss der organischen Chemie*, Grundriss der Chemie (Verlag von Duncker & Humblot, 1877).

[2] A. Walsh, A. A. Sokol, J. Buckeridge, D. O. Scanlon, and C. R. A. Catlow, Oxidation states and ionicity, Nat. Mater. **17**, 958 (2018).

[3] C. H. L. Goodman, Ionic-covalent bonding in crystals, Nature **187**, 590 (1960).

[4] E. Mooser and W. Pearson, The ionic character of chemical bonds, Nature **190**, 406 (1961).

[5] W. Cochran, 'Effective' ionic charge in crystals, Nature **191**, 60 (1961).

[6] H. Raebiger, S. Lany, and A. Zunger, Charge self-regulation upon changing the oxidation state of transition metals in insulators, Nature **453**, 763 (2008).

[7] R. Resta, Charge states in transition, Nature **453**, 735 (2008).

[8] P. Karen, Oxidation state, a long-standing issue!, Angew. Chem. Int. Ed. **54**, 4716 (2015).

[9] L. Zhang, X. Cheng, G. Zhang, W. Qiu, H. He, and G. Chen, High active platinum clusters on titanium dioxide supports toward carbon monoxide oxidation, Appl. Catal., B **266**, 118629 (2020).

[10] Z.-Z. Wu, F.-Y. Gao, and M.-R. Gao, Regulating the oxidation state of nanomaterials for electrocatalytic CO_2 reduction, Energy Environ. Sci. **14**, 1121 (2021).

[11] K. M. Jablonka, D. Ongari, S. M. Moosavi, and B. Smit, Using collective knowledge to assign oxidation states of metal cations in metal-organic frameworks, Nat. Chem. **13**, 771 (2021).

[12] R. A. De Souza and D. N. Mueller, Electrochemical methods for determining ionic charge in solids, Nat. Mater. **20**, 443 (2021).

[13] K. Siegbahn, D. Hammond, H. Fellner-Feldegg, and E. F. Barnett, Electron spectroscopy with monochromatized x-rays, Science **176**, 245 (1972).

[14] B. J. Lindberg, K. Hamrin, G. Johansson, U. Gelius, A. Fahlman, C. Nordling, and K. Siegbahn, Molecular spectroscopy by means of ESCA II. Sulfur compounds. Correlation of electron binding energy with structure, Phys. Scr. **1**, 286 (1970).

[15] U. Gelius, Binding energies and chemical shifts in ESCA, Phys. Scr. **9**, 133 (1974).

[16] E. Sokolowski, C. Nordling, and K. Siegbahn, Chemical shift effect in inner electronic levels of Cu due to oxidation, Phys. Rev. **110**, 776 (1958).

[17] F. J. Himpsel, J. F. Morar, F. R. McFeely, R. A. Pollak, and G. Hollinger, Core-level shifts and oxidation states of Ta and W: Electron spectroscopy for chemical analysis applied to surfaces, Phys. Rev. B **30**, 7236 (1984).

[18] T. C. Kaspar, T. Droubay, S. A. Chambers, and P. S. Bagus, Spectroscopic evidence for Ag(III) in highly oxidized silver films by x-ray photoelectron spectroscopy, J. Phys. Chem. C **114**, 21562 (2010).

[19] H. Grönbeck, S. Klacar, N. M. Martin, A. Hellman, E. Lundgren, and J. N. Andersen, Mechanism for reversed photoemission core-level shifts of oxidized Ag, Phys. Rev. B **85**, 115445 (2012).

[20] M. Gajdoš, A. Eichler, and J. Hafner, Ab initio density functional study of O on the Ag(001) surface, Surf. Sci. **531**, 272 (2003).

[21] M. Schmid, A. Reicho, A. Stierle, I. Costina, J. Klikovits, P. Kostelnik, O. Dubay, G. Kresse, J. Gustafson, E. Lundgren, J. N. Andersen, H. Dosch, and P. Varga, Structure of Ag(111)$-p(4\times4)-$O: No silver oxide, Phys. Rev. Lett. **96**, 146102 (2006).

[22] G. Schön, J. Tummavuori, B. Lindström, C. Enzell, and C.-G. Swahn, ESCA studies of Ag, Ag_2O and AgO, Acta. Chem. Scand. **27**, 2623 (1973).

[23] T. Pu, H. Tian, M. E. Ford, S. Rangarajan, and I. E. Wachs, Overview of selective oxidation of ethylene to ethylene oxide by Ag catalysts, ACS Catal. **9**, 10727 (2019).

[24] M. Huš and A. Hellman, Ethylene epoxidation on Ag(100), Ag(110), and Ag(111): A joint ab initio and kinetic monte carlo study and comparison with experiments, ACS Catal. **9**, 1183 (2019).

[25] M. V. Ganduglia-Pirovano, M. Scheffler, A. Baraldi, S. Lizzit, G. Comelli, G. Paolucci, and R. Rosei, Oxygen-induced Rh $3d_{5/2}$ surface core-level shifts on Rh(111), Phys. Rev. B **63**, 205415 (2001).

[26] S. Lizzit, A. Baraldi, A. Groso, K. Reuter, M. V. Ganduglia-Pirovano, C. Stampfl, M. Scheffler, M. Stichler, C. Keller, W. Wurth, and D. Menzel, Surface core-level shifts of clean and oxygen-covered Ru(0001), Phys. Rev. B **63**, 205419 (2001).

[27] B. Hammer and J. K. Nørskov, Theoretical surface science and catalysis–calculations and concepts, in *Advances in Catalysis*, Vol. 45 (Academic Press, 2000) pp. 71–129.

[28] W. E. Kaden, T. Wu, W. A. Kunkel, and S. L. Anderson, Electronic structure controls reactivity of size-selected Pd clusters adsorbed on TiO_2 surfaces, Science **326**, 826 (2009).

[29] C. R. Henry, C. Chapon, C. Goyhenex, and R. Monot, Size effect in the CO chemisorption on palladium clusters supported on magnesium oxide, Surf. Sci. **272**, 283 (1992).

[30] B. Richter, H. Kuhlenbeck, H.-J. Freund, and P. S. Bagus, Cluster core-level binding-energy shifts: The role of lattice strain, Phys. Rev. Lett. **93**, 026805 (2004).

[31] J. Alonso, *Structure and Properties of Atomic Nanoclusters*, EngineeringPro collection (Imperial College Press, 2005).

[32] I. Aruna, B. R. Mehta, L. K. Malhotra, and S. M. Shivaprasad, Size dependence of core and valence binding energies in Pd nanoparticles: Interplay of quantum confinement and coordination reduction, J. Appl. Phys. **104**, 064308 (2008).

[33] P. S. Bagus, A. Wieckowski, and H. Freund, The contribution of lattice strain to core-level binding energy shifts in metal nanoparticles: Generality and origin of the shifts, Comput. Theor. Chem. **987**, 22 (2012).

[34] F. Loi, M. Pozzo, L. Sbuelz, L. Bignardi, P. Lacovig, E. Tosi, S. Lizzit, A. Kartouzian, U. Heiz, R. Larciprete, D. Alf è, and A. Baraldi, Breakdown of the correlation between oxidation states and core electron binding energies at the sub-nanoscale, Applied Surface Science **619**, 156755 (2023).

[35] R. Dietsche, D. C. Lim, M. Bubek, I. Lopez-Salido, G. Ganteför, and Y. D. Kim, Comparison of electronic structures of mass-selected Ag clusters and thermally grown Ag islands on sputter-damaged graphite surfaces, Appl. Phys. A **90**, 395 (2008).

[36] S. Peters, S. Peredkov, B. Balkaya, N. Ferretti, A. Savci, A. Vollmer, M. Neeb, and W. Eberhardt, Inner-shell photoionization spectroscopy on deposited metal clusters using soft x-ray synchrotron radiation: An experimental setup, Rev. Sci. Instrum. **80**, 125106 (2009).

[37] M. Taleblou, M. F. Camellone, S. Fabris, and S. Piccinin, Oxidation of gas-phase and supported Pt nanoclusters: An ab initio investigation, J. Phys. Chem. C **126**, 10880 (2022).

[38] J. P. Allen, D. O. Scanlon, and G. W. Watson, Electronic structures of silver oxides, Phys. Rev. B **84**, 115141 (2011).

[39] T. B. Rawal, S. Hong, A. Pulkkinen, M. Alatalo, and T. S. Rahman, Adsorption, diffusion, and vibration of oxygen on Ag(110), Phys. Rev. B **92**, 035444 (2015).

[40] S. Klacar, A. Hellman, I. Panas, and H. Grönbeck, Oxidation of small silver clusters: A density functional theory study, J. Phys. Chem. C **114**, 12610 (2010).

[41] L. Bianchettin, A. Baraldi, S. de Gironcoli, E. Vesselli, S. Lizzit, L. Petaccia, G. Comelli, and R. Rosei, Core level shifts of undercoordinated Pt atoms, J. Chem. Phys. **128**, 114706 (2008).

[42] T. J. Chuang, C. R. Brundle, and D. W. Rice, Interpretation of the x-ray photoemission spectra of cobalt oxides and cobalt oxide surfaces, Surf. Sci. **59**, 413 (1976).

[43] P. S. Bagus, G. Pacchioni, C. Sousa, T. Minerva, and F. Parmigiani, Chemical shifts of the core-level binding energies for the alkaline-earth oxides, Chem. Phys. Lett. **196**, 641 (1992).

[44] A. Zangwill, *Physics at Surfaces* (Cambridge University Press, 1988).

[45] J. Slater, *Quantum theory of molecules and solids*, International series in pure and applied physics No. v. 1 (McGraw-Hill, 1963).

[46] A. S. Chaves, M. J. Piotrowski, and J. L. F. Da Silva, Evolution of the structural, energetic, and electronic properties of the 3d, 4d, and 5d transition-metal clusters (30 TM_n systems for n = 2–15): a density functional theory investigation, Phys. Chem. Chem. Phys. **19**, 15484 (2017).

[47] F. J. Himpsel, F. R. McFeely, A. Taleb-Ibrahimi, J. A. Yarmoff, and G. Hollinger, Microscopic structure of the SiO_2/Si interface, Phys. Rev. B **38**, 6084 (1988).

[48] A. Pasquarello, M. S. Hybertsen, and R. Car, Si 2p core-level shifts at the Si(001)-SiO_2 interface: A first-principles study, Phys. Rev. Lett. **74**, 1024 (1995).

[49] Y. Pan, K. Sun, Y. Lin, X. Cao, Y. Cheng, S. Liu, L. Zeng, W.-C. Cheong, D. Zhao, K. Wu, Z. Liu, Y. Liu, D. Wang, Q. Peng, C. Chen, and Y. Li, Electronic structure and d-band center control engineering over M-doped CoP (M= Ni, Mn, Fe) hollow polyhedron frames for boosting hydrogen production, Nano Energy **56**, 411 (2019).

[50] Y. Cheng, H. Zhang, and X. Qu, Electronic band-engineered nanomaterials for biosafety and biomedical application, Acc. Mater. Res. **2**, 764 (2021).

[51] Y. Zhang, J. Li, J. Cai, L. Yang, T. Zhang, J. Lin, X. Wang, C. Chen, L. Zheng, C.-t. Au, B. Yang, and L. Jiang, Construction of spatial effect from atomically dispersed Co anchoring on subnanometer Ru cluster for enhanced N_2-to-NH_3 conversion, ACS Catal. **11**, 4430 (2021).

[52] Y. Zhou, X. Peng, T. Zhang, H. Cai, B. Lin, L. Zheng, X. Wang, and L. Jiang, Essential role of Ru-anion interaction in Ru-based ammonia synthesis catalysts, ACS Catal. **12**, 7633 (2022).

[53] Y. Chang, Y. Cheng, Y. Feng, K. Li, H. Jian, and H. Zhang, Upshift of the d band center toward the fermi level for promoting silver ion release, bacteria inactivation, and wound healing of alloy silver nanoparticles, ACS Appl. Mater. Interfaces **11**, 12224 (2019).

[54] J. J. Mortensen, Y. Morikawa, B. Hammer, and J. K. Nørskov, Density functional calculations of N_2 adsorption and dissociation on a Ru(0001) surface, J. Catal. **169**, 85 (1997).

[55] B. Hammer and J. K. Nørskov, Adsorbate reorganization at steps: NO on Pd(211), Phys. Rev. Lett. **79**, 4441 (1997).

[56] J. J. Mortensen, B. Hammer, and J. K. Nørskov, Alkali promotion of N_2 dissociation over Ru(0001), Phys. Rev. Lett. **80**, 4333 (1998).

[57] J. J. Mortensen, B. Hammer, and J. K. Nørskovi, A theoretical study of adsorbate-adsorbate interactions on Ru(0001), Surface Science **414**, 315 (1998).

[58] R. A. van Santen, I. Tranca, and E. J. M. Hensen, Theory of surface chemistry and reactivity of reducible oxides, Catal. Today **244**, 63 (2015).

CHAPTER 6

Asymmetric oxidation of Pt_n clusters on graphene

The oxidation method that we developed in the previous chapters successfully allowed to reach a high degree of oxidation in the Ag clusters on graphene at T = 20 K. Therefore, we decided to extend this approach to clusters composed of other materials whose oxides are of major technological relevance both as stand-alone catalysts and in combination with a C based template such as graphene. These requirements motivated us to focus the experiment described in this chapter on size-selected platinum clusters.

Pt is one of the most used and studied chemical elements in catalysis [1]. The interest in the properties of this element arose more than a century ago, with the observed reactivity of the usually inert platinum metal under aggressive chemical conditions [2]. Nowadays, the majority of platinum demand originates from its application as a catalyst in the automotive industry [3], where it is employed for the oxygen reduction reaction (ORR) [4, 5] and to oxidize uncombusted hydrocarbons and carbon monoxide present in the exhausts [6]. The advent of nanotechnology further busted the interest on this precious materials. The possibility to include it in catalysts dispersed as of single atoms, clusters or nanoparticles allows to overcome the limit imposed by Pt high cost and low abundance, taking full advantage of the high surface-to-volume ratio to optimize its use [7, 8].

In operando, Pt nanostructures undergo continuous potential fluctuations and their surfaces alternate repeatedly between metallic and oxidized states [4], suggesting that the oxide phase plays a crucial role in the reactions [9, 10]. Therefore, the oxidation process of Pt has been intensively studied for bulk [6, 9], thin films [11], surfaces [12] and nanostructures [13].

Pt bulk oxides exist mainly in five phases: PtO, Pt_3O_4, α-PtO_2, β-PtO_2 and β'-PtO_2, with an oxidation state ranging form 0 to 4+ [6]. The unique behavior of size-selected clusters makes their oxidation different from their bulk counterparts, starting from the relative stability of the different phases. Studies on the formation energy per atom for Pt_nO_n and Pt_nO_{2n} clusters revealed that their oxidation proceeds according to the sequence $Pt_n \longrightarrow Pt_nO_n \longrightarrow Pt_nO_{1.5n} \longrightarrow Pt_nO_{2n}$ [14, 15]. On the contrary, in bulk oxides the PtO phase is not thermodynamically stable [10]. Moreover, the properties of these materials are strongly related to the Pt oxidation state [16] and local environment [13]. Therefore, it is of pivotal importance to understand the oxidation process of Pt clusters at an atomic level to rationalize and further optimize Pt-based catalysts [17].

Besides a wide range of studies on reducible oxide supports such as CeO_x [18], CeO_2 [19] and TiO_2 [20], graphene has emerged as a potential template for Pt-nanostructures. In particular, the weakly interacting graphene/Ir(111) system (GR/Ir) is among the most studied ones, as the moiré-induced corrugation provides an optimal template where to anchor Pt clusters in a regular hexagonal array [21, 22]. The high stability of this system is due to a $sp^2 \longrightarrow sp^3$ rehybridization of C atoms underneath the adsorbed Pt clusters, which leads to a substantial buckling of the graphene layer itself [23].

In this thesis, we decided to focus on this substrate to study the oxidation of supported size-selected Pt_n clusters with $n = 7, 12$ and 13 exploiting the photodissociation approach at T = 20 K to provide atomic oxygen as already discussed in the previous chapters. Pt_{13} is of great interest being a magic cluster associated to increased stability, while it has been shown that the catalytic activity for the ORR significantly increases by removing just a single atom from this cluster to obtain the misshapen Pt_{12} [24, 25]. We also included Pt_7 in the experiment to have a comparison with a different and much smaller cluster, whose oxidation in the gas-phase and

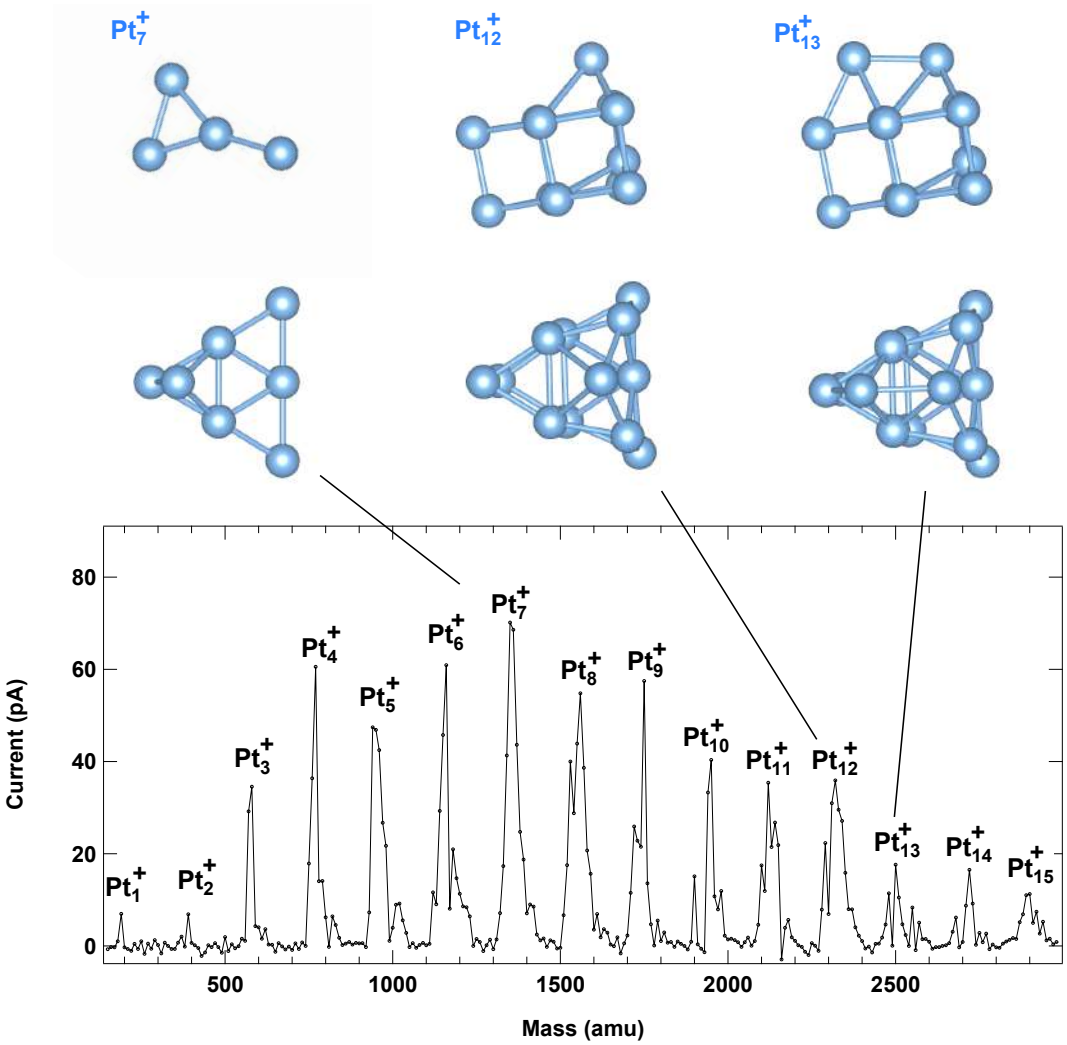

Figure 6.1: *Minimum energy configurations of the Pt_n^+ clusters in the gas-phase and mass spectrum optimized for the production of Pt_7.*

on different oxide supports was recently investigated by means of DFT calculations [14]. Our results, obtained combining synchrotron-based XPS with *ab initio* DFT calculations, indicate that the oxidized clusters reach different oxygen densities depending on their size. In particular, Pt_7 reaches the complete stoichiometry Pt_7O_7, as demonstrated by the very good agreement between experimental and theoretical 4f core level spectra. On the contrary, only a small portion of Pt_{12} and none of Pt_{13} can reach the Pt_nO_n configuration, limiting the adsorption to mostly 6 oxygen atoms. However, all the final oxidized clusters share a layered structure induced by the interaction with the buckled graphene, where the topmost atoms in the cluster reach the highest oxidation state and a geometric and electronic configuration that resembles that of Pt_3O_4 bulk oxide. This particular oxide phase has shown a high catalytic oxidation activity that can be relevant in the contexts of Pt-based automobile catalysts and in the application for gas-sensing [10].

6.1 Cluster Deposition and XPS measurements

The Pt_n^+ clusters were deposited at T = 20 K under soft-landing conditions on a GR/Ir surface, where they are electronically neutralized. With respect to the experiment with Ag clusters, we did not use Ru(0001) for the graphene growth because of an overlap between the Pt 4f and Ru 4s core levels [27]. The main difference between Gr on Ir(111) and Ru(0001) is a much less pronounced corrugation of the former with respect to the latter. In the case of the deposition of Ag cluster, this would have been a problem for the mobility of the clusters due to the very low diffusion barrier of Ag on Gr. On the contrary, the diffusion barrier for Pt is high enough to ensure the cluster stability at T = 20 K [28], also thanks to the $sp^2 \longrightarrow sp^3$ rehybridization of graphene C atoms which takes place for both the Ru(0001) [29] and Ir(111) [23] surfaces.

We performed DFT calculations to obtain the minimum energy configurations of the positively charged gas-phase clusters, which are shown in Fig. 6.1 together with a mass-spectrum optimized for the production of Pt_7. The geometries of the clusters are in agreement with previous reports [25, 30] and are dominated by a triangular motif. Pt_7 has a triangular shape, with one corner composed by two atoms displaced vertically with respect to the triangle plane. Pt_{12} is composed of two deformed 6-atom triangles stacked on top of each others, both having the central atom of one side lifted with respect to the triangle planes. Pt_{13} is the same as Pt_{12}, but with an extra atom that occupies the three-fold site of the topmost triangle. The cluster coverage was kept constant for all the depositions to about 0.14 % ML calculated with respect to the Ir(111) surface density ($\rho_s = 1.57 \times 10^{15}$ atoms cm^{-2}), which corresponds to a statistical occupation of one cluster each 9 moiré cells (about one cluster every 2000 C atoms), similarly to the deposition on GR/Ru discussed in the previous chapters.

The Pt 4f spectra acquired after each cluster deposition (photon energy of 250 eV, T = 20 K) are reported in Fig. 6.2. Each spectrum can be fitted with a spin-orbit couple of relatively broad components separated by about 3.33 eV (red lines). The fitting parameters obtained from the spectral analysis (Tab 6.1), reveal that the Pt $4f_{7/2}$ binding energy (BE) of the clusters is $\sim$ 850 meV higher than their bulk counterpart in a Pt(111) single crystal (70.92 eV) [26] (Fig. 6.3a). The Pt $4f_{7/2}$ BE Pt_{12} and Pt_{13} are very similar (71.71 and 71.73 eV), within the fitting error bar of 50

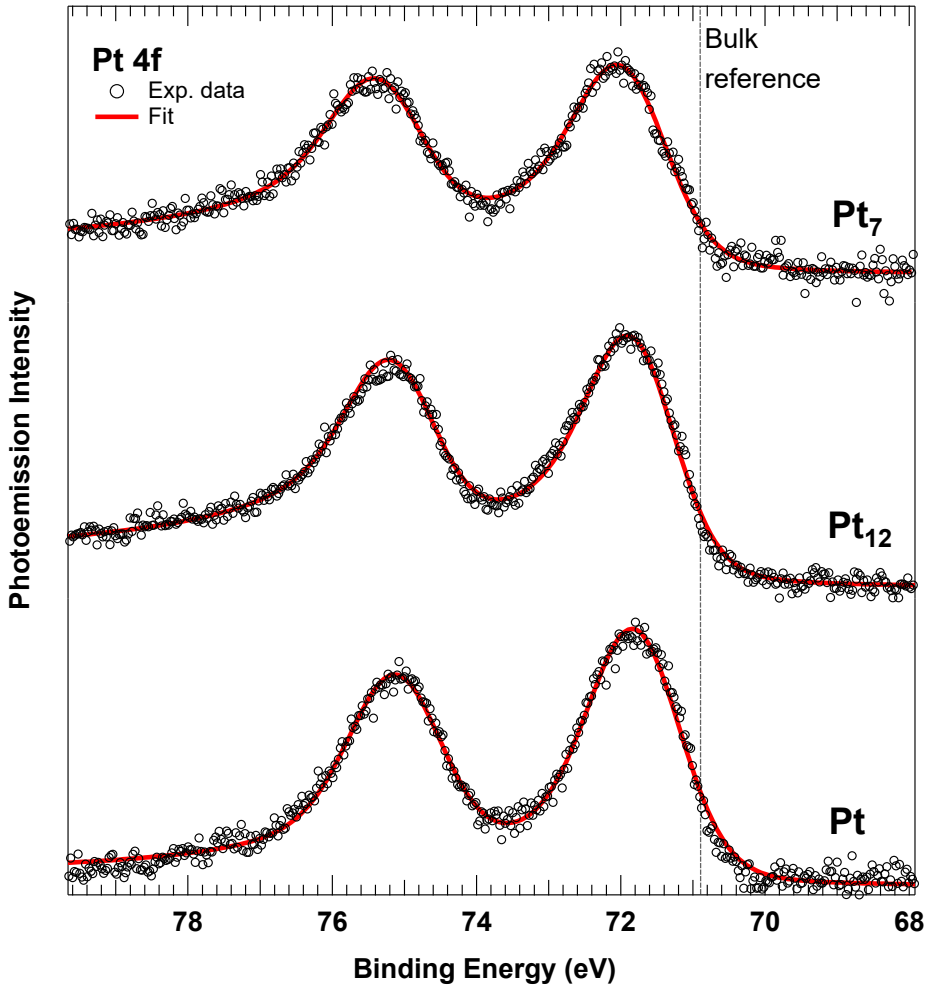

Figure 6.2: *Pt 4f XPS core levels of the as-deposited size-selected clusters acquired with a photon energy of 250 eV and at T = 20 K. The vertical dashed line indicates the BE of Pt bulk according to Ref. [26].*

	BE (eV)	Γ (eV)	G (eV)	α
Pt_{bulk} [a]	70.92	0.42	0.09	0.22
Pt_{surf} [a]	70.50	0.38	0.08	0.14
Pt_7	71.85 ± 0.05	0.32 ± 0.02	1.26 ± 0.05	0.26 ± 0.02
Pt_{12}	71.71 ± 0.05	0.30 ± 0.02	1.20 ± 0.05	0.26 ± 0.02
Pt_{13}	71.73 ± 0.05	0.29 ± 0.02	1.32 ± 0.05	0.14 ± 0.02

Table 6.1: *Fitting parameters obtained from the spectral analysis performed with Doniach-Šunjić lines.*
[a] *Ref. [26].*

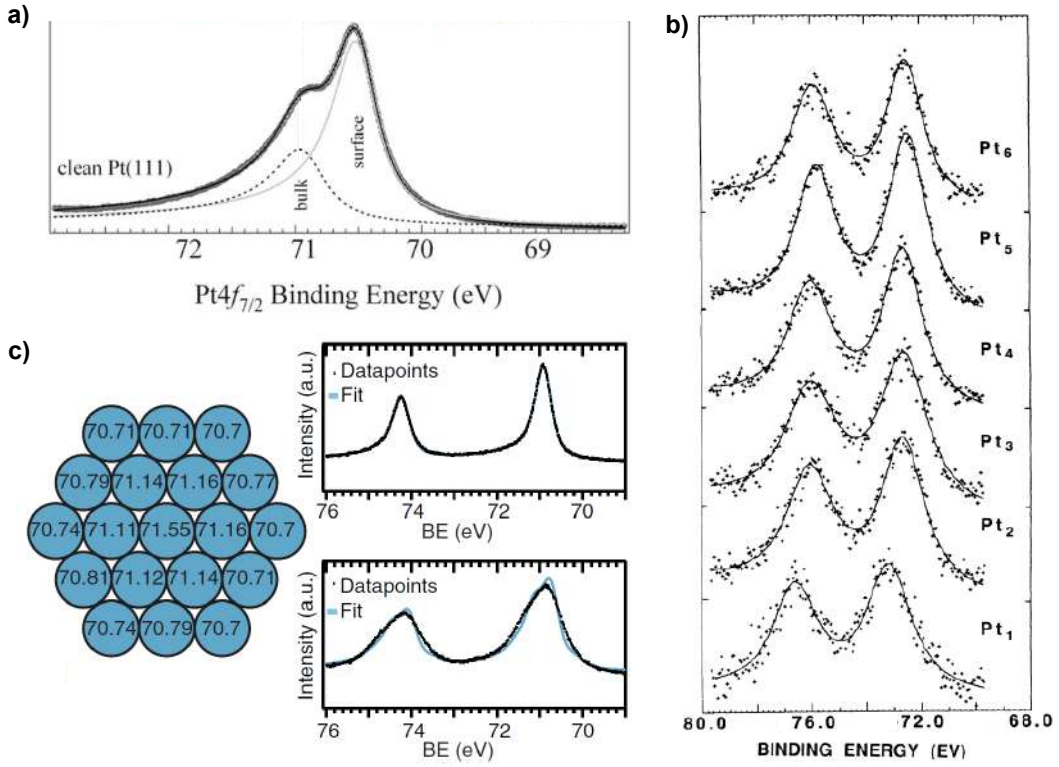

Figure 6.3: *a) Pt $4f_{7/2}$ core level spectrum of the clean Pt(111) acquired with a photon energy of 120 eV. Black dashed line and gray line indicate bulk and surface components. Adapted from [26]. b) Pt 4f core level spectrum of Pt_n clusters deposited onto an oxidized Si(100) wafer. The spectra were taken at a photon energy of 280 eV with an overall resolution of 0.6 eV. Adapted from Ref. [31]. c) On the left, calculated Pt $4f_{7/2}$ core levels for the shown Pt_{19} planar cluster. On the top right, experimental Pt 4f spectrum (dots) of single-layer Pt islands (0.5 ML) adsorbed on a clean Ir(111) surface. The light blue line shows the result of the curve fitting. The lineshape obtained from this fit was used to fit the experimental Pt 4f spectrum (dots) of 0.18 ML Pt deposited onto graphene (bottom right), with CLS fixed to the DFT calculated values. Adapted from Ref. [23].*

meV. The Pt $4f_{7/2}$ core level of Pt_7 is unambiguously shifted towards higher values and is centered at 71.85 ± 0.05 eV. The fact that mass-selected clusters show larger Pt 4f BEs with respect to their bulk counterparts is a well-known result related the a combined contribution arising from both initial- and final-state effects. Initial-state effects can arise from charge transfer between the clusters and the support: if bonding to the support transfers an electron to the clusters, the cluster BE shifts to lower energy, while if it transfers an electron from the clusters, the BE shifts to higher energy [32]. Quantum confinement [33] and lattice strain effects [34] also are initial-state effects, with shorter metallic bond lengths in the clusters that lead to an higher BE [35]. Final-state effects contribute to a blue-shift of the BEs as a consequence to the decrease of core-hole screening in small particles (relative to bulk matter) and to the size-dependent charging energy for clusters deposited on an insulating support [36]. Examples of such effects are represented by Pt_n clusters supported on a Si wafer covered by a thin native oxide [31] and on TiO_2(110) [37]. The former is one of the very first synchrotron-based XPS experiments performed on supported

size-selected clusters, and the CLSs induced by final-state effects for the Pt_n clusters ($n = 1 - 6$) with respect of the bulk reference were between 1.3 and 2.0 eV, with an inverse dependence on the cluster size (Fig. 6.3b). In the second case, the BE trend for Pt_n clusters with $n = 2 - 5, 7, 8$ was similar, although less pronounced. In this case, the authors excluded final-state contributions arising from charging effects due the conductivity of the substrate, and the Pt $4f_{7/2}$ BE of the Pt_7 cluster was found to be of 71.64 ± 0.05 eV. This value is 200 meV lower with respect to our results for the same cluster, although the different substrate may be involved. In another work, the Pt 4f core levels of clusters on our same substrate GR/Ir(111) have been studied with a combined experimental and theoretical approach exploiting the patterned growth of Pt clusters induced by the corrugated moiré lattice. Although not experimentally mass-selected, the DFT calculations for 2D islands composed of exactly 19 Pt atoms showed a $4f_{7/2}$ core level of Pt up to 71.55 eV for the fully in-plane coordinated atoms at the center of the islands, with lower values obtained for atoms closer to the edges (Fig. 6.3c) [23] . In this case, an important role in the electronic properties of the system was played by the electron transfer between Pt- and Ir-bonded C atoms that induced a $sp^2 \longrightarrow sp^3$ rehybridization of the C atoms underneath the supported clusters. Compared to our results, these values are in agreement with the trend that larger clusters show smaller BEs. However, due to the different nature of size-selected clusters and small 2D islands, a more meaningful comparison can be performed only with the support of DFT calculations.

Before moving to the the comparison with the results obtained with theoretical DFT calculations, it is worth to discuss the lineshapes of the Pt 4f spectra for different clusters and with respect to bulk Pt. In general, the clusters show much broader spectra compared to the Pt bulk and surface components measured for a Pt(111) single crystal at room temperature. In particular, the Gaussian parameter G in the clusters is in the range 1.20 - 1.32 eV, while it is smaller than 100 meV for the two components used to fit the Pt(111) spectrum. As mentioned also in the previous chapters, this effect represent a common trend for supported clusters and can be caused by the presence of nonequivalent adsorption geometries that can be obtained due to the low symmetry of the clusters [38] or by phonon broadening [31]. Another possible source of broadening can arise from the isomers that Pt clusters are known to posses [39–41].

Finally, some interesting information can be extrapolated also from the asymmetry parameter α. The α parameter in the Doniach-Šunjić function, which describes the probability to excite electron-hole pairs, is related to the density of states at the Fermi energy [42] and thus to the chemical reactivity of the system [43]. Pt_7 and Pt_{12} show the same asymmetry parameter of 0.26 ± 0.02. This value is smaller for Pt_{13} (0.14 ± 0.02), suggesting that Pt_{13} is potentially less reactive than the two other clusters. This is in agreement with the fact that $n = 13$ is a magic number for Pt clusters, for which an increased stability and lower reactivity are expected [24, 25]. Similarly to the case of size-selected Ag clusters, the different lineshapes for Pt_{12} and Pt_{13} prove that, despite the very similar Pt 4f BEs, the two systems are indeed different, assuring that mass selection is preserved upon deposition.

6.2 DFT calculations of size-selected Pt_n clusters on graphene/Ir(111)

We relied on DFT calculations to understand the electronic and geometrical modification induced on the clusters by the interaction with the substrate. In this section, we will focus on two main aspects: (i) how different rotational configurations affect the stability of the clusters and what is their role in the large Gaussian parameter of the Pt 4f core levels; (ii) how the experimental trend of the Pt 4f BEs compares with theoretical predictions.

6.2.1 Cluster rotations and interaction with the substrate

As discussed above, the large Gaussian parameter G could indicate the coexistence of different Pt configurations. A possible origin of such inhomogeneous broadening comes from rotations of the clusters on the surface due to their asymmetric morphology [38]. Therefore, the first step of our analysis was focused on a comparison of clusters adsorbed with different rotations with respect to the surface. Specifically we performed DFT calculations for four different rotations of Pt_{12} and Pt_{13} and for two rotations of Pt_7. Due to the crucial role played by the moiré lattice in the cluster stability [22, 23], we performed the calculations for the complete 10×10 graphene unit cell supported by four layers of Ir. Similarly to the case of Ag cluster adsorption on GR/Ru, the most favorite site on the surface for the adsorption of Pt clusters on GR/Ir are the *fcc* sites of the moiré lattice [22, 23]. For this reason, the calculations are performed placing the minimum energy structures of the positively charged size-selected Pt_n clusters in this preferred site and letting the system relax.

The outcomes for the structures of the GR/Ru-supported clusters are reported in Fig. 6.4, together with a top and side view of the clean GR/Ir unit cell that was used for the calculations. Next to each structure, the gas-phase configurations of each rotation are shown for comparison. In the gas-phase structure, one atom is highlighted in red to provide a reference to compare the different rotations. The adsorption energies E_a for all the considered configurations are reported in Tab 6.2, where the minimum energy rotations are highlighted in bold. Similarly to the case of Pt islands on GR/Ir, also for size-selected clusters the Pt adsorption leads to an $sp^2 \longrightarrow sp^3$ rehybridization of the graphene C atoms, as evidenced by its buckling towards the Ir(111) surface underneath the clusters. In previous works, the graphene buckling was observed also from the C 1s XPS spectrum, with the formation of small components at higher BEs [23]. However, a similar effect can also be attributed to the presence of a very low quantity of contaminants such as oxygen and water on the surface of the sample [44]. Due to the extremely low cluster coverage in our experiment, it was not possible to unambiguously appreciate the modifications induced by the clusters on the graphene C 1s spectrum.

Interestingly, the graphene rehybridization does not occur for every configuration, but only for those with the highest E_a, in particular for those where this value exceeds a threshold value of about -3 eV/atom. If we refer to the distance of the barycenter of each cluster to the plane of the Ir(111) surface (defined by the average z coordinate of the first-layer Ir atoms) as a parameter to quantify the Gr buckling (the shorter the distance, the higher the Gr buckling), we can see that it is indeed strongly related to E_a (Fig. 6.5a). In particular, the closer the cluster is to the Ir(111) surface, the higher is its adsorption energy E_a. Moreover, the adsorption energy and the Gr buckling

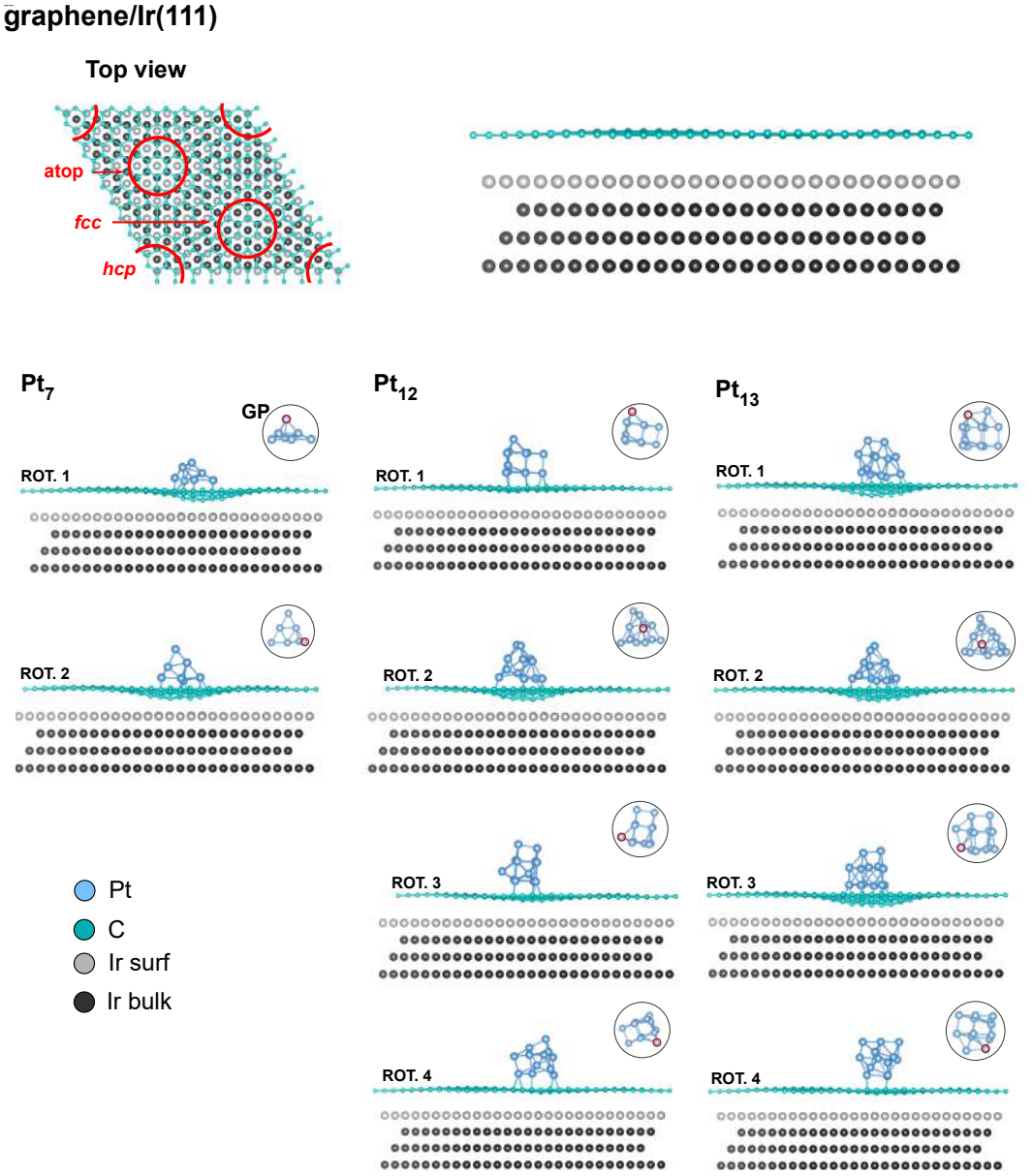

Figure 6.4: *Top and side views of the GR/Ir unit cell with the different adsorption sites indicated and minimum energy configurations of different Pt_n rotations on GR/Ir. Next to each configuration, the gas-phase (GP) rotation is shown for comparison. Black is used for Ir bulk atoms, gray for Ir surface atoms, turquoise stand for C and light blue is used for Pt. In the GP models, a Pt atom is highlighted in red to provide a reference for the rotations.*

Cluster size (n)	E_a (eV) Rot. 1	Rot. 2	Rot. 3	Rot. 4
7	**-3.85**	−3.20		
12	−2.91	**-3.32**	−2.47	−2.49
13	−3.40	**-3.82**	−3.76	−2.50

Table 6.2: *Adsorption energies (E_a) of the rotational configurations of the Pt_n clusters on the GR/Ir template considered in our calculations. The favorite rotation for each cluster is highlighted in bold.*

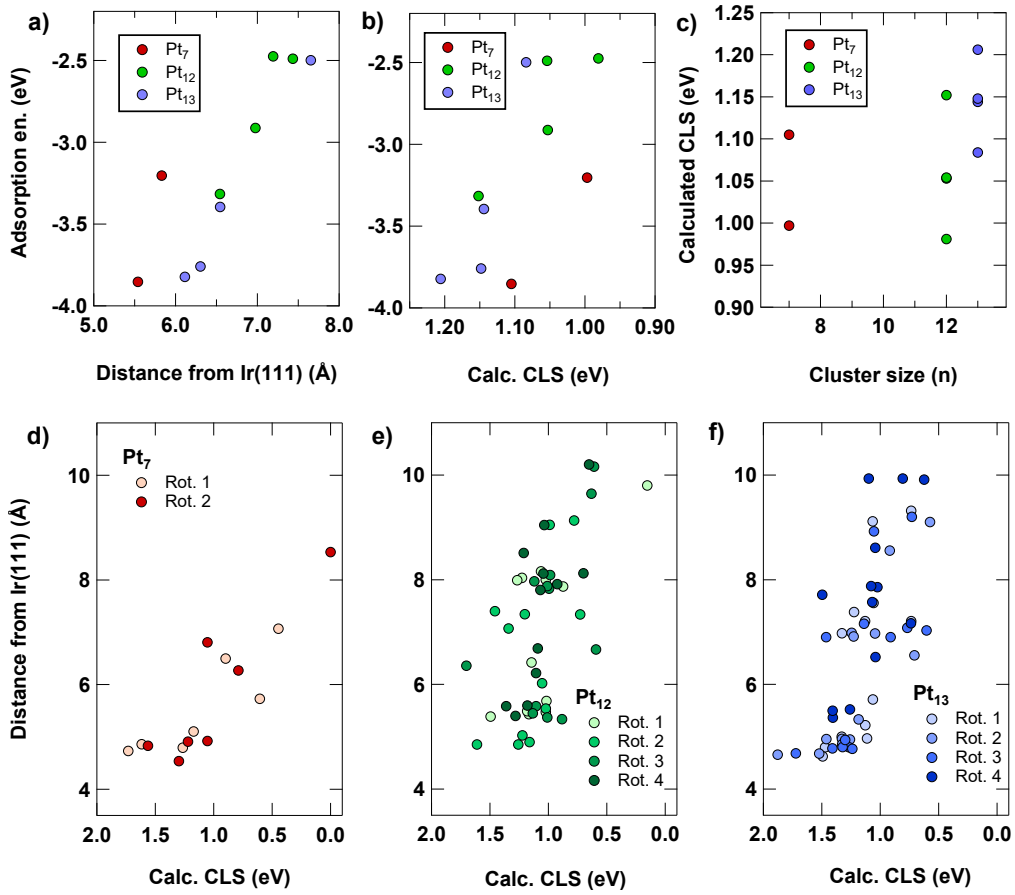

Figure 6.5: *a) Adsorption energies of the clusters in different rotational configuration as a function of the distance of their barycenter to the Ir(111) surface and b) of their DFT calculated average Pt 4f CLS. c) Comparison of theoretical DFT calculated Pt 4f CLS for different cluster sizes. d-f) Distance from the Ir(111) surface of each single atom in the clusters as a function of their Pt 4f CLS and linear fit.*

influence the Pt 4f BE of the atoms composing the clusters. Fig. 6.5b indicates that a higher E_a (and, therefore, shorter cluster-Ir(111) distances and a more pronounced buckling) leads to a greater CLS towards higher BEs. At this stage, we do not have yet a reference to turn the relative theoretical BEs into absolute values, therefore the CLSs are referred to an arbitrary reference which was set to the BE of the atom in the clusters with the lowest Pt 4f core level energy. It is important to stress that the 4f BE of the clusters can fall in a wide interval because of the different rotations, with differences that can be as high as 200 meV (Fig. 6.5b,c). The 4f BE distribution is even wider if we consider the 4f CLS of each single atom forming the clusters, where difference can be as high as 1.5 eV and with a correlation to the distance from the substrate. In particular, the Pt atoms at the cluster/graphene interface show an higher BE than the atoms in the topmost layers. This trend is consistent with the fact that the C rehybridization that takes place underneath the clusters involves an electron transfer from Pt- to Ir-bonded C atoms [22]. Therefore, Pt atoms at the interface are binding to a more electronegative C atoms that can induce a positive CLS by removing electrons from the clusters. To investigate this process, we performed a Bader charge analysis on the Pt atoms as a function of the distance

from the surface and of their Pt 4f CLS. The results, which are reported in Fig. 6.6, confirm that the atoms at the interface and with the highest CLS posses a positive charge (electron deficit) that can be as high as 0.25 e. On the contrary, the atoms on the topmost layers and with the lowest CLS show a negative charge (electron surplus) up to -0.18 e, with a similar charge redistribution that was observed for Pt cluster supported on oxides such as Co_3O_4 and TiO_2 where Pt atoms bind directly to oxygen [14]. Since these atoms have lowest CLSs, lowest coordination number and the highest electron charge, they may represent the most catalytic active sites in the clusters [37, 45].

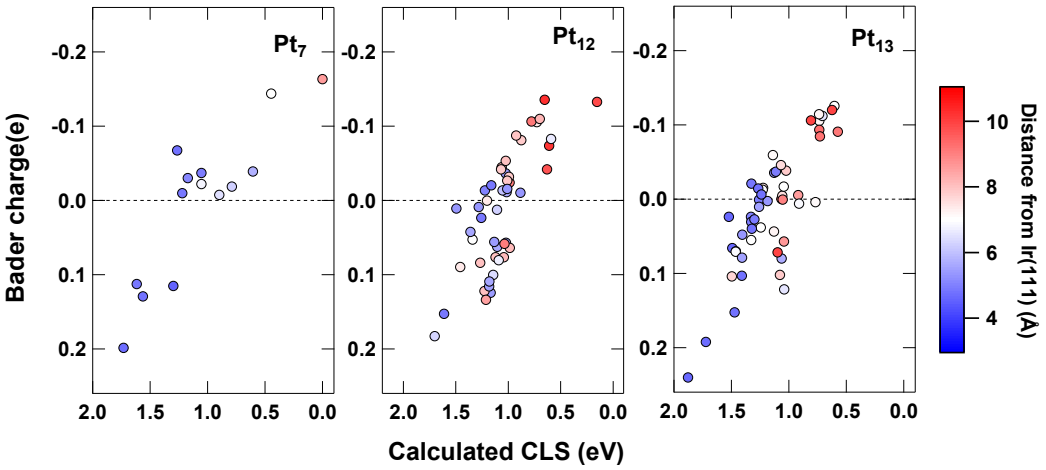

Figure 6.6: *Bader charge of each single atom forming the clusters in the different rotational configurations as a function of their Pt 4f CLS. The color scale represent their distance from the Ir(111) surface.*

The large BE dispersion of the atoms composing the clusters in different rotations can justify the G parameter obtained from the experimental analysis. In fact, given the DFT calculated E_a and the low temperature at which we performed the experiment, it is possible that more rotational configurations coexist on our surface. However, to proceed with the analysis of the experimental and theoretical data, we will focus on the configurations with the highest E_a for each cluster according to our calculations: Rotation 1 for Pt_7, Rotation 2 for Pt_{12} and Pt_{13}. This choice is motivated by the fact that the higher adsorption energy of these rotations will make them the most abundant configurations in our system.

6.2.2 Comparison with the experiment

Figure 6.7a shows a direct comparison between the experimental Pt $4f_{7/2}$ BEs (red triangles) and calculated CLS for the most favorite rotations (light blue diamonds). The two set of data are in good agreement for the relative BEs of Pt_{12} and Pt_{13}, but experiment and theory are in contrast regarding Pt_7. The experimental analysis indicates that this cluster has the highest BE of 71.85 ± 0.05 eV, while theory predicts that it has the lowest BE among the three clusters, ca. 50 meV smaller than Pt_{12}. This discrepancy is not related to the fact that we are only comparing the configurations with the highest E_a, as the trend is preserved also considering each rotation. Instead, the different trends could be related to the presence of a small amount of oxygen on the sample already upon deposition due to the relatively long deposition time, which was about 90 minutes. Despite the very good background

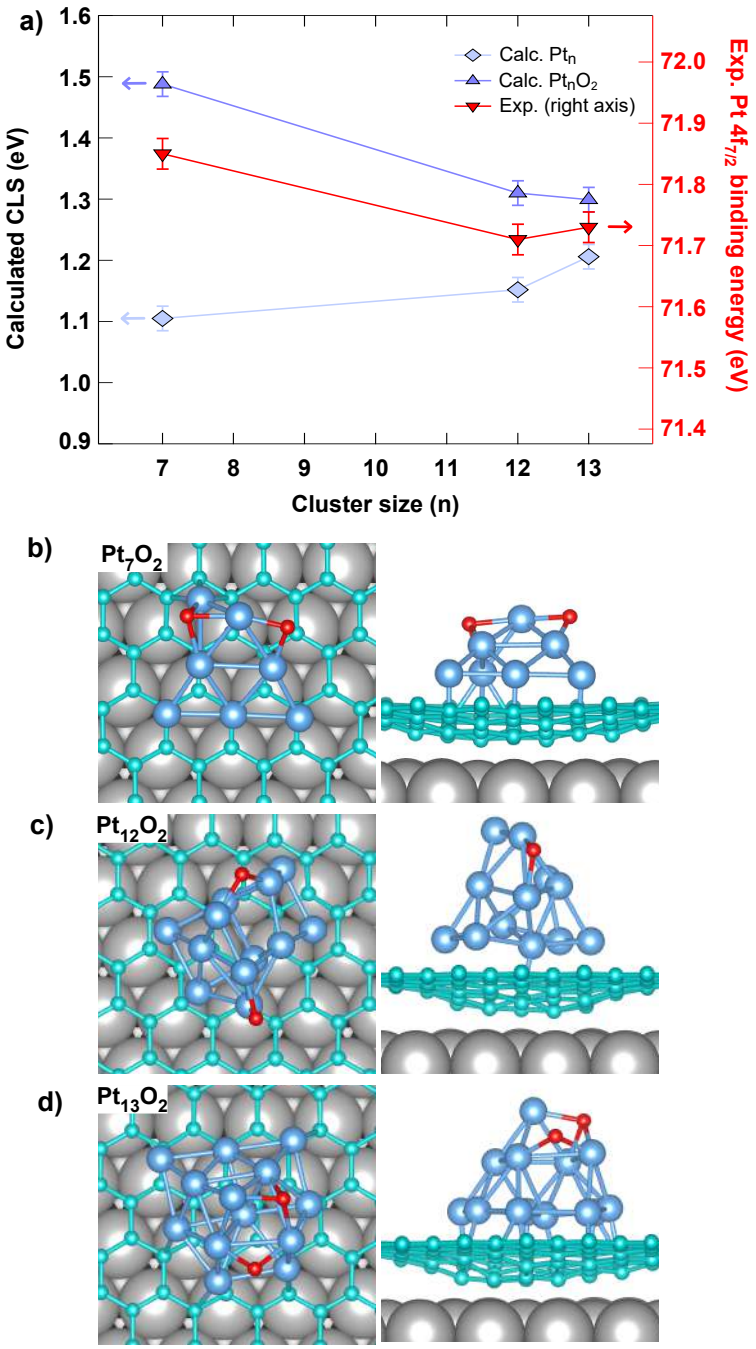

Figure 6.7: *a) Comparison of the DFT calculated Pt 4f CLS with the experimental Pt $4f_{7/2}$ BEs. b-d) Minimum energy configurations of Pt_nO_2 clusters obtained starting from the most favorite rotations on the substrate. O atoms are shown as red balls.*

pressure in the chamber ($< 1 \times 10^{-10}$ mbar), 90 minutes at such partial O_2 pressure correspond to an exposure of up to 0.05 L. As we saw in the previous chapter for the oxidation of Ag clusters, a similar amount of O_2 in our experimental conditions is enough to lead to a partial oxidation.

To verify the impact of such small amount of oxygen on the sample, we calculated the Pt 4f CLS of oxidized Pt_nO_2 cluster (Fig. 6.7b-d) and compared it with the experimental outcomes (Fig. 6.7a, blue triangles). The adsorption of 2 O atoms

leads to the largest CLS for Pt_7, whose BE increases by 380 meV with respect to its metallic counterpart. The O induced shift is smaller for Pt_{12} and Pt_{13}, and their BE increase by 160 and 90 meV, respectively. The much larger shift calculated for the smaller cluster is consistent with the fact that, given the same O coverage of 2 atoms for all the clusters, the oxygen density (amount of O atoms/cluster size) is larger for Pt_7 (0.29 O/Pt) than for the larger clusters (ca. 0.17 O/Pt). The final trend of the BEs is more similar to the experimental results, with $Ag_7 > Ag_{12} \approx Ag_{13}$, supporting the hypothesis of the presence of O on the sample.

The small oxygen contamination does not have negative implications on the main purpose of the experiment, which is the study of the maximum oxidation state of the supported clusters after a controlled exposure at T = 20 K, besides the lack of a clear experimental reference for the supported pristine clusters. However, such values can be extrapolated from the DFT calculations by aligning the calculated CLS to the experimental BEs. This can be done by comparing the different trends reported in Fig. 6.7a. The higher CLS of Pt_7 clearly suggest that some oxygen is attached to the clusters. However, considering the case of two O atoms adsorbed on each cluster, the experimental BE of Pt_{12} would result to be higher than for Pt_{13}. Since this is not the case, we can conclude that the average oxygen coverage in the as-deposited clusters is intermediate between 0 and 2 O atoms we can align the two set of data setting the experimental Pt $4f_{7/2}$ value of Pt_{13} at the center of theoretical values for Pt_{13} and $Pt_{13}O_2$, with an error bar that is half the distance between the two theoretical CLSs (50 meV).

According to this alignment, the Pt $4f_{7/2}$ BEs of the pristine clusters adsorbed in the minimum energy configurations are lower than the experimental values, and correspond to 71.58, 71.63 and 71.69 ± 0.05 eV for Pt_7, Pt_{12} and Pt_{13}, respectively. The value obtained for Pt_7 is in close agreement with the measurement performed by Ref. [37], where a BE of 71.64 ± 0.05 eV was experimentally obtained for the Pt_7 clusters supported on $TiO_2(110)$, suggesting that the reference that we used for DFT calculated CLS is reliable. The two systems are comparable despite the different substrates in light of recent calculations on the Bader charge of TiO_2-supported small Pt_4 clusters [14]. Three Pt atoms of Pt_4 at the cluster/substrate interface were calculated to have a charge between 0.02 and 0.20e, while the fourth atom, which does not directly bind with the surface, had a charge of -0.20e. These values are in good agreement with our calculations for Pt_n in our system (Fig. 6.6) and differ, for example, from the same calculations performed for Pt_4 on Co_3O_4, where the Pt atoms at the interface had a charge up to +0.5e. In this latter case, a larger CLS would be expected according to a simple model described in the Introduction of chapter 5 that links the charge in a cation to the chemical shifts [46].

With the definition of the BE reference, we accomplished the main goals that we set for the DFT calculations on the metallic clusters. A deeper comparison on the geometric and electronic structure on the partially oxidized clusters with respect to the metallic ones will be performed in the next sections, together with the analysis of the fully oxidized clusters.

6.3 Oxidation of the Pt_n clusters

The oxidation of the clusters was achieved with the same photo-dissociation approach that was described in the previous chapters to obtain atomic oxygen on the surface at T = 20 K. In particular, the clusters where exposed to 1 L of O_2, maintaining a

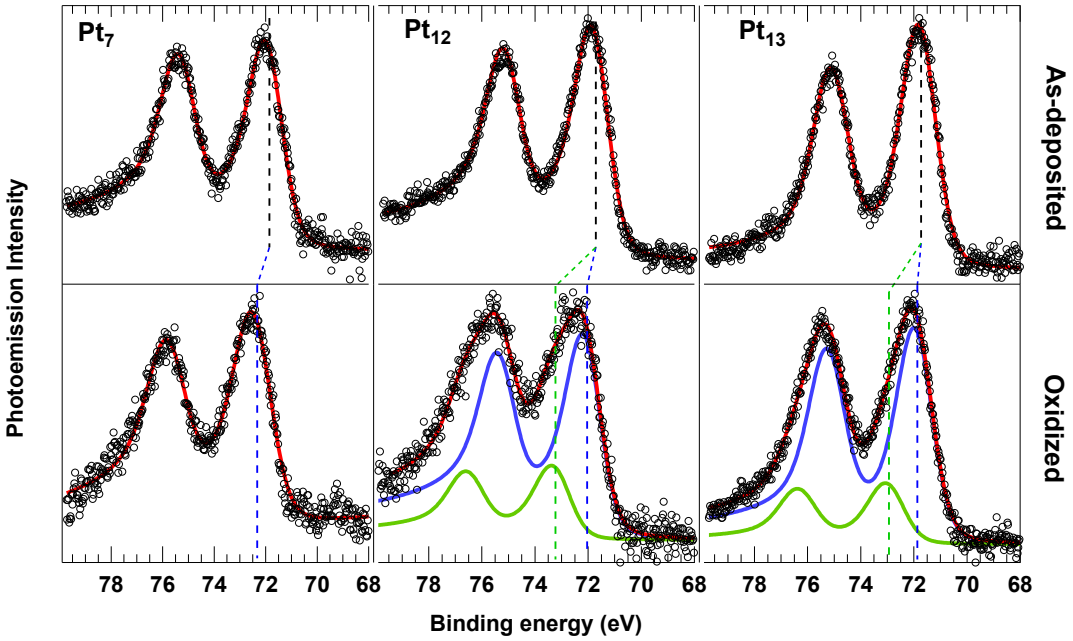

Figure 6.8: *Pt 4f XPS core levels of the as-deposited and oxidized clusters acquired with a photon energy of 250 eV and at T = 20 K.*

	As-deposited	Oxidized
Pt_7	71.85 ± 0.05	72.33 ± 0.05
Pt_{12}	71.71 ± 0.05	72.03 ± 0.05; 73.21 ± 0.05
Pt_{13}	71.73 ± 0.05	71.86 ± 0.05; 72.94 ± 0.05

Table 6.3: *Pt $4f_{7/2}$ BEs of the components obtained from the spectral analysis of the as-deposited and oxidized clusters*

partial pressure of 2×10^{-9} mbar for 665 s. The exposure was performed with the system kept under a constant flux of soft X-rays with a photon energy of 250 eV to induce the photo-dissociation. The XPS spectra of the Pt 4f core levels after the oxidation are reported in Fig. 6.8 with their spectral decomposition. The as-deposited spectra are shown again for comparison.

Upon oxidation, the Pt 4f XPS spectra shifts towards higher BEs. This is the fingerprint of the oxidation of Pt [47], and confirms the effectiveness of the photo-dissociation method at T = 20 K. In fact, the exposure to molecular oxygen at a similar temperature for a Pt(111) surface leads only to the physisorption of molecular oxygen, which does not modify the 4f BE of surface atoms [47].

The XPS spectra after the oxidation indicate different behaviors depending on the cluster size. The oxidized Pt_7 can be fitted with a single couple of large components (G = 1.45 eV) separated by 3.36 eV, with the Pt $4f_{7/2}$ component centered at 72.33 ± 0.05 eV. This is 0.5 ± 0.1 meV higher than the as-deposited and partially oxidized spectra, and 0.8 ± 0.1 meV higher than the pristine metallic value obtained from the comparison with the DFT calculations (BE = 71.58 ± 0.05). This shift is larger compared to the one induced by the (2 × 2) oxidized phase of a Pt(111) surface (CLS = 600 meV [47]), while it is similar to the Pt 4f component that was obtained

exposing a Pt(111) surface to 0.5 torr of O_2 at T = 420 K [48]. This component showed a CLS with respect to surface atoms in the range 700 - 800 meV, and it was associated to the formation of a surface oxide phase comprising square-planar PtO_4 units resembling bulk PtO. The oxidation state Pt(II) of PtO is, in fact, typically associated to a BE in the range 72 - 72.7 eV [9, 49], in very good agreement with our experimental output. Instead, the BE of the higher oxidation state Pt(IV), which composes the bulk oxide PtO_2, is generally associated higher BE in the range of 73.7 - 74.1 eV [9, 48, 49].

The Pt 4f spectra of the larger Pt_{12} and Pt_{13} are better fitted using two couple of components rather than one. If we focus on the Pt $4f_{7/2}$ components, for Pt_{12} the first peak (blue line), which corresponds to approximately 70% of the total spectral intensity, is centered at 72.03 ± 0.05 eV; the second component (green line) has a BE 1.2 eV higher and is centered at 73.21 ± 0.05 eV. Compared to the metallic value obtained from the comparison between DFT calcualted and experimental BEs (71.63 ± 0.05 eV), these components show a CLS of 0.4 ± 0.1 and 1.6 ± 0.1 eV, respectively. The trend is similar for Pt_{13}, although the CLSs are smaller. The two components that better fit the spectrum are centered at 71.86 ± 0.05 and 72.94 ± 0.05, with a ratio 4:1 in favor of the component at the lowest BE. The CLSs with respect to the metallic value (71.69 ± 0.05 eV) are 0.2 ± 0.1 and 1.3 ± 0.1 eV. The smaller shift measured for Pt_{13} compared to Pt_{12} can be related to its higher stability arising from the fact that it is composed of a magic number of atoms [24, 25]. In both cases, the component at higher BEs is centered at an intermediate position between the reported values for the oxidation state Pt(II) and Pt(IV) [49]. This may indicate the presence in our clusters of atoms with an intermediate oxidation state, similar to the ions forming the Pt_3O_4 bulk oxide. This oxide phase is composed of ions with an oxidation state of 2.67+, and since the oxidation state of Pt in Pt_3O_4 is higher than in PtO and lower than in PtO_2, an intermediate BE is expected for this oxide species [50]. In few works on oxidized Pt(111) and Pt(100) single crystals, this oxide phase was assigned to a BE of ∼ 73.6 eV [51–53], although it is not possible to distinguish this oxide phase from PtO_2 solely with experimental XPS [49]. The attribution is even more complicated when clusters are considered, since positive BE shifts with respect to bulk references may be observed due to electronic initial- and final-state effects [49]. To proceed with the analysis, we relied on DFT calculations to estimate the oxygen coverage of our clusters and to assign the correct oxidation state to the atoms composing them.

6.4 Oxygen density in the clusters

To evaluate the oxygen coverage on the clusters, we calculated the Pt 4f CLS induced by the adsorption of an increasing number m of oxygen atoms and compared it with the experimental results. In the analysis, two Pt and O atoms will be considered to be bonded if their distance is below the threshold value of 2.20 Å [6, 54], while the limit for the metallic coordination number between two Pt atoms is set to 3.2 Å [6].

Starting form the oxidation of Pt_7, whose experimental spectra indicate one single Pt $4f_{7/2}$ component centered at 72.33 ± 0.05, we performed calculations on oxidized Pt_7O_m clusters for $m = 2, 4$ and 7. The minimum energy configurations are shown in Fig.6.9, where also the metallic cluster ($m = 0$) is reported for comparison.

The adsorption of O modifies the geometry of the cluster. Clean Pt_7 has the shape of a deformed, tilted triangle composed of 6 atoms. One side of the triangle is

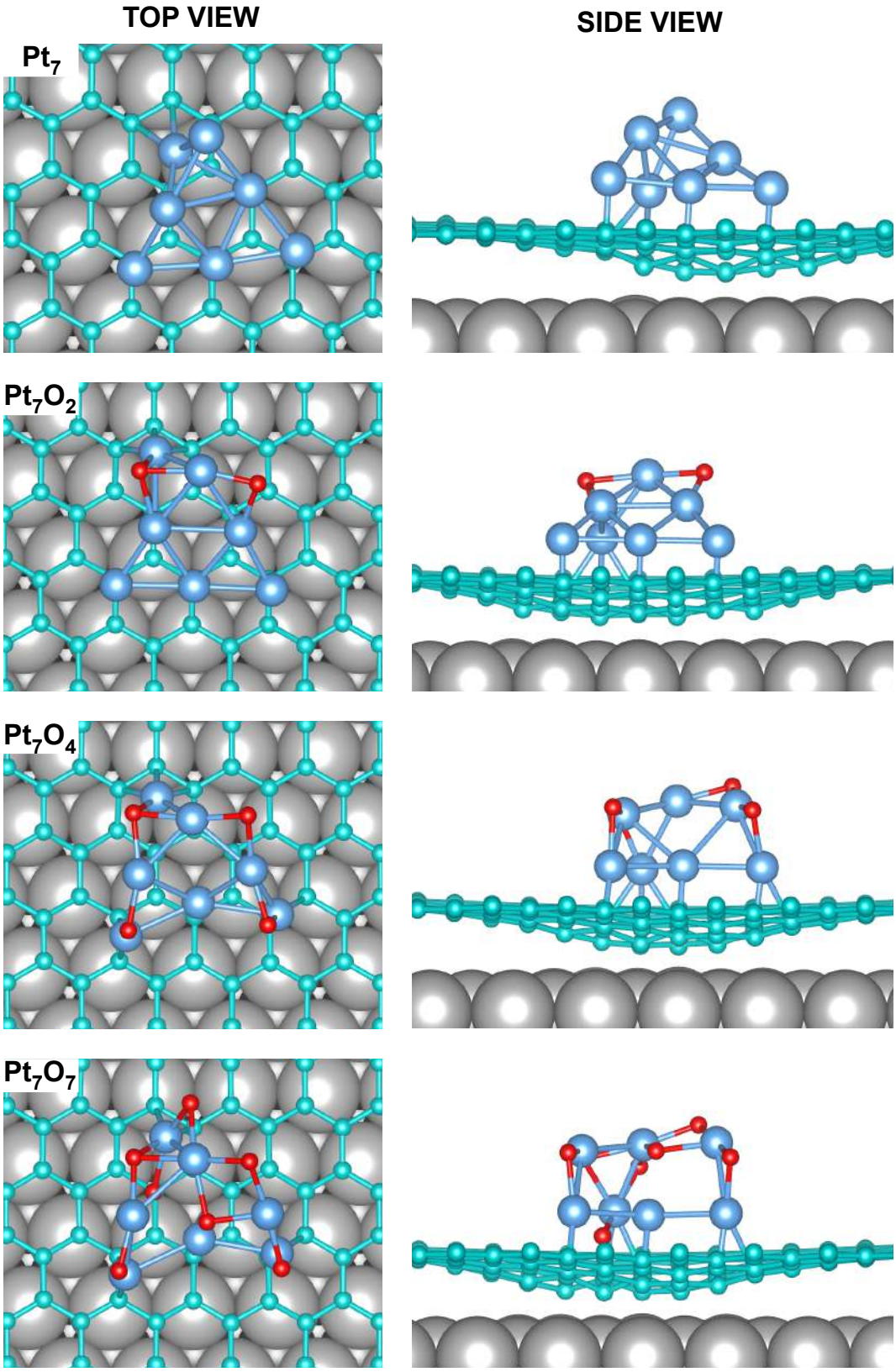

Figure 6.9: *Top and side views of the minimum energy configurations calculated for Pt_7O_m clusters for $m = 0, 2, 4 and 7$.*

formed by 3 Pt atoms adsorbed ontop on the graphene layer (Pt−C bond length of 2.13 Å). The opposite vertex is lifted from the surface plane, forming an angle of ca. 33°. The 7th atom is located underneath the lifted vertex of the triangle, adsorbed on a graphene hollow site. Upon the adsorption of two O atoms, the cluster assumes a more ordered structure, with the triangle that flattens out while preserving the same tilt of 33° with respect to the surface. It is also interesting to note that the triangle side adsorbed on the graphene ontop sites is now almost parallel with respect to the lattice vectors of graphene and of the Ir(111) surface. The Pt−C bond length of the two atoms at the triangle corners decreased to 2.08 Å, while the atom at the middle has a bond length of 2.14 Å. The Pt−Pt average distance between nearest neighbors (Fig. 6.10a) is almost unchanged, increasing from 2.59 Å to only 2.60 Å. The oxygen atoms are adsorbed in the same plane of the triangle, one in a bridge site (Pt−O bond length of 1.94 Å), the second one in an asymmetric three-fold site, with one bond length (2.10 Å) longer than the other two (2.02 and 2.05 Å). The bridge site adsorption is in agreement with previous calculations on gas-phase Pt clusters [15], while the asymmetric three-fold adsorption was studied by means of DFT calculations for larger clusters used to model a Pt(111) surface, where the different bond lengths were associated to two covalent bonds (2.01 Å) and to one donor-acceptor bond (2.21 Å) [54].

For higher oxygen density, the triangular shape is heavily deformed. The four Pt atoms bonded to graphene C atoms keep their adsorption sites, while the remaining three atoms lift up forming a second atomic layer. Now the average Pt−Pt is increased to 2.66 and 2.67 Å for Pt_7O_4 and Pt_7O_7, respectively. Also in these cases, O adsorbs mostly onto bridge sites. In Pt_7O_4, the four O atoms are in the same plane of the topmost Pt layer, with each Pt atom binding to two O in a linear O−Pt−O morphology. The Pt−O bond lengths range from 1.91 Å up to 2.03 Å (average value of 1.96 Å), depending on the O adsorption site. The three O atoms in bridge sites show a shorter Pt−O distance which is, on average, 1.91 Å. The only O atom in three-fold site (that is now symmetric) has a longer average bond length of 2.01 Å. When we move to the cluster with the highest oxygen density, we assist to the appearance of a Pt atom bonding to four O atoms, with an average Pt−O bond length of 2.03 Å. The layered structure of the cluster is preserved, with almost all the O atoms that sit in bridge sites in the topmost layer of the cluster. Only one O atom is in the bottom layer, in a bridge Pt−O−C adsorption site. Except for this atom, the trend that O atoms in bridge sites show a shorter bond length is preserved also in this case, and the average Pt−O bond length is 1.98 Å.

A direct comparison of the experimental and theoretical results show that the Pt $4f_{7/2}$ BEs of the Pt_7O_7, which contains a square-planar PtO_4 unit, is in good agreement with the experiment (Fig. 6.10b). To further compare the theoretical and experimental data at an atomic level, we built the Doniach-Šunjić lines associated to each oxidized cluster based on the lineshape obtained from the experimental analysis combined with the seven DFT calculated BEs of each single Pt atom composing the clusters. The Doniach-Šunjić line profiles obtained following this procedure are compared to the experimental spectrum in Fig. 6.11. The match between the experimental data and the spectrum obtained from the Pt_7O_7 cluster is almost perfect, indicating that this is the final configuration that we obtain in our experiment. The good match is proven by the fitting residuals shown in the figure are obtained performing a fit of the experimental data using the theoretical Doniach-Šunjić line of Pt_7O_7, with the G parameter thay was let free and the absolute values of the theo-

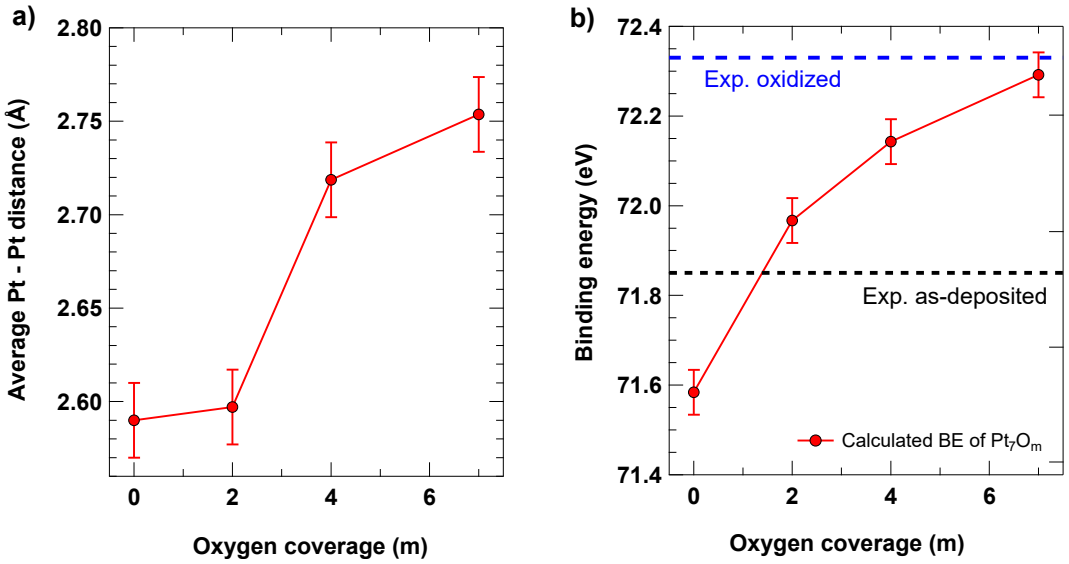

Figure 6.10: *a) Calculated average Pt−Pt distances and b) Pt $4f_{7/2}$ BEs in the Pt_7O_m clusters as a function of m. The BEs are compared to the experimental results for the as-deposited (black dashed line) and oxidized (blue dashed line) Pt_7 clusters.*

retical BEs where allowed to move within the error bar of the DFT calculations (50 meV), while the relative positions where kept fixed.

Given the correspondence between Pt_7O_7 and the experimental data, it is worth investigating the electronic properties of the atoms composing this cluster more deeply. The cluster shows an hybrid structure where the atoms on the topmost layer are bonding to an higher number of O atoms with $N_B = 2 - 4$, while $N_b \leqslant 1$ for the Pt atoms at the cluster/graphene interface. The effect on the Pt 4f BE of different N_B is shown in Fig. 6.12, where the trends of the absolute values of the Pt $4f_{7/2}$ BE and the CLS of each atom with respect to their BE in the metallic cluster are shown separately. The electronic structure of the clusters reflect their geometry, with atoms in different local morphology also having a different BEs. In particular, the Pt $4f_{7/2}$ BE of atoms in Pt_7O_7 ranges from 71.65 up to 73.14 eV, with a linear correlation to the number of oxygen bonds N_B of 0.31 eV/N_B (linear correlation coefficient = 0.72 ± 0.14). It is important to underline that the presence of nonequivalent atoms in Pt_7O_7 contributes to the large Gaussian parameter obtained from the analysis. In fact, as demonstrated in Fig. 6.11, the wide range of BEs in the cluster perfectly fits the lineshape and width of the experimental spectrum.

For the larger clusters, we proceeded in the same way as for Pt_7, studying the effects of the adsorption of an increasing number $m = 2, 4, 6$ and 8 of oxygen atoms. We also included in the calculations the structures with the stoichiometry Pt_nO_n, which are the most stable structures for clusters of this size in the gas-phase [14]. The minimum energy configurations of each oxidized cluster are displayed in Fig. 6.13, where I also included the metallic clusters for comparison. From a geometrical perspective, Pt_{12} and Pt_{13} behave in a very similar way up to $m = 6$. Oxygen is mostly adsorbed in bridge sites or, more rarely, in asymmetric three-fold sites where one of the Pt−O bond lengths is shorter than the remaining two, similarly to what we observed for Pt_7 and in agreement with previous reports [15, 54]. For $m = 4$, the O adsorption induces the formation of a zig-zag oxide stripe on the upper side of the cluster. The stripe is composed of three consecutive linear O−Pt−O sub-units which

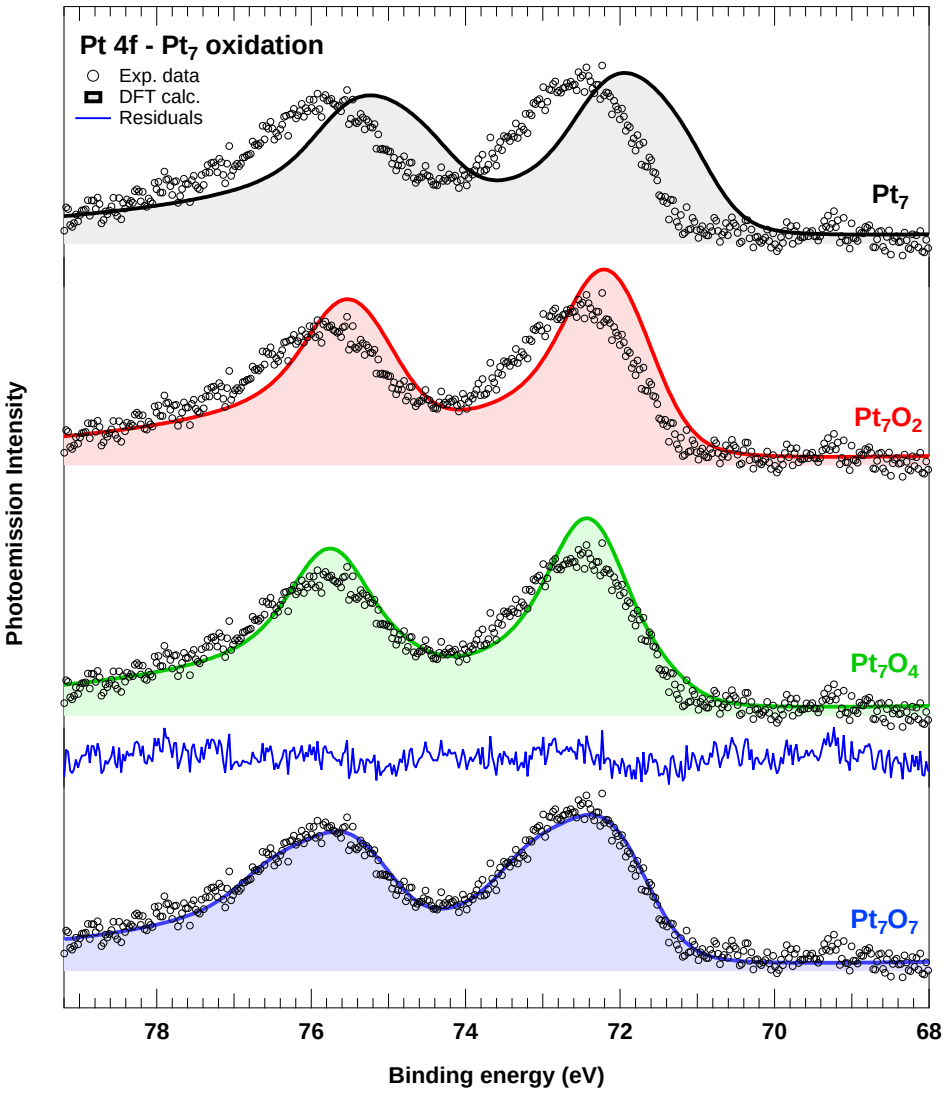

Figure 6.11: *Comparison of Doniach-Šunjić built from the theoretical calculated Pt $4f_{7/2}$ BEs of the Pt_7O_m clusters for $m = 0, 2, 4$ and 7 (filled lines) and the experimental results of the oxidized Pt_7 (empty circles). The residuals obtained by fitting the experimental data with the Pt_7O_7 theoretical spectra are reported (blue line).*

are connected with an angle of ca. 80°. For both Pt_{12} and Pt_{13}, the Pt−O bond length is shorter at the edges of the stripe (1.93 Å) and longer in the inner part (2.02 Å). When we increase m to 6, the two clusters assume very similar structures. As for Pt_7, the oxygen atoms are confined in the topmost layer of the clusters, where a Pt atom assumes the bulk-like PtO_4 local morphology and a second atom binds to three oxygen atoms. The average Pt−O bond length for the first Pt atom in both Pt_{12} and Pt_{13} is 1.97 Å, while for the second atom it decreases to 1.86 Å. For $m = 8$, the two clusters start behaving in a different way, with only Pt_{12} that undergoes a strong reconstruction. Finally, when they reach the stoichiometry Pt_nO_n, they assume a similar highly distorted structure where the top-most part of the clusters is rich in Pt atoms with $N_B = 4$ with an average Pt−O bond length of 2.01 (Pt_{12}) and 1.98

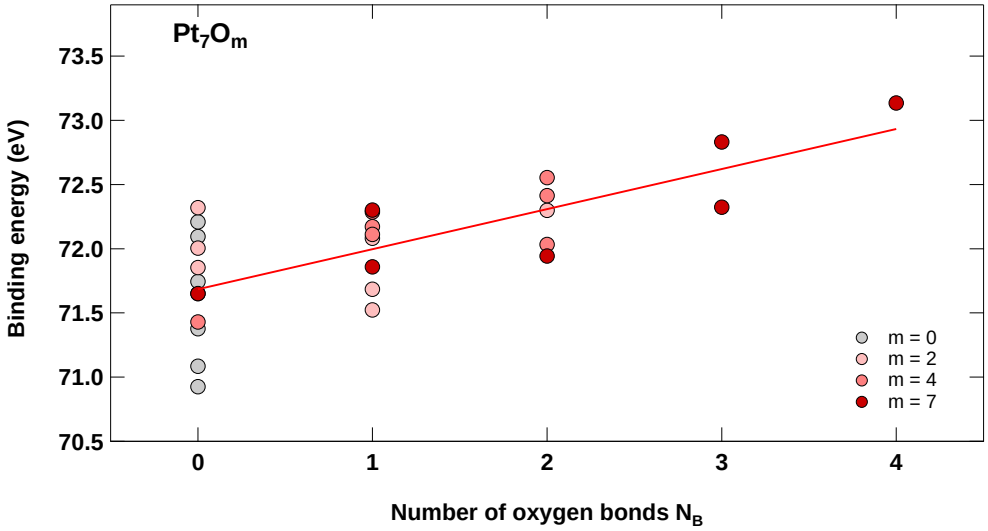

Figure 6.12: *a) DFT calculated Pt $4f_{7/2}$ BEs of the atoms composing the Pt_7O_m clusters as a function of the number of oxygen bonds N_B.*

Å (Pt_{13}).

The Pt−Pt bond lengths and Pt $4f_{7/2}$ BEs follow similar trends for the two clusters (Fig. 6.14a), but the values for Pt_{12} fluctuates in a larger range, starting from 2.61 Å for $m = 0$ and reaching 2.80 Å for the highest O density, with a total strain of +7%. For the same oxygen coverages, the strain for Pt_{13} is smaller (+5%), increasing from 2.65 to 2.79 Å.

Unlike for Pt_7, the oxygen induced Pt 4f CLS for the two clusters follows a linear trend with a slope of 80 meV/O atom (Fig. 6.14b). Since the experimental spectra showed two different components at very different BEs, we calculated the Pt $4f_{7/2}$ BEs of each atom composing the clusters to verify if some structures lead to two distinct set of atoms. These BEs are shown in Fig. 6.15a, where each horizontal line corresponds to the BE of one single atom. The BEs of the atoms in the clusters progressively increase with the oxygen coverage, but the structures with $m = 6$ clearly show two set of atoms separated by about 1.4 eV. Similarly to Pt_7, also in this case the Pt $4f_{7/2}$ BE of the atoms in the clusters increase linearly with the number of oxygen bonds N_B that they form (Fig. 6.15b). The slope for both the large clusters (330 meV/N_B and linear correlation coefficient 0.77 ± 0.08) is very similar to the one obtained for Pt_7 (310 meV N_B), with the highest BE associated to the atoms with $N_B = 4$ in square-planar PtO_4 units. The two oxidized clusters with 6 O adsorbed assume a peculiar asymmetric structure where the upper part is composed of a square-planar PtO_4 unit and of a second Pt atom with $N_B = 3$, while the remaining atoms mostly bind with 1 or 0 O atoms. Therefore, the BE on the upper part of the clusters are greatly shifted to higher values, above 73 eV, while the bottom part remains nearly unaffected and their BE is close to 72 eV. This hybrid structure is matches well with the fitting analysis we performed considering exclusively the experimental data in Fig. 6.8.

To compare in more detail the BE distributions with the experimental results, we followed the same procedure adopted for the Pt_7O_m clusters and built Doniach-Šunjić lines combining the experimental fitting parameters with the theoretical calculated Pt 4f CLSs. The results obtained with this approach is shown in Fig. 6.16. For both the

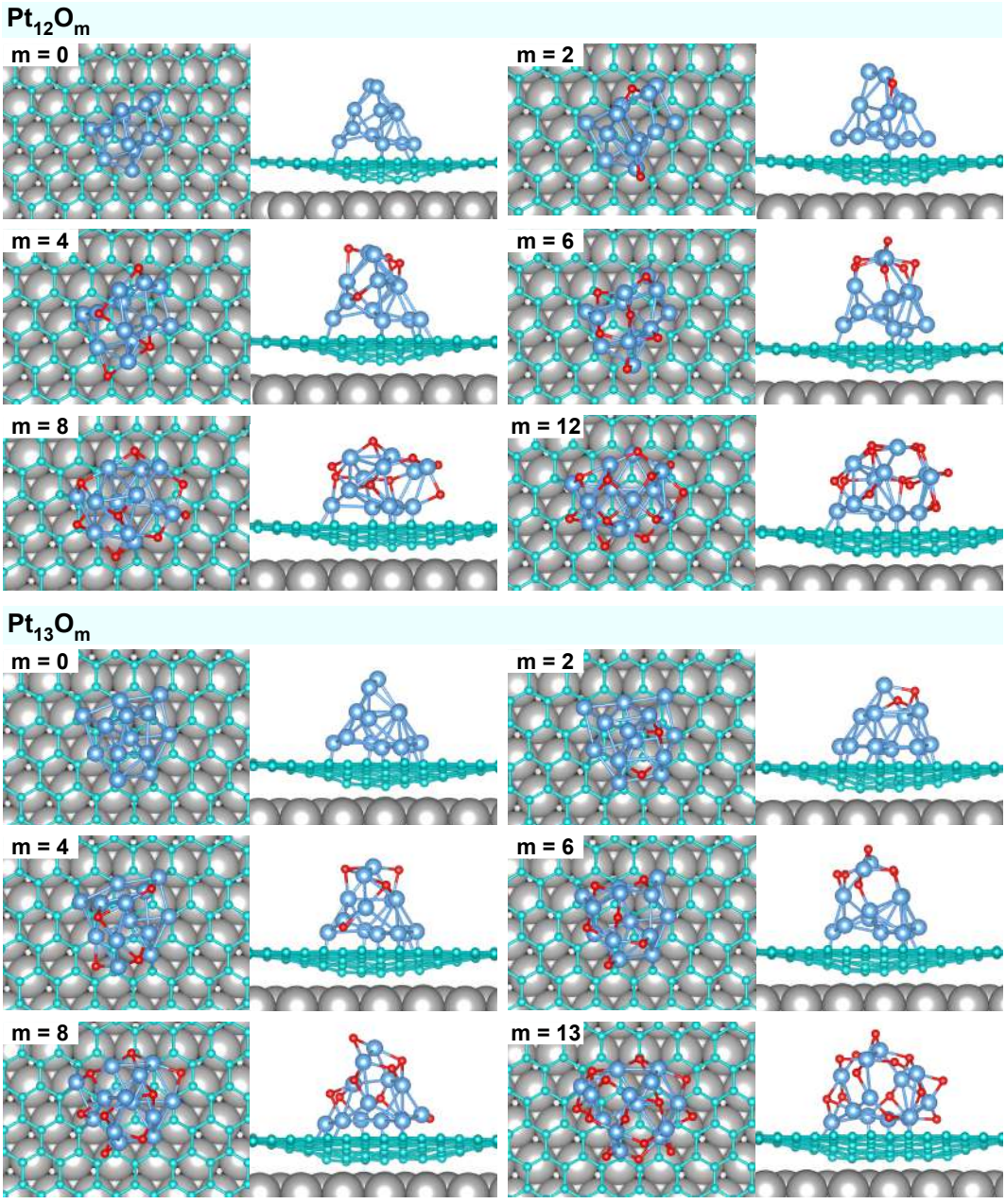

Figure 6.13: *Top and side views of the relaxed minimum energy configurations calculated for Pt_nO_m clusters for $n = 12, 13$ and $m = 0, 2, 4, 8$ and n.*

clusters, the analysis indicates that the Pt_nO_6 configurations are the most abundant in the experimental spectra. For Pt_{12}, this configuration corresponds to ca. 65% of the total spectral weight, with the remaining 35% attributed to the fully oxidzed $Pt_{12}O_{12}$. For Pt_{13}, the percentage of $Pt_{13}O_6$ reaches 85%, with a small amount of $Pt_{13}O_4$.

The different final coverage in the three clusters is consistent with previous reports on the their different oxygen affinity and stability. Pt_7 is the cluster which reaches the highest O density, as the experimental spectrum can be entirely attributed to Pt_7O_7. This agrees with previous calculations that predicted that smaller clusters are easier to oxidized compared to larger ones [14]. Similarly, Pt_{12} is more reactive than Pt_{13}

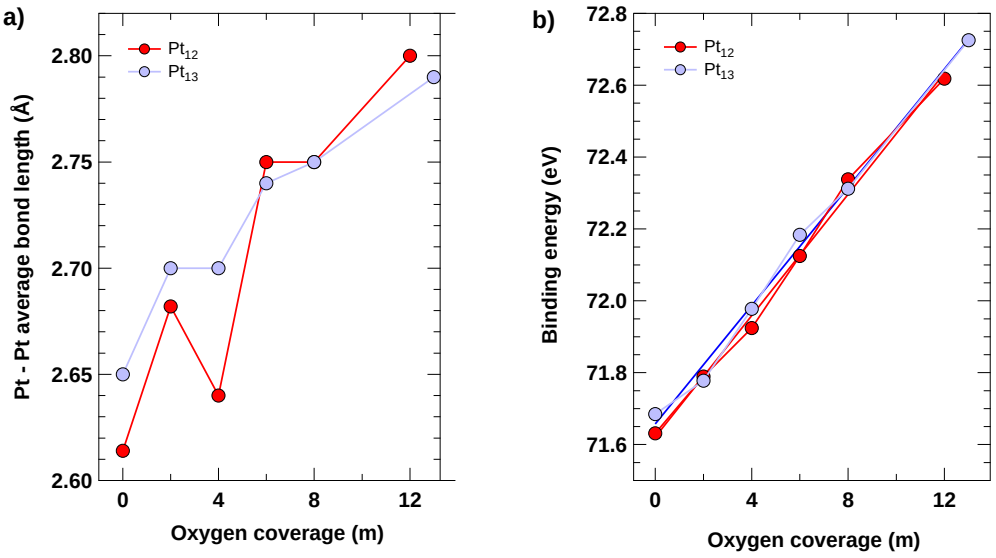

Figure 6.14: *Average calculated Pt−Pt distances and Pt $4f_{4/f}$ BEs of Pt_nO_m clusters with $n = 12, 13$ and $m = 0, 2, 4, 8$ and n.*

as a result of an electronic structure that fluctuates to a greater extent compared to that of Pt_{13} [25]. However, all the oxidized structure that fit our experimental data share the same layered geometry where the atoms in the topmost part of the clusters show the highest BEs and the largest number of oxygen bonds.

6.5 Determination of the oxidation state

The last step to complete the characterization of the oxidized clusters is the determination of the oxidation state of the atoms composing them. As mentioned earlier, an assignment based entirely on the XPS BEs cannot be performed in the case of Pt due to the similarity of the BEs associated to different oxidation states and their dependency on different environments [49]. Moreover, the square-planar PtO_4 unit is present in different phases (PtO and Pt_3O_4), and the Pt−O distances are similar for all the bulk oxides [6]. Therefore, to determine the oxidation state of the clusters we performed a Bader charge analysis. In fact, the Bader charge on Pt ions in different oxide phases is roughly proportional to the nominal value of the oxidation state. It is within 1.53 and 1.69e for α-PtO_2, within 1.62 and 1.73e for β-PtO_2, 1.13e for Pt_3O_4, and it is in the range $0.86 - 0.99e$ for PtO [10, 14]. For small size-selected Pt_n clusters in the gas-phase, the Bader charge of Pt atoms in Pt_nO_n and Pt_nO_{2n} configurations resulted to be lower compared in their bulk counterparts [14, 15]. For example, in Pt_7O_7 and Pt_7O_{14} was calculated to be 0.68 and 1.05 e/atom, respectively. In our clusters, the average Bader charge per atom assumes similar values: for Pt_7O_7, $Pt_{12}O_{12}$ and $Pt_{13}O_{13}$, it is 0.60, 0.66 and 0.63e, respectively. For $Pt_{12}O_6$ and $Pt_{13}O_6$, it decreases to 0.30 and 0.29e, which is accounted for by the reduced oxygen coverage. However, the charge is not distributed uniformly in the clusters, but it is affected by their layered structure and increases linearly with N_B (Fig. 6.17). Also in this case, the three clusters behave in very similar ways, with slopes of 0.24 e/N_B (linear correlation coefficients in the range 0.95 ± 0.06). The atoms in the Pt_7O_7 can be divided into three subsets: three atoms on the bottom layer of the

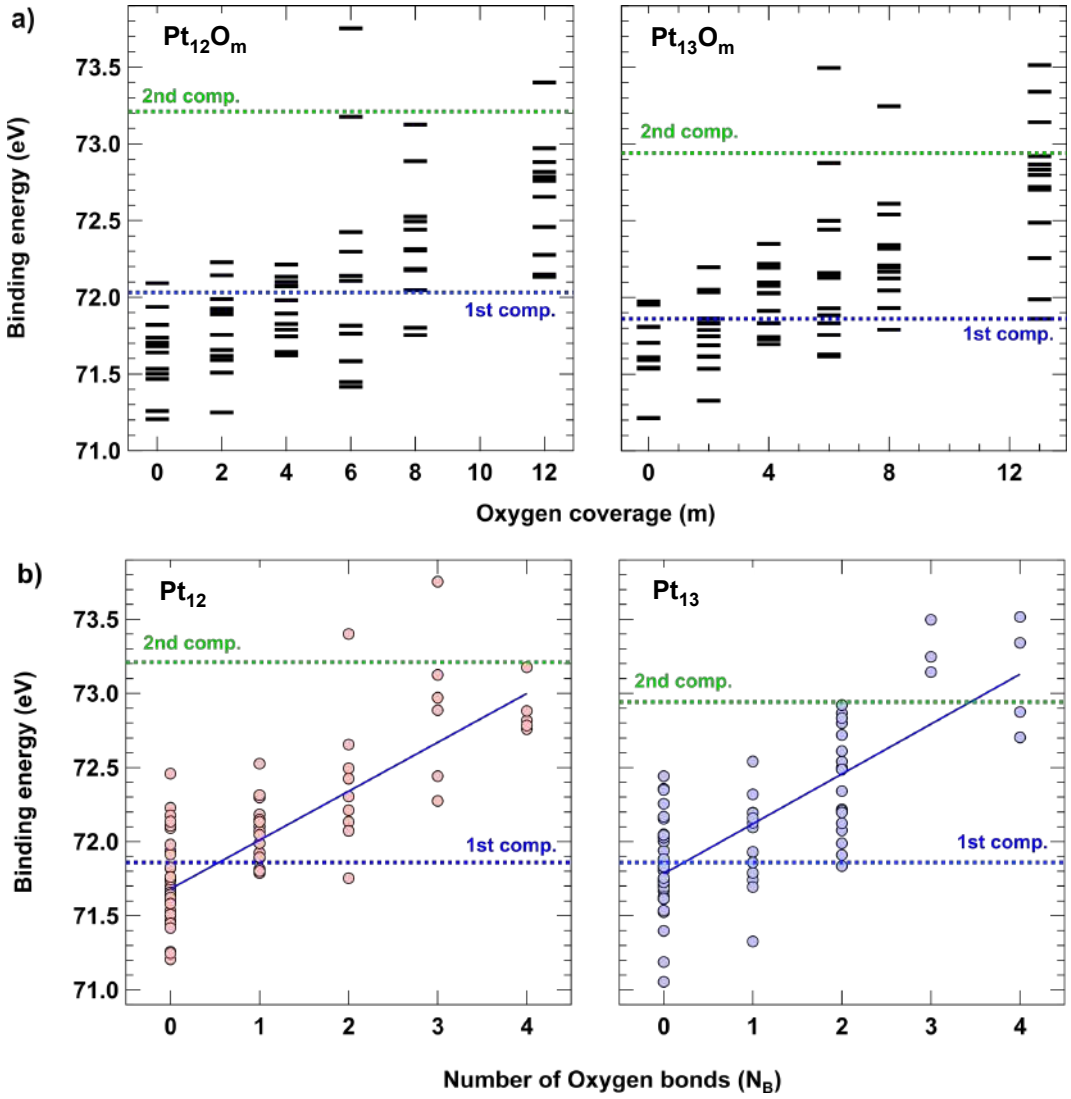

Figure 6.15: *a) DFT calculated Pt $4f_{4/f}$ BEs of each atom forming the Pt_nO_m clusters with $n = 12, 13$ and $m = 0, 2, 4, 8, n$ and b) their behavior for increasing N_B. The BEs of the two components obtained by fitting the experimental data are reported as dashed lines.*

cluster with $N_B = 0 - 1$ and a charge between 0.30 and 0.39e, three atoms with $N_B = 2 - 3$ with a charge between 0.68 and 0.82e and the atom with $N_B = 4$ with a charge of 0.95e. The values for the second subset of atoms are in agreement with previous studies on similar clusters and can be associated to an oxidation state 2+ [14, 55]. The larger positive charge and the Pt $4f_{7/2}$ BE of 73.14 ± 0.05 eV of the atom with $N_B = 4$ suggests that it has a greater oxidation state with respect to the others. In particular, these values and the local morphology of the atoms do not fit the 4+ oxidation state (whose ions possess $N_B = 6$ [6]), but match well with the configuration of Pt atoms composing the Pt_3O_4 bulk oxide. The ions in this bulk phase are in the oxidation state 2.67+ and possess a Bader charge and a Pt 4f BE that are intermediate with respect to the 2+ and 4+ oxidation states. While the Pt−O bond lengths in the different bulk oxide are very similar with each other, with DFT calculated (and experimental) values that range between 2.00 and 2.06 Å (1.97

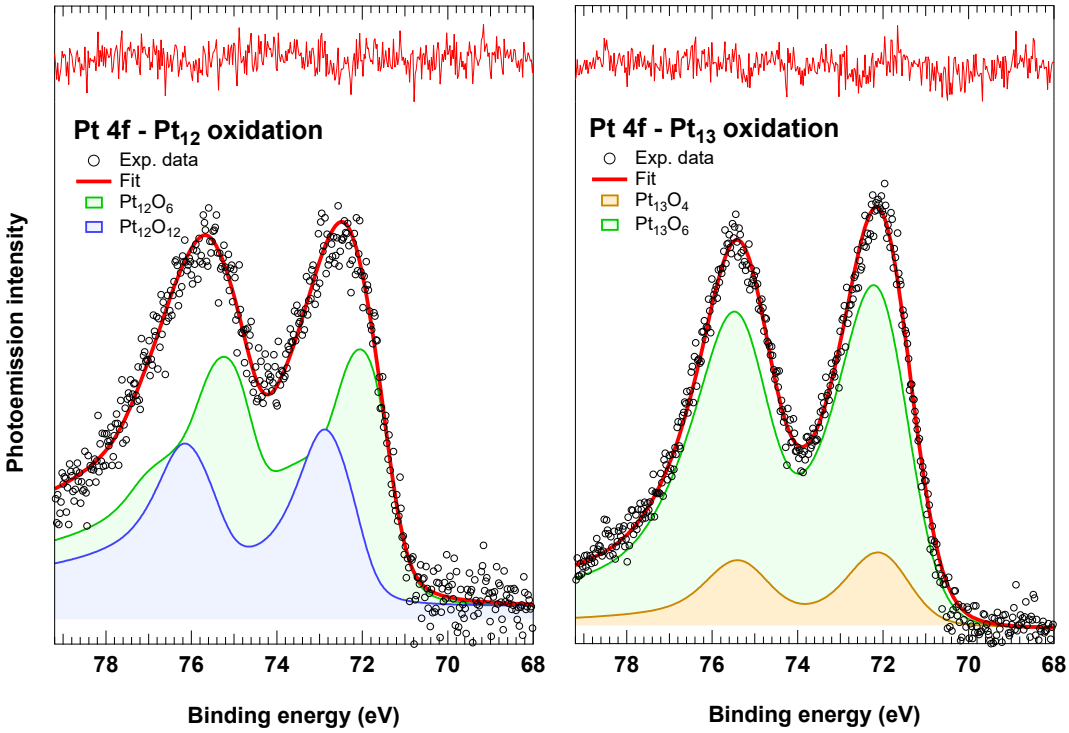

Figure 6.16: *Experimental Pt 4f XPS spectra (empty circles) acquired after the oxidation of Pt_{12} and Pt_{13} fitted with the DFT calculated BEs of the oxidized clusters (filled lines) as described in the main text.*

and 2.04 Å) [6], the Pt_3O_4 phase is characterized by a much shorter Pt−Pt bond lengths with respect to the other phases. This value was calculated (measured) to be 2.83 Å (2.79 Å) for Pt_3O_4, while it ranges between 3.10 and 3.15 Å (3.08 and 3.14 Å) for the other bulk oxides [6]. In Pt_7O_7, the average Pt−O bond length in the square-planar PtO_4 unit is 2.03 Å, whiled the Pt−Pt distance of the atom at its center to its nearest neighbors is 2.76 Å. Both these values are very similar to those calculated for Pt_3O_4. The same considerations apply to the oxidized larger clusters that better fit the experimental results, i.e. $Pt_{12}O_{12}$, $Pt_{12}O_6$ and $Pt_{13}O_6$. In this latter case the Bader charge on the atoms forming the square-planar PtO_4 units is in the range $0.96 - 1.11e$ and the average Pt−Pt distances is between 2.74 and 2.80 Å, in agreement with the values associated to Pt_3O_4.

6.6 Discussion: The substrate tunes the oxidation state

The metal-substrate interaction plays a key role in determining the electronic and geometric properties of supported size-selected clusters and nanoparticles [56–60]. In the case of Pt, the formation and stability of different oxide phases in small nanoparticles with a diameter of few nm were studied using different supports such as SiO_2, ZrO_2, and TiO_2. The result was that each support influences the morphological and thermal stability of the nanoparticles in a different way [50]. Moving to size-selected clusters, recent calculations for Pt_n in the range $n = 2 - 8$ have shown that the adsorption on TiO_2 and Co_3O_4 hinders the oxidizability compared to the gas phase [14]. Oxide supports are widely used to tune the properties of the clusters for the high interaction which can lead, for example, to charging effects that can

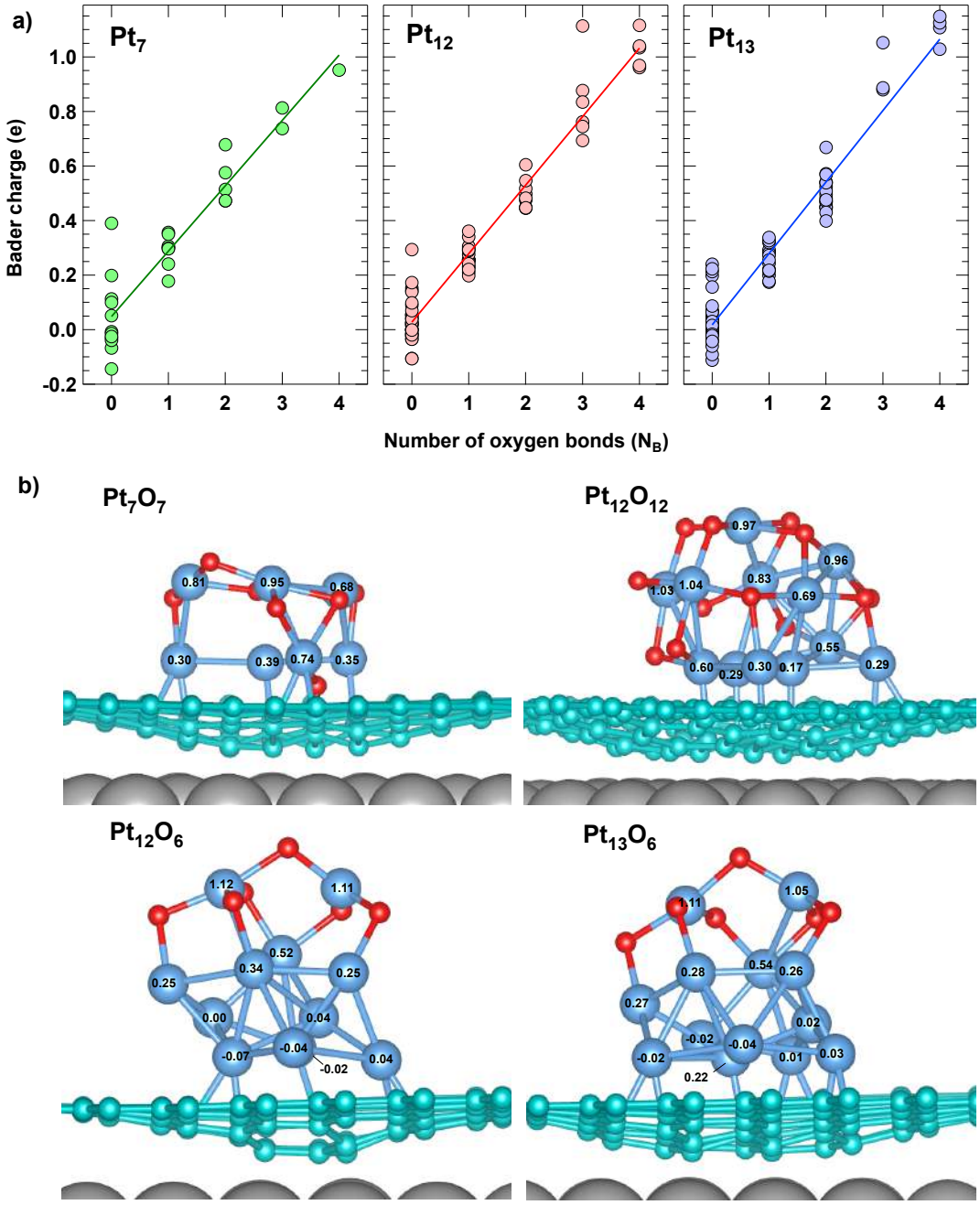

Figure 6.17: *a) Bader charge analysis for oxidized Pt_n clusters as a function of N_B. b) Zoomed view of the minimum energy configurations of Pt_7O_7, $Pt_{12}O_{12}$, $Pt_{12}O_6$ and $Pt_{13}O_6$ where the Bader charge of the Pt atoms in the clusters is reported on top of them.*

promote the chemical activity of the clusters [45]. A similar charging effect occurs in our clusters deposited on GR/Ir, thanks to the electron transfers involved in the $sp^2 \longrightarrow sp^3$ rehybridization of graphene C atoms underneath the adsorbed Pt cluster [23]. This interaction leads to an electron surplus in the topmost under-coordinated atoms in the cluster, suggesting that they could be the most reactive site on the cluster. This was observed also in the case of Pt clusters deposited on $TiO_2(110)$, where the transition from 2D to 3D structures resulted in a significant decrease in

the activation energy of the CO oxidation reaction, and the upper-layer Pt atoms were proposed to play an important role in this result [37].

To fully exploit the formation of multi-layered Pt clusters, it is much more efficient to deposit size-selected clusters rather than growing them with a conventional evaporator exploiting the regular moiré template of the GR/Ir interface. With the evaporator, besides the low control on the exact number of atoms in the clusters, the growth mostly leads to the formation of 1-layered Pt_n islands for coverage up to 0.25 ML [21]. On the contrary, the controlled deposition of mass-selected clusters leads to 3D multi-layered structures already for extremely low Pt coverage, since our result indicate that they do not flatten out upon deposition on the substrate.

In our case, the interaction with the substrate and the layered structure of the clusters leads to an asymmetry in the distribution of the oxidation state, with the topmost Pt atoms being able to reach an higher oxidation state than those at the cluster/graphene interface. In particular, our results indicate that the upper atoms can reach an oxidation state 2.66+ similar to the Pt_3O_4 oxide phase, which was reported to show surprisingly high catalytic oxidation activity [10]. The formation of an oxidation state close to 2+ rather than to 4+ (which is the most stable bulk oxide [6]) can be related to the limited size of the cluster and to the local morphology of the different oxide phases. Both PtO and Pt_3O_4 are composed of square-planar PtO_4 units, similar to those composing also the AgO bulk oxide. On the contrary, in PtO_2 Pt atoms are coordinated octahedrally by six O atoms in a three-dimensional structure. Similar 3D building blocks would require a relevant reconstruction in the clusters, which could result energetically unfavorable and hinder the formation of the oxidation state 4+. As a matter of fact, calculations on oxidized clusters have shown that even if it is possible to reach a stroichiometry of Pt_nO_{2n}, these clusters do not have the octahedral units, and the atoms composing them do not formally reach the oxidation state 4+ [14].

6.7 Conclusions

The properties of oxidized size-selected Pt_n clusters are dominated by their size, oxidation state and by the interaction with the support on which they are deposited [13, 16]. In this chapter, we studied their interaction and oxidation process on the GR/Ir interface, which is an optimal template for the cluster deposition and growth due to its corrugated morphology [22]. The cluster sizes chosen for the experiment where $n = 7, 12$ and 13 and their deposition and oxidation was studied by means of synchrotron-based XPS and *ab initio* DFT calculations. The interaction with the substrate was investigated comparing the experimental results with the calculation on different rotational configurations of the clusters on the substrate, which indicated that the most stable structure are those where the C atoms underneath the Pt clusters undergo a $sp^2 \longrightarrow sp^3$ rehybridization. According to a Bader charge analysis, this modification of the substrate induces a charge distribution in the clusters and to an electron surplus in their topmost layers.

A comparison between the experimental spectra acquired after the cluster oxidation at T = 20 K obtained with the photo-dissociation method indicates that the charge arrangement induced by the substrate promotes an asymmetric cluster oxidation. The most abundant configuration after the oxidation are represented by Pt_7O_7, $Pt_{12}O_6$ and $Pt_{13}O_6$, which share a layered structure with and increasing oxidation state for atoms that are further away from graphene. In particular the upper atoms

of the clusters reach an electronic and geometrical configuration which resembles the Pt_3O_4 bulk oxide. Due to the high catalytic oxidation activity of this oxide phase [10], we believe that these outcomes could be interesting in terms of technological applications of size-selected Pt clusters supported on GR/Ir.

References

[1] N. Tian, Z.-Y. Zhou, S.-G. Sun, Y. Ding, and Z. L. Wang, Synthesis of tetrahexahedral platinum nanocrystals with high-index facets and high electro-oxidation activity, Science **316**, 732 (2007).

[2] S. Jörgensen, Kleinere mittheilungen, Journal für Praktische Chemie **16**, 342 (1877).

[3] T. Yoshida and K. Kojima, Toyota MIRAI fuel cell vehicle and progress toward a future hydrogen society, Electrochem. Soc. Interface **24**, 45 (2015).

[4] K. Kodama, T. Nagai, A. Kuwaki, R. Jinnouchi, and Y. Morimoto, Challenges in applying highly active Pt-based nanostructured catalysts for oxygen reduction reactions to fuel cell vehicles, Nat. Nanotechnol. **16**, 140 (2021).

[5] F. Xiao, Q. Wang, G.-L. Xu, X. Qin, I. Hwang, C.-J. Sun, M. Liu, W. Hua, H.-w. Wu, S. Zhu, J.-C. Li, J.-G. Wang, Y. Zhu, D. Wu, Z. Wei, M. Gu, K. Amine, and M. Shao, Atomically dispersed Pt and Fe sites and Pt−Fe nanoparticles for durable proton exchange membrane fuel cells, Nat. Catal. **5**, 503 (2022).

[6] N. Seriani, W. Pompe, and L. C. Ciacchi, Catalytic oxidation activity of Pt_3O_4 surfaces and thin films, J. Phys. Chem. B **110**, 14860 (2006).

[7] X. Zou and Y. Zhang, Noble metal-free hydrogen evolution catalysts for water splitting, Chem. Soc. Rev. **44**, 5148 (2015).

[8] X. Ren, Q. Lv, L. Liu, B. Liu, Y. Wang, A. Liu, and G. Wu, Current progress of Pt and Pt-based electrocatalysts used for fuel cells, Sustainable Energy Fuels **4**, 15 (2020).

[9] R. Mom, L. Frevel, J.-J. Velasco-Vélez, M. Plodinec, A. Knop-Gericke, and R. Schlögl, The oxidation of platinum under wet conditions observed by electrochemical x-ray photoelectron spectroscopy, J. Am. Chem. Soc. **141**, 6537 (2019).

[10] N. Seriani, Z. Jin, W. Pompe, and L. C. Ciacchi, Density functional theory study of platinum oxides: From infinite crystals to nanoscopic particles, Phys. Rev. B **76**, 155421 (2007).

[11] J. R. McBride, G. W. Graham, C. R. Peters, and W. H. Weber, Growth and characterization of reactively sputtered thin-film platinum oxides, J. Appl. Phys. **69**, 1596 (1991).

[12] M. A. van Spronsen, J. W. M. Frenken, and I. M. N. Groot, Observing the oxidation of platinum, Nat. Commun. **8**, 429 (2017).

[13] J. Ke, W. Zhu, Y. Jiang, R. Si, Y.-J. Wang, S.-C. Li, C. Jin, H. Liu, W.-G. Song, C.-H. Yan, and Y.-W. Zhang, Strong local coordination structure effects on subnanometer PtO_x clusters over CeO_2 nanowires probed by low-temperature CO oxidation, Acs Catal. **5**, 5164 (2015).

[14] M. Taleblou, M. F. Camellone, S. Fabris, and S. Piccinin, Oxidation of gas-phase and supported Pt nanoclusters: An ab initio investigation, J. Phys. Chem. C **126**, 10880 (2022).

[15] Y. Xu, W. A. Shelton, and W. F. Schneider, Thermodynamic equilibrium compositions, structures, and reaction energies of Pt_xO_y (x = 1-3) clusters predicted from first principles, J. Phys. Chem. B **110**, 16591 (2006).

[16] L. Zhang, X. Cheng, G. Zhang, W. Qiu, H. He, and G. Chen, High active platinum clusters on titanium dioxide supports toward carbon monoxide oxidation, Appl. Catal., B **266**, 118629 (2020).

[17] A. Mahata, A. S. Nair, and B. Pathak, Recent advancements in Pt-nanostructure-based electrocatalysts for the oxygen reduction reaction, Catal. Sci. Technol. **9**, 4835 (2019).

[18] P. Li, X. Chen, L. Ma, A. Bhat, Y. Li, and J. W. Schwank, Effect of ce and la dopants in Co_3O_4 nanorods on the catalytic activity of CO and C_3H_6 oxidation, Catal. Sci. Technol. **9**, 1165 (2019).

[19] L. Nie, D. Mei, H. Xiong, B. Peng, Z. Ren, X. I. P. Hernandez, A. DeLaRiva, M. Wang, M. H. Engelhard, L. Kovarik, A. K. Datye, and Y. Wang, Activation of surface lattice oxygen in single-atom Pt/CeO_2 for low-temperature CO oxidation, Science **358**, 1419 (2017).

[20] L. DeRita, S. Dai, K. Lopez-Zepeda, N. Pham, G. W. Graham, X. Pan, and P. Christopher, Catalyst architecture for stable single atom dispersion enables site-specific spectroscopic and reactivity measurements of CO adsorbed to Pt atoms, oxidized Pt clusters, and metallic Pt clusters on TiO_2, J. Am. Chem. Soc. **139**, 14150 (2017).

[21] N. Podda, M. Corva, F. Mohamed, Z. Feng, C. Dri, F. Dvorák, V. Matolin, G. Comelli, M. Peressi, and E. Vesselli, Experimental and theoretical investigation of the restructuring process induced by CO at near ambient pressure: Pt nanoclusters on graphene/Ir(111), Acs Nano **11**, 1041 (2017).

[22] Y. Du, D. Yi, and X. Wang, Carbon-rehybridization-induced templated growth of metal nanoclusters on graphene moiré patterns, Carbon **192**, 295 (2022).

[23] J. Knudsen, P. J. Feibelman, T. Gerber, E. Grånäs, K. Schulte, P. Stratmann, J. N. Andersen, and T. Michely, Clusters binding to the graphene moiré on Ir(111): X-ray photoemission compared to density functional calculations, Phys. Rev. B **85**, 035407 (2012).

[24] T. Imaoka, H. Kitazawa, W.-J. Chun, S. Omura, K. Albrecht, and K. Yamamoto, Magic number Pt_{13} and misshapen Pt_{12} clusters: Which one is the better catalyst?, J. Am. Chem. Soc. **135**, 13089 (2013).

[25] K. Miyazaki and H. Mori, Origin of high oxygen reduction reaction activity of Pt_{12} and strategy to obtain better catalyst using sub-nanosized Pt-alloy clusters, Sci. Rep. **7**, 45381 (2017).

[26] L. Bianchettin, A. Baraldi, S. de Gironcoli, E. Vesselli, S. Lizzit, L. Petaccia, G. Comelli, and R. Rosei, Core level shifts of undercoordinated Pt atoms, J. Chem. Phys. **128**, 114706 (2008).

[27] J. Moulder and J. Chastain, *Handbook of X-ray Photoelectron Spectroscopy: A Reference Book of Standard Spectra for Identification and Interpretation of XPS Data* (Physical Electronics Division, Perkin-Elmer Corporation, 1992).

[28] X. Liu, Y. Han, J. W. Evans, A. K. Engstfeld, R. J. Behm, M. C. Tringides, M. Hupalo, H.-Q. Lin, L. Huang, K.-M. Ho, D. Appy, P. A. Thiel, and C.-Z. Wang, Growth morphology and properties of metals on graphene, Progress in Surface Science **90**, 397 (2015).

[29] D. Yi, W. Zhao, and F. Ding, Stable AA-stacked Pt nanoclusters supported on graphene/Ru(0001) and the selective catalysis: A theoretical study, ACS Appl. Nano Mater. **2**, 2921 (2019).

[30] A. S. Chaves, G. G. Rondina, M. J. Piotrowski, P. Tereshchuk, and J. L. F. Da Silva, The role of charge states in the atomic structure of Cu_n and Pt_n (n = 2-14 atoms) clusters: A DFT investigation, J. Phys. Chem. A **118**, 10813 (2014).

[31] W. Eberhardt, P. Fayet, D. M. Cox, Z. Fu, A. Kaldor, R. Sherwood, and D. Sondericker, Photoemission from mass-selected monodispersed Pt clusters, Phys. Rev. Lett. **64**, 780 (1990).

[32] W. E. Kaden, T. Wu, W. A. Kunkel, and S. L. Anderson, Electronic structure controls reactivity of size-selected Pd clusters adsorbed on TiO_2 surfaces, Science **326**, 826 (2009).

[33] I. Aruna, B. R. Mehta, L. K. Malhotra, and S. M. Shivaprasad, Size dependence of core and valence binding energies in pd nanoparticles: Interplay of quantum confinement and coordination reduction, J. Appl. Phys. **104**, 064308 (2008).

[34] B. Richter, H. Kuhlenbeck, H.-J. Freund, and P. S. Bagus, Cluster core-level binding-energy shifts: The role of lattice strain, Phys. Rev. Lett. **93**, 026805 (2004).

[35] P. S. Bagus, A. Wieckowski, and H. Freund, The contribution of lattice strain to core-level binding energy shifts in metal nanoparticles: Generality and origin of the shifts, Comput. Theor. Chem. **987**, 22 (2012).

[36] C. R. Henry, C. Chapon, C. Goyhenex, and R. Monot, Size effect in the CO chemisorption on palladium clusters supported on magnesium oxide, Surf. Sci. **272**, 283 (1992).

[37] Y. Watanabe, X. Wu, H. Hirata, and N. Isomura, Size-dependent catalytic activity and geometries of size-selected pt clusters on TiO_2(110) surfaces, Catal. Sci. Technol. **1**, 1490 (2011).

[38] S. Peters, S. Peredkov, B. Balkaya, N. Ferretti, A. Savci, A. Vollmer, M. Neeb, and W. Eberhardt, Inner-shell photoionization spectroscopy on deposited metal clusters using soft x-ray synchrotron radiation: An experimental setup, Rev. Sci. Instrum. **80**, 125106 (2009).

[39] E. T. Baxter, M.-A. Ha, A. C. Cass, A. N. Alexandrova, and S. L. Anderson, Ethylene dehydrogenation on $Pt_{4,7,8}$ clusters on Al_2O_3: Strong cluster size dependence linked to preferred catalyst morphologies, Acs Catal. **7**, 3322 (2017).

[40] H. Zhai and A. N. Alexandrova, Fluxionality of catalytic clusters: When it matters and how to address it, Acs Catal. **7**, 1905 (2017).

[41] R. H. Lavroff, H. W. T. Morgan, Z. Zhang, P. Poths, and A. N. Alexandrova, Ensemble representation of catalytic interfaces: soloists, orchestras, and everything in-between, Chem. Sci. **13**, 8003 (2022).

[42] S. Doniach and M. Sunjic, Many-electron singularity in x-ray photoemission and x-ray line spectra from metals, J. Phys. C: Solid State Phys. **3**, 285 (1970).

[43] R. Van Santen and M. Neurock, Concepts in theoretical heterogeneous catalytic reactivity, Catalysis Reviews **37**, 557 (1995).

[44] R. Larciprete, S. Fabris, T. Sun, P. Lacovig, A. Baraldi, and S. Lizzit, Dual path mechanism in the thermal reduction of graphene oxide, J. Am. Chem. Soc. **133**, 17315 (2011).

[45] B. Yoon, H. Häkkinen, U. Landman, A. S. Wörz, J.-M. Antonietti, S. Abbet, K. Judai, and U. Heiz, Charging effects on bonding and catalyzed oxidation of CO on Au_8 clusters on MgO, Science **307**, 403 (2005).

[46] B. J. Lindberg, K. Hamrin, G. Johansson, U. Gelius, A. Fahlman, C. Nordling, and K. Siegbahn, Molecular spectroscopy by means of ESCA II. Sulfur compounds. Correlation of electron binding energy with structure, Phys. Scr. **1**, 286 (1970).

[47] C. Puglia, A. Nilsson, B. Hernnäs, O. Karis, P. Bennich, and N. Mårtensson, Physisorbed, chemisorbed and dissociated O_2 on Pt(111) studied by different core level spectroscopy methods, Surf. Sci. **342**, 119 (1995).

[48] D. J. Miller, H. Öberg, S. Kaya, H. Sanchez Casalongue, D. Friebel, T. Anniyev, H. Ogasawara, H. Bluhm, L. G. M. Pettersson, and A. Nilsson, Oxidation of Pt(111) under near-ambient conditions, Phys. Rev. Lett. **107**, 195502 (2011).

[49] L. K. Ono, B. Yuan, H. Heinrich, and B. R. Cuenya, Formation and thermal stability of platinum oxides on size-selected platinum nanoparticles: Support effects, J. Phys. Chem. C **114**, 22119 (2010).

[50] L. K. Ono, J. R. Croy, H. Heinrich, and B. Roldan Cuenya, Oxygen chemisorption, formation, and thermal stability of Pt oxides on Pt nanoparticles supported on SiO_2/Si(001): Size effects, J. Phys. Chem. C **115**, 16856 (2011).

[51] K. Kuribayashi and S. Kitamura, Preparation of Pt-PtO_x thin films as electrode for memory capacitors, Thin Solid Films **400**, 160 (2001).

[52] J. F. Weaver, H. H. Kan, and R. B. Shumbera, Growth and properties of high-concentration phases of atomic oxygen on platinum single-crystal surfaces, J. Phys.: Condens. Matter **20**, 184015 (2008).

[53] C. R. Parkinson, M. Walker, and C. F. McConville, Reaction of atomic oxygen with a Pt(111) surface: chemical and structural determination using XPS, CAICISS and LEED, Surf. Sci. **545**, 19 (2003).

[54] T. Jacob, R. P. Muller, and W. A. Goddard, Chemisorption of atomic oxygen on Pt(111) from DFT studies of Pt-clusters, J. Phys. Chem. B **107**, 9465 (2003).

[55] Y. Xu, R. B. Getman, W. A. Shelton, and W. F. Schneider, A first-principles investigation of the effect of Pt cluster size on CO and NO oxidation intermediates and energetics, Phys. Chem. Chem. Phys. **10**, 6009 (2008).

[56] E. C. Tyo and S. Vajda, Catalysis by clusters with precise numbers of atoms, Nature Nanotechnology **10**, 577 (2015).

[57] S. Vajda and M. G. White, Catalysis applications of size-selected cluster deposition, ACS Catal. **5**, 7152 (2015).

[58] B. S. Mitchell, A. Chirila, J. A. Kephart, A. C. Boggiano, S. M. Krajewski, D. Rogers, W. Kaminsky, and A. Velian, Metal-support interactions in molecular single-site cluster catalysts, J. Am. Chem. Soc. **144**, 18459 (2022).

[59] I. T. Ghampson, G.-N. Yun, A. Kaneko, V. Vargheese, K. K. Bando, T. Shishido, and S. T. Oyama, Effect of support and Pd cluster size on catalytic methane partial oxidation to dimethyl ether using a NO/O_2 shuttle, ACS Catal. **12**, 11190 (2022).

[60] J. Jašík, S. Valtera, M. Vaidulych, M. Bunian, Y. Lei, A. Halder, H. Tarábková, M. Jindra, L. Kavan, O. Frank, S. Bartling, and S. Vajda, Oxidative dehydrogenation of cyclohexene on atomically precise subnanometer $Cu_{4-n}Pd_n$ ($0 \leq n \leq 4$) tetramer clusters: the effect of cluster composition and support on performance, Faraday Discuss. **242**, 70 (2023).

CHAPTER 7

Oxidation of Fe_n clusters: trends and stoichiometry

An alternative approach to overcome the prohibitive cost and low abundance of precious metals, such as Pt, in catalysis is to replace them (entirely or in part) with cheaper elements with an improved cost-to-efficiency ratio [1, 2]. In this respect, Fe-based nanostructures are particularly promising [3–5].

The catalytic properties of Fe are known and have being exploited for decades. Its main applications comes from the production of ammonia (NH_3) in the Haber-Bosch process [6–8]. Various metals have been shown to catalyze this vital reaction, which is used to produce NH_3 at a scale of roughly 150 million tons per year for a variety of applications [9]. However, Fe is widely used especially for its low cost and high abundance [10]. The mechanism of the Fe-catalyzed Haber-Bosch process is generally described through a complete reduction of N_2 into nitrides on Fe surface sites [11]. In the reaction, N_2 and H_2 are combined to form NH_3, with Fe that is able to provide the six electrons which are needed to fully reduce N_2 [12]. However, this process requires high pressure ($\sim$100 bar) and high temperature ($\sim$ 700 K) [2] due to the required compromise between thermodynamic equilibrium and kinetics [13]. On the contrary, Fe-based nanostructures composed of Fe_3 clusters anchored on the θ-Al_2O_3(010) surface were recently proposed to overcome this limitation thanks to the large spin polarization, low oxidation state of Fe, and multi-step redox capability of Fe_3 clusters [14].

The applications of Fe at the nanoscale are not limited to the Haber-Bosch process. Atomically precise Fe clusters on N-doped carbon and pyrolyzed Fe-N-carbon catalyst exhibits excellent acidic oxygen reduction reaction activity [15, 16]. Moreover, Fe_2 clusters supported on mesoporous carbon nitride have shown superior performance for alkene epoxidation [17].

Prior to these recent applications as supported catalysts, Fe_n clusters have been intensively studied in the gas-phase with many experimental techniques and by means of theoretical calculations [19]. The first attempts to experimentally probe the Fe cluster electronic structure dates back to 1995, when Wang and co-workers used a higher resolution magnetic bottle photoelectron spectrometer to study the clusters in the gas-phase [18] (Fig. 7.1). Such experiment showed a clear dependency of the photoelectron spectral features on the cluster size. This pioneering study, combined with the peak distribution observed in time-of-flight mass spectra [20] was crucial to propose the first geometric structures for the clusters and to identify the magic numbers of Fe_n, which correspond to $n = 7, 13, 15, 19$ and 23. The progress

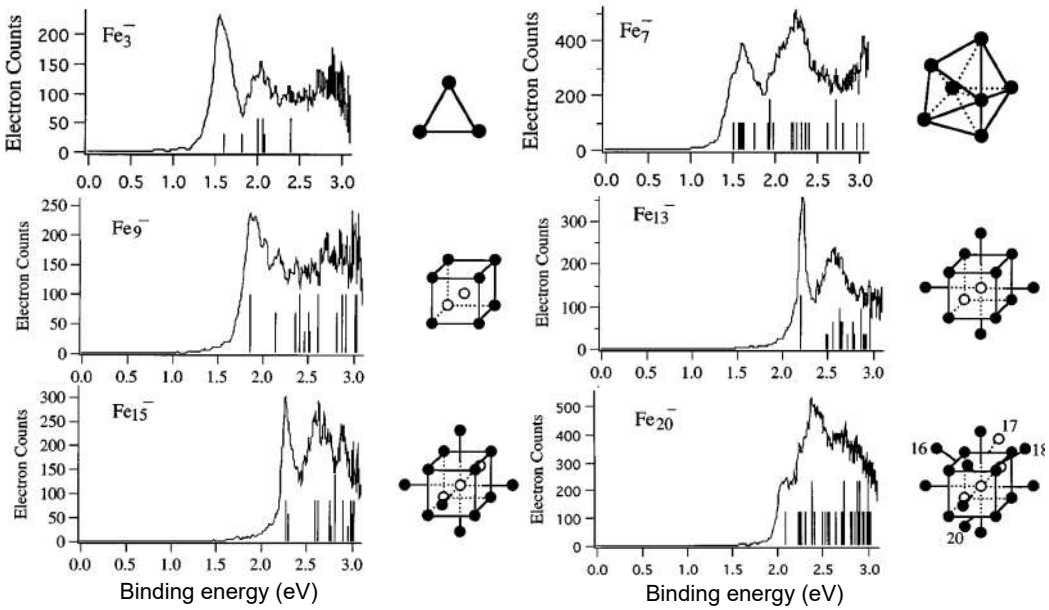

Figure 7.1: *Photoelectron spectra of Fe_n^- clusters with $n = 3, 7, 9, 13, 15$ and 20 at 3.49 eV photon energy. The sticks in the spectra are calculated occupied energy levels for the structures next the each graph. The stick height is proportional to the orbital degeneracy and occupancy. Adapted from Ref. [18].*

in the experimental characterization was paralleled and supported by theory, which confirmed the experimentally assigned magic numbers by means of DFT calculations on their structure [21], relative stability and fragmentation energy [22]. As a matter of fact, the magic numbers follow the geometric structure of the cluster. For example, the structure of the highly stable Fe_{13} is a complete close-packed icosahedron [19, 21], which is a geometry generally associated to high stability [23]. Similarly, also Fe_{15} has the shape of an icosahedron, but with the two 5-atom rings that are replaced by rings of 6 atoms.

More recently, joint experimental and theoretical investigations have been focused on Fe_n oxide clusters, which stand out for their potential applications in an even wider range of fields than their metallic counterparts. In particular, they are of great interest for several reactions such as the oxidation of carbon monoxide [24], the water splitting [25], the Water Gas Shift reaction [26] and for their potential application in fuel cells [27]. Similarly to Pt clusters, the relative stability of the oxide phases are different for size-selected clusters than in larger scales. In particular, the FeO oxide phase is not thermodynamically stable as a bulk material [28], and the FeO phase is only an intermediate step in the oxidation of Fe(100), Fe(111) and Fe(110) surfaces, where it rapidly further oxidized to Fe_2O_3 [29, 30]. On the contrary, mass spectra of $Fe_nO_m^+$ clusters revealed that the stoichiometric species with $n = m$ are predominant for $n < 10$, while the Fe-to-O ratio only slightly increases for $10 \leq m \leq 20$ ($Fe_nO_{n+1}^+$) and for $21 \leq m \leq 30$ ($Fe_nO_{n+2}^+$) [31]. Therefore, a relevant effort has been dedicated to the structural optimization of $(FeO)_n$ clusters by means of DFT calculations for $n = 1 - 16$ [32–34]. $(FeO)_{12}$ was found to be a turning point between the formation of cage structures ($n < 12$) and the chemisorption of oxygen atoms on triangular Fe facets on the cluster surface (Fig. 7.3). For this reason, $(FeO)_{12}$ was further studied,

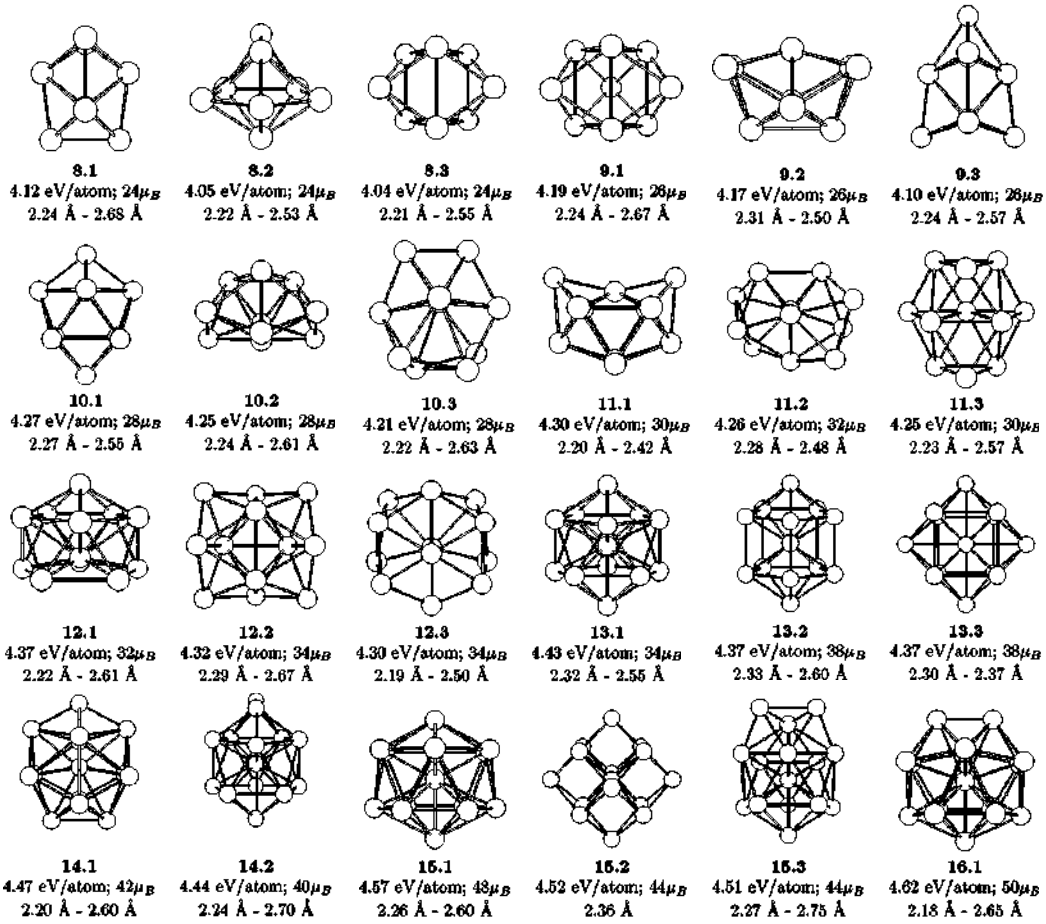

Figure 7.2: *DFT calculated geometries of Fe_n clusters for $n = 8-16$ in the minimum energy configurations and for few isomers. Their binding energies, total magnetic moments, and nearest neighbor distances are also reported. Adapted from [21].*

and the most recent results report that this cluster shows a cage-shaped geometry and an unexpected stability, with an extremely large energy gap (2.00 eV) which is greater than that of C_{60}, Au_{20} and Al_{13}^- clusters [35].

Compared to their metallic counterparts, and despite their interesting potential applications, experimental studies on oxidized Fe clusters are limited to the gas-phase [36–38]. This represents a fundamental approach to study these systems and provides a benchmark for theoretical works, but it is still far from the complexity of supported catalysts. In this regard, a necessary step towards technological applications is the transition from the gas-phase to supported clusters [39]. In this chapter, I will discuss our results on the oxidation of Fe_n clusters ($n = 11, 12, 13, 15$ and 20) supported on GR/Ru. The experiment follows the same pattern adopted in the previous chapters, with the Fe_n clusters that are produced with ENAC and deposited directly on the sample located in the SuperESCA experimental chamber to perform *in situ* XPS with synchrotron radiation. The oxidation (performed at T = 20 K with the photo-induced dissociation of O_2) leads to a homogeneous structure in the clusters where all the atoms can be associated to the oxidation state 2+, similar to the FeO bulk oxide phase. This confirms the trend observed in the gas-phase, since the oxidation

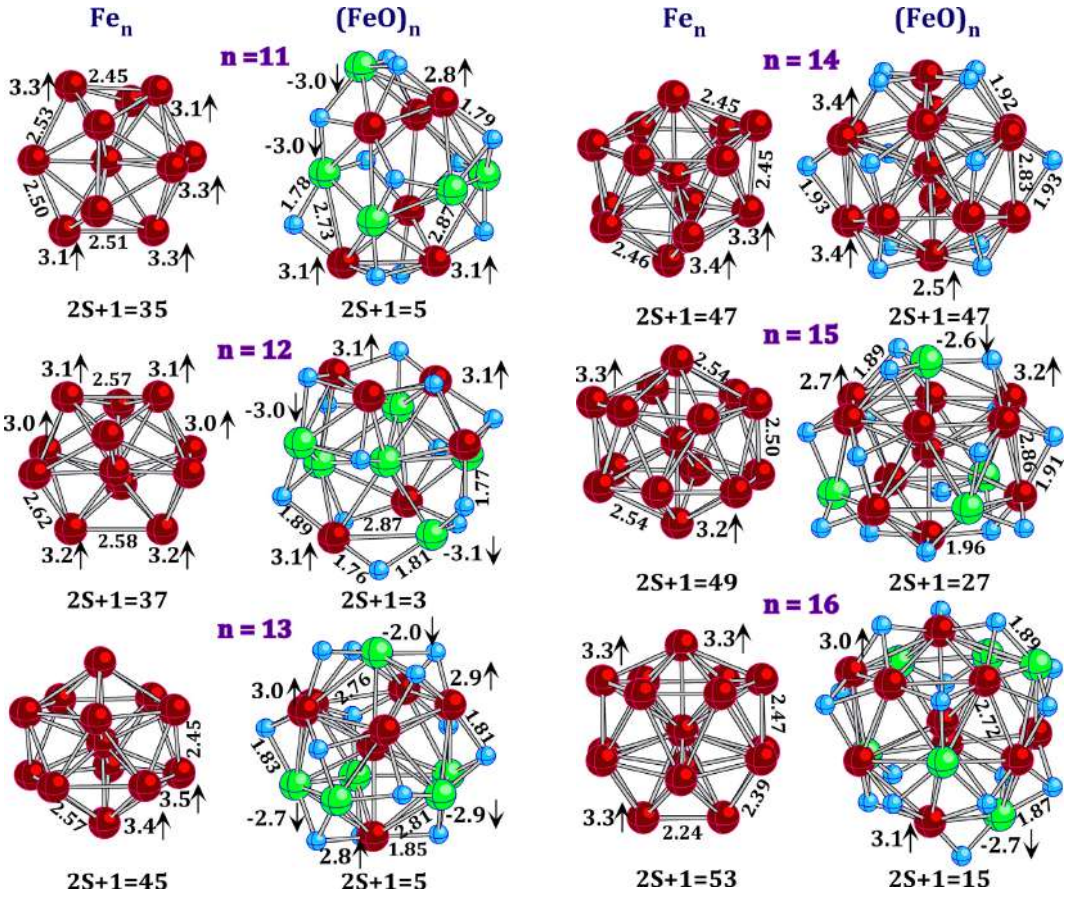

Figure 7.3: *Geometrical structures and local spin magnetic moments of the lowest total energy states of the Fe_n and $(FeO)_n$ clusters, $n = 11 - 16$. Bond lengths are in* Å *and local spin magnetic moments are in μ_B. Different colors are used for the iron atoms with spin-up and spin-down local magnetic moments. Adapted from [34].*

state 2+ indicates an O-to-Fe ratio close to 1, and further highlights the different behavior of the clusters with respect to bulk materials and metallic surfaces, where the FeO oxide phase is thermodynamically unstable.

The results reported in this chapter have been accepted for publication in the journal *Communications Chemistry*, with the title "The highest oxidation state observed in graphene-supported sub-nanometer iron oxide clusters".

7.1 Pristine clusters, BEs and potential reactivity

Fe_n^+ clusters with $n = 11, 12, 13, 15$ and 20 were produced with ENAC and deposited on GR/Ru, where they are electrically neutralized. The cluster sizes were chosen to compare the properties of some remarkable clusters, such those composed of magic number of atoms (Fe_{13} and Fe_{15} [19]) or Fe_{12}, whose oxide is particularly stable [35]. Moreover, we included Fe_{11} and Fe_{20} to make a comparison also for non-magic clusters of different sizes. The interaction of Fe with Gr is of intermediate strength compared to Ag (weak) and Pt (strong) [40], suggesting that the Fe−C interaction may not be completely negligible. On this regard, it was recently reported that a hybridization

occurs between Fe and C atoms at the interface that provides stability to the clusters [41]. However, the substrate-induced changes in the electronic properties are much smaller, but still noticeable, for the oxidized $(FeO)_n$. The total cluster coverage for all the depositions was kept to about one cluster each 9 moiré unit cells, following the same procedure adopted in the previous chapters.

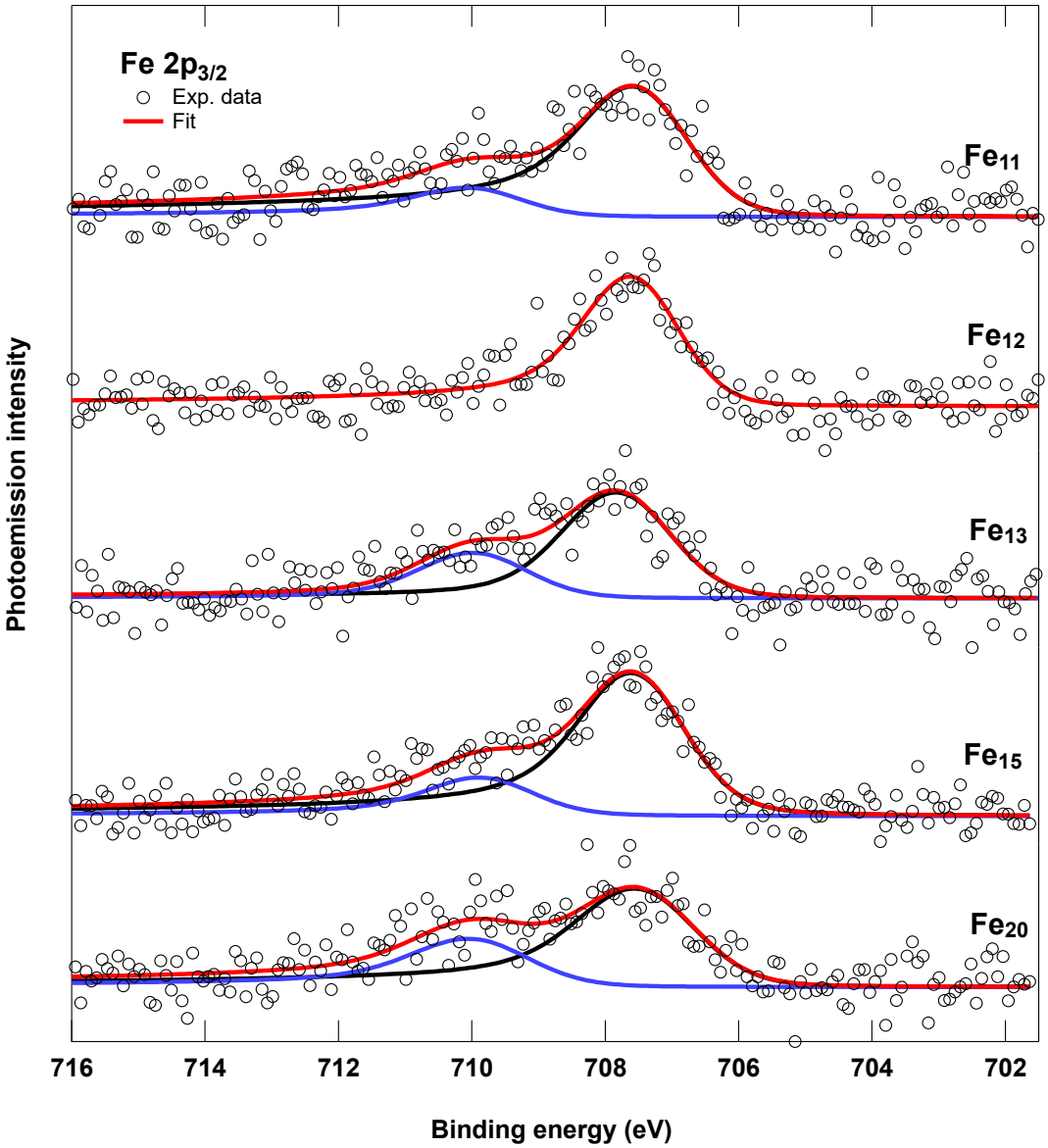

Figure 7.4: *Fe $2p_{3/2}$ XPS core level spectra of the as-deposited size-selected Fe_n clusters acquired with a photon energy of 800 eV and at T = 20 K.*

The Fe $2p_{3/2}$ core level spectra of the as-deposited clusters are reported in Fig. 7.4, together with the best fit and the spectral components. Compared to the spectra acquired for Ag_n and Pt_n clusters, the signal-to-noise ratio is noticeably lower. This is due to several factors such as the lower photon flux at the SuperESCA beamline at the energy used to study the Fe $2p_{3/2}$ core level (800 eV), and the lower photoionization cross section and larger intrinsic broadening of 2p core levels compared to the 3d and 4f core levels that we measured for the other clusters. Therefore, the analysis was

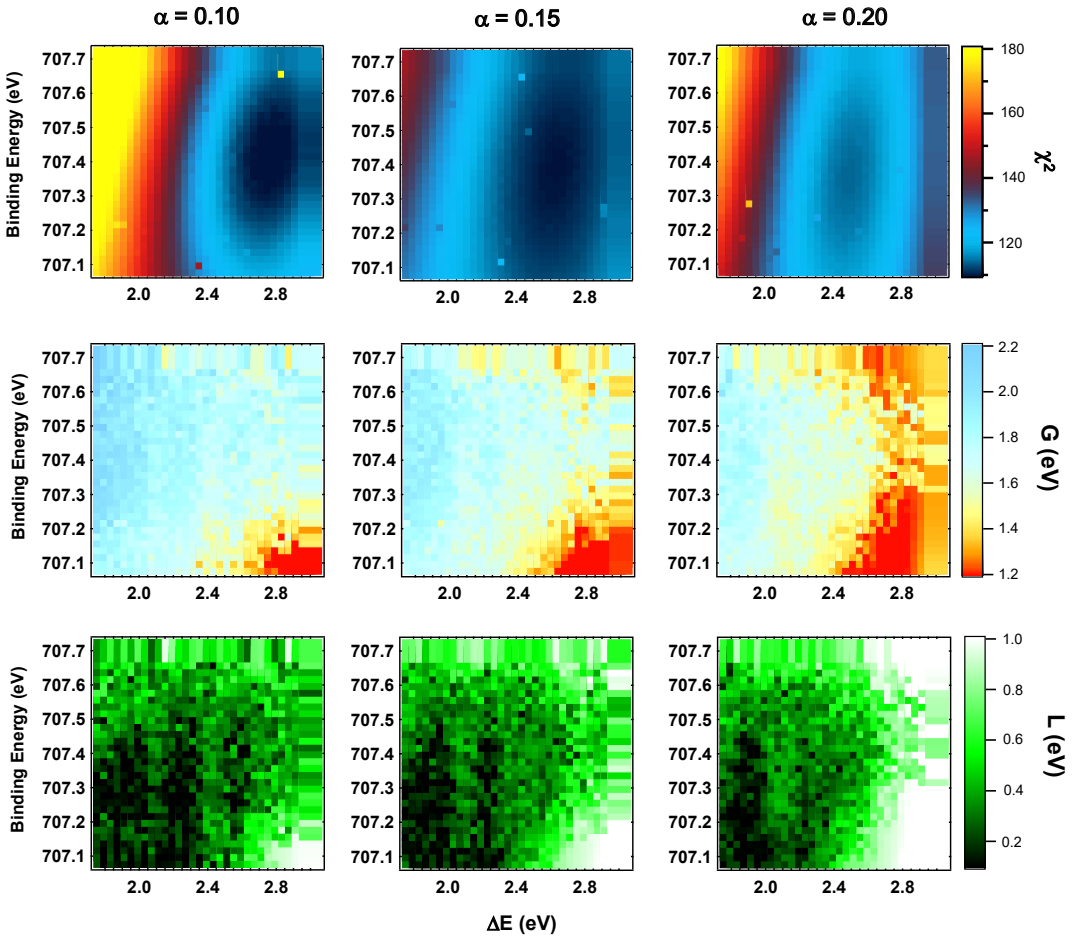

Figure 7.5: *Fe $2p_{3/2}$ XPS core level spectra of the as-deposited size-selected Fe_n clusters acquired with a photon energy of 800 eV at T = 20 K.*

	BE (eV)	Γ (eV)	G (eV)	α
Fe_{11}	707.38; 709.87	0.22 ± 0.03	1.63 ± 0.16	0.22 ± 0.03
Fe_{12}	707.50	0.17 ± 0.05	1.51 ± 0.10	0.15 ± 0.05
Fe_{13}	707.77 ; 709.92	0.21 ± 0.03	1.76 ± 0.3	0.21 ± 0.02
Fe_{15}	707.47; 709.75	0.37 ± 0.04	1.58 ± 0.28	0.15 ± 0.05
Fe_{20}	707.38; 709.87	0.24 ± 0.03	1.83 ± 0.22	0.24 ± 0.02

Table 7.1: *Fitting parameters obtained from the spectral analysis of the Fe $2p_{3/2}$ core levels of the as-deposited clusters. The error associated to the BEs is 0.08 eV.*

performed by adopting a novel procedure aiming to obtain reliable information not only on the Fe $2p_{3/2}$ core level BEs and on the number of non-equivalent components, but also of the core level photoemission line shape parameters. Specifically, each spectrum was fitted with Doniach-Šunjić lines following a 4-step procedure. In each step, a cross-evaluation of two parameters of the Doniach-Šunjić lines was performed based on the χ^2 maps obtained by fitting the data with the remaining parameters fixed to different values within a reasonable range. For example, Fe_{15} was fitted with

two components separated by an energy ΔE. In the first step of the analysis, the Gaussian (G) and Lorentzian (L) widths were used as free parameters in several fitting cycles where the remaining parameters (BE, ΔE and the asymmetry parameter α) where fixed and combined in several different ways. By doing so, we obtained a G, L and χ^2 value for each combination of BE, ΔE, α (Fig. 7.5). Based on this result, we selected the G parameter associated to the best χ^2 among all the combinations and kept G fixed to this value for the following steps. Similarly, in the second step we obtained the best BE, in the third step we obtained α and finally, in the fourth step we obtained L and ΔE.

The spectral analysis indicates the presence of two different components for each of the investigated clusters besides Fe_{12}. The position of the low BE component, which exhibits most of the spectral weight (Fig. 7.4, black lines), is affected non-monotonically by the cluster size, ranging from 707.38 eV for Fe_{11} and Fe_{20} up to 707.77 eV for Fe_{13} (Tab. 7.1). We associated this component to Fe atoms in a metallic state. They show a positive CLS up to $\sim$ 1.1 eV with respect to the bulk value (706.7 eV) [42], and to Fe(110) (706.3 eV) and Fe(100) (706.5) films grown on Cu(100) ([43]). This is consistent with the typical trend of supported size-selected clusters that we discussed in the previous chapters, where initial- and final-state effects shift the BEs to higher values [44–46]. In the specific case of 3d metals such as Fe, it was reported that initial-state effects induced by lattice strain may affect the BEs to a larger extent than in the case of heavier metals [47, 48]. For Cu, Ag and Au clusters composed of 13 atoms, it was calculated that a negative strain of 6 % induces a positive CLS of 0.72, 0.52 and 0.50 eV, respectively. The average bond lengths in Fe_n clusters with $10 \leq n \leq 20$ is typically $\sim$ 2.5 Å [21, 34], which correspond to a reduction of $\sim$ 9 % with respect to the bulk lattice parameter $a = 2.86$ Å [49]. Given the Fe $2p_{3/2}$ CLSs that we measured, which are within the range 0.68 - 1.07 eV, we can deduce that initial-state effects arising from lattice strain play the main role in the Fe_n clusters BEs. As a matter of fact, given the metallicity of the GR/Ru substrate we do not expect a relevant final-state contribution arising from charging effects [46].

If the CLSs are dominated by initial-state effects, then they can be linked to the chemical properties of the clusters [44]. Initial state effects are rich in chemical information as they depend also on the modifications of the d-band center, a well-known indicator of chemical reactivity [13]. In particular, higher BEs can be associated to higher stability, while lower BEs can predict an higher chemical reactivity. To investigate this aspect, we compared the trends of the Fe $2p_{3/2}$ with the asymmetry parameter α obtained from the fitting analysis. The α parameter in the Doniach-Šunjić function, which describe the probability to excite electron-hole pairs, is related to the density of states at the Fermi energy [50] and thus to the chemical reactivity of the system [51].

In Fig. 7.6 the trend of the Fe $2p_{3/2}$ CLS (black, left axis) and α parameter (blue, axis on the right hand side) are displayed for the different cluster sizes that we studied. The two parameters follow very similar trends, suggesting a correlation. In particular, Fe_{13} shows the largest CLS (+1.07 eV) and lowest α (0.07), thus suggesting that this cluster is the most stable among the examined ones. This result is not surprising, but confirm the gas-phase experimental and theoretical studies which predicted that 13 is a magic number for Fe clusters, therefore it is associated to a particularly stable configuration and low chemical reactivity [18–21]. According to the trend of the CLS and α parameter, the most reactive clusters are Fe_{11} and Fe_{20}, which both show a BE CLS of +0.68 eV and α = 0.22 and 0.17, respectively. Clusters composed of

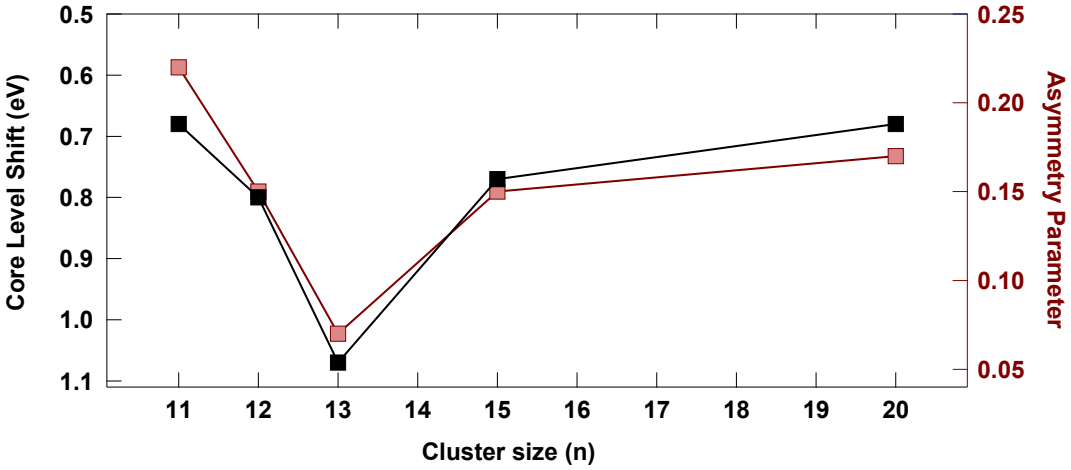

Figure 7.6: *Fe $2p_{3/2}$ CLS (black, left axis) and asymmetry parameters α (red, right axis) of the graphene-supported Fe_n clusters.*

$n = 20$ atoms were found to be particularly reactive also in the case of Pd_n clusters supported on TiO_2, suggesting that this cluster size could be more generally linked to enhanced reactivity.

Finally, the spectral analysis shows that the Gaussian width G assumes values within the range 1.51 and 1.83 eV. As discussed in the previous chapters, it is common for supported clusters to show large G width in their core level spectra. In the case of Fe, another contribution that could contribute to increase G comes from unresolved multiplets that are typically adopted to fit the Fe $2p_{3/2}$ spectra of magnetized Fe single crystal surfaces. In particular, this core level can be fitted with four components associated to the m_j = -3/2, -1/2, 1/2 and 3/2 quantum numbers [52]. However, there is no consensus in literature on the energy splitting of these components for the crystalline surfaces of Fe (ranging from 0.3 to 1.0 eV) [53]. Therefore, rather than fitting the XPS spectra of the clusters with 4 different components, with an energy splittings set as free parameters, we decided to use a single component, whose G width also takes into account the possible presence of multiplet splitting.

7.2 Cluster oxidation and final stoichiometry

The second components observed in the as-deposited spectra, which are shifted with respect to the main peak by $\sim$ 2.3 eV (on average) can be related to a partial oxidation of the clusters upon deposition, similarly to what we observed for Pt_n clusters. This is confirmed after the complete oxidation of the clusters achieved with a O_2 exposure of 1 L at T = 20 K and after irradiating the sample for 45 minutes with X-rays ($h\nu = 800$ eV) to obtain atomic oxygen. The Fe $2p_{3/2}$ spectra acquired after the oxidation are shown in Fig 7.7. The oxidation induces a CLS towards higher BEs, confirming the well-established trend found for Fe surfaces [29, 54, 55]. The oxidized spectra are centered at similar BEs as the second components of the as-deposited clusters, confirming that they were indeed related to a partial oxidation of the clusters.

The Fe $2p_{3/2}$ core level spectra of oxidized Fe_{11}, Fe_{12} and Fe_{15} clusters can be fitted using a single component, while an additional component at higher BE (green

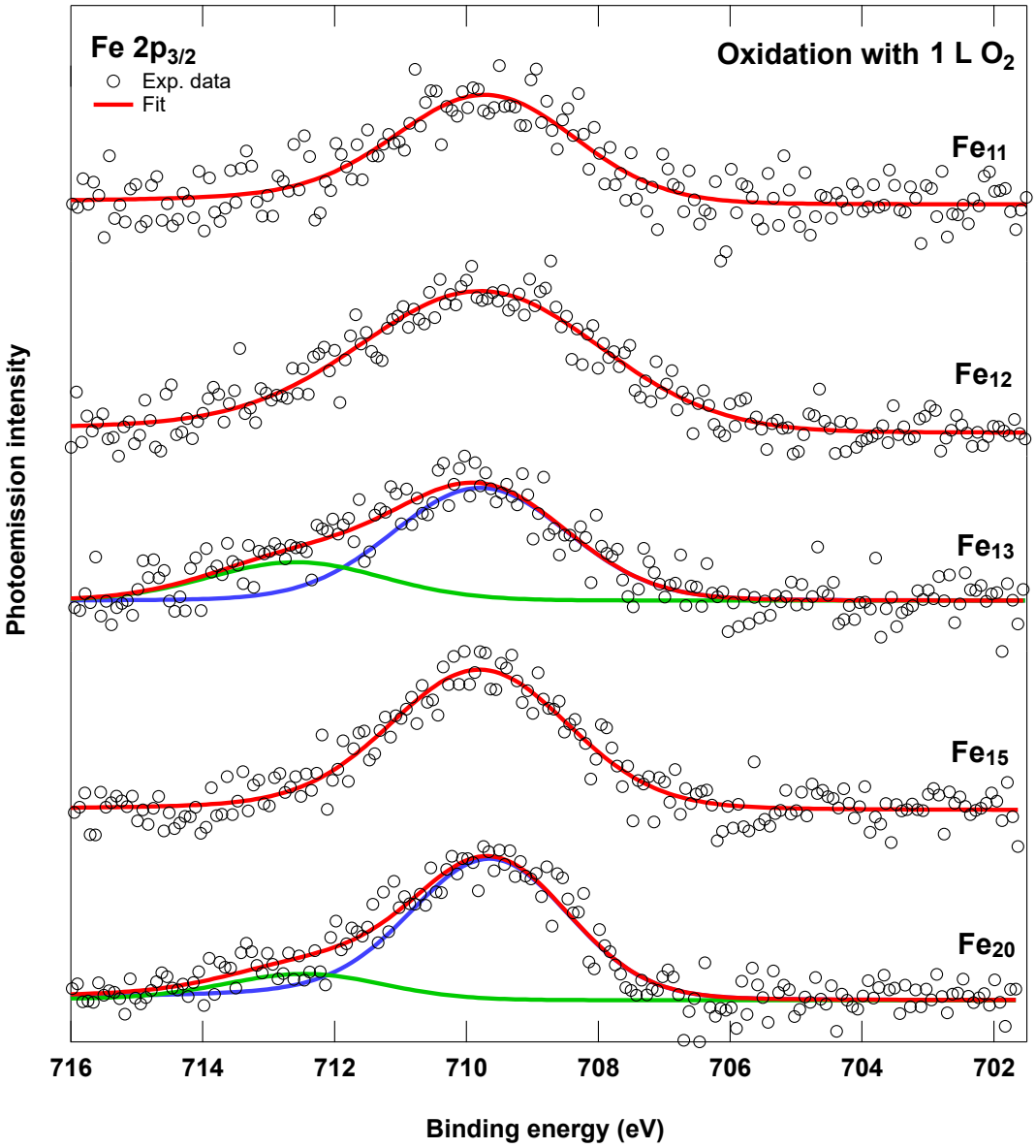

Figure 7.7: *Fe $2p_{3/2}$ XPS core level spectra of the oxidized size-selected Fe_n clusters acquired with a photon energy of 800 eV and at $T = 20$ K.*

line curve) has to be included to fit the oxidized Fe_{13} and Fe_{20} clusters spectra. As it happened for the BEs of the metallic clusters, the Fe $2p_{3/2}$ BE of oxidized spectra is affected by the cluster size. The main components are centered at BEs ranging from 709.58 eV for Fe_{11} up to 709.79 eV for Fe_{13} (Tab. 7.2). They still show a positive CLS with respect to oxidized bulk and surfaces, although in a smaller extent than in the metallic case. The reduced CLS for the oxidized clusters is consistent with the results discussed in the previous chapters, where we have observed that oxidized clusters are more similar to their bulk counterparts than they were in the metallic phase. In particular, this can be related to the dominant role played by Fe−O bonds and charge transfer between Fe and O in determining the $2p_{3/2}$ BE of the clusters with respect to the global structure and metallic coordination. For example, while the Fe−Fe distances in the clusters are on average 9 % shorter than in bulk Fe, the

	BE (eV)	Γ (eV)	G (eV)	α
Fe_{11}	709.62	0.22 ± 0.02	3.04 ± 0.02	0.06 ± 0.02
Fe_{12}	709.68	0.17 ± 0.05	4.12 ± 0.02	0.05 ± 0.05
Fe_{13}	709.79 ; 712.59	0.21 ± 0.02	3.01 ± 0.20	0.00 ± 0.01
Fe_{15}	709.27	0.37 ± 0.03	2.97 ± 0.28	0.02 ± 0.01
Fe_{20}	709.58; 712.39	0.24 ± 0.02	2.63 ± 0.20	0.05 ± 0.02

Table 7.2: *Fitting parameters obtained from the spectral analysis of the Fe $2p_{3/2}$ core levels of the oxidized clusters. The error associated to the BEs is 0.08 eV.*

Fe−O bond lengths in oxidized $(FeO)_n$ clusters (1.81 - 1.96 Å)[34] are similar to the values calculated for the O adsorption on a Fe(110) surface (1.78 - 1.91 Å) [56]. When adsorbed on graphene, the Fe−O bond lengths in the clusters do not appreciably change with respect to the gas-phase [41].

By comparison with previous XPS experiments, the main component in the oxidized spectra can be associate to Fe(II) cations (BE = 709.5 eV) [42, 57]. Therefore, since the clusters on graphene are electrically neutral and the vast majority of the Fe atoms present an oxidation state 2+, and given the usual oxidation state 2- for O anions on the clusters, we can conclude that the Fe-to-O ratio is close to 1, with a final stoichiometry close to $(FeO)_n$. If the ratio were higher, i. e., there were more Fe than O atoms, we would have expected to observe an additional spectral component associated to metallic Fe atoms or to atoms with a lower oxidation state. For example, the cage-like structure that was proposed for the $Fe_{13}O_8$ oxidized cluster contains a metallic Fe atom in its core [58]. Since from our spectra we can disregard the presence of atoms in the metallic state, we can exclude a similar Fe:O ratio. At the same time, if we had more O than Fe atoms in our clusters, we would expect to observe a component in the Fe $2p_{3/2}$ spectra compatible with a higher oxidation state. This is what happens in the case of Fe_{13} and Fe_{20}, where a small second component at 712.59 and 712.39 eV was observed. It is not trivial to unambiguously interpret these components, given their low contribution to the total spectral intensity (less than 20 %). However, we can exclude that they could arise from the formation of Fe(III) ions in the clusters, which typically show a lower BE around 711 eV [57]. On the contrary, it could originate from oxidized Fe atoms at the cluster/graphene. As a matter of fact, Fe(II) ions composing the material known as siderite ($FeCO_3$), show a BE of ∼ 712 eV [42]. In this material Fe and C are not binding directly, but through an O atom. Therefore, a structure with an O atom adsorbed in a bridge site between the clusters and the graphene layer could induce the formation of a Fe $2p_{3/2}$ component above 712 eV, such as those that we measure.

From the spectral analysis it is not possible to resolve the presence of oxidized clusters with a stoichiometry of Fe_nO_{n+1} or Fe_nO_{n+2}, which ware found for positively charged oxidized Fe clusters on the gas-phase [31]. However, the Gaussian widths of the spectra, which are larger than in the metallic phase and can be as high as 4 eV for Fe_{12}, suggests that similar small fluctuations on the Fe-to-O ratio could also be obtained. The large G values do not allow to test the presence of clusters with stoichiometries Fe_nO_{n+1} or Fe_nO_{n+2}, which were found in previous works on positively charged oxidized Fe clusters in the gas-phase [31]. Moreover, the G width could be affected by the presence of several oxidized isomers. For example, the cage-

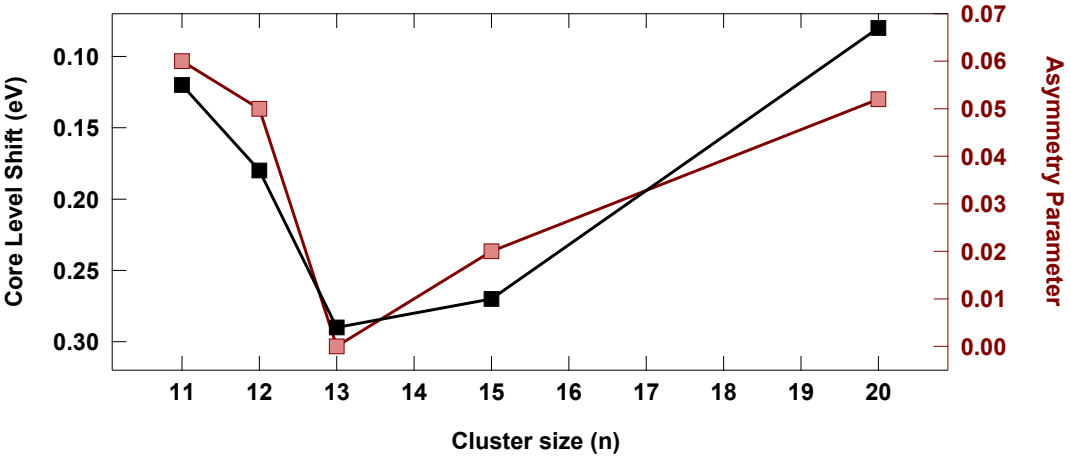

Figure 7.8: *Fe $2p_{3/2}$ CLS (black, left axis) and asymmetry parameters α (red, right axis) of the oxidized graphene-supported Fe_n clusters.*

shaped minimum energy configuration of $Fe_{12}O_{12}$ is favored by just 0.07 eV with respect of two tower structures composed of 3×3 and 4×4 rings which are nearly degenerate, with an energy difference of just 0.01 eV [32].

Similarly to the metallic case, also for the oxidized clusters it is possible to correlate the Fe $2p_{3/2}$ CLSs (with respect to the FeO bulk oxide BE = 709.5 eV [42, 57]) to the chemical properties of the clusters through the asymmetry parameter α. Based on the comparison of the two parameters, which is shown in Fig. 7.8, oxidized Fe_{13} still appears to be the most stable cluster. Among the oxidized clusters in the gas-phase, $(FeO)_{12}$ was predicted to be surprisingly stable, with an energy gap of 2.00 eV [35]. However, our data indicates that the density of state at the Fermi level is not zero. This can be a consequence of having different isomers and to the interaction with graphene, which can reduce to zero the band gap in oxidized Fe clusters. This was calculated in the case of FeO and $(FeO)_2$ clusters, which had a energy gap respectively of 0.24 and 0.51 eV in the gas-phase, while it decreased to zero when the clusters were adsorbed on free-standing graphene [41].

7.3 Discussion: From gas-phase to supported $(FeO)_n$ clusters

Our experiment on the oxidation of supported Fe clusters returns similar results with respect to the oxidation in the gas-phase, where the $(FeO)_n$ stoichiometry was found to be particularly stable both experimentally [31] and with DFT calculations [34, 35]. This is a potentially relevant achievement towards the application of oxidized Fe clusters as graphene-supported catalysts, as it indicates that the properties of the clusters are only slightly affected by the interaction with the substrate. As a matter of fact, it was predicted by DFT calculations that the graphene-induced changes in the electronic properties of oxidize $(FeO)_n$ are smaller than for their metallic counterparts [41]. However, we have shown in the previous chapters that the corrugated morphology of the moiré lattice of graphene epitaxially grown on Ru(0001) or Ir(111) and the interaction with the metallic surface underneath could affect the properties of the clusters, both in terms of mobility and electronic properties.

Therefore, in to order deepen our knowledge of the system that we studied in this chapter, it is pivotal to extend DFT calculations for clusters not only on free-standing graphene, but also for the complete corrugated moiré cell of graphene on a metallic surface.

In the previous chapter, we discussed the role played by the square-planar PtO_4 units in determining the oxidation state in the clusters. This is the same unit observed also for the Ag clusters, although it corresponds to an higher oxidation state 3+. While for bulk materials, the PtO phase with a similar unit is not as stable as the PtO_2 phase (oxidation state 4+), this latter structure is composed of three-dimensional PtO_6 octahedra, which appear to be not easily obtainable at the sub-nanoscale as the three-dimensional geometry would require a major reconstruction of the Pt clusters. In the case of Fe_n, we can think of a similar scenario to rationalize the formation of the oxide FeO phase rather than Fe_2O_3. Contrary to Ag and Pt, Fe oxides do not present have square-planar unit, but both FeO and Fe_2O_3 are composed of Fe ions that bind with 6 O atoms each [28]. However, the unit cell of Fe_2O_3 accommodates 32 O^{2-} ions, while there are only 4 in the unit cell of FeO [28, 59]. Therefore, it seems reasonable to expect that the formation of such a large unit cell would be strongly unfavorable, hindering the formation of Fe(III) ions. This especially applies for Fe_n for $n \geq 12$, where DFT calculations have predicted for clusters in the gas-phase that the reconstruction of the gas-phase clusters into cage structures is less favorite than a simple chemisorption mechanism of O on the cluster surface [34].

7.4 Conclusion

Oxidized Fe clusters are interesting in a wide range of technological applications, but up to now their properties have been investigated mainly in the gas-phase. We applied the oxidation method based on the photo-induced dissociation of O_2 to extend the characterization on their oxidation process also to the case of graphene-supported Fe_n clusters ($n = 11, 12, 13, 15$ and 20) by means of high resolution XPS. Metallic Fe clusters show a Fe $2p_{3/2}$ CLS towards higher binding energies with respect to their bulk counter parts that can mainly attributed to initial-state effects due to lattice strain. Moreover, the CLSs can be related to the chemical reactivity of the system through a comparisons with the asymmetry parameter α obtained from an accurate fitting procedure performed with Doniach-Šunjić functions. In particular, the similar trend of the CLS and α for different cluster sizes allows to conclude that the magic Fe_{13} cluster is the most stable among the ones we studied, in agreement with the results obtained in the gas-phase. The BE of Fe clusters after the oxidation are more similar to bulk and surface oxide with respect to their metallic counterparts, following a similar behavior than oxidized Ag_n and Pt_n clusters that appear more similar to their bulk counterparts than they were in the metallic phase.

The complete disappearance of the metallic component in Fe $2p_{3/2}$ core level spectra of the oxidized clusters, which is paralleled by the growth of a single new component at higher BE consistent with the Fe(II) oxidation state is interpreted as the formation of Fe clusters with a stoichiometry close to $(FeO)_n$, in agreement with previous works on oxidized clusters in the gas-phase. In the case of Fe bulk or metallic surfaces, the formation of the FeO phase is less favorite than F_2O_3 (oxidation state Fe(III)), highlighting a difference between the oxidation of Fe at the sub-nanoscale.

References

[1] X. Zou and Y. Zhang, Noble metal-free hydrogen evolution catalysts for water splitting, Chem. Soc. Rev. **44**, 5148 (2015).

[2] N. Cherkasov, A. O. Ibhadon, and P. Fitzpatrick, A review of the existing and alternative methods for greener nitrogen fixation, Chem. Eng. Process. Process Intensif. **90**, 24 (2015).

[3] A. Zitolo, V. Goellner, V. Armel, M.-T. Sougrati, T. Mineva, L. Stievano, E. Fonda, and F. Jaouen, Identification of catalytic sites for oxygen reduction in iron- and nitrogen-doped graphene materials, Nat. Mater. **14**, 937 (2015).

[4] K. Sun, H. Shan, H. Neumann, G.-P. Lu, and M. Beller, Efficient iron single-atom catalysts for selective ammoxidation of alcohols to nitriles, Nat. Commun. **13**, 1848 (2022).

[5] S. Liu, C. Li, M. J. Zachman, Y. Zeng, H. Yu, B. Li, M. Wang, J. Braaten, J. Liu, H. M. Meyer, M. Lucero, A. J. Kropf, E. E. Alp, Q. Gong, Q. Shi, Z. Feng, H. Xu, G. Wang, D. J. Myers, J. Xie, D. A. Cullen, S. Litster, and G. Wu, Atomically dispersed iron sites with a nitrogen-carbon coating as highly active and durable oxygen reduction catalysts for fuel cells, Nat. Energy **7**, 652 (2022).

[6] F. Haber and G. van Oordt, Über die bildung von ammoniak den elementen, Z. Anorg. Chem. **44**, 341 (1905).

[7] G. Ertl, Reactions at surfaces: From atoms to complexity (nobel lecture), Angew. Chem. - Int. Ed. **47**, 3524 (2008).

[8] S. M. Bhutto and P. L. Holland, Dinitrogen activation and functionalization using β-diketiminate iron complexes, Eur. J. Inorg. Chem. **2019**, 1861 (2019).

[9] U. S. G. Survey and J. A. Ober, *Mineral commodity summaries 2018*, Tech. Rep. (Reston, VA, 2018).

[10] B. Kubias, M. Fait, and R. Schlögl, Handbook of heterogeneous catalysis, Handbook of Heterogeneous Catalysis. 2nd Edition, 571-583 (2008) 10.1002/9783527610044.hetcat0028 (2008).

[11] A. Hellman, E. J. Baerends, M. Biczysko, T. Bligaard, C. H. Christensen, D. C. Clary, S. Dahl, R. van Harrevelt, K. Honkala, H. Jonsson, G. J. Kroes, M. Luppi, U. Manthe, J. K. Nørskov, R. A. Olsen, J. Rossmeisl, E. Skúlason, C. S. Tautermann, A. J. C. Varandas, and J. K. Vincent, Predicting catalysis: Understanding ammonia synthesis from first-principles calculations, J. Phys. Chem. B **110**, 17719 (2006).

[12] G. Ertl, S. B. Lee, and M. Weiss, Kinetics of nitrogen adsorption on Fe(111), Surf. Sci. **114**, 515 (1982).

[13] B. Hammer and J. K. Nørskov, Theoretical surface science and catalysis–calculations and concepts, in *Advances in Catalysis*, Vol. 45 (Academic Press, 2000) pp. 71–129.

[14] J.-C. Liu, X.-L. Ma, Y. Li, Y.-G. Wang, H. Xiao, and J. Li, Heterogeneous Fe_3 single-cluster catalyst for ammonia synthesis via an associative mechanism, Nat. Commun. **9**, 1610 (2018).

[15] W. Ye, S. Chen, Y. Lin, L. Yang, S. Chen, X. Zheng, Z. Qi, C. Wang, R. Long, M. Chen, J. Zhu, P. Gao, L. Song, J. Jiang, and Y. Xiong, Precisely tuning the number of fe atoms in clusters on N-doped carbon toward acidic oxygen reduction reaction, Chem **5**, 2865 (2019).

[16] X. Wan, Q. Liu, J. Liu, S. Liu, X. Liu, L. Zheng, J. Shang, R. Yu, and J. Shui, Iron atom-cluster interactions increase activity and improve durability in Fe−N−C fuel cells, Nat. Commun. **13**, 2963 (2022).

[17] S. Tian, Q. Fu, W. Chen, Q. Feng, Z. Chen, J. Zhang, W.-C. Cheong, R. Yu, L. Gu, J. Dong, J. Luo, C. Chen, Q. Peng, C. Draxl, D. Wang, and Y. Li, Carbon nitride supported Fe_2 cluster catalysts with superior performance for alkene epoxidation, Nat. Commun. **9**, 2353 (2018).

[18] L. Wang, H. Cheng, and J. Fan, Photoelectron spectroscopy of size-selected transition metal clusters: Fe_n, n = 3 - 24, J. Chem. Phys. **102**, 9480 (1995).

[19] G. L. Gutsev, C. A. Weatherford, P. Jena, E. Johnson, and B. R. Ramachandran, Structure and properties of Fe_n, Fe_n^-, and Fe_n^+ clusters, n = 7-20, J. Phys. Chem. A **116**, 10218 (2012).

[20] M. Sakurai, K. Watanabe, K. Sumiyama, and K. Suzuki, Magic numbers in transition metal (Fe, Ti, Zr, Nb, and Ta) clusters observed by time-of-flight mass spectrometry, J. Chem. Phys. **111**, 235 (1999).

[21] O. Diéguez, M. M. G. Alemany, C. Rey, P. Ordejón, and L. J. Gallego, Density-functional calculations of the structures, binding energies, and magnetic moments of Fe clusters with 2 to 17 atoms, Phys. Rev. B **63**, 205407 (2001).

[22] A. Aktürk and A. Sebetci, BH−DFTB/DFT calculations for iron clusters, AIP Adv. **6**, 055103 (2016).

[23] H. Haberland, *Clusters of Atoms and Molecules: Theory, Experiment, and Clusters of Atoms*, Springer Series in Chemical Physics (Springer Berlin Heidelberg, 2013).

[24] W. Xue, Z.-C. Wang, S.-G. He, Y. Xie, and E. R. Bernstein, Experimental and theoretical study of the reactions between small neutral iron oxide clusters and carbon monoxide, J. Am. Chem. Soc. **130**, 15879 (2008).

[25] A. Steinfeld, S. Sanders, and R. Palumbo, Design aspects of solar thermochemical engineering–a case study: Two-step water-splitting cycle using the Fe_3O_4/FeO redox system, Sol. Energy **65**, 43 (1999).

[26] M. Zhu and I. E. Wachs, Iron-based catalysts for the high-temperature water-gas shift (HT−WGS) reaction: A review, ACS Catal. **6**, 722 (2016).

[27] H. J., Ferrous iron oxide as a geochemical energy source, Nat. Resour. **6**, 115 (2016).

[28] R. Cornell and U. Schwertmann, *The Iron Oxides: Structure, Properties, Reactions, Occurrences and Uses*, Wiley Online Library (Wiley, 2003).

[29] S. J. Roosendaal, B. van Asselen, J. W. Elsenaar, A. M. Vredenberg, and F. H. P. M. Habraken, The oxidation state of Fe(100) after initial oxidation in O_2, Surf. Sci. **442**, 329 (1999).

[30] R. Subbaraman, S. A. Deshmukh, and S. K. R. S. Sankaranarayanan, Atomistic insights into early stage oxidation and nanoscale oxide growth on Fe(100), Fe(111) and Fe(110) surfaces, J. Phys. Chem. C **117**, 5195 (2013).

[31] D. N. Shin, Y. Matsuda, and E. R. Bernstein, On the iron oxide neutral cluster distribution in the gas phase. I. detection through 193 nm multiphoton ionization, J. Chem. Phys. **120**, 4150 (2004).

[32] N. O. Jones, B. V. Reddy, F. Rasouli, and S. N. Khanna, Erratum: Structural growth in iron oxide clusters: Rings, towers, and hollow drums, Phys. Rev. B **73**, 119901 (2006).

[33] G. L. Gutsev, K. G. Belay, K. V. Bozhenko, L. G. Gutsev, and B. R. Ramachandran, A comparative study of small 3d-metal oxide $(FeO)_n$, $(CoO)_n$, and $(NiO)_n$ clusters, Phys. Chem. Chem. Phys. **18**, 27858 (2016).

[34] G. L. Gutsev, K. G. Belay, L. G. Gutsev, and B. R. Ramachandran, Geometrical and magnetic structure of iron oxide clusters $(FeO)_n$ for n>10, Comp. Mater. Sci. **137**, 134 (2017).

[35] X. Yu, X. Zhang, and X.-W. Yan, Stability of the $Fe_{12}O_{12}$ cluster, Nano Res. **11**, 3574 (2018).

[36] J.-J. Chen, Z. Yuan, X.-N. Li, and S.-G. He, A vuv photoionization time-of-flight mass spectrometer for the formation, distribution, and reaction of nano-sized neutral metal oxide clusters, Int. J. Mass Spectrom. **422**, 98 (2017).

[37] S.-Y. Lv, Q.-Y. Liu, J.-J. Chen, and S.-G. He, Oxidation of isoprene by neutral iron oxide nanoclusters in the gas phase, J. Phys. Chem. C **123**, 25949 (2019).

[38] J. M. Garcia, R. E. Shaffer, and S. G. Sayres, Ultrafast pump–probe spectroscopy of neutral Fe_nO_m clusters (n, m $<$ 16), Phys. Chem. Chem. Phys. **22**, 24624 (2020).

[39] C. Dong, Y. Li, D. Cheng, M. Zhang, J. Liu, Y.-G. Wang, D. Xiao, and D. Ma, Supported metal clusters: Fabrication and application in heterogeneous catalysis, ACS Catal. **10**, 11011 (2020).

[40] X. Liu, C. Z. Wang, M. Hupalo, W. C. Lu, M. C. Tringides, Y. X. Yao, and K. M. Ho, Metals on graphene: correlation between adatom adsorption behavior and growth morphology, Phys. Chem. Chem. Phys. **14**, 9157 (2012).

[41] A. Bano, L. Patra, and R. Pandey, Stability and electronic properties of the graphene-supported FeO nanostructures including clusters and monolayer, Appl. Surf. Sci. **569**, 150976 (2021).

[42] M. C. Biesinger, B. P. Payne, A. P. Grosvenor, L. W. M. Lau, A. R. Gerson, and R. S. C. Smart, Resolving surface chemical states in XPS analysis of first row transition metals, oxides and hydroxides: Cr, Mn, Fe, Co and Ni, Appl. Surf. Sci. **257**, 2717 (2011).

[43] R. d. Mendonça, M. D. Martins, M. Silly, F. Sirotti, and W. A. A. Macedo, A photoemission spectroscopy study of the initial oxidation of epitaxial fcc and bcc Fe films grown on cu(100), Thin Solid Films **636**, 567 (2017).

[44] W. E. Kaden, T. Wu, W. A. Kunkel, and S. L. Anderson, Electronic structure controls reactivity of size-selected Pd clusters adsorbed on TiO_2 surfaces, Science **326**, 826 (2009).

[45] S. Peters, S. Peredkov, B. Balkaya, N. Ferretti, A. Savci, A. Vollmer, M. Neeb, and W. Eberhardt, Inner-shell photoionization spectroscopy on deposited metal clusters using soft x-ray synchrotron radiation: An experimental setup, Rev. Sci. Instrum. **80**, 125106 (2009).

[46] Y. Watanabe, X. Wu, H. Hirata, and N. Isomura, Size-dependent catalytic activity and geometries of size-selected Pt clusters on TiO_2(110) surfaces, Catal. Sci. Technol. **1**, 1490 (2011).

[47] B. Richter, H. Kuhlenbeck, H.-J. Freund, and P. S. Bagus, Cluster core-level binding-energy shifts: The role of lattice strain, Phys. Rev. Lett. **93**, 026805 (2004).

[48] P. S. Bagus, A. Wieckowski, and H. Freund, The contribution of lattice strain to core-level binding energy shifts in metal nanoparticles: Generality and origin of the shifts, Comput. Theor. Chem. **987**, 22 (2012).

[49] W. P. Davey, Precision measurements of the lattice constants of twelve common metals, Phys. Rev. **25**, 753 (1925).

[50] S. Doniach and M. Sunjic, Many-electron singularity in x-ray photoemission and x-ray line spectra from metals, J. Phys. C: Solid State Phys. **3**, 285 (1970).

[51] R. Van Santen and M. Neurock, Concepts in theoretical heterogeneous catalytic reactivity, Cataly. Rev. **37**, 557 (1995).

[52] G. Rossi, G. Panaccione, F. Sirotti, S. Lizzit, A. Baraldi, and G. Paolucci, Magnetic dichroism in the angular distribution of Fe 2p and 3p photoelectrons: Empirical support to zeeman-like analysis, Phys. Rev. B **55**, 11488 (1997).

[53] J. Weissenrieder, M. Göthelid, M. Månsson, H. von Schenck, O. Tjernberg, and U. O. Karlsson, Oxygen structures on Fe(110), Surf. Sci. **527**, 163 (2003).

[54] T.-C. Lin, G. Seshadri, and J. A. Kelber, A consistent method for quantitative XPS peak analysis of thin oxide films on clean polycrystalline iron surfaces, Appl. Surf. Sci. **119**, 83 (1997).

[55] R. Davies, D. Edwards, J. Gräfe, L. Gilbert, P. Davies, G. Hutchings, and M. Bowker, The oxidation of Fe(111), Surf. Sci. **605**, 1754 (2011).

[56] T. Ossowski and A. Kiejna, Oxygen adsorption on Fe(110) surface revisited, Surf. Sci. **637-638**, 35 (2015).

[57] A. P. Grosvenor, B. A. Kobe, M. C. Biesinger, and N. S. McIntyre, Investigation of multiplet splitting of Fe 2p XPS spectra and bonding in iron compounds, Surf. Interface Anal. **36**, 1564 (2004).

[58] Q. Sun, Q. Wang, K. Parlinski, J. Z. Yu, Y. Hashi, X. G. Gong, and Y. Kawazoe, First-principles studies on the intrinsic stability of the magic $Fe_{13}O_8$ cluster, Phys. Rev. B **61**, 5781 (2000).

[59] G. S. Parkinson, Iron oxide surfaces, Surf. Sci. Rep. **71**, 272 (2016).

CHAPTER 8

Conclusions and future perspectives

Within my PhD project, the commissioning of the cluster source ENAC was finally completed. This exciting result allowed to perform the experiments reported in this thesis using ENAC in combination with the SuperESCA beamline, which together represent a unique experimental apparatus to investigate the properties of size-selected clusters by means of high-resolution XPS.

The capabilities of this experimental setup were first tested by studying the adsorption of size-selected Ag_n clusters on bare Ru(0001) at room temperature, where we looked for size-related features in the Ag $3d_{5/2}$ core level spectra. Thanks to the support of DFT calculations, it was possible to associate small Ag $3d_{5/2}$ CLSs to different structures formed by the clusters on the surfaces. In particular, their high mobility on Ru(0001) induces the formation of 2D islands with an average in-plane coordination number that is determined by the cluster size and shape. The possibility to tune the density of under-coordinated atoms in nanostructures using clusters as building block is particularly promising given the importance of the coordination number in determining the chemical properties of a material.

Afterwards, we moved to experiments focused on the main scientific topic of my PhD, the oxidation of graphene-supported size-selected clusters. We selected three different elements based on their technological relevance, especially in heterogeneous catalysis, and spectroscopic properties: Ag, Pt and Fe. Our choice was also based on the different atomic masses of these elements, spanning from 56 amu for Fe, up to 195 amu for Pt, which allowed to further test the capabilities of ENAC in working with different transition metals. The graphene template was selected for its low interaction with the clusters and it was epitaxially grown on the surface of transition metals where it forms a corrugated moiré lattice which reduces the mobility of the clusters. In the case of Ag and Fe clusters, graphene was grown on Ru(0001), which is one of the substrates with the highest corrugation and diffusion barriers. Pt clusters where deposited on graphene/Ir(111) because the Pt 4f core level overlaps with the Ru 4s, but the lower corrugation of this template was compensated by the higher interaction of Pt with graphene.

The previous study on bare Ru(0001) highlighted the high mobility of the clusters at room temperature, therefore the experiments were performed at extremely low temperature (T = 20 K) to prevent sintering and preserve the mass selection. However, the oxidation of the clusters at this temperature is particularly challenging, since none of them are able the dissociate O_2 molecules at T = 20 K. To overcome this limitation, we adopted a method based on the photo-induced dissociation of physisorbed O_2 to obtain atomic oxygen in UHV. This method was previously used to oxidize noble

metal surfaces and nanostructures, but it has been implemented for the first time in this thesis to obtain a high degree of oxidation in supported size-selected clusters. A key ingredient to reach this result was the possibility to study the clusters produced with ENAC *in situ*, which allowed to always keep the sample at T = 20 K and in UHV to drastically reduce the cluster mobility and the presence of contaminants.

The analysis described in chapter 4, 6 and 7 for Ag, Pt and Fe clusters highlights the general trend of the oxidized clusters at the sub-nanoscale to assume a final conformation typical of the MO (M = Ag, Pt, Fe) oxide phase. This is particularly interesting since this phase is not the most favorite at larger scales, where Ag_2O, PtO_2 and Fe_2O_3 are respectively preferred. In particular, the DFT calculations on both Ag_n and Pt_n clusters highlighted the formation of square-shaped MO_4 bulk motifs, with a metallic atom surrounded by four oxygen atoms. This is the building block of Ag_2O_3 and AgO bulk oxides, but the hybrid structure of the oxidized clusters, with the simultaneous presence of atoms in the oxidation state 3+ and 1+, indicates that the clusters are more similar to AgO. In the case of Pt, the PtO_4 motif is typical of both PtO and Pt_3O_4, two oxides with similar oxidation states and Pt−O bond lengths. Interestingly, the higher interaction of Pt with GR/Ir led to an asymmetric oxidation, with the atoms at the interface that were almost unaffected by the oxygen exposures (especially for larger clusters) and the PtO_4 motifs that appears only in the topost layer of the cluster. On the contrary, the oxidation of Fe_n clusters was more similar to the case of Ag, since XPS measurements indicated that all the atoms reach the same oxidation state 2+ which corresponds to a stoichiometry close to $(FeO)_n$. The appearance of bulk motifs at this scale is a clear difference with respect to metallic clusters, which are characterized by peculiar shapes based, for example, on icosahedral geometries. This information can be potentially relevant for the tailor-made growth of nanocatalysts based on these material and to incorporate sub-nanometric clusters in important catalytic reactions.

Besides the analogies with bulk oxides, in chapter 5 we studied the core level shift anomaly of Ag in size-selected Ag_7 and Ag_{11} clusters, finding that the typical trend of the Ag $3d_{5/2}$ core level for increasing oxygen densities does not apply at this scale. This anomaly, as well as the formation of bulk motifs, seems to be related to the fact that the clusters can be completely oxidized, without a distinction between surface and bulk atoms. Therefore, one could speculate that this anomaly will persist until the clusters reach a structure with a well defined surface that prevents the oxidation of the core. It is not trivial to predict a precise cluster size where this would happen, but a similar analysis could inspire future works.

Our experimental outcomes highlighted, also in the case of high-resolution XPS performed with synchrotron radiation, the large Gaussian broadening characteristic of small size-selected clusters compared to surfaces and nanomaterials. This feature does not allow to obtain an atomistic understanding on the electronic and geometric properties of the clusters based entirely on the experimental XPS data, but required a major support by DFT calculations. To make progress towards a more complete experimental characterization on the cluster, it would be extremely useful to support the XPS data with other techniques. The data reported in this thesis are entirely based on XPS since the SuperESCA beamline is specialized on this experimental technique and, up to date, ENAC can be connected only to this beamline. However, several other spectroscopic techniques based on synchrotron radiation are available at this beamline. A prime example is X-ray absorption spectroscopy (XAS), a widely used technique to investigate the local geometric and/or electronic properties of mat-

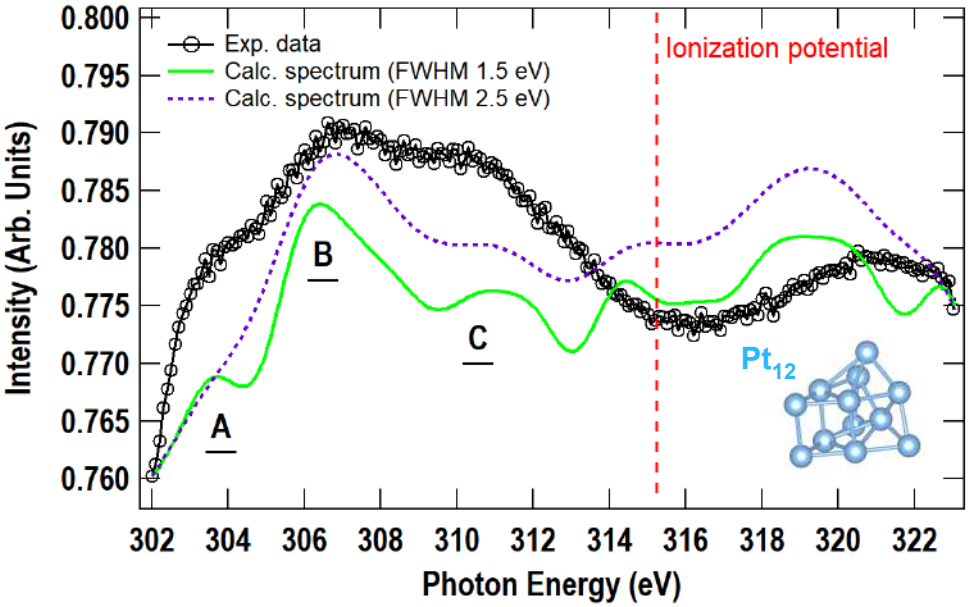

Figure 8.1: *Comparison of the experimental and theoretical NEXAFS spectra for the N5 edge of the Pt_{12} cluster (shown in the insertion). The experimental spectra (black circles) are acquired at T = 77 K and with the cluster deposited on Gr/Ru. The theoretical data (green and dashed purple line, see text) are performed for the cluster adsorbed on free-standing graphene.*

ter [1, 2]. The photon energy available at the SuperESCA beamline is not optimized for XAS experiments, which often require energies of several thousand of eV, and therefore it is not trivial to be able to study the clusters at a coverage as low as those used in this thesis (less than 0.1% ML). Nevertheless, we recently tested this technique to stady the NEXAFS region (near-edge X-ray absorption spectroscopy) of the $N5$ edge of a Pt_{12} cluster deposited on Gr/Ru, which corresponds to the excitation of the Pt $4d_{5/2}$ core level.

The spectrum that we obtained is shown in Fig. 8.1, together with the geometry of the cluster and with a comparison with theoretical calculations (convoluted with Gaussian functions with different FWHM) on the same cluster performed in collaboration with the group of Prof. Mauro Stener, from the University of Trieste. The comparison of the theoretical and experimental results is very promising in the NEXAFS region that precedes the ionization potential, where theory predicts the three distinct features (labeled A, B and C) that are observed in the experimental spectrum. The analysis of the theoretical data is not yet complete, and other calculations are scheduled to verify the behavior of these features also if Pt_{12} isomers and different rotations are considered. Nevertheless, this preliminary result indicates that XAS experiments can also be performed *in situ* at the SuperESCA beamline to support the XPS data.

Several upgrades are scheduled for the upcoming months to further increase the experimental techniques that can be used to characterize the clusters. In particular, ENAC will soon be connected to the main chamber of the nmLab through a preparation chamber equipped with a manipulator that will allow to transfer the samples

a position where clusters can be deposited into the main experimental chamber of the nmLab. In this chamber, it will be possible to threat the sample with different gasses and to perform XPS measurements using a conventional X-ray source. Moreover, the chamber is equipped with a spot profile analysis low-energy electron diffraction (SPA-LEED) apparatus, which allows to investigate the long range order of the cluster on a sample. In addition, a new low-temperature scanning tunneling microscopy apparatus will be installed in the upcoming months, giving the possibility to support the information on the electronic properties acquired at the SuperESCA beamline with data regarding the structure and dispersion of the clusters on the surface. In particular, this combined approach will be instrumental to find solutions to maintain the clusters mono-dispersed in given experimental conditions that can then be investigated by XPS. A similar result would allow to find adequate templates and conditions where it is possible to avoid sintering also at room or higher temperatures and at higher pressures. Such achievement would be particularly relevant as it would open to the possibility of characterizing the clusters in conditions closer to their technological applications as catalysts. As a matter of fact, the conditions used to study their oxidation in this thesis, i.e., UHV and T = 20 K, are optimized to understand their fundamental behavior, but far from real applications. Finally, having more control on the mobility of the clusters at different temperatures would allow to exploit the vacuum suitcase that will be connected to ENAC in the nmLab and that will be used to transport several samples to different beamlines of Elettra and to other synchrotron facilities. This will permit to further expand the range of experimental techniques that can be used to study, for example, the magnetic properties of the clusters or to perform near ambient pressure XPS measurements and open to a new, wide range of possible discoveries.

References

[1] J. Evans, *X-ray Absorption Spectroscopy for the Chemical and Materials Sciences* (Wiley, 2018).

[2] D. Popmintchev, B. R. Galloway, M.-C. Chen, F. Dollar, C. A. Mancuso, A. Hankla, L. Miaja-Avila, G. O'Neil, J. M. Shaw, G. Fan, S. Ališauskas, G. Andriukaitis, T. Balčiunas, O. D. Mücke, A. Pugzlys, A. Baltuška, H. C. Kapteyn, T. Popmintchev, and M. M. Murnane, Near- and extended-edge x-ray-absorption fine-structure spectroscopy using ultrafast coherent high-order harmonic supercontinua, Phys. Rev. Lett. **120**, 093002 (2018).

[3] M. Benfatto and C. Meneghini, A close look into the low energy region of the xas spectra: The xanes region, in *Synchrotron Radiation: Basics, Methods and Applications*, edited by S. Mobilio, F. Boscherini, and C. Meneghini (Springer Berlin Heidelberg, Berlin, Heidelberg, 2015) pp. 213–240.

List of publications

Published on peer-reviewed journals

- L. Sbuelz, F. Loi, M. Pozzo, L. Bignardi, E. Nicolini, P. Lacovig, E. Tosi, S. Lizzit, A. Kartouzian, U. Heiz, D. Alfè, A. Baraldi, Atomic Undercoordination in Ag Islands on Ru(0001) Grown via Size-Selected Cluster Deposition: An Experimental and Theoretical High-Resolution Core-Level Photoemission Study, Journal of Physical Chemistry C **125**, 9556 (2021)

- F. Loi, M. Pozzo, L. Sbuelz, L. Bignardi, P. Lacovig, E. Tosi, S. Lizzit, A. Kartouzian, U. Heiz, D. Alfè, A. Baraldi, Oxidation at the Sub-nanoscale: Oxygen Adsorption on Graphene-Supported Size-Selected Ag Clusters, Journal of Materials Chemistry A **10**, 14594 (2022).

- F. Loi, M. Pozzo, L. Sbuelz, L. Bignardi, P. Lacovig, E. Tosi, S. Lizzit, A. Kartouzian, U. Heiz, R. Larciprete, D. Alfè, A. Baraldi, Breakdown of the Correlation Between Oxidation States and Core Electron Binding Energies at the Sub-nanoscale, Applied Surface Science **619**, 156755 (2023).

- D. Perco, F. Loi, L. Bignardi, L. Sbuelz, P. Lacovig, E. Tosi, S. Lizzit, A. Kartouzian, U. Heiz, A. Baraldi, The highest oxidation state observed in graphene-supported sub-nanometer Fe oxide clusters, Communications Chemistry, *accepted*.

In preparation

- F. Loi, M. Pozzo, L. Sbuelz, L. Bignardi, P. Lacovig, S. Lizzit, D. Alfè, A. Baraldi, Surface oxidation of size-selected Pt_n clusters on graphene.

- F. Loi, M. Pozzo, L. Sbuelz, L. Bignardi, P. Lacovig, E. Tosi, S. Lizzit, R. Larciprete, D. Alfè, A. Baraldi, Enolate or Epoxide? A spectroscopic fingerprint for the oxidation of epitaxial graphene on Ru(0001).

Other publications

- F. Loi, M. Pozzo, L. Sbuelz, L. Bignardi, P. Lacovig, E. Tosi, S. Lizzit, A. Kartouzian, U. Heiz, D. Alfè, A. Baraldi, The Smallest Silver Oxide, Elettra Highlights 2021-2022.

Acknowledgements

In this thesis I tried to summarize the main results and achievements of the three-years long (and a bit more) adventure that was my PhD. Just like any other trip in any other story, it would not have been the same without all the people that accompanied me through it and whom I met on the way. Therefore, I would like to spend few words to thank all the amazing people that contributed in making this adventure so unique and positive.

First of all, my deepest gratitude goes to my supervisor prof. Alessandro Baraldi for guiding me in these first years of my life as a young researcher and for teaching me the key role that human values play in turning a working environment into a place where to constantly grow as a person. Similarly, I would like to thank my co-supervisor dr. Luca Bignardi for the amazing scientist, mentor, co-worker, person and friend that he has been every day since I had the privilege of meeting him.

A heartfelt thank goes also to the people of the nmLab and SuperESCA teams with whom I had the pleasure to spend so much time and to fight so many battles to learn something about those small objects that we call clusters. Silvano and Paolo, for the invaluable assistance in so many moments of my PhD, and Luca Sbuelz, Ezequiel, Deborah, Andrea and Monika for making the time spent in the labs always so delightful (and, sometimes, delicious).

A special thanks goes to our international collaborators, in particular to prof. Dario Alfè, for his great passion in science and never ending desire to collaborate to uncover the mysteries of science, and to dr. Aras Kartouzian, for the fundamental support he has always been ready to provide and for giving me the opportunity to visit the laboratories of the TUM university.

Finally, I would like thank all the people outside the labs that helped, in different ways, in making the most out of the last three years: Matteo, Lorenzo, Giovanni, and all the people whom I had the privilege to meet at some point of my life and that I have the luck to call my friends.

Last but not least, thanks to my family for literally everything and thanks to Elena, for supporting me through writing this thesis and for being by my side.

To all of you goes my deepest and everlasting gratitude.